A SEARCH FOR NOVEL DECAY MODES IN 11-BERYLLIUM

By

Jason Tyler Surbrook

A DISSERTATION

Submitted to
Michigan State University
in partial fulfillment of the requirements
for the degree of

Physics and Astronomy – Doctor of Philosophy

2022

ABSTRACT

A SEARCH FOR NOVEL DECAY MODES IN 11-BERYLLIUM

By

Jason Tyler Surbrook

About a decade ago, the measurement of the decay products of ^{11}Be yielded an unexpectedly large abundance of ^{10}Be. The presence of ^{10}Be daughters was interpreted as a signature of the novel β^- -delayed proton emission. An alternative hypothesis soon followed, that free neutrons and loosely-bound neutrons in atomic nuclei may decay into unseen dark particles. This alternative hypothesis could explain the abundance of ^{10}Be daughters and the long-standing neutron lifetime puzzle. Such a hypothesis has impacts on the stability of neutron stars, elemental abundances from Big Bang nucleosynthesis, and physics beyond the Standard Model. In low-energy nuclear physics specifically, the new hypothesis brought a sharp focus to the behavior of nuclear systems near particle-emission thresholds and the mechanism of β^--delayed proton emission.

More recently, a number of experiments have been conducted with beams of short-lived ^{11}Be (13.8 s) and long-lived ^{10}Be (1.5 MYr) to measure directly the β^--delayed proton and β^--delayed α decays of ^{11}Be and related structure in ^{11}B. Similarly, many new theoretical calculations have made pre- and post-dictions on the energies and intensities of these decay channels in ^{11}Be. Most theoretical model calculations predict β^--delayed proton branching ratios smaller than reported by experiment. The branching ratio of the β^--delayed proton decay in ^{11}Be remains an open question.

At the National Superconducting Cyclotron Laboratory (NSCL), on the campus of Michigan State University, we used the Gaseous Detector with Germanium Tagging (GADGET) system to measure the β^--delayed charged particle decay of ^{11}Be, in search of the β^- -delayed proton decay. R-matrix calculations and Bayesian methods were employed to describe the competing (and far more frequent) β^--delayed α channel. This dissertation covers the experimental and analysis methods used to produce the second reported measurement of the novel β^- -delayed proton emission and early interpretation of this new result.

ACKNOWLEDGEMENTS

This portion will be updated in a future version of this document.

TABLE OF CONTENTS

LIST OF TABLES

LIST OF FIGURES

CHAPTER 1

THE ATOMIC NUCLEUS: A LABORATORY FOR FUNDAMENTAL INTERACTIONS

The focus of this dissertation is measurement of the novel β^--delayed proton ($\beta^- p$) decay in 11-beryllium, ^{11}Be. Concurrent to the work presented in this dissertation, many related investigations by other researchers were undertaken, and for a variety of scientific motivations. That is to say, the scientific interest in the ^{11}Be($\beta^- p$) decay has been and continues to be multi-faceted. This chapter will introduce the atomic nucleus as a laboratory of physical phenomena and set the stage for the unique case of ^{11}Be.

1.1 The Atomic Nucleus

The atom is the basic building block of the tangible, bulk matter that we interact with. By volume, the atom is dominated by a diffuse cloud of *electrons*, e^-, orbiting a central, dense nucleus. By mass, the atom is dominated by the atomic nucleus, which is a collection of tightly bound, strongly interacting *protons, p,* and *neutrons, n*. The number of protons, carrying positive charge, is the *atomic number, Z,* and the element classification of a nucleus. The number of electrically-neutral neutrons is the *isotone* or neutron number, N, classification of a nucleus. A specific number of protons and neutrons uniquely defines a nuclide and all nuclei of a particular nuclide are identical. The expression of a particular nuclide is often abbreviated to ${}^{A}_{Z}X$ or ${}^{A}X$, where the *mass number* $A = Z + N$ denotes the total number of *nucleons* and X is the chemical symbol. Thus 11-beryllium can be written as ^{11}Be. Beryllium, being the fourth element, has $Z = 4$ and $N = A - Z = 11 - 4 = 7$ neutrons. Naturally present beryllium is ^{9}Be and has $Z = 4$, $N = 5$.

More than 3000 unique isotopes have been observed, while some ~7000 are predicted to exist [9]. Each isotope has distinct properties such as mass, (charge) radius, magnetic moment, excitation spectra, and, for many, decay rates of various decay modes to more- stable isotopes. Many general features of nuclei can be predicted by placing a nucleus on the *Chart of the Nuclides*, which plots nuclei in a tile-mosaic fashion by their proton and neutron numbers. Figure 1.2 shows the Chart of

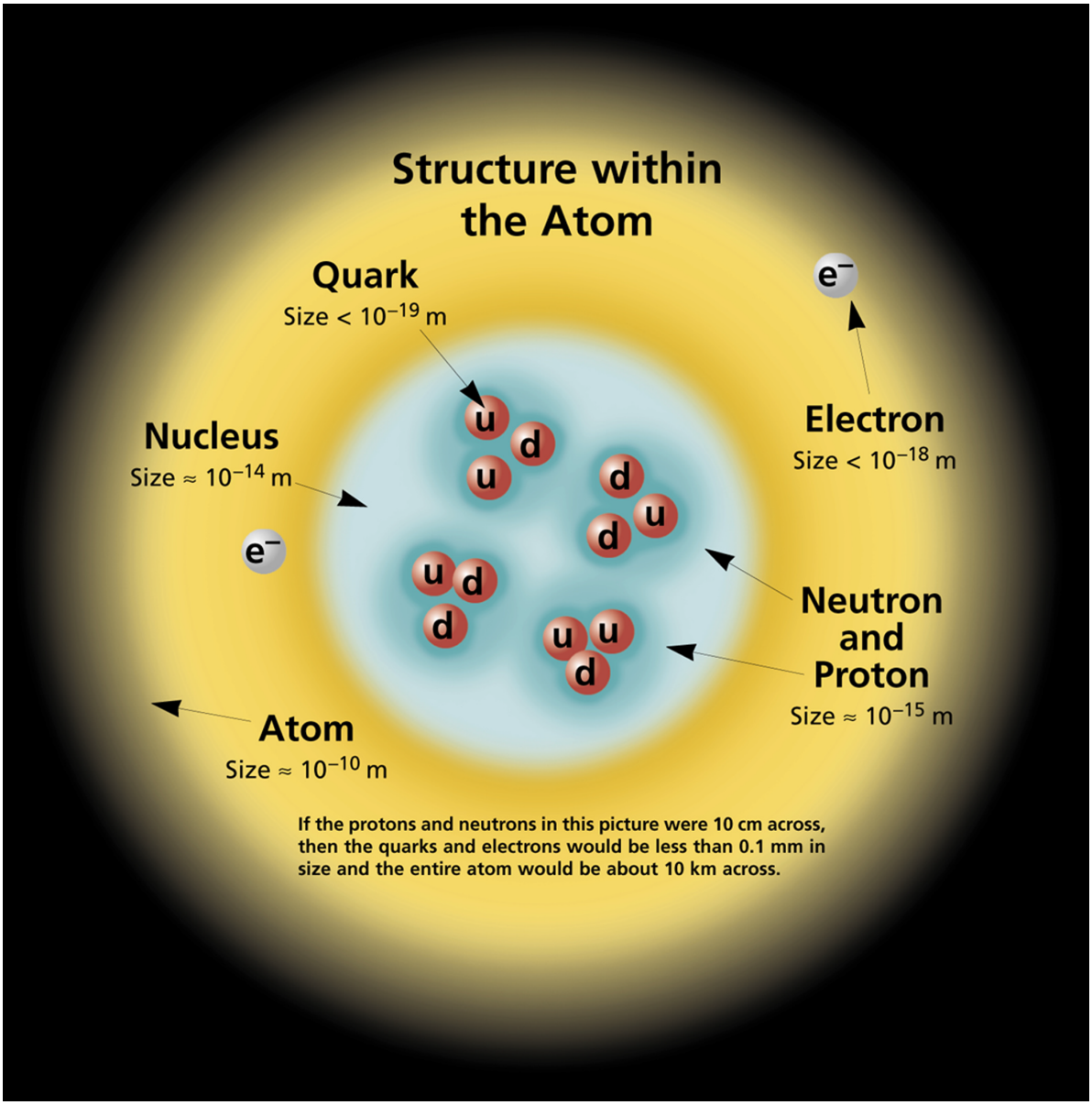

Figure 1.1: A cartoon diagram of a helium (He) atom and constituent subatomic particles with labels and approximate physical size. The atom is made of an electron cloud and an atomic nucleus. The atomic nucleus is made of protons and neutrons, which are composed of *quarks*. Protons are made of two *up* quarks and one *down* quark. Neutrons are made of one *up* quark and two *down* quarks. Figure Credit: Contemporary Physics Education Project, Lawrence Berkeley National Laboratory.

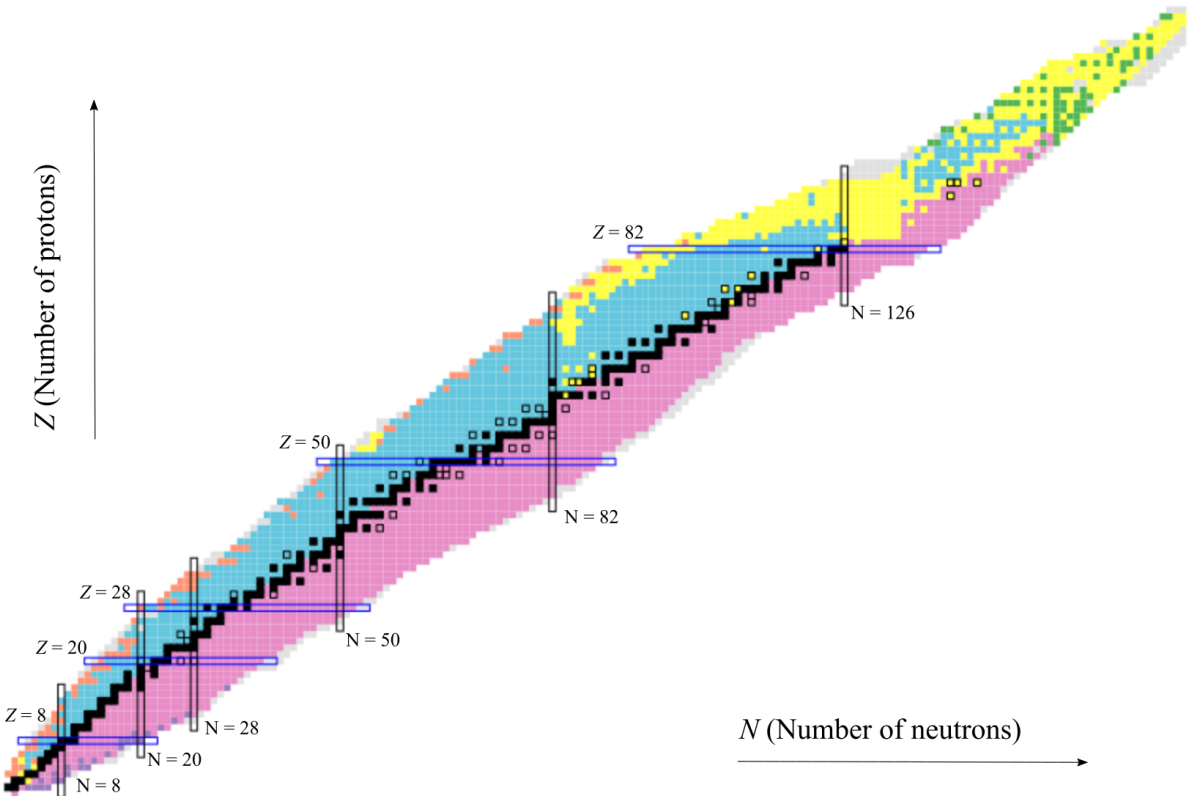

Figure 1.2: The Chart of the Nuclides. Nuclei are represented by colored squares, where the color depicts their primary decay mode. The colors represent: stable (black), β^+ or electron capture (blue), β^- (pink), α (yellow), spontaneous fission (green), spontaneous proton (orange), spontaneous neutron (purple), and unknown (grey). Black-outlined, color-filled squares are radioactive, but very long lived, in excess of 1 Billion years. Vertical and horizontal lines are so-called *magic* numbers. Figure Credit: National Nuclear Data Center (NNDC), Brookhaven National Laboratory.

the Nuclides, color coded for primary decay mode. For light nuclei of $A \lesssim 40$, nuclei are stable if $Z = N$ to within 1 unit or so. Above $A \sim 40$, the line of stability flattens and the stable nuclei tend to have greater number neutrons than protons. For most of the chart, nuclei that have greater Z than the stability line will undergo β^+ or electron capture decay, converting a proton into a neutron by emission of a β^+ particle (a high-energy positron) or capturing an electron, respectively, and emission of a neutrino. Similarly, most neutron-rich nuclei primarily decay by β^-, converting a neutron into a proton by emission of a β^- particle (a high-energy electron) and an anti-neutrino. Multi-step decays are possible too. β-delayed particle emission is the emission of a nuclear particle (a proton, neutron, α/He-nucleus, or others) immediately following a β decay.

For β-delayed particle emissions, there are strong patterns in the type of β decay and the emitted particle. The proton *separation energy*, or the energy required to remove a proton, is smaller when Z is large compared to N. Similarly, the neutron separation energy usually is large when Z is large compared to N. The converse of each of these statements is true (when Z is small relative to N). Putting all this together, β-delayed particle emissions are almost always β^+-delayed proton (β^+p) decays, β^--delayed neutron (β^-n) decays, β^+-delayed ($\beta^+\alpha$) decays, or β^--delayed ($\beta^-\alpha$) decays. In fact, prior to observation of ^{11}Be(β^-p) reported in 2019, no β^-p decay in any nucleus had been measured [3]. Our first was performed in May 2018 and, to our knowledge, was the very first measurement of the β^-p decay in the world. Those efforts and the follow-up measurement and analysis lead us to report the second ever measurement of the β^-p decay.

1.2 Motivating a Measurement of the Novel ^{11}Be(β^-p) Decay

In 2018, Fornal and Grinstein [10] noted that the decades-long, technique-specific discrepancy in neutron lifetime measurements [11, 12] could be reconciled alongside the then recent (2014) surprisingly large measurement of the the $^{11}\text{Be}\longrightarrow{}^{10}\text{Be}$ transmutation [5] measured by Accelerator Mass Spectrometry (AMS). The reconciliation was that the neutron may have a $\sim 1\%$ probability to decay into an ensemble of dark particles with mass less than, but within 1.665 MeV, of the neutron mass.

1.2.1 The Neutron Lifetime Problem

The lifetime of a particle is one of its most fundamental properties. Due to quark confinement, the proton and the neutron are among the simplest objects with which to study quark behavior. Protons and neutrons can exist as free particles or be bound into atomic nuclei. The free proton is observationally stable against radioactive decay with a decay lifetime of $> 7.7 \cdot 10^{33}$ years [13]. The free neutron however, is radioactive, and its lifetime is about 15 minutes. Furthermore, the neutron lifetime has consequences for big bang nucleosynthesis [14] and quark mixing behavior in the Standard Model [15]. There are two general techniques in which the neutron lifetime is

measured: the bottle technique and the beam technique [12].

In the bottle technique, *the lifetime of neutrons is measured*. Briefly, ultra-cold ($T < 100$neV) neutrons are confined in a material bottle or a magnetic bottle. Ideally, there are no mechanisms for the loss of the neutron except by the free decay of the neutron. A packet of neutrons is prepared and injected into this bottle and an amount of time Δt_1 elapses, during which the neutrons can decay. The neutrons are then ejected and counted, yielding the number of *remaining* neutrons N_1. The measurement is repeated for a different amount of holding time, Δt_2, yielding remaining neutrons N_2. If the bunches start with the same number of neutrons and the bottle is loss-less except that by neutron decay, then the decay lifetime can be calculated as:

$$\tau = \frac{\Delta t_2 - \Delta t_1}{\ln(N_1/N_2)} \tag{1.1}$$

In the beam method, *the rate of proton generation is measured* from a beam of cold neutrons entering a reflective electromagnetic trap. The neutron beam energy and length of the trap are known, so the time the neutrons spend in the electromagnetic trap is calculable. Neutrons decaying by their usual $n \rightarrow p + e^- + \bar{\nu}$ generate protons that are reflected by the electromagnetic trap and counted. Un-reacted neutrons pass through the trap and are measured. The rate of proton creation is proportional to the neutron flux and inversely to the $n \rightarrow p + e^- + \bar{\nu}$ lifetime:

$$\dot{N} = \frac{dN}{dt} = -\frac{N}{\tau_p} \tag{1.2}$$

If the only decay mode of the neutron is the usual Standard Model decay $n \rightarrow p + e^- + \bar{\nu}$, then the lifetimes measured by the disappearance of neutrons (bottle) and the appearance of protons (beam) should equal. However, as experiments using both techniques have improved and become more precise, there has emerged a discrepancy between the lifetimes extracted between the two measurements as large as 5σ statistical significance. The most recent bottle measurement lifetime value is $\tau_{\text{bottle}} = 877.75 \pm 0.28_{\text{stat}} + 0.22/-0.16_{\text{syst}}$ [16] and the most recent beam measurement is $\tau_{\text{beam}} = 887.7 \pm 1.2_{\text{stat}} \pm 1.9_{\text{syst}}$ [17].

If the assumption of the Standard Model decay $n \rightarrow p + e^- + \bar{\nu}$ is loosened, then the two measurements can be reconciled by a $\sim 1\%$ branch into unseen particles. The bottle measurement

would measure the total decay lifetime ($\tau_{\text{total}} \sim 877$ s), the beam measurement would measure the Standard Model process ($\tau_p \sim 887$ s), and the missing decay rate comes from the dark decay with lifetime of $\sim 8 \cdot 10^4$ s.

$$1/\tau_{\text{bottle}} = 1/\tau_{\text{beam}} + 1/\tau_{\text{dark}} \tag{1.3}$$

1.2.2 The Large ^{11}Be$\longrightarrow^{10}$Be Transmutation Rate

In 2014, an Accelerator Mass Spectrometry measurement of the decay products of a sample of radioactive ^{11}Be ($t_{1/2} = 13.8$s) decay products was performed. They measured the presence of ^{10}Be at a with a ^{11}Be$\longrightarrow^{10}$Be probability of $8.3(9) \cdot 10^{-6}$ [5], far in excess of the $\sim 3 \cdot 10^{-8}$ predicted of $\beta^- p$ beforehand by Baye and Tursunov [18]. The structure of ^{11}Be is unusual due to its low neutron separation energy of $S_n = 501.6(3)$ keV and valence s-wave neutron wavefunction. The confluence of these effects gives ^{11}Be an extended neutron halo that could enhance the $\beta^- p$ rate if the neutron were able to decay into the continuum, in a "quasi-free" way, and generate more ^{10}Be than previously expected. Similarly, if the valence neutron were to not decay by $\beta^- p$ but instead by a dark mechanism, the observed ^{10}Be production rate would be enhanced as both the $\beta^- p$ and dark decays produce ^{10}Be in their final states.

1.2.3 The Possibility of Dark Matter Decay in Nuclei

In the original paper, Formal and Grinstein suggested the possibility of detecting $n \rightarrow \chi_{\text{dark}}$ in nuclei with low neutron separation energies, $S_n < 1.665$ MeV. This was explored in greater detail by Pfützner and Riisager [19] and ^{11}Be was identified as the ideal candidate. Its low neutron separation energy $S_n = 501.6(3)$ MeV leaves most of the allowed decay energy requirement and its relatively long 13.8 s half-life allows time for hypothetical dark decays to have a branching ratio of up to $2.0 \cdot 10^{-4}$.

Since both the $\beta^- p$ and neutron dark decay create ^{10}Be in the final state, the distinguishing feature between the two channels is the emission (or not) of the visible β^- particle, proton, and ^{10}Be recoil. The recommendation to pursue measurements to disentangle visible and dark decays

in ^{11}Be was published in April 2018. We took our first ^{11}Be($\beta^- p$) data, *the* first ^{11}Be($\beta^- p$) data in May 2018.

1.3 Status of ^{11}Be($\beta^- p$) Decay

A great deal of work has been performed since May 2018. The subsequent chapters will describe my own contributions, but here is a summary of the work done by others.

Quickly after the neutron dark decay proposal, it was pointed out that this decay softened the nuclear equation of state and makes the existence of neutron stars above 0.7 $M_\odot$ (solar mass) stars difficult to explain [20, 21]. Neutron stars of $2M_\odot$ are restored if the dark matter can interact with the visible neutron star [22]. A recent review of baryon number violation in neutron stars can be found in [23].

The Standard Model predicts relations between different neutron β-decay observables. One is the relationship between the neutron lifetime and the angular correlation coefficient between the emitted β and $\bar{\nu_e}$, λ. Another input is the Ft value, which is determined most precisely by the $0^+ \rightarrow 0^+$ β-decay in nuclei such as ^{10}C, ^{14}O, ^{22}Mg, and ^{26m}Al [24]. The relation is

$$\tau = \frac{5172.3(31)\text{s}}{1 + 3 \cdot \lambda^2} \tag{1.4}$$

The world average of λ is $\lambda = -1.2754(11)$ and yields a neutron lifetime consistent with the bottle method and inconsistent with the beam method [25, 26]. There is tension with a recent measurement of the $\beta - \bar{\nu_e}$ asymmetry yielding $\lambda = -1.2677(28)$. This value implies the neutron lifetime to be consistent with the beam method and inconsistent with the bottle method [27].

In 2019, the first observation of $\beta^- p$ was reported in ^{11}Be($\beta^- p$) by Ayyad *et al.* [3]. They used a gaseous time projection chamber and measured a 178 keV proton from a stopped beam of ^{11}Be produced at by the Isotope Separation On Line (ISOL) technique at TRIUMF. From this proton measurement, they inferred a resonant state in ^{11}B at 196(20) keV above the proton separation threshold with width 12(5) keV and a $\beta^- p$ branching ratio of $b_p = 1.3(3) \cdot 10^{-5}$, consistent with the earlier AMS result of $8.3(9) \cdot 10^{-6}$ intensity for ^{10}Be creation.

In 2020, a series of measurements by the same AMS group refuted their earlier claim of ^{11}Be$\rightarrow^{10}$Be production at $8.3(9)\cdot10^{-6}$ and proposed a new limit for ^{10}Be production (by *all* decay mechanisms) of $< 2.2\cdot10^{-6}$ [28].

A number of nuclear structure theory efforts have been published to better clarify expectations around the Standard Model -allowed $\beta^- p$ decay, especially in light of these conflicting claims of the measured ^{11}Be($\beta^- p$) branching ratio.

In 2020, Volya [29] performed shell model calculations using the *psdu* and *fsu* Hamiltonians and reported no shell model states that could mediate the $\beta^- p$ at 196(20) keV observed in [3]. Between the small β decay energy window, competition from $\beta^-\alpha$ emission, and lack of a clear resonant state in ^{11}B, Volya concluded that $b_p \sim 5\cdot10^{-10}$, perhaps upwards of $b_p \sim 10^{-7}$ if a resonant state existed. Okołowicz *et al.* [30] performed calculations of ^{11}B structure with shell model embedded in the continuum (SMEC) [31] and found a candidate resonant state that could mediate the $\beta^- p$ at $E_p \sim 142$ keV, slightly lower than that measured in Ayyad *et al.* [3].

In 2021, Elkamhawy *et al.* [32] published Effective Field Theory calculations that reproduce the Baye and Tursunov [18] branching ratio of $b_p \sim 3\cdot10^{-8}$ to a factor of 2 for non-resonant $\beta^- p$. By assuming a resonance at $E_p = 196(20)$ keV, a branch of $b_p = 4.9^{+5.6}_{-2.9}$(experiment)$^{+4.0}_{-0.8}$(theory) with intrinsic width of $9.0^{+4.8}_{-3.3}$(ex.)$^{+5.3}_{-2.2}$(th.) keV was found, which is in excellent agreement with the measured branch $b_p = 1.3(3)\cdot10^{-5}$ and width of 12(5) keV.

In 2022, Okołowicz *et al.* [30] calculated a $\beta^- p$ branching ratio using SMEC as well as the interplay between the β feeding and proton-penetrability. They concluded that the $\beta^- p$ branching ratio and width measured in Ayyad *et al.* [3] are incompatible. They calculated the branch to be $b_p \sim 3\cdot10^{-7}$ after model tuning to the 12(5) keV intrinsic width of [3]. Atkinson *et al.* performed a no-core shell model calculation and found resonant states that could mediate the ^{11}Be($\beta^- p$), but calculate a small branching ratio of $b_p = 1.3(5)\cdot10^{-6}$ [33]. Finally, Le Ahn *et al.* calculated scattering properties of ^{10}Be+p with the method of self-consistent Skyrme Hartree-Fock in the continuum and inferred a resonant state in ^{11}B with energy of $E_p \sim 182$ keV and width $\Gamma \sim 6$ keV.

Experimentally, another couple of publications are worth noting. Ayyad et al. [34] performed

^{10}Be(p, p') resonant scattering. They performed an R-matrix fit [35] to their measurement and reported a resonance at $E_p = 171(20)$ keV with partial widths $\Gamma_p = 4.5(11)$ keV and total width $\Gamma_T = 16(3)$ keV. Similarly, Lopez-Saavedra *et al.* [36] performed a transfer reaction to a ^{11}B resonance with ^{10}Be$(d, n)^{10}$Be$+p$. They reported a resonant state at 211(40) keV with a small α width component. This small α component seems at odds with the small proton component of the proton resonance scattering measurement of Ayyad *et al.*, unless there are multiple states at *very* similar energies that were preferentially probed by the choice of production mechanism.

Generally, there seems to be building consensus between theory and experiment of a resonant state in ^{11}B capable of enhancing the ^{11}Be$(\beta^- p)$ rate. There is a spread of possible resonance energies from 140 keV to 210 keV. There is some tension in the width of this resonance. Perhaps most importantly, there is still only the one direct measurement of the ^{11}Be$(\beta^- p)$ branching ratio and it is incompatible with indirect measurements of the total ^{11}Be$\rightarrow$ ^{10}Be decay rate. Theory predictions are not unified in their predictions of the $\beta^- p$ branching ratio to even an order of magnitude. To clarify experimental inconsistencies and provide insight to the theory models predicting branching ratios, an independent measurement of the ^{11}Be$(\beta^- p)$ branching ratio, by direct detection of the $\beta^- p$ radiation, is sorely needed.

CHAPTER 2

EXPERIMENT: MEASURING THE NOVEL ^{11}Be(β^-p) RATE

The measurement of ^{11}Be(β^-p) is hallmarked by three experimental challenges: the short lifetime of ^{11}Be, requiring online production at a rare-isotope facility; the low rate and rare incidence of such decays and the resulting large backgrounds from more common decay processes; the low energy of emitted protons restricting the use of several classes of detectors frequently used in nuclear β-decay studies. This chapter will describe the facilities and equipment used in measurements conducted to measure ^{11}Be(β^-p) and their solutions to each of these challenges.

2.1 GADGET: The Gaseous Detector with Germanium Tagging

The Gaseous Detector with Germanium Tagging (GADGET) system [37] was developed to measure low-intensity, low-energy, β-delayed proton decays of radioactive nuclei, with the purpose of constraining thermonuclear reaction rates important to understanding of explosive nucleosynthesis. It has conducted several measurements of β^+, specifically, -delayed proton (β^+p) decays in nuclei of mass A=20-31 nuclei, measuring the emission of β-delayed protons as low as 200 keV [7, 6, 8] at the National Superconducting Cyclotron Laboratory (NSCL). The GADGET system is the synthesis of coupling the NSCL Segmented Germanium Array (SeGA), an array of high-resolution germanium crystal γ-ray detectors, with the Proton Detector, a gaseous proportional counter. SeGA is installed about the body of the Proton Detector in its “barrel" configuration. As will be explained, the coupling of these two detector systems enables our search of rare β-delayed charged particle events.

2.1.1 Proton Detector: Principle of Operation

The schematic of Figure 2.1 depicts the operational components of the Proton Detector. The detector is filled with a gas, which is selected for its desirable properties such as high electrical resistance and quenching of non-ionizing atomic and molecular excitations. The detector gas acts

as both a beam stopper/catcher as well as a medium which is ionized in the presence of charged particle radiation. An electric field is applied within the detector to drift positive ions to the detector cathode and freed electrons toward the MICROMEGAS detection pads at a constant velocity and without amplification. Electrons reaching the MICROMEGAS will pass through the Micromesh and enter the charge amplification region, with an electric field capable of inducing a *Townsend avalanche* which produces a measurable amount of charge to be measured by the MICROMEGAS anode.

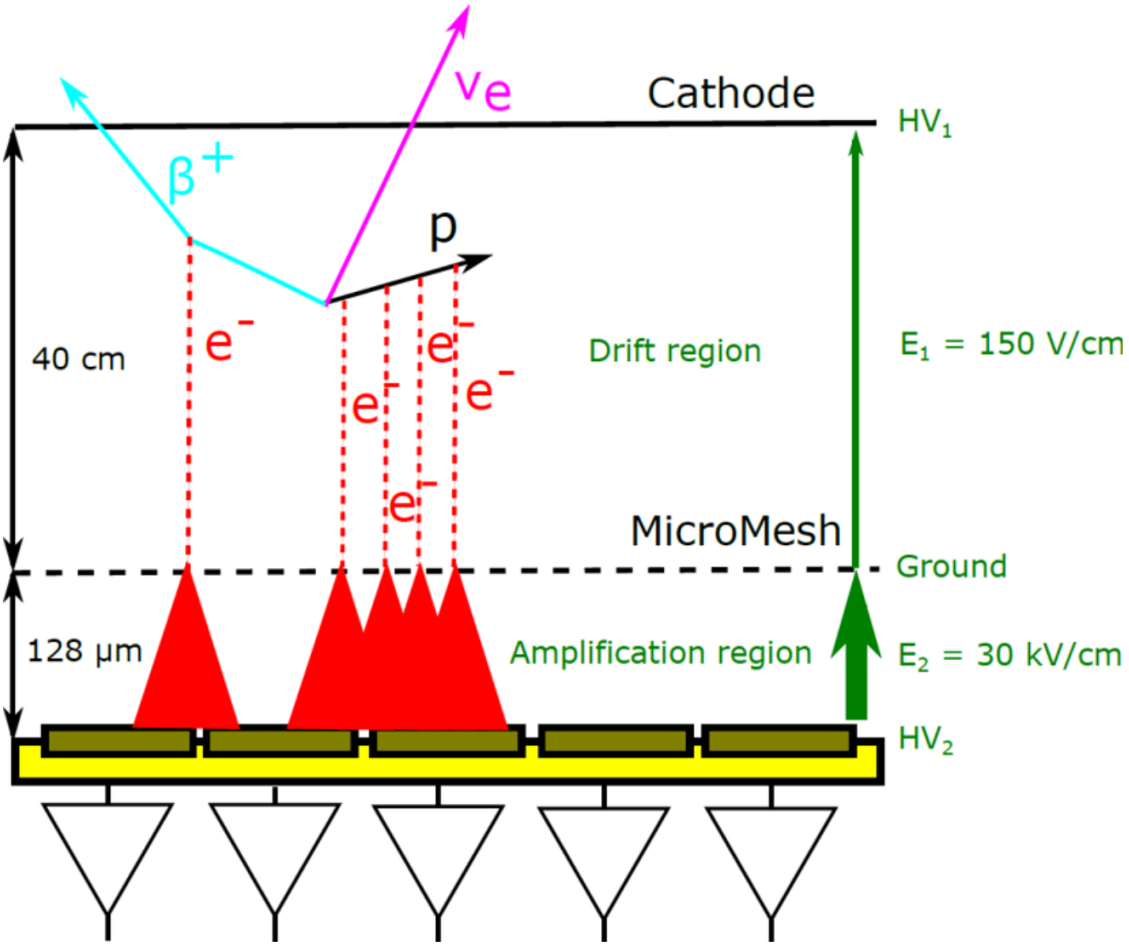

Figure 2.1: Schematic depicting the detection of a β^{+}p decay. β particle and proton (and any other, non-depicted charged particles) create ionization in the detector media gas. Liberated electrons are drifted, amplified in number, and detected my the MICROMEGAS pad (unlabeled, gold and yellow). Electric field numbers are representative of nominal operating conditions. See text for current electronics settings.

One important operational characteristic of the gas is its low density relative to other detectors such as plastic or glass scintillators and semiconductor materials such as silicon or germanium detectors. With their relativistic velocity and long tracks, emitted β radiations will typically deposit only a fraction of their kinetic energy in their gas before reaching the detector boundaries. Low-energy protons, α-particles, and the complementary nuclear residues will stop near the site of the decay, losing all of their energy to interactions with the gas within several milli- or centimeters. This suppression of the β spectrum allows measurement of β-delayed lights ions, such as protons and α particles, to lower energies than possible in higher-density detector media.

2.1.2 Proton Detector: Design

Figure 2.2 shows an undimensioned cut-away mechanical drawing. Key operational components are labeled. The body of the Proton Detector is a cylinder of stainless steel with dimensions of roughly 49 cm long by 16.5 cm in diameter. The detector active volume is roughly 40 cm in length and 10 cm in diameter. Radioactive beam enters through a 1.5 μm thick, 50.2 mm diameter aluminized mylar Kapton window in the upstream end cap. This end cap is also equipped with a high voltage feedthrough, which is coupled to the detector cathode, and four small gas outlets, which allow for the removal of detector gas. Along the interior of the detector volume is the electric field cage, which electrically connects the cathode to the MICROMEGAS Micromesh by Kapton sheet with printed copper bands, rolled into a cylinder and held in place with insulating polyether ether ketone (PEEK) material. The alternating conductive-resistive sections act as a voltage divider and help ensure a uniform electric drift field in the detector bulk. The gating grid is a wire grid before the MICROMEGAS and can be used to disrupt the electric drift field to protect the MICROMEGAS from large currents produced during beam deposition. The rear of the detector chamber has four gas inlets to introduce fresh gas, a valve for rough pumping of the detector, and voltage feedthroughs to control the MICROMEGAS anode and gating grid voltages. The downstream end is capped by the MICROMEGAS circuit board. The MICROMEGAS has two primary components: a gold plated copper anode and an electro-formed stainless steel micromesh supported by insulating pillars at

128 μm above the anode plane.

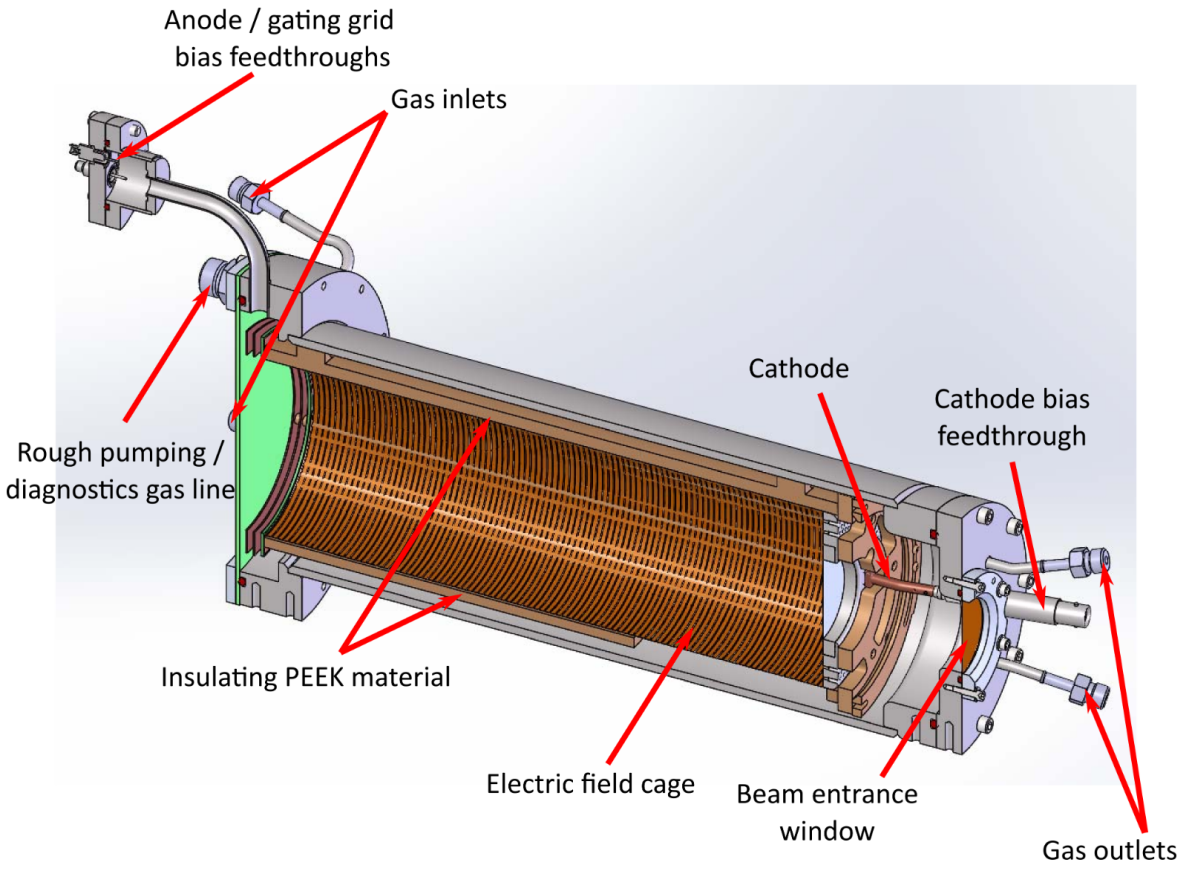

Figure 2.2: An undimensioned mechanical design drawing of the Proton Detector. Key operational components are labeled. The bulk of the detector is roughly 49 cm long by 16.5 cm in diameter, while the sensitive detection volume is roughly 40 cm by 10 cm in diameter.

The detector is cycled between beam-accepting and decay-measurement modes synchronously with the delivery of beam to the detector. The voltage on the gating grid is alternated to allow or prevent the passage of drifted electrons to the MICROMEGAS. In beam-accepting mode, a beam of radioisotopes is passed into the detector. Interactions between the impinging beam and the detector gas thermalize the beam. Nuclei of the beam may be neutralized and form neutral atoms, which then diffuse under Brownian motion until their radioactive decay. In the case of incomplete neutralization, positively-charged atoms will drift to the detector cathode. The gating grid voltage is set to 119 V, so ionization electrons created via beam stopping will drift to the gating grid, but not pass into the MICROMEGAS. In decay-measurement mode, the beam is no longer deposited

and the gating grid voltage is set to -225 V, to be electrically transparent with respect to the drift field and allow ionization electrons into the MICROMEGAS.

Component	z-axis position	beam-accepting voltage	decay-measurement voltage
Cathode	+40 cm	-4.8 kV	-4.8 kV
Gating Grid	+1.5 cm	119 V	-225 V
Micromesh	0 cm	0 V	0 V
Anode	-128 μm	330 V	330 V

Table 2.1: Voltage states for the Proton Detector components in beam-accepting and decay-measurement operation modes.

The geometry of the MICROMEGAS anodes is shown in Figure 2.3. The anodes are split into three concentric circles of radius 1.4, 4.0, 5.0 cm. The ring between 1.4 and 4.0 cm is segmented fourfold, every 90°. The ring between 4.0 and 5.0 cm is segmented eightfold, every 45°. The pads are labeled alphabetically, inwards to outwards, from A to M. Pad A is the singular pad in the radius 1.4 cm segmentation. Pads B, C, D, and E are identical quadrant pads between the radius 1.4 cm and 4.0 cm segmentations. The remaining eight pads are identical octal pads between the 4.0 cm and 5.0 cm radial segmentations. The large areas of Pads A-E make these the primary measurement pads, while the thin radial sizes of the outer octal Pads F-M make them useful diagnostics to, in software, exclude counting of events corresponding to charged-particle tracks that are not confined in the sensitive volume of the Proton Detector. The measurement pads may be operated independently for higher energy resolution and greater suppression of the β-particle background or jointly as a single interior pad for higher efficiency.

2.1.3 SeGA: The Segmented Germanium Array

The Segmented Germanium Array (SeGA) [38] is an array of high-resolution, coaxial high-purity germanium (HPGe), γ-ray detectors. HPGe detectors work under high-voltage bias. As a γ ray interacts with the Ge, typically in a photoelectric effect complete absorption or with a Compton-scatter which deposits only part of the incident γ energy, electrons are excited to the crystal's *conduction band* producing *electron-hole pairs*. The bias voltage drifts these to cathode(s) and

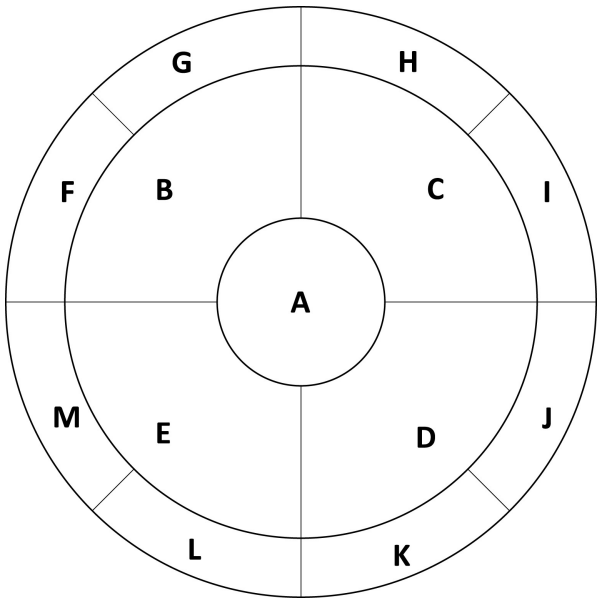

Figure 2.3: Diagram of the detector pad plane. The MICROMEGAS anode is segmented into 13 pads labeled alphabetically A-M. Pads A-E are used for measurements while F-M are diagnostic. The pad geometry is segmented radially at 1.4, 4.0, and 5.0 cm.

anode(s), respectively, where a current can be measured, ideally proportional to the number of liberated pairs and, in turn, the deposited γ-ray energy.

Ge is used for several desirable properties. First, Ge is a semiconductor, with electrical properties between that of common conductors and insulators. The *band gap* is the energy required to promote an electron in a crystal from the valence state to a conducting state. Ideal conductors have band gaps smaller than the Fermi energy of the valence electrons, so there always exist conduction electrons, and insulators have large band gaps on order the ionization energy, so there are never bound electrons in the conduction state. Semi-conductors, like Ge, have small band gaps, which allow application of biasing voltages to drift conduction electrons to readout electronics while also producing large numbers of charge carriers for an amount of deposited energy due to the low cost of promotion. The small band gap in (and large number of created charge carriers of) Ge gives HPGe detectors their excellent energy resolution as statistical fluctuations in the number of charge carriers shrink relative to the total as the total becomes large. One notable limitation of Ge's small band gap is the electrical current produced by thermal excitation of valence electrons, so HPGe detectors

must be operated at cryogenic temperatures involving refrigerators or LN2 (77K) cooling. Another desirable feature of HPGe is that it has a moderately high atomic number for a semi-conductor of $Z = 32$. The cross-section of MeV γ rays to interact with a material scale roughly as Z^2 of the material, so the *intrinsic efficiency* of Ge is higher than other semi-conductors including Si [39].

The segmentation of with SeGA gets its namesake is a 32-fold, 8-layer quadrant segmentation. This segmentation allows for position reconstruction of a γ-ray event in the detector, which can be useful for Doppler reconstruction of γ rays produced in fast beam experiments. As our nuclei were stopped, only the central contact carrying the total current in the crystal was recorded in our measurements.

2.2 Measurements at the National Superconducting Cyclotron Laboratory

^{11}Be is a radionuclide with a half-live of just 13.76(7) s. This short half-life requires that ^{11}Be must be produced in the same laboratory as experimental studies of it. Two measurements of the β decay of ^{11}Be were conducted with GADGET at the now-retired National Superconducting Cyclotron Laboratory. The NSCL experiment numbers were E18507, which ran in May 2018, and E19030, which ran in July 2019. The NSCL operated the Coupled Cyclotron Facility and earlier cyclotron-enabled rare isotope production programs, and provided world-competitive rates of short-lived radioisotopes like ^{11}Be for over 50 years.

2.2.1 ^{11}Be production by Projectile Fragmentation

A beam of ^{11}Be was produced by projectile fragmentation at the Coupled Cyclotron Facility at NSCL by accelerating a beam of stable ^{18}O to 120 MeV/u and impinging it on a 3196 mg/cm^2 Be production target. The initial ^{18}O beam was created by Electron Cyclotron Resonance which ionizes gas with microwave-driven electrons trapped in a magnetic bottle. Ionized $^{18}O^+$ is extracted with an electrostatic nozzle and transported to the CCF. Cyclotrons provide ion acceleration by two primary elements: a magnetic field for confinement within the accelerator and radio frequency high voltage to drive ions' motion at their cyclotron frequency until reaching their desired energy.

The CCF uses the K500 to do primary acceleration before impinging beam upon a carbon foil to strip the beam of electrons down to bare nuclei. Acceleration of $^{18}O^{8+}$ is completed in the K1200. At ~ 120 MeV/u, a variety of nuclear reactions on the Be target are possible, such as nuclear charge exchange, nucleon knockout, and collective fragmentation which can remove many nucleons, including the desired reaction(s) to produce ^{11}Be [40]. The A1900 fragment separator [4] used magnetic beam steering and position-selective slits to remove the unreacted $^{18}O^{8+}$ and reduce the cocktail of undesired reaction products. The radioisotope production up to this point is depicted in Figure 2.4 and further reading can be found in [4]. Beam was then delivered to the experimental setup.

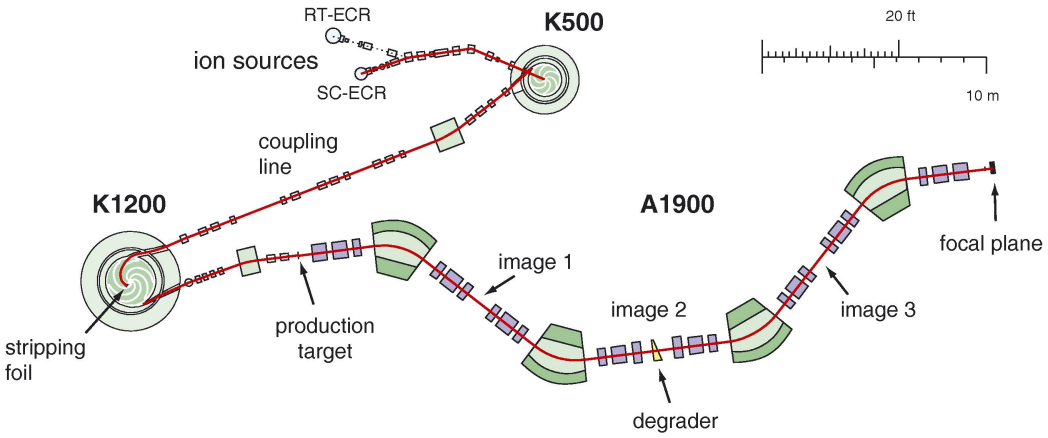

Figure 2.4: Schematic diagram of the Coupled Cyclotron Facility and the A1900 fragment separator. A variety of ion sources feed low-energy beams into the K500 and K1200 coupled cyclotrons for acceleration. Fast, ~ 200 MeV/nucleon beams are impinged on the production target. The A1900 fragment separator uses magnetic rigidity separation to purify the beam before delivery to the experiment. Figure Credit: Ref. [4].

2.2.1.1 Silicon P.I.N. Detector

The principle of particle identification from this two-dimensional matrix is as follows. Beam bunches are prepared to a particular magnetic rigidity $B\rho$, giving particles in a beam bunch the same momentum to charge ratio, $\frac{p}{q}$. As the beam travels to the experiment, the lighter mass species will have higher velocity and arrive sooner. The instantaneous energy deposition in the silicon detector is well-modeled by the *Bethe formula* [39]:

$$-\frac{dE}{dx} = \frac{4\pi e^4 z^2}{m_0 v^2} NB \tag{2.1}$$

where

$$B = Z[\ln(\frac{2m_0 v^2}{I}) - \ln(1 - \frac{v^2}{c^2}) - \frac{v^2}{c^2}] \tag{2.2}$$

Here, v and z are the velocity and atomic number of the incident particle. N and Z are the number density and atomic numbers of the detector material. m_0 is the electron mass and e is the electron charge. The MSX detector was selected for its thin 300μm profile, so energy loss of the fast beam would be small relative to the total energy. In the approximation of small energy loss (no velocity change), that instantaneous energy deposition is proportional to the square ratio of the beam-particle's atomic charge to its velocity, $\frac{z^2}{v^2}$. Thus, beam species should have unique energy deposition and time profiles.

2.2.2 Electronics and Data Acquisition

Figure 2.5 depicts the operational and readout electronics as instrumented in E19030. The two bias-voltage modules powered GADGET sub-systems and were controlled remotely by a dedicated network-connected Linux machine. SeGA electronics were installed and operated by the NSCL Gamma Group.

The instrumentation of NSCL E18507 and E19030 were quite similar. Notable exceptions were the implementation of a beam time-of-flight (ToF) timing circuit and implementation of the full Proton Detector MICROMEGAS pads in E19030. The ToF timing circuit was used to measure the time of flight of the beam specifically between the A1900 Focal Plane scintillator detector and our insertable Silicon PIN detector, less than 1 m upstream of the Proton Detector. The detector was inserted into the beam for short, dedicated measurements with attenuated beam between some full-intensity production runs to produce an independent measurement the delivered beam composition. Prior to E18507, several channels of the Proton Detector signal preamplifier were damaged and E18507 ran with only eight of the thirteen MICROMEGAS pads implemented. In E19030, all thirteen of the Proton Detector pads were implemented.

2.2.2.1 Implementation of GADGET electronics

The drift field in the Proton Detector was imposed by a CAEN N1470B programable high voltage supply through the safe high voltage (SHV) feedthrough installed in the upstream end of the Proton Detector. To produce the 120 V/cm electric field in the drift region, the N1470B provided −4.8 kV. This field strength was calculated to provide a $\sim$ 8 μs drift time from the detector cathode to the MICROMEGAS. To limit the risk of electrical discharges, the high voltage bias was slowly ramped ($\sim$ 5 V/s) to the nominal voltage, where it remained for the duration of the experiment.

The second high voltage supply module was the Mesytec MHV-4. The first channel produced the bias voltage for the charge-amplification field between the MICROMEGAS anodes and the Micromesh. The bias was set to 330 V to produce a field of ~2.6e4 V/cm. The second channel produced the +40 V bias for the silicon PIN detector. The final two channels of the MHV-4 were used to operate the gating grid. The third channel was set to -225 V for the "decay-measurement" operation mode and the fourth channel was set to +119 V for the "beam-delivery" operation mode. The two gating-grid voltages were modulated by a CGC Instruments NIM-AMX500-3 model high-voltage switch module operating on the TTL standard for voltage logic set by the synchronizing circuit.

The "beam-delivery" and "decay-measurement" cycle was set by a synchronizing circuit made of two LeCroy 222 NIM Dual Gate and Delay Generator modules [41]. Each module consists of two identical, independent sub-modules. The first module acts as a clock for the experiment cycle and the second module prepared an analog logic signal that was delivered to the facility to coordinate delivery of the pulsed ^{11}Be beam. The synchronizing circuit works as follows. In the first ("clock") module, upon a receiving *Start* signal, the logic output of the first unit will turn positive for a screwdriver-programmable amount of time (from $\sim$ 100 nsec to $\sim$ 11 sec). At the end of the logical-on period, a short ($\sim$ 10 ns FWHM) NIM-level signal will originate from the *DEL* output. The *DEL* output of the first sub-module triggers the *Start* of the second and the the *DEL* of the second triggers the *Start* of the first. Each unit was programmed to 1 second intervals allowing for 1 second of "beam-delivery" operation and 1 second of "decay-measurement" operation. The

length of the cycle was chosen to be short relative to the 13.8 s ^{11}Be halflife to minimize decay losses during the "beam-delivery" operation, while long compared to the $\sim 10-100$ ms short-lived contaminants. Longer cycles also reduce the relative detector dead time originating from switching between operation modes. The synchronizing circuit reset itself every 2 seconds. The second LeCroy 222 module was used to prepare the "beam-on" signal to the facility. To ensure that the Proton Detector gating-grid voltage was set and beam would not be delivered before the safety of the GADGET electronics was ensured, the first unit of the second module was used to insert a $\sim$ 10 ms delay before the complementary unit indicated beam should be delivered. The length of this "beam-on" logic pulse was short of 1 second ($\sim$ 950 ms total) so that there would similarly be time between beam delivery and the transition of the gating grid to allow ionization to the MICROMEGAS again. A copy of the clock signal was sent to the data acquisition (Sec. 2.2.2.2) to correlate data events against the measurement cycle. A diagram of this logic is shown in Figure 2.6.

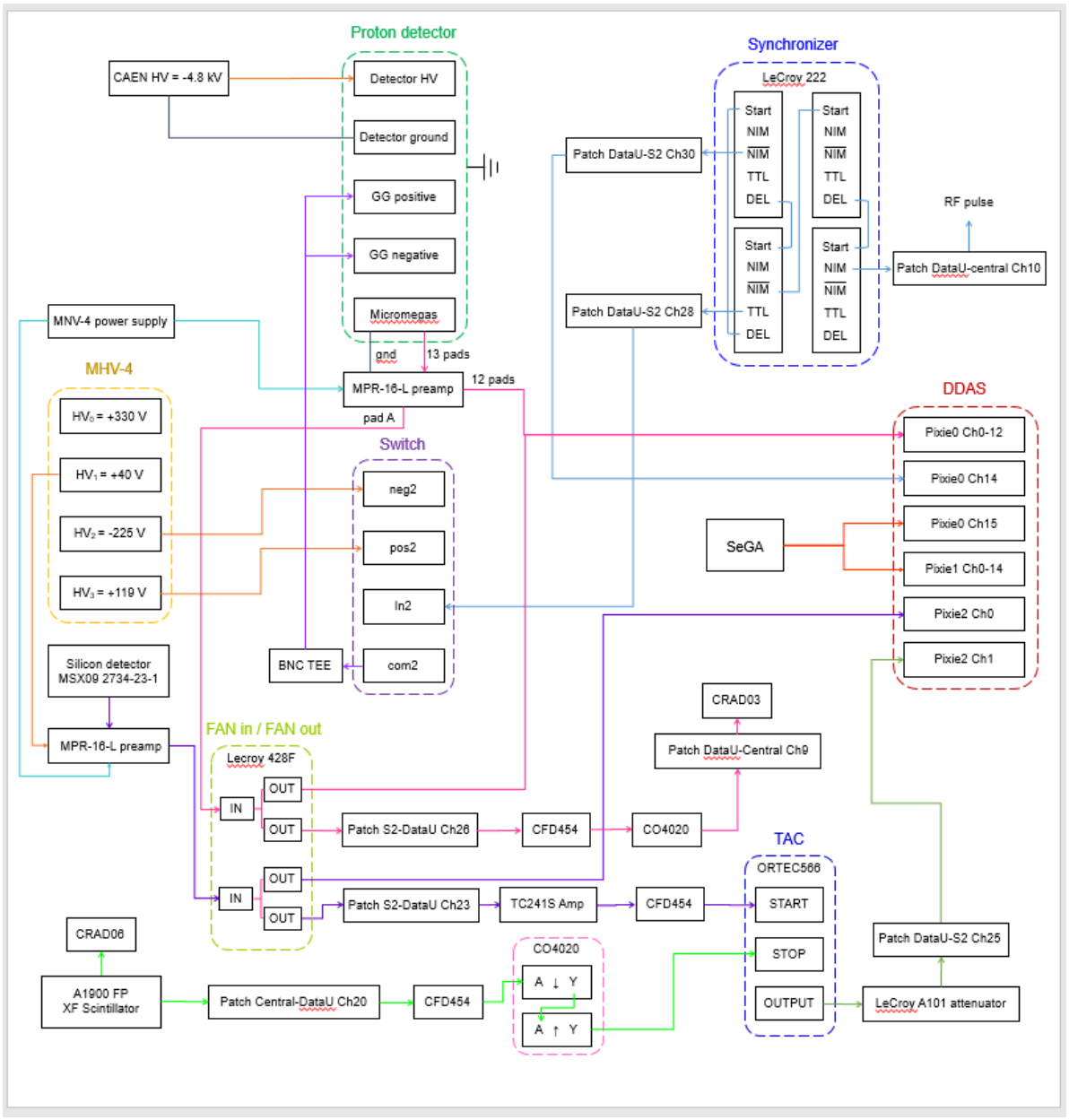

Figure 2.5: Schematic of electronics, with some settings, and wiring for E19030. Dashed lines are meant to indicate devices, such as the Proton Detector, or various electronics or readout modules. Figure Credit: Lijie Sun

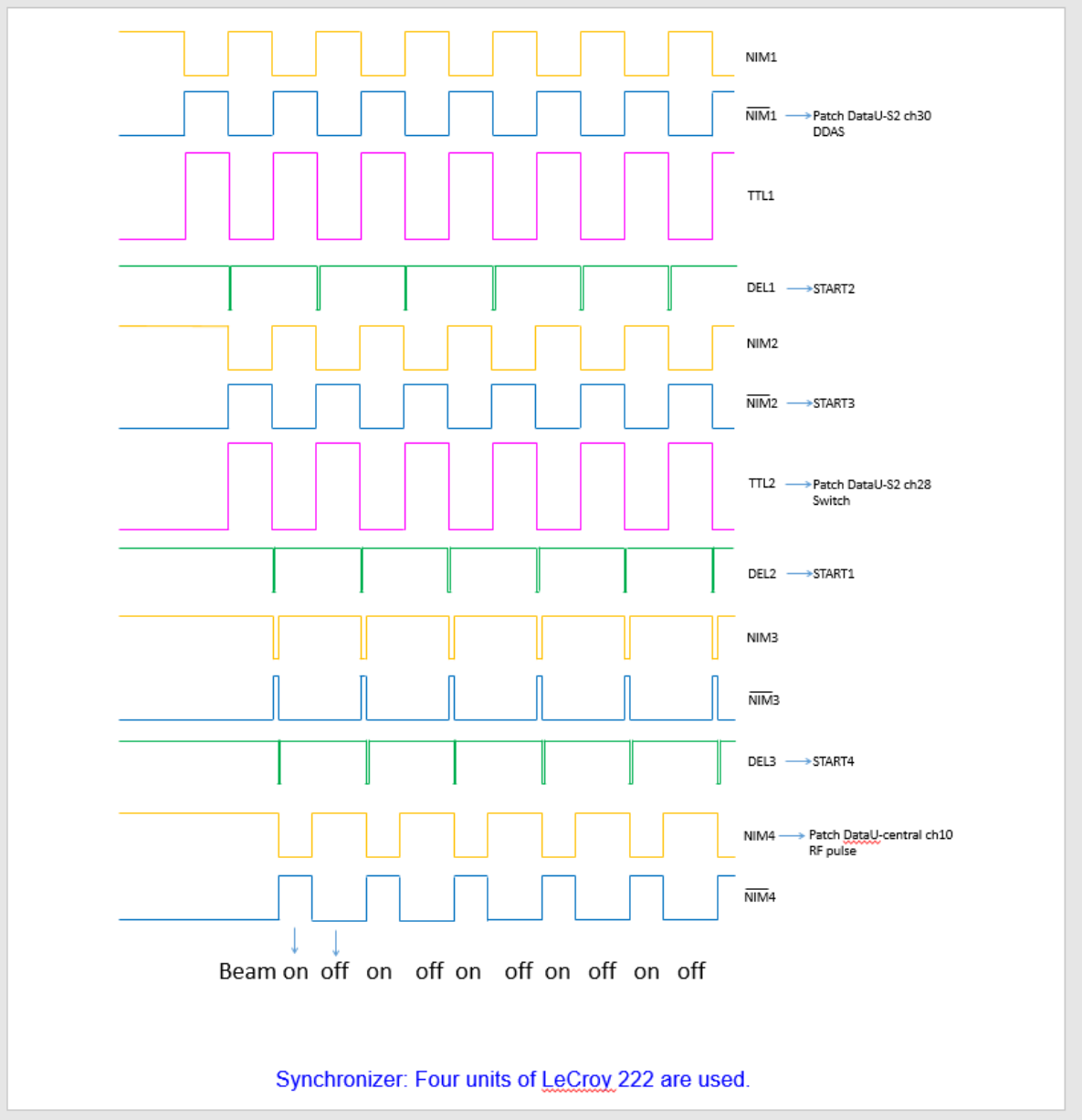

Figure 2.6: Schematic of electronics logical pulses controlling the Proton Detector and K1200 RF cycling for E19030. The numbers indicate the sub-module of the LeCroy222 the signal originates from. The first two sub-modules operate as a clock for the experiment. When NIM2/TTL2 are "on", the gating grid is set to its opaque setting. After a delay generated by DEL3, NIM4 signals "on" for the CCF RF and beam delivery. Figure Credit: Lijie Sun

2.2.2.2 Data Acquisition

Data acquisition of GADGET sub-systems was performed with NSCL's Digital Data Acquisition System (DDAS). DDAS was developed to work with SeGA for the purposes of in-beam γ spec-

troscopy for detection of and identification of nuclear reaction residues [42] and expanded to work with most familiar detectors in [43]. It is meant to replace large portions the catalog of traditionally-used analog Nuclear Instrument Modules (NIM) electronics used for signal shaping, timing, and other frequently used pre-analysis tools, such as coincidence matching between different detector (sub-) systems. In DDAS, analog electronic signals are fed into standard digitization electronics and parameter extraction such as peak voltages, voltage rise-times, and incident timing of radiation events are extracted in software and saved to disk. Digitized traces may also be stored for further offline (re-)analysis. In stopped beam experiments, such as our ^{11}Be(β^-p) measurements, DDAS allows for essentially zero-dead-time measurements of rare decays.

In both of our measurements, we utilized three 250-MHz, 16-channel PXI Digital Pulse Processors in a PXIE-CRATE-P16X14 from XIA, which will be referred to as Pixie0, Pixie1, and Pixie2. The first thirteen channels of Pixie0 recorded the Proton Detector's MICROMEGAS voltages after passing through a Mesytec MPR-16-L preamplifier. Channel 14 of Pixie0 recorded the $\overline{\text{NIM}}$ output of the LeCroy222. Channel 15 of Pixie0 and Channels 0-14 of Pixie1 recorded the 16 SeGA central-contact, full-energy, signals. Pixie2 measured the signal of the silicon PIN detector in channel 0 and voltage from an Ortec566 Time To Charge NIM module [44] in channel 1. The output voltage of the Ortec566 singularly maps the timing between the A1900 Focal Plane scintilator and the upstream silicon detector. It returns a larger voltage for a greater delay.

2.2.3 NSCL Experiment E18507

Our first ^{11}Be(β^-p) measurement was NSCL Experiment in E18507 and ran in May 2018. To our knowledge, this measurement was the first of several across several groups world-wide to be conducted following the dark neutron hypothesis put forth by Fornal and Grinstein [10]. E18507 ran as an extension of E17023, the GADGET commissioning experiment [37], with 12 hours of NSCL director-appointed discretionary beam time. Roughly six hours were used by the facility for beam-tuning and roughly six hours of beam was delivered. Figure 2.7 shows the facility-provided particle identification using the A1900 focal plane scintillator energy loss and timing with respect to

the CCF RF. The beam was 85% pure ^{11}Be at a rate of 580000 particles per second. Contaminants were identified as ^{13}B, ^{12}B, and ^{9}Li. Of the contaminants, ^{13}B was the most intense.

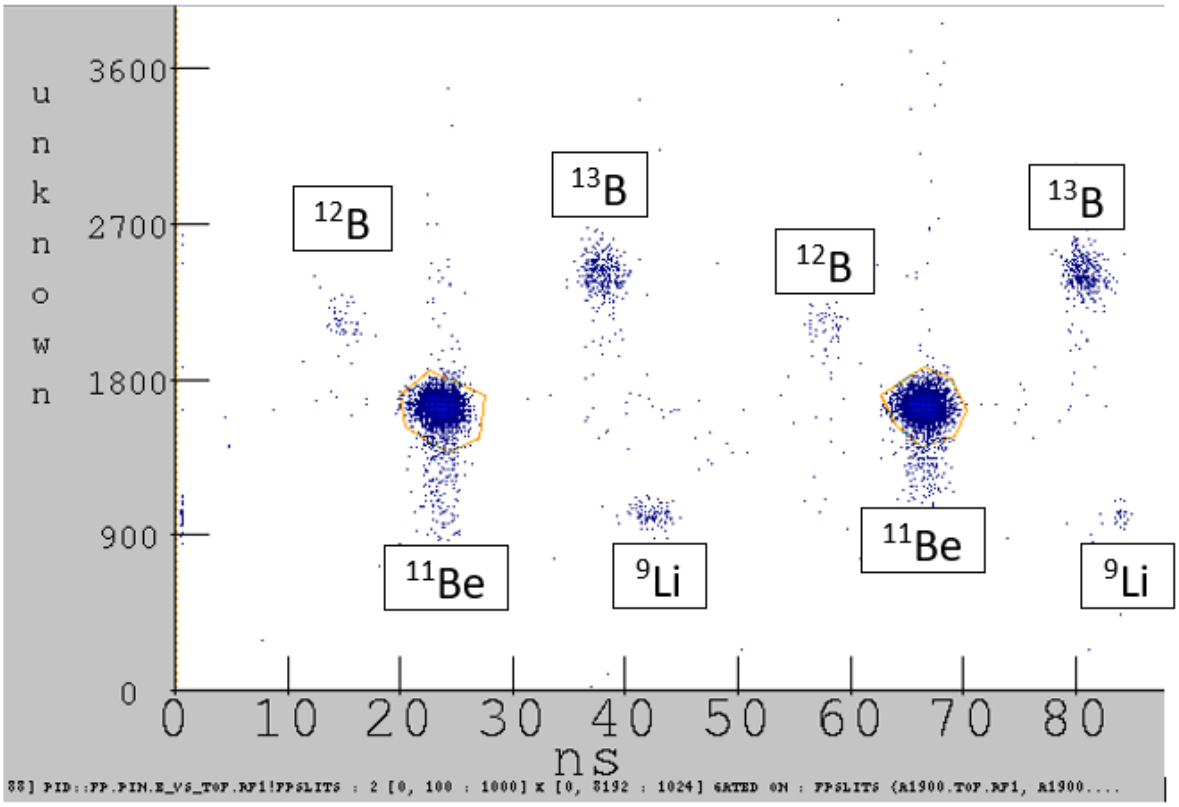

Figure 2.7: Particle identification plot provided by NSCL facility in E18507. ^{11}Be is the dominant species. The beam has low levels of contamination with ^{12}B, ^{13}B, and ^{9}Li. The repeated structure every~ 45 ns caused by the arrival of the next RF beam bunch.

Despite the 15% beam contamination, the measured charged-particle β decay was essentially contamination free. The 1s-1s long on-off beam cycling removed most radioactive contaminants by way of letting them decay during beam delivery. The half-life of ^{13}B is 17.33(17)ms and the half-life of ^{12}B is 20.20(2)ms. The only contaminant with a half-live close to the 1 second on-off cycle length is 178 ms ^{9}Li and it's delivered on a level of just a couple percent. It may decay in the beginning of the 1 second measurement and will be entirely absent toward the end. ^{9}Li will decay by β^- decay, but will appear in the detector virtually identically as those β^- particles from ^{11}Be. (The ^{9}Li(β^-) Q-value is 13606.45(20) keV and the ^{11}Be(β^-) Q-value is 11509.46(24) keV.) There exists a poorly constrained ^{9}Li(β^-n)^{8}Be branch that will produce back-to-back α particle from the

breakup of the daughter ^{8}Be. The Q-value for $^{8}\text{Be} \longrightarrow 2\alpha$ is 91.84(4) keV, which is dominated by the $^{11}\text{Be}(\beta^{-})$ background and not experimentally accessible with GADGET.

As E18507 was a serendipitous opportunity after the commissioning of GADGET, the full MICROMEGAS was not able to be implemented. During GADGET commissioning, several preamplifier channels were damaged so Pads F, G, L, and M were not instrumented. Pads B and E were demoted to diagnostic veto pads and only Pads A, C, and D were used for measurements.

2.2.4 NSCL Experiment E19030

Following the analysis of NSCL E18507 described in Section 3.2, we proposed a subsequent measurement to gather greater statistics and improve the search sensitivity. Our proposal was awarded 96 hours of NSCL beam time, with roughly 76 hours of beam delivery to GADGET. The experimental setup for E19030 was nearly the same as E18507, but the full MICROMEGAS was instrumented as described in Section 2.1.2 and a MSX09 300μm silicon PIN detector by Micron Semiconductor Ltd was implemented upstream of GADGET. During dedicated runs with an attenuated beam, the silicon detector was inserted into the beam to perform energy-loss vs time-of-flight measurements between the silicon detector and the A1900 focal plane scintillator. These measurements were used for an independent particle identification of the incoming beam. Figure 2.8 shows the beam particle identification measurements from the facility. In E19030, the delivered beam was 89% pure ^{11}Be at a rate of 660,000 particles per second. Beam contaminants were similar to the previous measurement and were, in order of abundance, were ^{13}B, ^{12}B, and ^{9}Li. Similarly, the anticipated impact of the decays of these contaminants in the measured charged-particle spectrum was negligible. For the GADGET-side particle identification runs, to protect the silicon detector and related electronics, the beam was attenuated by a factor of 3000 to roughly 200 particles per second.

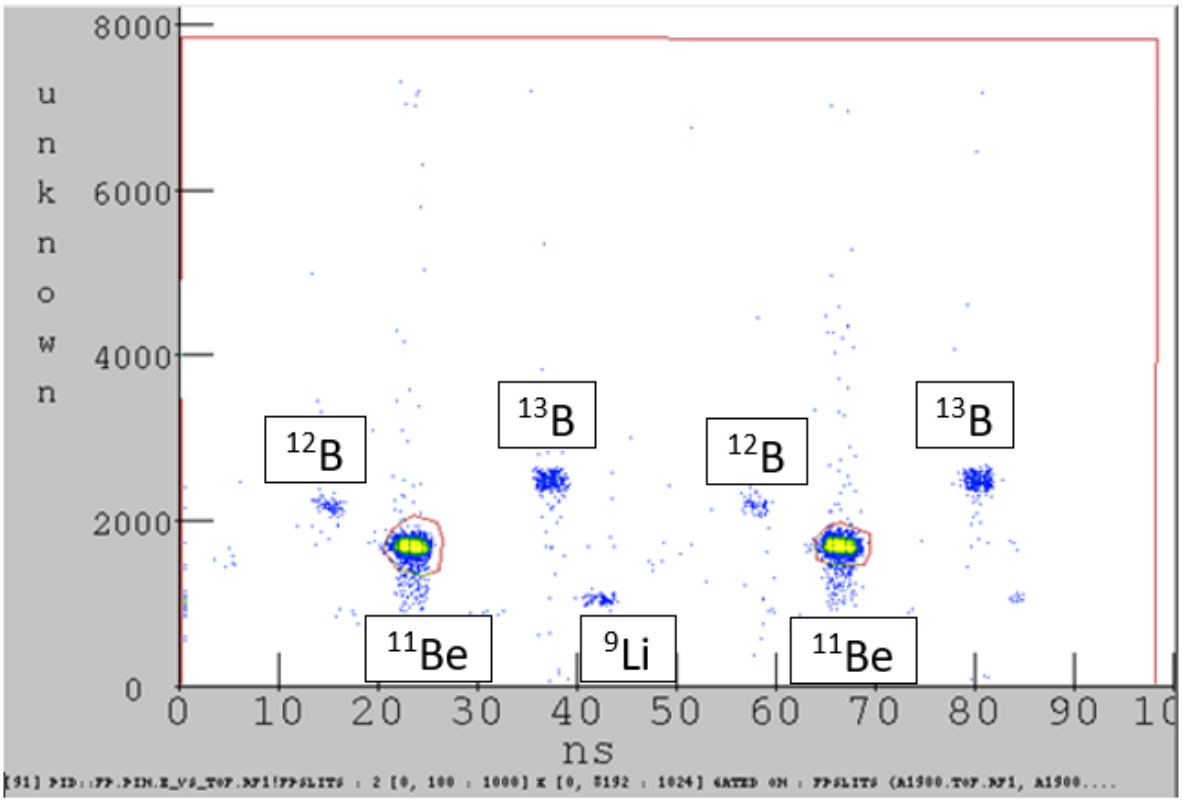

Figure 2.8: Particle identification plot provided by NSCL facility in E19030. ^{11}Be is the dominant species. The beam has low levels of contamination with ^{12}B, ^{13}B, and ^{9}Li. The repeated structure every~ 45 ns caused by the arrival of the next RF beam bunch.

CHAPTER 3

ANALYSIS: DATA SORTING, INFERENCE WITH χ^2-MINIMIZATION

The analysis of data from NSCL experiments E18507 and E19030 share similarities from being conducted with the same experimental set up. Primitive data from DDAS was first extracted and combed for a number of correlations between the Proton Detector and SeGA detector systems to make histogramed charged-particle and γ spectra to which quantitative analysis was applied. A number of analysis techniques will be discussed as ultimately, the E18507 dataset was statistics limited and did not reach desired precision goals. It was found that applying the E18507 analysis to the larger E19030 dataset lead to a systematically limited result that also missed desired precision goals, and a new Bayesian Markov Chain Monte Carlo code (Chapter 4) was developed to handle model-fitting the domineering $^{11}\mathrm{Be}(\beta^-\alpha)^7\mathrm{Li}$ background.

3.1 Data Sorting

To save data with the NSCL DDAS described in Section 2.2.2.2, a common template was used to store values from the various detectors and detector sub-systems. That is, data was extracted from each channel and saved when any single channel triggered the threshold for a "valid" event. Thus, most event files have a single entry from a single detector sub-system. This choice was made to reduce detector deadtime and provide greater flexibility to vary coincidence and threshold cuts in software, by scanning over events and selecting coincident events by their DDAS timestamps.

To organize the DDAS events into "physical" events, a data file is searched chronologically for a charged-particle measurement on a MICROMEGAS pad. For every hit, the subsequent DDAS events are searched up to a period of 12 μs later, which is in excess of the approximately 8 μs drift time for charges traveling the full length of the detector. The analysis software looks for other events on MICROMEGAS pads, veto (outer) and measurement (inner). Events that have triggered an outer veto pad are discarded as the charged-particle was not confined to the sensitive volume of the Proton Detector. There are two data-sorting schemes to deal with events in the 12

μs time window and stay within the Proton Detector sensitive volume: the *composite pad* scheme and the *individual pad* scheme. In the composite pad scheme, charge measurements from all five interior MICROMEGAS pads A-E are added together to create a single charge-particle spectrum. Contributions are *gain matched*, a pre- energy calibration, to spectral features to standardize the outputs across the pads before summation and inclusion in the histogram to be analyzed. In the individual pad scheme, every other pad is treated as a veto pad and one histogram is created per pad. In this way, the individual pads each function as their own, smaller detector. The composite pad scheme has greater efficiency due to the larger functional-pad area, however has worse energy resolution due to differences in the individual pad electronics and a higher-energy β background that reaches into the $\sim$ 200 keV energy region of interest from the large volume for β particles to deposit energy. The individual pad scheme suppresses the β background and has better resolution, but has worse detection efficiency, due to the more selective veto/exclusion cuts.

3.2 NSCL Experiment E18507

Figure 3.1 shows the unsorted charged-particle events on all instrumented pads. Individual features are difficult to identify, due to incomplete charge deposition per pad, except for a sharp feature around ADC channel 12000 in only the quadrant Pads B, C, D, and E. Application of the individual pad veto scheme yields Figure 3.2. The sharp features in the quadrant pads disappear and five distinct features remain. At the lowest energies, we have the β^- spectrum, attenuated by the low-density detector gas. The other features are related to the $\sim 3\%$ ^{11}Be($\beta^-\alpha$) branch [45, 46, 2].

3.2.1 Understanding the Li+A spectrum

The nuclear structure information used came from the compilation and review of Ref. [1] and the β-decay feeding information from [46, 45]. The ^{11}Be($\beta^-\alpha$) proceeds through the 3/2+ state located at 9873(4) keV with a total intensity of 3.1(4)%. This 3/2+ state has an intrinsic width of 109(14) keV and decays via emission of an α particle to α and ^{7}Li, primarily to the ^{7}Li ground state. Some fraction of these decays populate the 478 keV excited state of ^{7}Li. Ref. [46, 45] measured this

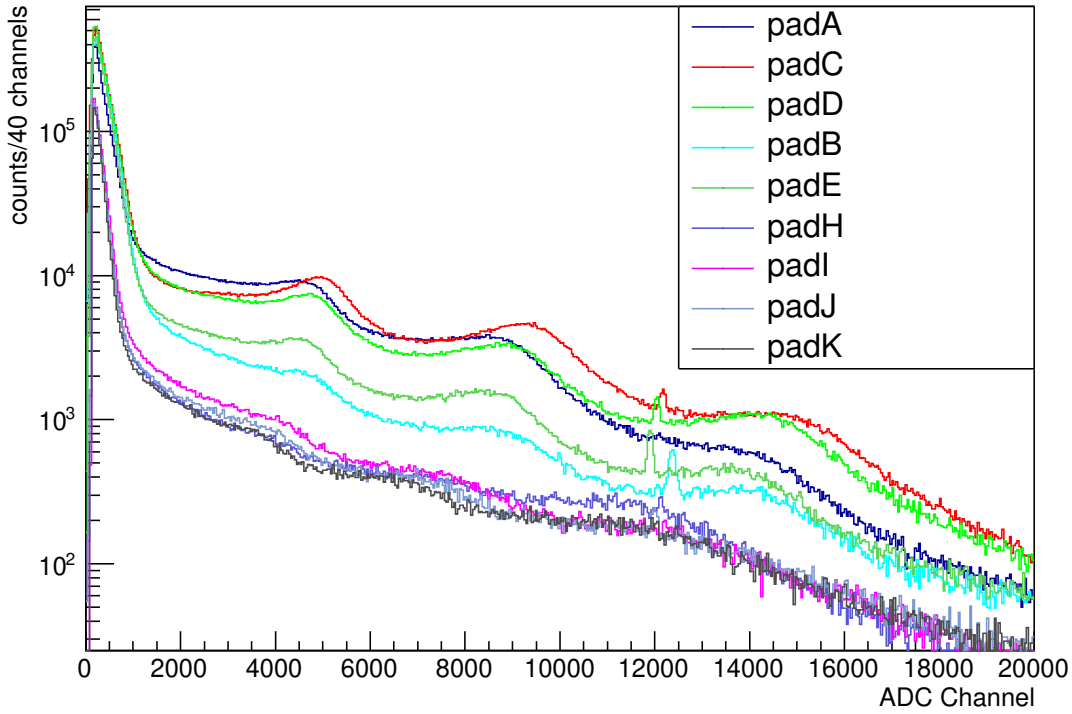

Figure 3.1: The unsorted, raw spectra of Pads A, C, D in E18507. There are general features such as a large amount of counts below channel 1000, subtle peaks around channels 5000, 10000 and 15000, with fairly flat connections between peaks, and sharp peaks in some spectra around 12000. The behavior below 1000 channels comes from β particles. The broad peaks at 5000, 10000, and 15000 are associated with the ^{11}Be($\beta^-\alpha$) decay. The sharp peaks near 12000 channels are thought to be electronic noise, perhaps from inefficiencies in the transitions of the gating grid.

branch to populate the ground state 87.4(12)% and the 478 state 12.6(12)%. The α separation energy of ^{11}B is 8664.310(10) keV, so α-decays to the ^{7}Li ground state have 1209(4) keV center of mass kinetic energy and decays to the excited state have 731(4) keV center of mass kinetic energy. To make sense of Fig. 3.2, one must consider additional detector effects coming from decays originating on the wall of the detector. Either by diffusion of ^{11}Be, by incomplete neutralization of the ^{11}Be beam, or both of these effects, a significant fraction of decays can originate from the detector cathode. The $\beta^-\alpha$ decay will produce a back-to-back α and ^{7}Li pair, so decays originating on the interface of the detector gas and the detector body will lead to measurements of only one of the two nuclear-fragment charged-particle radiations. That is, for each of the two ^{7}Li final states,

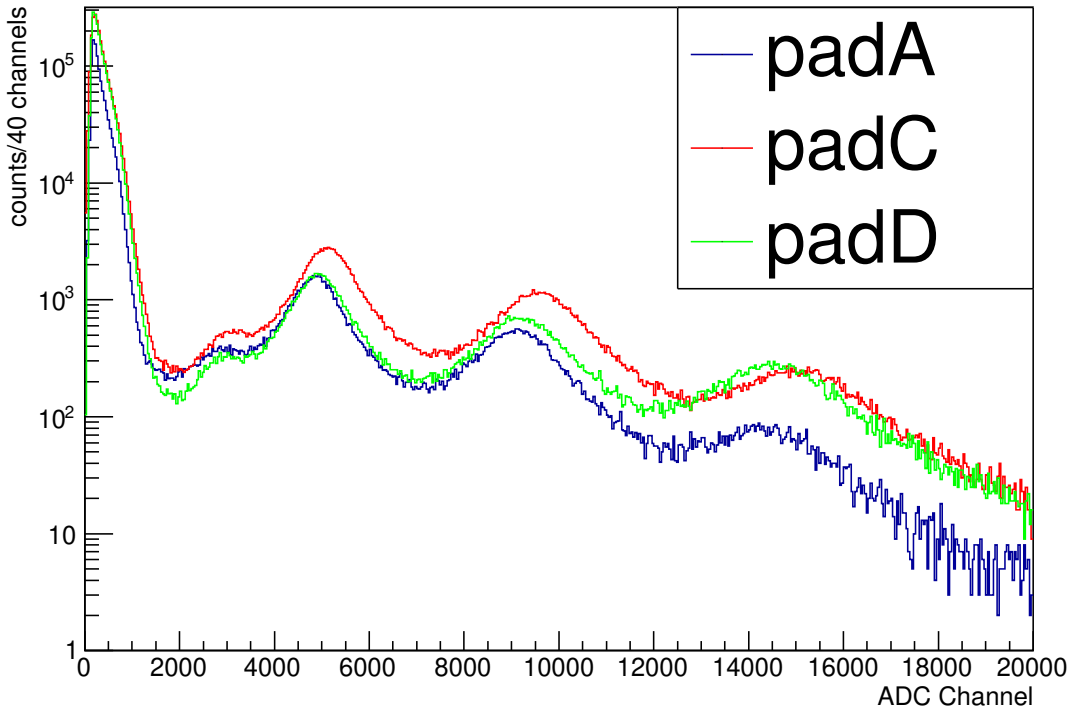

Figure 3.2: The sorted, raw spectra of Pads A, C, D in E18507. Comparing to the unsorted histograms shown in Fig. 3.1, there is finer structure here that was revealed by the data sorting and event-vetoing algorithm. There remain a large amount of counts below channel 1000. The peaks around channels 5000, 10000 and 15000 are now clearly visible, in addition to a new peak around channel 3000. The behavior below 1000 channels comes from β particles. The peaks peaks at 3000, 5000, 10000, and 15000 are associated with the ^{11}Be($\beta^-\alpha$) decay. The sharp peaks near 12000 channels are were present previously have been removed by the sorting and veto algorithm.

the following sets of charged-particle radiations will be measured: α and ^{7}Li both, α alone, or ^{7}Li alone. The energy sharing between the two fragments is given by kinematics determined by particle mass. Table 3.1 shows the breakdown of central energies for each detection possibility. Due to the broad nature (Γ = 109(14) keV) of the 9873 α-emitting state [1], the peaks from each of these radiations have substantial widths and considerable overlap in some cases.

With these more complex spectra from wall-effects in mind, we can now make sense of the structures in Fig. 3.2. At ADC channels <2000, we have the suppressed β^- spectrum. Around channel 3000, we have measurement of the cathode-originated ^{7}Li-recoil alone from the excited-state feeding of ^{7}Li (266 keV). The peak around channel 5000 is a composite peak made of two

Description	Center of Mass Energy	α contribution	^{7}Li contribution
^{11}Be($\beta^-\alpha$)^{7}Li(g.s.)	1209(4)	769(3)	440(2)
^{11}Be($\beta^-\alpha$)^{7}Li(γ) (478 keV)	731(4)	465(3)	266(2)

Table 3.1: Central energies of decay events seen by the Proton Detector. Actual energies are a distribution determined by the 109(14) keV intrinsic width of the emitting 9874 3/2+ state in ^{11}B [1]. Energies are in keV.

cathode-originating decays, the α-particle alone from the excited state feeding of ^{7}Li (465 keV) and the ^{7}Li-recoil alone of the ground state ^{7}Li feeding (440 keV). The peak around channel 10000 is another composite peak, consisting of the in-gas, full-energy measurement to the ^{7}Li excited state (731 keV) and the cathode-originating α-particle alone from the ground state feeding of ^{7}Li (769 keV). Finally, around channel 15000, we have the in-gas, full-energy decay to the ^{7}Li ground state (1209 keV). (Jumping ahead, see Fig. 4.9 for a calculation of all possible $\beta^-\alpha$ -component spectra and note the considerable overlap between some different components. The height of the curves are scaled by the ^{11}B(9873 keV)$\rightarrow^7$Li$^*+\alpha$ vs ^{11}B(9873 keV)$\rightarrow^7$Li+α fraction alone. No detector effects were included in these spectra.)

This is demonstrated further in Fig. 3.3 and 3.4. Fig. 3.3 shows the charged-particle spectra for Pads A, C, and D in the individual pad veto scheme in coincidence with a 478 keV γ ray (470 to 480 keV). The in-gas, full-energy peak is strongly suppressed and only appears from accidental coincidences, arising from a 478 keV gamma from a decay outside of the Proton Detector or a Compton scatter event depositing 478 keV worth of energy. Fig. 3.4 shows this same coincidence but subtracts a background of coincidence on γ rays from 482 to 492 keV. Now, the spectra are virtually pure ^{11}Be($\beta^-\alpha$)^{7}Li(γ). (The energies are roughly 266, 265, and 731 keV). Unfortunately, these spectra are severely statistically limited and have limited further utility.

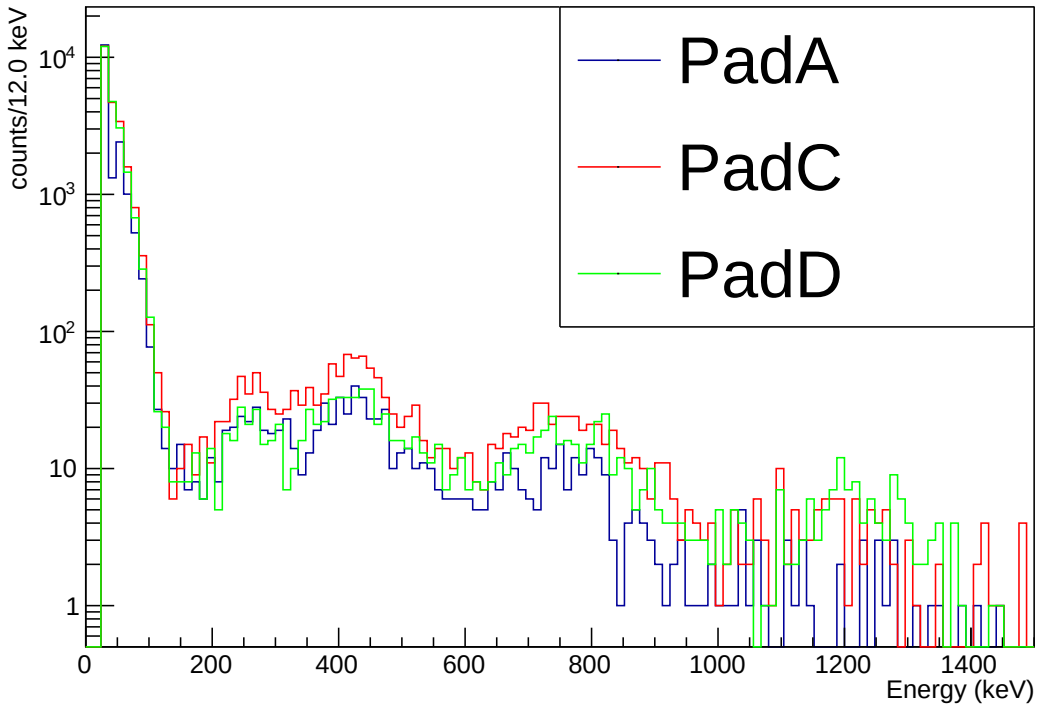

Figure 3.3: Individual pad spectra for Pads A, C, and D in E18507 coincident with a 478 keV gamma from the deexcitation of ^{7}Li* fed from the ^{11}Be($\beta^{-}\alpha$). Accidental coincidences with the ^{11}Be($\beta^{-}\alpha$)^{7}Li are present, but the low-energy portion of the spectra is enhanced relative to the high energy portion.

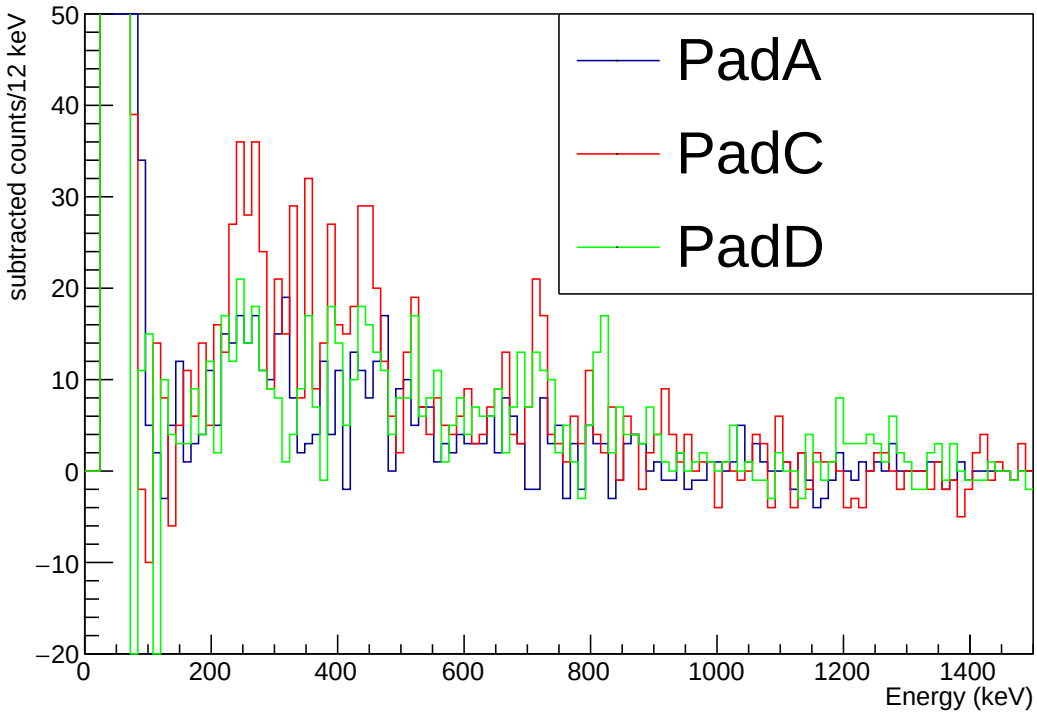

Figure 3.4: Individual pad spectra for Pads A, C, and D in E18507 coincident with a 478 keV gamma from the deexcitation of ^{7}Li* fed from the ^{11}Be($\beta^{-}\alpha$) with random coincidence background subtraction. Only the ^{11}Be($\beta^{-}\alpha$)^{7}Li* emissions are visible here, with poor counting statistics. There is the ^{7}Li-alone at $\sim$ 265 keV, the α-alone at $\sim$ 465 keV, and the ^{7}Li+α full-energy decay at $\sim$ 731 keV.

An important thing to note is that the properties of this state have been determined by a combination of ^{11}Be(β) decays and ^{7}Li(α,α), ^{9}Be(^{3}He,p), ^{12}C(t,$\alpha\gamma$), and ^{14}N(n,α) reactions [1]. The energy and intrinsic width of the α emitting state was determined by reaction measurements and are at odds with a recent ^{11}Be($\beta^{-}\alpha$) measurement Ref. [2], which is used in the E19030 analysis but not in the E18507 analysis. It was found in the the later analysis that the recent value of $\Gamma = 233(3)_{\mathrm{stat}}(3)_{\mathrm{syst}}$, measured by $\beta^{-}\alpha$ decay and not nuclear reaction quantities, better agreed with what we measured in our $\beta^{-}\alpha$ measurement. (See Fig. 4.6)

3.2.1.1 Energy Calibration

Application of the veto schemes and an energy calibration yields Figure 3.5. The energy calibration comes from fitting the peaks of the ^{7}Li ground state feeding decays at 440 (^{7}Li), 769 (α), and 1209 keV (^{7}Li and α) to Gaussian profiles per measurement pad. Due to the composite nature of the two lower-energy peaks, only the tops of the peaks ($\pm \sim 200$ channels) were fit under the assertion that the peak maximum is determined by the ground state feeding peak energies, even if the full peak shape is harder to describe.

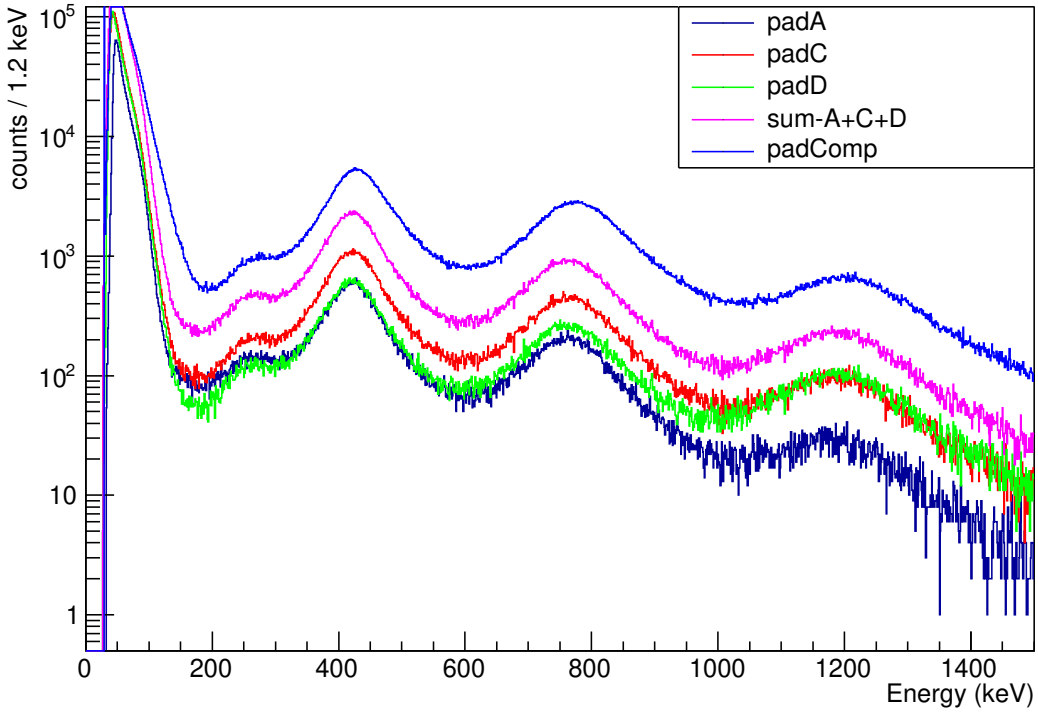

Figure 3.5: The sorted and energy calibrated analysis spectra of E18507. Both individual pad and composite pad schemes are shown. The β background is suppressed in the individual pad scheme, but at the cost of counting statistics.

In the composite scheme, the recorded energy is the sum of energies across all measurement pads, within the correlation time window, corrected by the individual-pad-scheme calibrations. There is a small shift of the composite pad spectrum to higher energy, as the larger effective pad yields greater β-particle energy deposition, but this effect is small ($\sim$ 10 keV).

3.2.1.2 Efficiency and Normalization to the 3% $\beta^-\alpha$ branch

To deduce a branching ratio, a measure of the total number of ^{11}Be decays is needed to normalize any measured intensity. For this, we used the intensity of our 3.1(4)% ^{11}Be($\beta^-\alpha$) background. By integrating the charged particle spectra and applying calculated efficiency corrections, we estimated the total number of ^{11}Be decays eligible for measurement on each pad. The ratio of detected counts and this calculated number of atoms is the branching ratio.

The first step in calculating efficiency corrections was to simulate the particle ranges in the detector gas using the code "SRIM: The Stopping and Range of Ions in Matter" [47]. SRIM is a particle based simulation code that calculates ion interactions in matter and can calculate a variety of useful descriptions, such as particle range, energy deposition profile, and fraction of energy lost to different ion stopping processes (ionization, lattice disruptions in solid targets, kinetic energy sharing with target). The simulated range distribution was modeled with a Gaussian profile. The average range as the central value and the calculated straggling was treated as the Gaussian width σ. Although physical events will have a distribution of energies from the intrinsic width of the α-emitting 9874 keV state in ^{11}B, only the central energy was modeled.

Decay Type	Location	Pad A	Pads C/D
p+^{10}Be	in-gas	77	86
	cathode	88	93
α+^{7}Li*	in-gas	54	71
	cathode	77	85
α+^{7}Li	in-gas	37	61
	cathode	68	79

Table 3.2: Simulated charged-particle detection efficiency per pad for possible ^{11}Be($\beta^-\alpha$)^{7}Li decay radiations. Numbers are in percent.

A Monte Carlo code was developed to estimate the efficiency of an event measured in a detector pad to survive the software veto cuts. This efficiency is normalized to each pad. To clarify, in calculating the pad efficiency, only tracks that project to the given pad are considered. In the limit of infinitesimal tracks, the efficiency of Pad A/C/D/ACD would be 100% as a track would originate

and terminate in the same location, in only the same single pad. The SRIM-calculated ranges were input for several particle-energy combinations to be calculated. We simulated the efficiency of a 180 keV proton, a 18 keV ^{10}Be recoil, α-particles at 466 and 770 keV, and ^{7}Li recoils at 266 and 440 keV. Simulations were run for both in-gas decays, where the total event length is used (as the ^{7}Li+α decay is back to back) and the cathode-originating decays, where only one particle will be measured, leading to an effective shorter track. Table 3.2 lists the estimated detection efficiency of each type of decay. These values are weighted by the frequency of the in-gas vs cathode-originating fractions ($\sim$ 60% vs $\sim$ 40%) and the ^{7}Li* vs ^{7}Li(g.s.) feedings (13% vs 87% [45]). The relative efficiency between β^{-}p and $\beta^{-}\alpha$ was determined to be 1.49 for Pad A and 1.25 for Pads C and D. Integrating the spectrum, events depositing 200 keV of center of mass energy or greater are interpreted as $\beta^{-}\alpha$ events and used in normalization. Pad A recorded 112285 events, Pad C recorded 223966 events, and Pad D recorded 141834 events. Assuming the $8 \cdot 10^{-6}$ branch of Ref. [5], we would expect to observe 40 to 75 β^{-}p counts per pad.

3.2.2 Statistical Inference of β^{-}p

Inference of the number of ^{11}Be($\beta^{-}p$) counts was done on an individual pad basis. The inferred $\beta^{-}p$ counts were normalized to the respective ^{11}Be($\beta^{-}\alpha$) spectra and efficiency calculations to calculate a branching ratio. The average branching ratio result(s) were averaged weighted by their standard 1 σ error(s). Extraction of ^{11}Be($\beta^{-}p$) counts was performed by a gradient-descent χ^{2} minimization algorithm implemented by ROOT's default histogram "Fit()" function. Spectra were fit by a function consisting of the sum of an exponential function meant to capture the β-particle background, a quadratic polynomial meant to capture the ^{11}Be($\beta^{-}\alpha$) in the minimum around $E \sim 200$ keV, and a Gaussian peak meant to capture the possible ^{11}Be($\beta^{-}p$) signal. In principle, the $\beta^{-}p$ signal has contributions from each of the decay locations: a peak at 91% of the center of mass energy of the cathode-originated proton alone and second peak at higher energy from the in-gas proton and ^{10}Be recoil. Usually, gas ionization and ion energy loss processes are assumed to be linear, but SRIM estimated that only $\sim$ 50% of the ^{10}Be recoil energy made its way to ionization.

(For all other particles, this fraction is ~95+%.) Additionally, there is the cathode-originated ^{10}Be-alone radiation, but the estimated energy of such a decay is ~ 20 keV and too low in energy to be detected by the Proton Detector. In this first and simplest analysis, these details were not investigated and the Gaussian peak was determined sufficient for a simple "bump hunt" analysis.

To search for the ^{11}Be($\beta^- p$), we still need to further define our search function, namely the detector resolution for our Gaussian search function. Due to the broad nature of the ^{11}Be($\beta^-\alpha$) in our spectra, further complicated by the cathode-originating decays and feeding of the ^{7}Li* state, extracting the detector resolution was not straightforward. Instead, the detector resolution was parameterized as a function of energy using the following $\beta^+ p$ peaks from previous GADGET measurements: 401, 555, 943 keV peaks from ^{25}Si [6]; 206, 267, 579, 866 keV peaks from ^{23}Al [7]; 259, 803, 1026 keV peaks from ^{31}Cl [8]. Data was fit per pad with a linear curve with χ^2 minimization. The adopted detector resolutions were calculated by the parameterization per fit, but were roughly 8.1%, 11.6%, and 6.4% for Pads A, C, and D, respectively.

With our search feature and background models defined, a series of fits to data were performed for center of mass energies from 160 keV to 250 keV on each of Pads A, C, and D. The fit window was from 60 keV below to 40 keV above the nominal search energy and moves as the nominal energy is scanned over the search range. This asymmetry in the fit window is afforded by the exceptional quality of the fit of the high-energy portion of the β-particle background to an exponential curve in this data and in previous GADGET experiments [6, 37, 7, 8]. Fig. 3.6 shows one fit to Pad C, searching for a peak at 175 keV. Additional fits to data can be found in the Appendix.

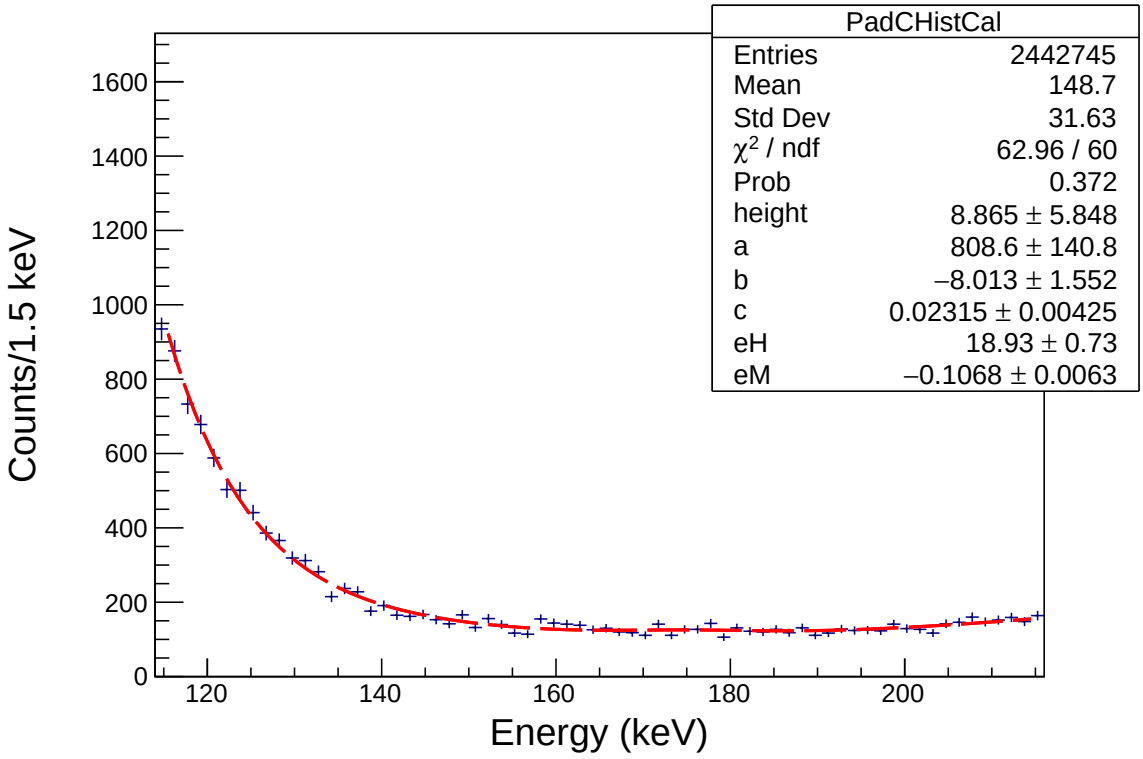

Figure 3.6: Data from Pad C and a fit of the data to a modeling function. The model was the sum of an exponential function with parameters eH and eM, a quadratic polynomial $a + b \cdot E + c \cdot E^2$, and a Gaussian with fixed $E = 175$ keV center and $\sim 11.6\%$ width. The Gaussian peak is meant to extract the number of β^p counts. This fit yields 9(6) $\beta^- p$ counts.

Fig. 3.7 shows the statistical-error-weighted average of this search over all three pads. Systematic errors are not estimated. There are two regions of note. The first is a clear excess is seen at E∼170 keV. This excess is greater than zero at the 2 σ level at its peak and exists over roughly the width of a peak with the average detector resolution. Secondly, the final point at E=250 keV also reaches a 2 σ significance above zero. The fit here incorporates the ^{7}Li* -alone peak to a large degree. Fitting a novel, small peak on top of a large peak may serve as an uncontrolled systematic error. This point deserves additional scrutiny before being taken too seriously.

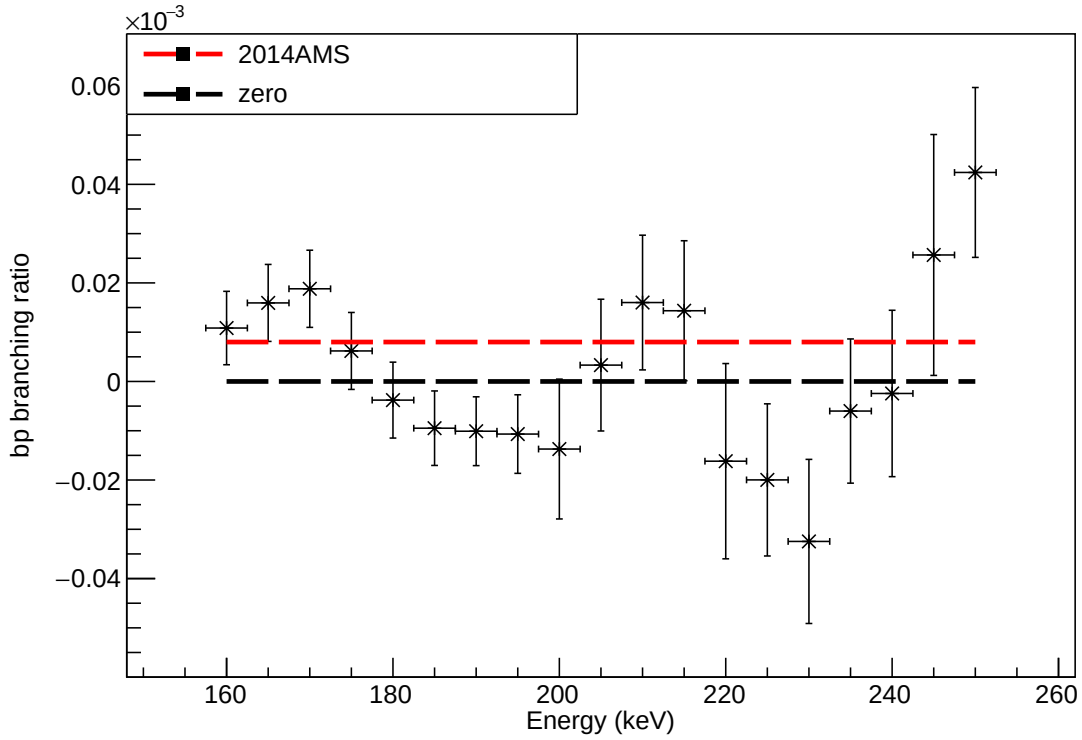

Figure 3.7: Results of E18507, averaging the results of Pads A, C, and D. The inferred ^{11}Be(β^{-}p) branching ratio is largely consistent with both zero and the then-only previous inference of the branching ratio [5]. At $E \sim 170$ keV, there is an excess of $\sim 2\,\sigma$ from zero over ~ 15 keV of search space.

With these averaged measurements, upper limits were derived, shown in Fig. 3.8. Upper limits were defined to normalize the assumed Gaussian probability density function so the physically-allowed zero and positive values integrate to unity. That is, the limit is determined by the following Eq. 3.1. Here, $g(x|\bar{x},\sigma)$ is the Gaussian distribution with central value $\bar{x}$ and standard 68% error bar σ. We plotted results for 90% and 95% confidence limits.

$$CI = \frac{\int_0^b g(x|\bar{x},\sigma)dx}{\int_0^\infty g(x|\bar{x},\sigma)dx} \tag{3.1}$$

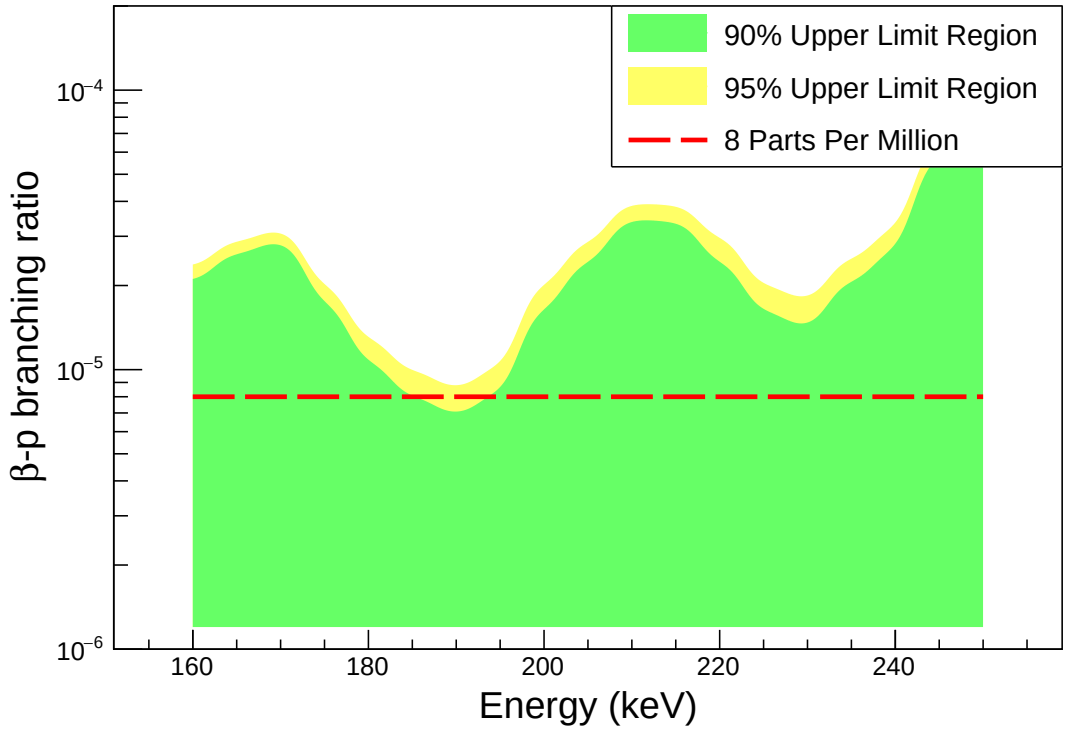

Figure 3.8: Upper limits derived from individual pad averaged results of E18507 in Fig. 3.7. The upper limit is defined in Eq. 3.1. The red-dashed line shows a branch of $8 \cdot 10^{-6}$, which was inferred from [5]. Over most of the search space, there is no ability to exclude the $8 \cdot 10^{-6}$ branching ratio. Exclusion occurs only for $185 \lesssim E \lesssim 195$ keV at $\sim 90\%$ significance.

From this upper limits plot, there is only a small range of energies with clear distinction from zero and the $\beta^- p$ rate of $8 \cdot 10^{-6}$ inferred from [5]. Only in the region of E=185-195 keV is there rejection of the finite value at a 90% but not 95% level. Given the short, roughly six hour, duration

of beam delivery in E18507 and the statistical error bars similar in magnitude between the extremes of the available $\beta^- p$ hypotheses, we concluded an order of magnitude greater statistics would likely allow discrimination between the presently available $\beta^- p$ predictions and inferences. This analysis was written up as part of the NSCL PAC proposal E19030 in PAC43 and was awarded the requested beam time.

3.3 NSCL Experiment E19030

The setup of E19030 is described in 2.2.4. The primary difference between E18507 and E19030 was full implementation of all 13 MICROMEGAS pads in E19030. The initial analysis of E19030 was similar to the E18507 analysis described in Sec. 3.2.2, but expanded upon a great deal and will be described here.

3.3.1 GADGET-side Particle Identification

In E19030, we also instrumented a dE-TOF circuit to conduct particle identification at the degrader and diagnostic cross, just upstream of GADGET. The structure of these data events was different than the usual GADGET events discussed before. In particle identification mode, only the MSX silicon detector and the ORTEC566 TAC signals were analyzed and values saved to disk. In the DDAS event building, TAC signals were always stored as separate events. (The TAC signals were delayed by the signal travel time from the experimental vault to the DataU user area, where the ORTEC566 was installed.) The DDAS events were sorted into physical correlations by the signature of a silicon detector event followed by the TAC event in the subsequent DDAS event. The dE-TOF matrix is shown in Fig. 3.9 and projections are shown in Fig. 3.10 (energy projection) and 3.12 (time projection). The red dashed lines show possible boundaries for the particle identification analysis.

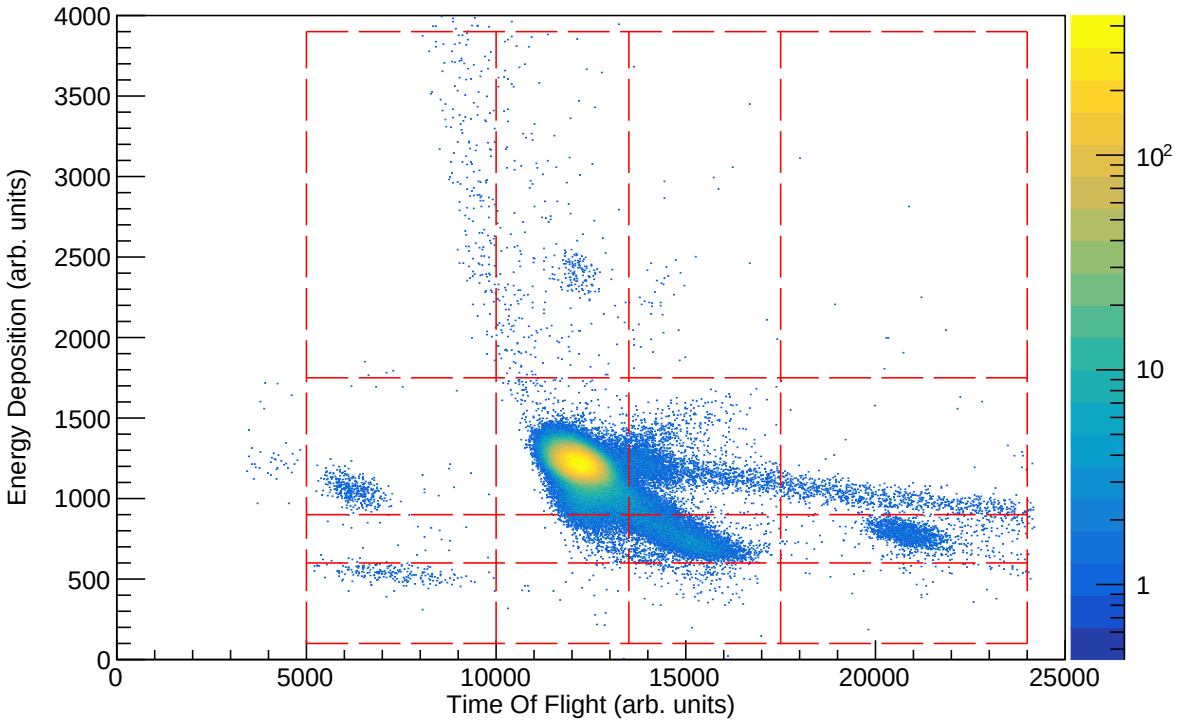

Figure 3.9: Silicon energy deposition and time of flight matrix color coded by intensity. The dashed lines are proposed thresholds that may be useful in particle identification. The primary observation is the dominance of one peak, assigned to the ^{11}Be component of the beam, at energy $E \sim 1250$ and time of flight $t \sim 12000$.

The silicon detector histogram has several peak-like features with only limited separation, but there may be peaks at ~500, ~750, ~1220, ~2500 channels. The relative intensities of these regions is 0.3%, 2.7%, 96.8%, and 0.2% respectively. The number of peaks nicely matches the NSCL-provided PID shown in Fig. 2.8, but the relative abundances are discrepant. Perhaps the low-energy shoulder of the ~1220 channel peak is another species. This is visualized in Fig. 3.11, which shows the silicon energy histogram and a fit with the sum of four Gaussian curves. While there is generally a nice match to data in shape, the extracted peak widths do not increase in a regular pattern, which one would expect as the energy increases.

The realized silicon detector energy resolution was roughly 11% at FWHM. This was determined by fitting the highest-intensity, (assumed) ^{11}Be energy peak with a Gaussian profile, shown in solid

red in Fig 3.10. Offline tests showed energy resolution of down to ~6%, which is still in excess of expectations for silicon detectors [39]. Additionally, LISE++ [48] calculations estimated energy depositions of 11(2) MeV, 19(3) MeV, 19(3) MeV, and 38(4) MeV for the ^{9}Li, ^{11}Be, ^{12}B, and ^{13}B, respectively. Taking the 19(3) MeV energy loss of ^{11}Be as the central value, perhaps the 11(2) MeV ^{9}Li is observed at roughly half the energy of the most intense-peak, but the 38(4) MeV ^{13}B at twice the energy of the most-intense peak is not.

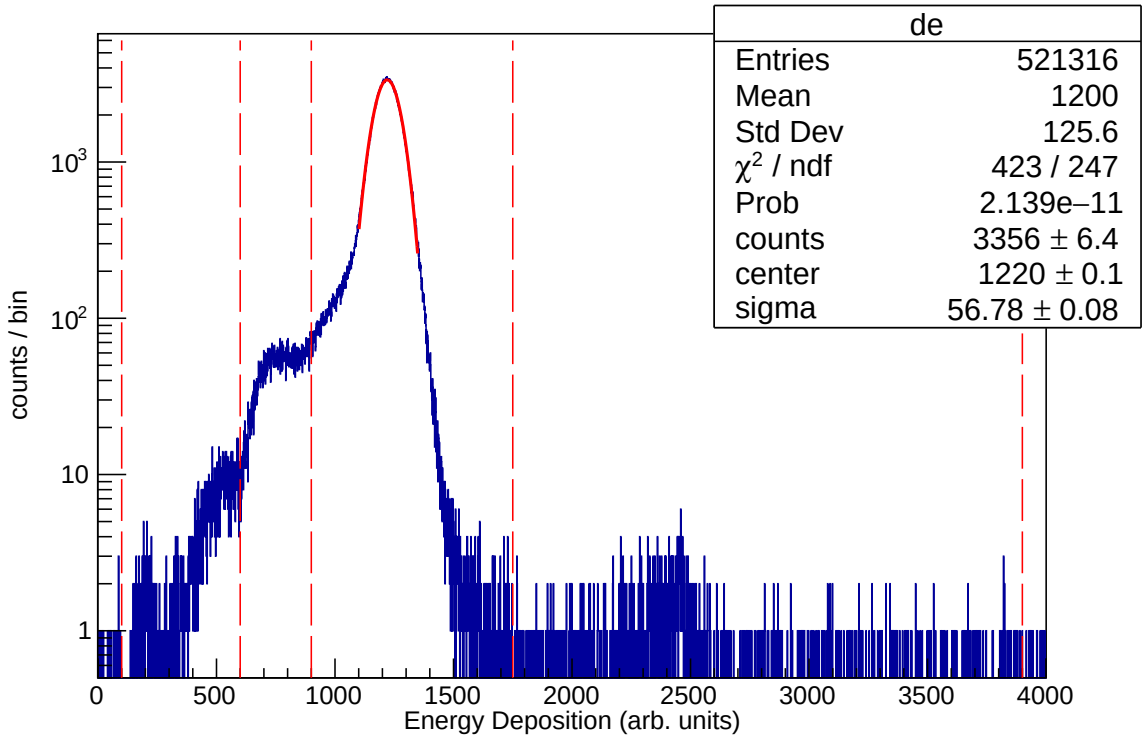

Figure 3.10: Silicon energy deposition (blue) used in the particle identification electronics. The dashed red lines are proposed thresholds that may be useful in particle identification. The solid red line is a superimposed Gaussian profile, fit by χ^2 minimization to measure the peak center and resolution.

Similarly, the TOF measurement was less insightful than expected. There are suggestive peaks at ~ 6000, ~12200, and ~21000 channels with relative intensities of 0.3%, 96.1%,3.2%, and 0.5%, respectively. Again, the odd, now high-energy, shoulder of the most-intense peak may arise from a true measurement of a contaminant or may be an artifact of the particle identification circuit. The resolution of the most intense peak was measured to be 6.8% in channels, but this is somewhat

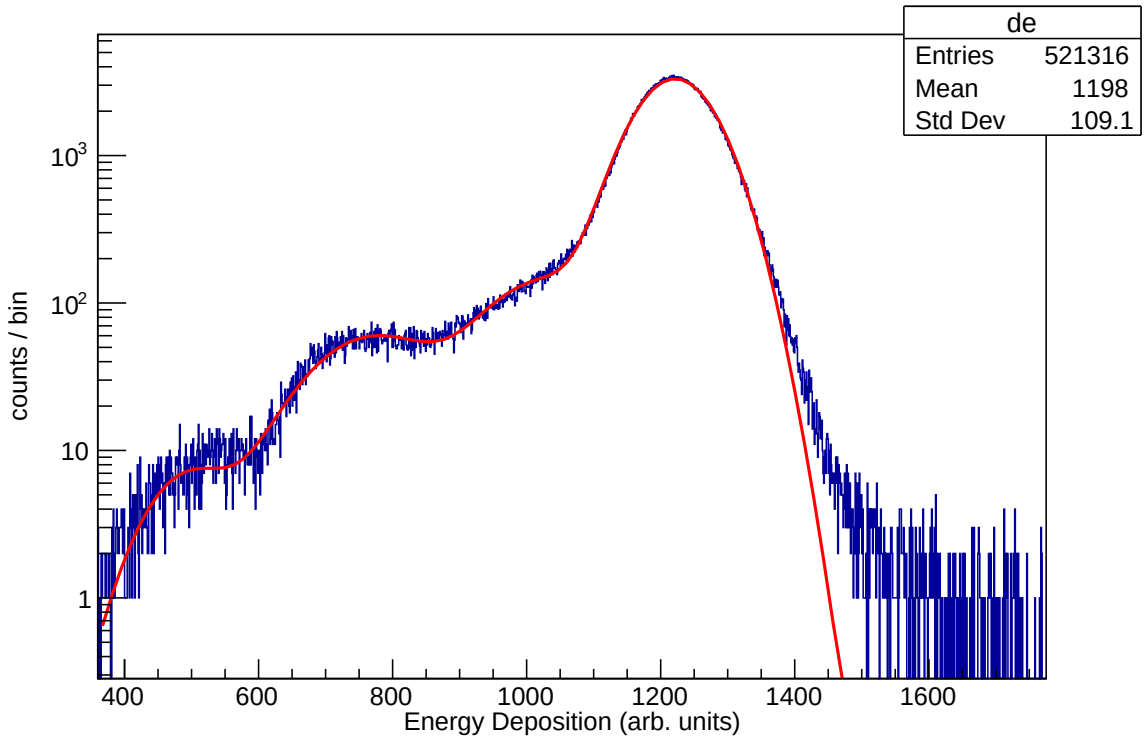

Figure 3.11: Silicon energy deposition (blue) used in the particle identification electronics with a smaller range than in previous Fig. 3.10. The solid red line is a superimposed sum of four Gaussian profiles, fit by χ^2 minimization. While the fit reproduces obvious features, all Gaussian parameters are all free parameters. It is not obvious what secondary features are from beam contaminants and what are from non-ideal behavior of the detector.

harder to quantify due to a lack of timing calibration. Offline tests with pulser signals showed sub-ns timing resolution. The same LISE++ simulations as a paragraph before predict time separation of ~40 ns between the first-arriving ^{12}B and the last-arriving ^{9}Li, with species-specific time spreads of ~4 ns, which closely matches the facility provided PID, shown in Fig. 2.8.

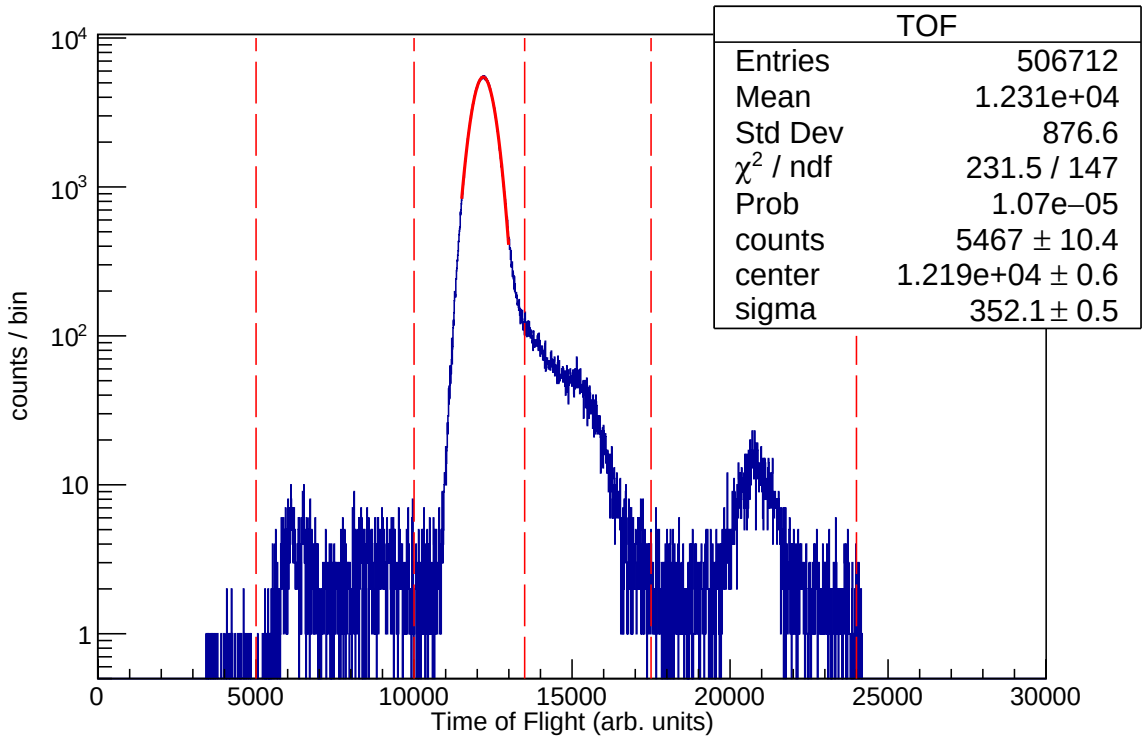

Figure 3.12: Time of Flight (blue) used in the particle identification electronics. The dashed red lines are proposed thresholds that may be useful in particle identification. The solid red line is a superimposed Gaussian profile, fit by χ^2 minimization.

In conclusion, while the supplementary GADGET-side particle identification was first implemented here in E19030, there are obvious limitations of the performance of the silicon detector and associated hardware during the online measurements. From arguments in Sec. 2.2.3 around the minimal impact of contaminants due to their short half-lives and non- charged-particle emitting behaviors, and very clear nature of the facility provided PID, this section is included for completeness only. Difficulties in this circuit are expected to have no bearing on the primary $\beta^- p$ measurement in GADGET.

3.3.2 Summarizing the Remaining χ^2-Minimization Analysis

3.3.2.1 Limitations of E18507 Analysis

The analysis of E19030 using the E18507 method, accounting for the additional instrumented pads, was quickly found to be of limited utility. With the increased statistics, the simple background of the sum of an exponential curve and a quadratic polynomial no longer provided adequate quality fits to the data over many of the pads. The search range with reasonable χ^2 p-values was E $\sim$ 180 – 220 keV, which is rather limited in scope. Further, even for these reasonable p-values, there is the question of large (several σ significance) negative values for the $\beta^- p$ peak height parameter. This is demonstrated in Fig. 3.13, which shows the fit of Pad C from 160 to 260 keV searching for a peak of 220 keV. (This $\sim 3\sigma$ negative-value peak at E=220 keV is common across pads, but Pad C is shown here for its large p-value of $\sim$ 0.5.) Negative branching ratio is nonphysical, so this highly significant negative intensity and decent p-value is suspect. Additional fits across pads, every 15 keV, are included in Appendix B.

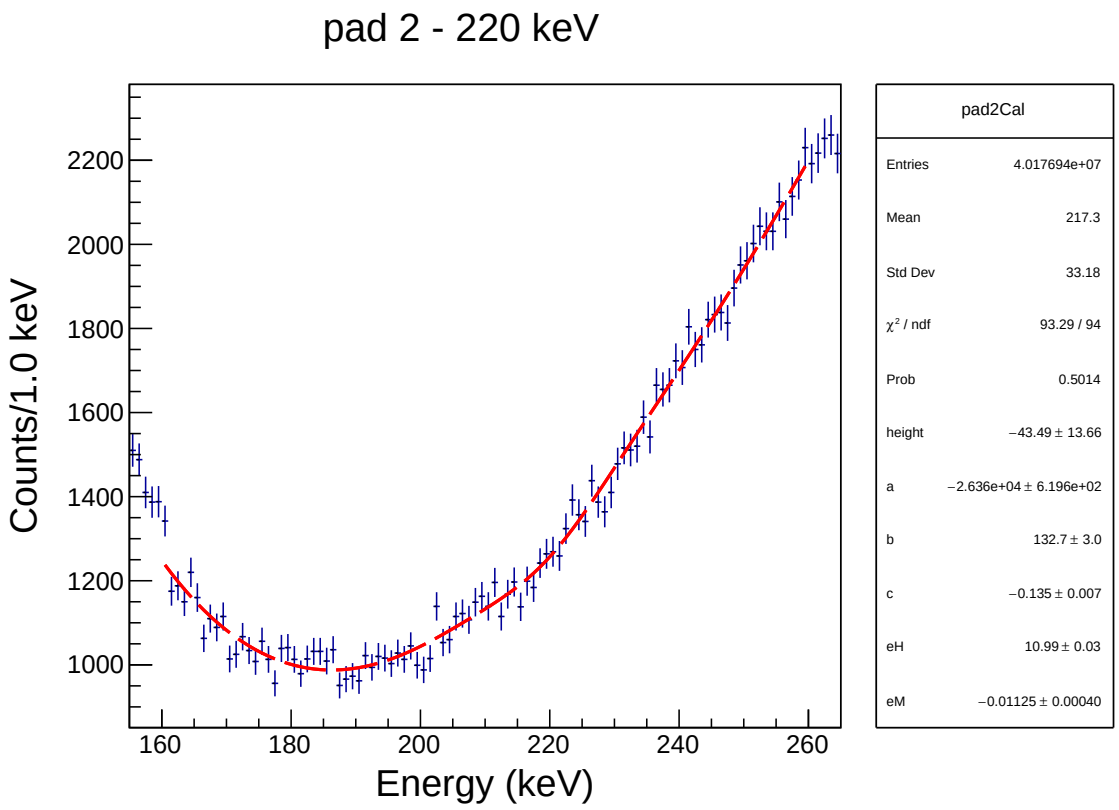

Figure 3.13: Pad C data from E19030 and a fit of the data to a modeling function. The model was the sum of an exponential function with parameters eH and eM, a quadratic polynomial $a + b \cdot E + c \cdot E^2$, and a Gaussian with fixed $E = 220$ keV center and $\sim 11.6\%$ width. The Gaussian peak is meant to extract the number of β^p counts. This fit yields $-44(13)$ $\beta^- p$ counts. The quality of the fit, as judged by p-value, is excellent, however, a negative amount of counts is nonphysical and this fit yields negative counts at nearly 3σ significance.

For completeness, Fig. 3.14 is the (statistical) error-weighted average branching ratio, determined across pads A, B, C, D in E19030 using the analysis of E18507. In comparison to the results of E18507 shown in Fig. 3.7, there are two notable features. First, the E19030 results have error bars of $\sim 2 \cdot 10^{-6}$ as we sought to attain, but secondly, significant swaths of the search region exist in nonphysical negative branching ratios with incredible statistical significance. The situation with the E18507 analysis is as follows: we limit ourselves to the search range of E = 175 to 220 keV and have to contend with explaining the $\sim 4\sigma$ nonphysical "signal" at E = 220 keV or we can reduce our search range but not on the merits of the p-value as a quality of the fit.

Is this evidence that the background is unknowable? Hardly, but a more sophisticated, *physically*

motivated model is needed and the idea of systematic errors needs to be forefront in the decision making.

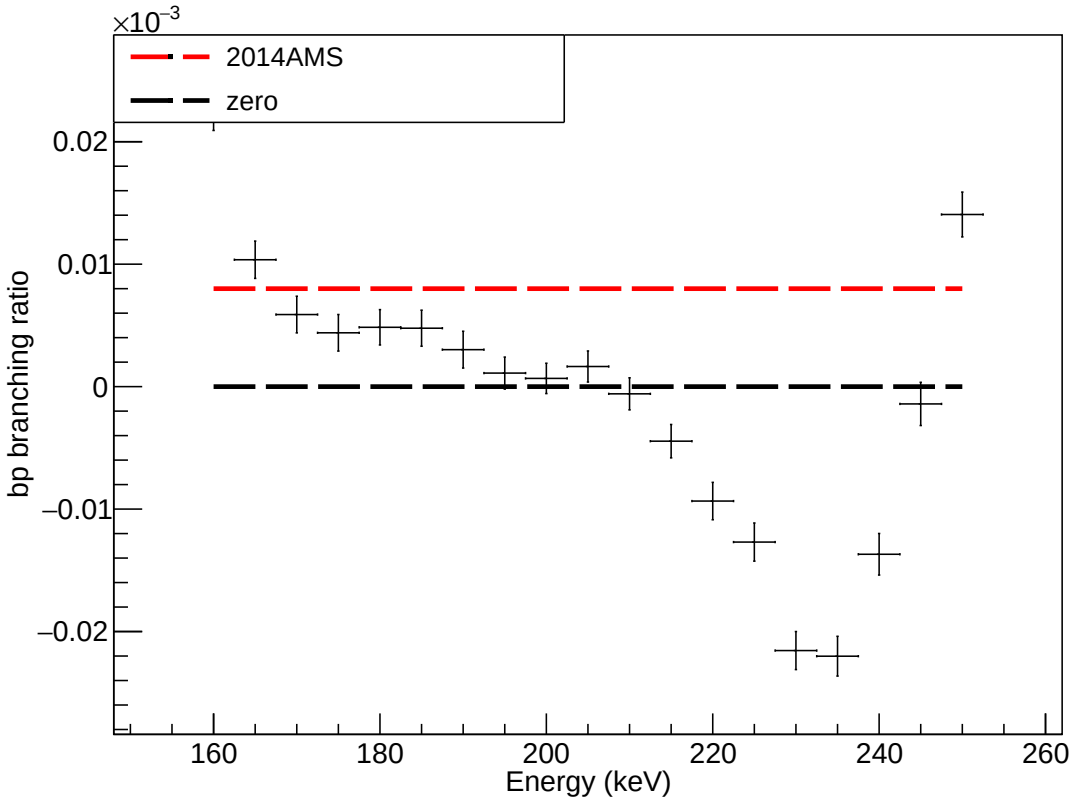

Figure 3.14: Results of E19030 with the E18507 analysis, averaging the results of Pads A, B, C, D, and E. Compare to Fig. 3.7. The inferred ^{11}Be(β^-p) branching ratio is consistent with zero only around $E \sim 200$ keV. Above $E \sim 210$ keV, highly significant nonphysical negative branching ratios found. These results suggest limitations of the simple model used in E18507, driven by the increase of statistics of E19030. A better model, a physically motivated model, of the background is needed.

The minimal χ^2 value is improved by inclusion of additional polynomial terms. (One additional term pushes fits to reasonable p-values across most pads at most energies.) However, beginning with a cubic function to model the lowest energy portions of the ^{11}Be($\beta^-\alpha$) spectrum, we can no longer guarantee the same selectivity between the $\beta^-\alpha$ background and any possible $\beta^- p$ signal. A search peak, whether a simple Gaussian or one more complicated, based out of greater inclusion of physics and detector features, as will be detailed soon, will be of mixed concavity. On the tails

of the peak, the second-derivative concavity will be positive. Near the maxima, the concavity will be negative. The choice of summed exponential and quadratic polynomial curves to describe the background provided some guarantee against background-selection of our search peak.

While χ^2-minimization fitting of a parameterized curve doesn't explicitly select parameters based upon their influence on any order derivative of the curve (only the trivial zeroth), this is meant as a qualitative argument against increasing the polynomial number until reaching a *satisfactory* χ^2 p-value. A polynomial of sufficiently high order will perfectly describe our background and $\beta^- p$ signal without differentiation of the two; inclusion of a search peak will only improve such a fit, with the only evidence of accidental equivalence between the background and signal is an increase of the correlation matrix elements between the signal strength parameter and the *sufficient*-ly numerous polynomial parameters. Furthermore, such a correlation matrix is defined at a singular solution and may present somewhat different values depending on exactly the amount of signal that is captured by the background model and exact shape of the contours of χ^2 space around that solution, for a *singular* fit out of the many fits performed across pads and energies.

3.3.2.2 Fitting With Other Background Models

One way to give greater detail to the background model while minimizing the risk of confusing signal for backgrounds (or vice versa), is to fit using not polynomials, but physically motivated functions that have more tightly constrained shapes. The β^- background is already well modelled by an exponential curve, but it is the ^{7}Li* peak (and low-energy tail of the ground state, ^{7}Li-alone and excited ^{7}Li* feeding α-alone peaks to a smaller degree) that need a better modelling function.

The energy spectra of isolated resonances are well described by a Lorentzian (alternatively Breit-Wigner or Cauchy, with different notations of Γ) curve [49]. The general shape of this curve is:

$$L(x) \sim \frac{1}{(x-\bar{x})^2 + \Gamma^2/4} \tag{3.2}$$

The simplest assumption of the detector response is a Gaussian response for a Delta function of a single energy. Previous measurements with GADGET [37, 7, 6, 8], have demonstrated that a Gaussian detector response is a fair approximation. The detector response of an input with width would be the mathematical convolution of the physical input and the Gaussian detector response as in Eq. 3.3. Here, $D(E)$ is the *observed* distribution of energies measured by the detector, g is the detector response at E for a physical signal at energy x, and d is the distribution of *actual*, physical energies.

$$D(E) = g \otimes d = \int g(E, x) d(x) dx \tag{3.3}$$

The convolution of the Lorentzian and Gaussian distributions is the so-called Voigt profile. This function does not have a closed form except for particular values of the Gaussian width σ or Lorentzian width Γ. Evaluation of the Voigt profile was implemented by ROOT's Voigt function, which is part of the TMath library.

The next background model that was attempted was the sum of three parts: an exponential curve to model the β^- particles, a Voigt profile to model the ^{7}Li* peak, and a constant term, from incomplete charge deposition, seen in previous measurements with narrow background peaks. A variety of fits were performed with this new background function with different fit ranges and assumptions for the correct Γ width of the ^{7}Li* peak. What will follow are fits over 145-250 keV in each of the quadrant pads. The width of the ^{7}Li* peak is left as a free parameter for two reasons. First, our background isn't purely one peak. From the energies included in the fit range, we largely exclude the higher energy peaks, but not entirely. Secondly, a R-matrix (Sec 4.2.1) analysis of ^{11}Be($\beta^-\alpha$) [2] was published during this analysis. The width of the α-emitting state in ^{11}B was significantly broader than the evaluated average that was determined from reaction and scattering measurements. The R-matrix deduced width was reported to be $\Gamma = 233(3)$[3] keV, which is a factor of two larger than the evaluated 109(4) keV. Perhaps the β^--fed width is greater than the reaction and scattering width, as the earlier $\beta^-\alpha$ measurement by Alburger *et al.* [46] of $\sim$ 330 keV, but they claim no significance due to a poor energy calibration. The search signal is a two-peaked

Voigt. The first peak is the full center of mass energy, originating from decays in the volume and the second peak is at $\sim 10/11$ of the full energy from the kinematics of the emitted proton and ^{10}Be, and comes from measuring just the cathode-originated protons. The Gaussian width σ of the peaks was assumed to be 7.5% of the full peak energy. The peaks are weighted by the measured split of in-gas and cathode decays, measured by the arrival time $^{11}\mathrm{Be}(\beta^-\alpha)^7\mathrm{Li}^*(\gamma)$. The inclusion of a finite width to the $\beta^- p$ signal comes from a measurement of the $^{11}\mathrm{Be}(\beta^- p)$ at TRIUMF with a similar detector [3]. The TRIUMF-measurement group measured the width to be $\Gamma = 12(5)$ keV.

Figures 3.15, 3.16, and 3.17 show the unnormalized results of this peak search for the quadrant pads, assuming a narrow ($\Gamma = 0$ keV), $\Gamma = 12$keV, and $\Gamma = 24$ keV $\beta^- p$ emitting resonance in ^{11}B, respectively. The range of Γ values shown here were informed by the TRIUMF measurement's value of 12(5) keV. To guide reading the unnormalized counts, with the new E19030 dataset, each 100 counts is $\sim 1 \cdot 10^{-6}$ branching ratio. At low widths, Pads B, C, and D each peak around E $\sim$ 175 keV, are largely consistent with zero, then at E $\sim$ 210 keV and greater report -2σ negative values. Pad E has similar behavior, but is shifted to higher energies $\sim$ 10 keV. As the Γ width increases, the measurements lose this peak-like behavior and develop into a step function with very large branching ratios ($\sim$ 20 to $100 \cdot 10^{-6}$) for energies below E $\sim$ 200 keV and moderately large negative branching ratios ($\sim -20 \cdot 10^{-6}$) at higher energies. It is hard to interpret these curves as a physical peak and the simplest description is that sufficiently wide search signals match some feature in the background better than or missed by our assumed model.

For an example, if we consider the behavior at E = 175 keV for $\Gamma = 0$, 12, and 24 keV. As the assumed proton intrinsic width Γ_p increases, so does the ^{7}Li* width Γ_{Li} and total ^{7}Li* intensity while the flat background decreases. This effect is usually $\lesssim 1\sigma$ in each of these parameters going from $\Gamma_p = 0$ keV to $\Gamma_p = 24$ keV, but this pattern is ubiquitous across all four pads. Further, the statistical error really is not relevant to this point. The data is the same for each fit with choice of Γ_p and not a re-measurement of the data itself, which is what the σ error tells your the expected variation of. This correlation is just that, a correlation, but the shared behavior across pads is suggestive (beyond the absurd step-function curves) that our background model has additional

systematic error. That is, if our background were modeled perfectly, the resulting intensity of the $\beta^- p$ signal would not have wild dependencies on the assumed signal shape.

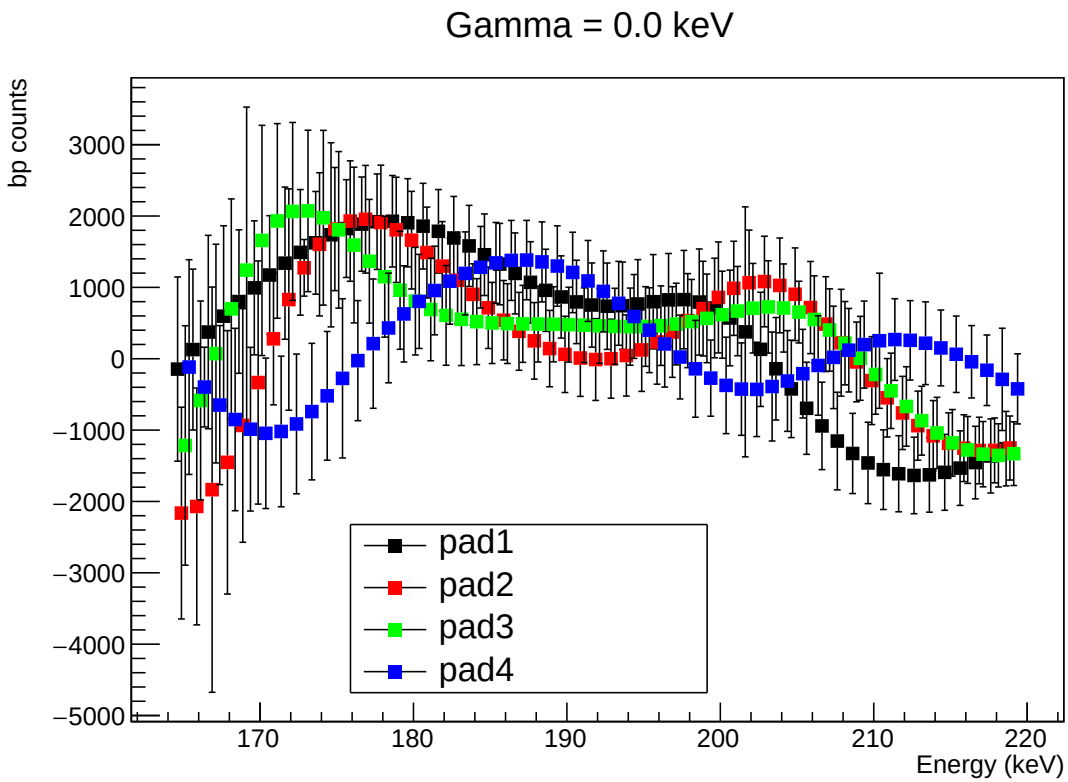

Figure 3.15: Inferred $\beta^- p$-like counts from fitting the E19030 quadrant pads with the Exponential+Flat+Voigt model. The peak shape is described in the text and the fits here assume a narrow, $\Gamma_p = 0$ keV proton-emitting resonance. Generally, an excess is seen for $E \sim 175$ keV. At high energies, nonphysical negative counts are extracted.

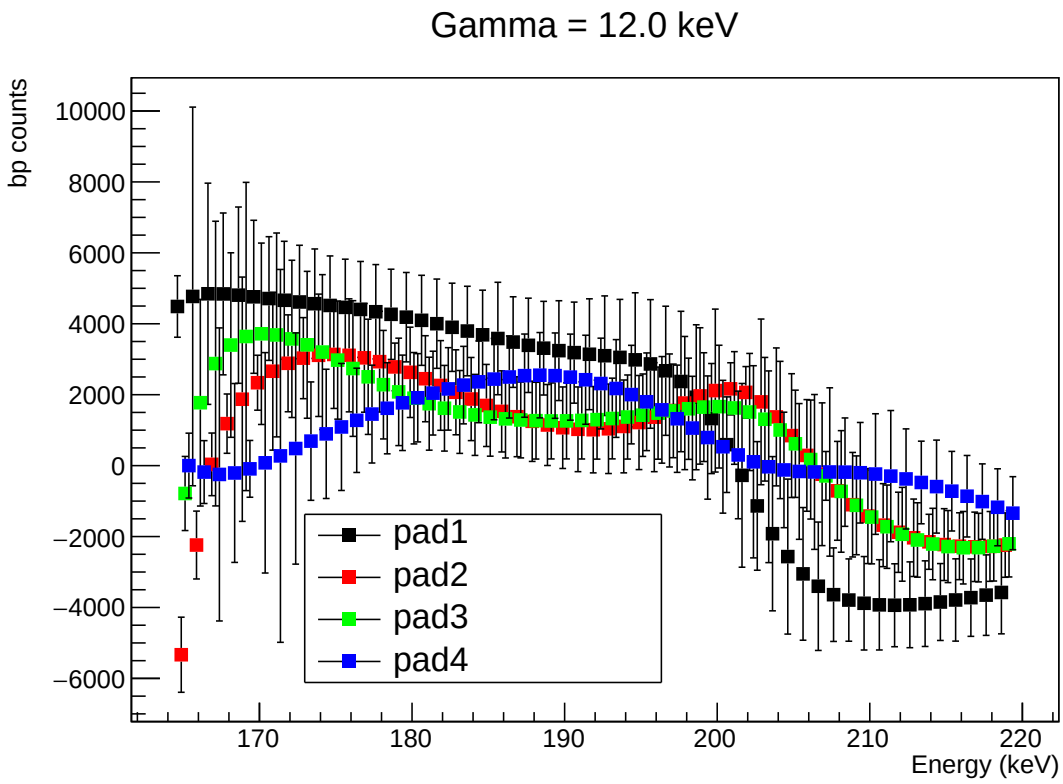

Figure 3.16: Inferred $\beta^- p$-like counts from fitting the E19030 individual pads with the Exponential+Flat+Voigt model. The peak shape is described in the text and the fits here assume a $\Gamma_p = 12$ keV proton-emitting resonance. Generally, below $E \sim 200$ keV, a somewhat flat amount of excess is observed. At higher energies, a somewhat flat "excess" of nonphysical negative counts are extracted.

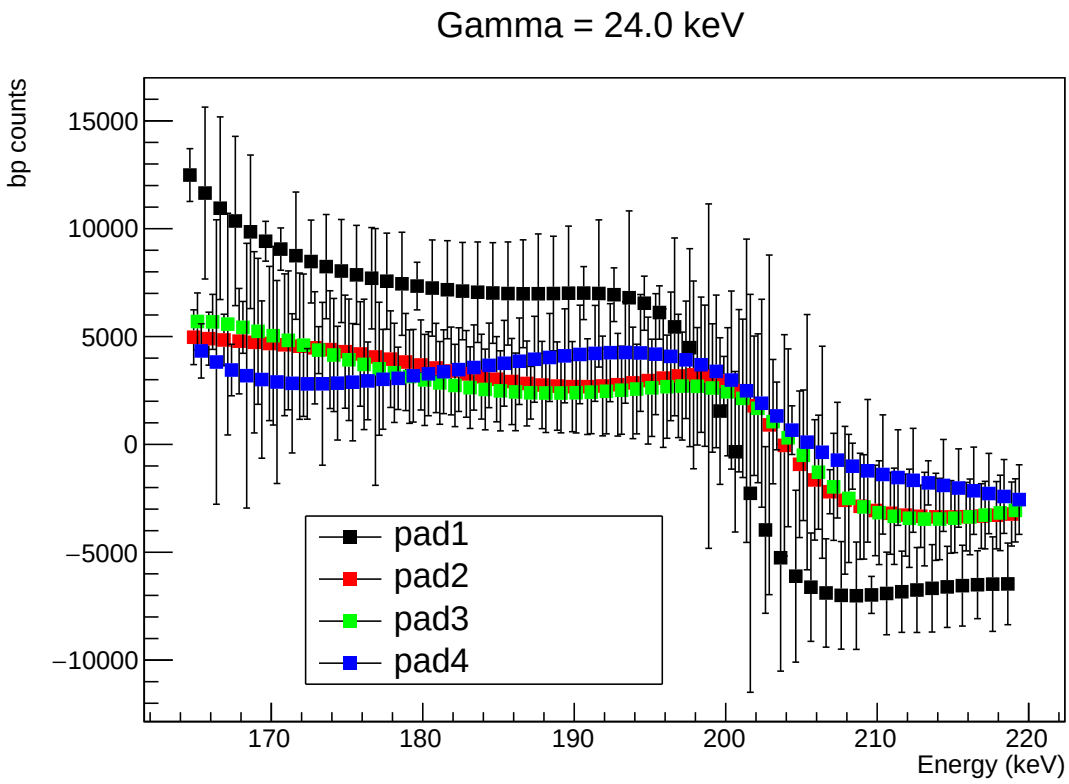

Figure 3.17: Inferred $\beta^- p$-like counts from fitting the E19030 individual pads with the Exponential+Flat+Voigt model. The peak shape is described in the text and the fits here assume a $\Gamma_p = 24$ keV proton-emitting resonance. Generally, below $E \sim 200$ keV, a somewhat flat amount of excess counts is observed. Counting excesses of this size yield branching ratios of $b_p \sim 50 - 100 \cdot 10^{-6}$, in excess of any previous measurement by more than a factor of five. At higher energies, a somewhat flat "excess" of nonphysical negative counts are extracted.

Concluding this chapter, a few other background models were utilized. The flatness of the flat background and the precise shape of the ^{7}Li* peak were tested with a variety of slightly different functional forms. One such model was a sum of two exponential functions (one steep for β^- particles and one shallow) and two Voigt profiles (one for ^{7}Li* peak and one for the composite ^{7}Li-α^* peak. An example of one of these fits is in the Appendix Fig. B.37, where it is shown that a χ^2 optimization provides an excellent fit to data far in excess of our search region of $E_p < 250$ keV. This high-parameter model did away with the step-function in the results of the simpler Expoential+Flat+Voigt model, but became very hard to work with. Seemingly insignificant changes in starting values for the χ^2 minimization or assumed peak energy could make extracted $\beta^- p$ intensities move on order

or even in excess of their 1σ statistical error. (See Appendix Fig. B.39.) In Chapter 4, I will explain how moving the fitting procedure from ROOT's χ^2 optimization by gradient descent into a from-scratch Markov Chain Monte Carlo method with Bayesian priors allowed for a sort of simplification of the analysis by doing away with inflexible Gaussian probability density functions and "baking in" all of our statistical and systematic uncertainties into one self-consistent analysis procedure.

CHAPTER 4

ANALYSIS: R-MATRIX, GAS STOPPING, BAYESIAN INFERENCE

Chapter 3 is a summary of how the data for E19030 came to exist and an exhibit of analysis difficulties of searching for a $\sim 10^{-5}$ $\beta^- p$ branch on the low-energy tails of the ~ 0.03 $\beta^- \alpha$ branch from the decay of ^{11}Be. This chapter will be a more direct account of the final analysis and motivations for the details of the analysis. The general data sorting from Chapter 3 will carry over, but other details will be revisited in this chapter with greater scrutiny. This additional scrutiny came from the implementation of the Bayesian analysis, which requires well defined uncertainty quantification of its inputs. This chapter is meant to show the complete state of the analysis for E19030. Results and discussion will continue in Chapter 5.

The development of the Markov Chain Monte Carlo used in this chapter was developed in close collaboration with Scott Pratt and Pablo Giuliani.

4.1 Summary of what we do know

Recapping, here are the following elements needed to infer the ^{11}Be($\beta^- p$) branching ratio:

- Data sorting to produce analysis spectra
- Determination of a background shape
- Determination of the $\beta^- p$ signal shape
- *Inference* of the number of $\beta^- p$ in the analysis spectra
- Normalization of the $\beta^- p$ counts to a branching ratio

The data sorting will not be revisited and the summary in Sec. 3.1 is complete. The determination of the background shape will be revisited with information from the recent R-matrix analysis of ^{11}Be($\beta^- \alpha$) decay [2] in Sec. 4.2. The shape of the assumed $\beta^- p$ signal shape will be revisited through the lens of low-energy ion-stopping processes which, in addition to the new recommended

energy of the $\beta^-\alpha$ decay from [2], has carryover consequences for the energy calibration. Statistical inference took a large step in complexity - Sec. 4.4 will introduce both Bayes' theorem, the Markov Chain Monte Carlo method to "solve" Bayes' theorem, and how these ideas were implemented to infer the ^{11}Be($\beta^- p$) decay rate.

4.1.1 Some data-inferred details

Before diving into new interpretation and analysis tools, there are a couple important details that still need to be presented that can be pulled from the data alone.

4.1.1.1 Normalization of the $\beta^- p$ counts

First, we will to revisit the Proton Detector detection efficiency calculations which allow us to normalize to the well-studied ^{11}Be($\beta^-\alpha$) decay branch and calculate a branching ratio from a number of counts. Following the detailed work of Tamas Budner with his own GADGET analysis [50], the efficiency code described in Sec. 3.2.1.2 was updated to include diffusion of the ionization electrons as they drift through the detector gas toward the MICROMEGAS. Tyler Wheeler performed MAGBOLTZ calculations for each of us to estimate this effect. MAGBOLTZ numerically performs particle-tracking based simulations that solve the Boltzmann transport equation for electrons drifting in a medium, pushed by an external electric field. The simulations include atomic excitation such as bound-electron orbital promotion and vibrational excitation in polyatomic molecules like CH_4 [51, 52].

For our ^{11}Be measurements at 600 Torr, it was calculated that the electric-drift-field transverse diffusion coefficient of these electrons was $D_t = 14060 cm^2/s$. Decays were assumed to happen uniformly throughout the $\sim 8\mu$s drift length of the Proton Detector. The results of this new simulation for in-gas ^{7}Li(g.s.)+α decays are shown in Fig. 4.1. Simulations were run for cathode-originated ^{7}Li-alone and α-alone peaks, but are not included here. The general behavior of the these cathode-originated efficiency curves were similar to that of in-gas decays shown here. For in-gas decays of $E \sim 1200$ keV, the detection efficiency for Pad A ($\sim 31\%$) is similar to the quadrant

pads (~ 39%, shown as Pad B). This is roughly half of the estimated ~ 72% for the composite ABCDE pad. The composite pad would be expected to have much greater detection efficiency due to the larger area compared to its edge, relative to the area/edge ratio of the constituent pads.

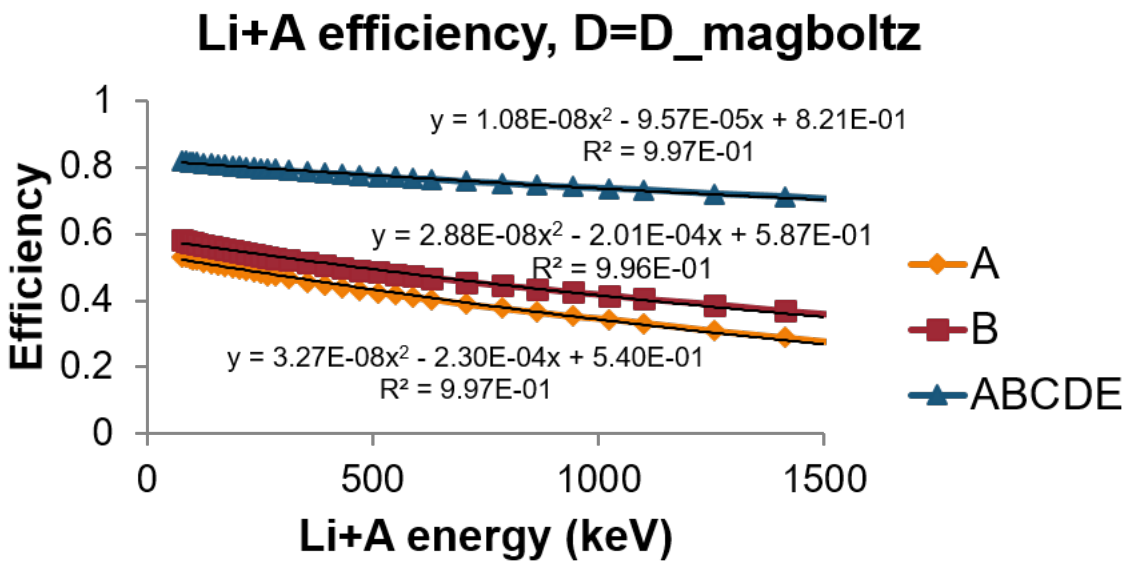

Figure 4.1: Simulated detection efficiency of in-gas ^{7}Li(g.s.)+α decay for different pad schemes and geometries. The quadratic polynomial fits are meant to parameterize the output of the simulation for fast calculations of arbitrary energy.

Figure 4.2 shows a comparison of the individual pads spectra, the sum of the individual pad spectra, and the composite ABCDE pad spectrum. Ignoring subtle differences in the energy calibration, the individual pad summed spectrum is nearly as intense as the composite pad spectrum. This goes against expectations based on the efficiency calculation based off of SRIM and MAGBOLTZ, which predicted nearly a factor of 2 between individual pad efficiencies and the composite pad efficiency. Figure 4.3 shows the bin by bin ratio of the summed spectrum over the composite pad scheme spectrum. The efficiency is somewhat flat with respect to energy, with the individual pad scheme capturing ~ 85% of the events that the composite pad scheme captured. This indicates that many more charged-particle events are confined to a single measurement pad than the simulation suggested. This suggests the SRIM calculated ranges or the MAGBOLTZ diffusion coefficient or both are too large, and simulated events cross over measurement pad boundaries in excess of real

events. While the normalization of the $\beta^- p$ decay is performed against the $\beta^- \alpha$ in the individual pad scheme, pad by pad, and not across different pad schemes as shown here, the takeaway is that the sum of individual pads only is equivalent to the composite pad only when charged-particle tracks were far shorter than calculated and activate only a single pad most of the time. For radiations that rarely activate other pads, the detection efficiency of every $\beta^- \alpha$ radiation in either scheme is quite high. Hereon, the detection efficiency between $\beta^- \alpha$ radiations and $\beta^- p$ decay both will be treated as unity with a $\lesssim 20\%$ error.

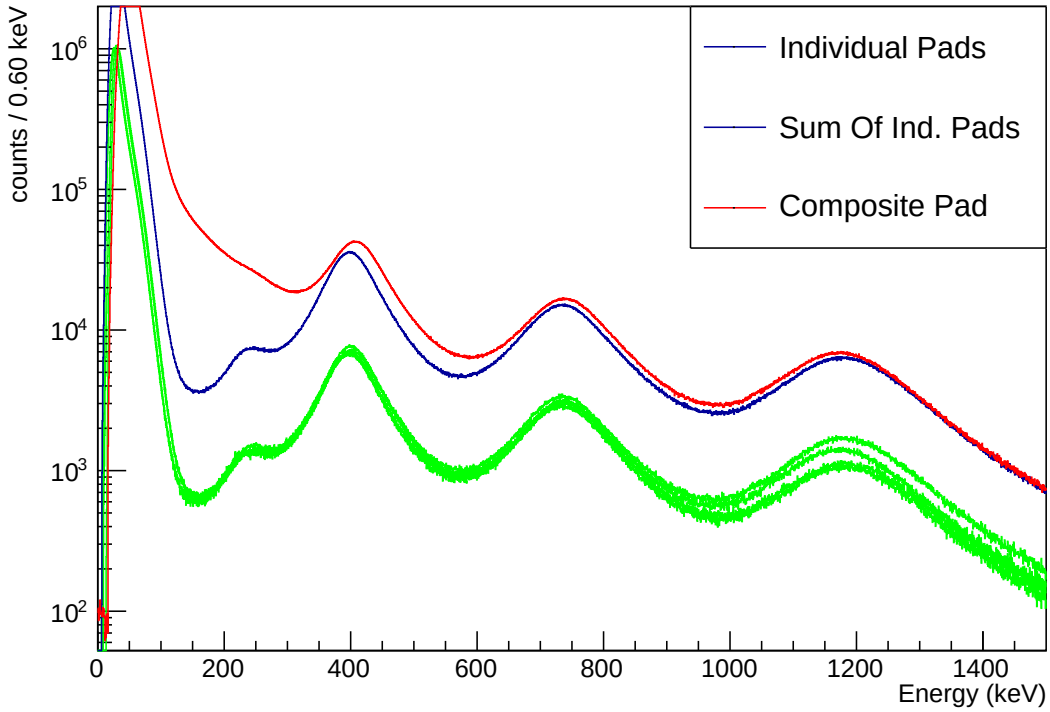

Figure 4.2: Individual pad spectra (green), summed individual pad spectrum (blue), and composite pad spectrum (red). The sum of individual pad spectra is similar in counts to the composite pad spectrum over much of the spectrum which is suggestive of relatively flat detection efficiency curves as a function of energy.

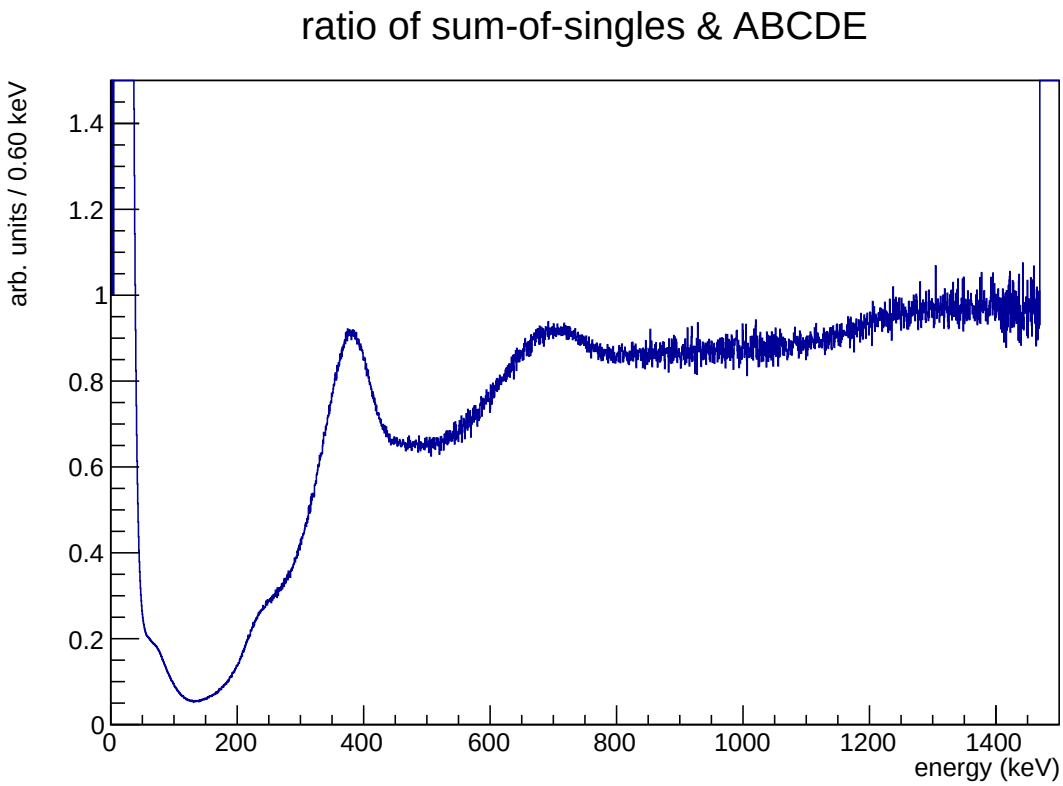

Figure 4.3: Bin-by-bin ratio of the summed individual pad spectra and the composite pad spectrum shown in Fig. 4.2. Overall, the sum of individual pads tend to have ~ 85% of the total counts of the composite ABCDE pad.

The number of $\beta^-\alpha$ decays measured in each pad are shown in Table 4.1. This is calculated by integrating the individual pad spectra above $E = 200$ keV. This choice of the boundary includes minimal β particles and captures all but the lowest-energy tails of the $\beta^-\alpha$ spectrum. The inference of ^{11}Be normalization comes from the 3.30(10)% measurement of the $\beta^-\alpha$ branching ratio reported in Refsgaard *et al.* [2]. We would expect just about 1000 counts of $\beta^- p$ per pad, assuming a 10^{-5} branch, similar to that reported by Ayyad *et al.* [3]. This is a small signal when most of the background in the search region is ~ 1000 counts with 1 keV binning and the search signal will be ~ 20 keV wide. However, assuming Poisson counting statistics, the error in counts of a bin or a region of bins is $\sigma \sim \sqrt{N}$, where N is the number of counts in the region. A 20 keV wide signal will cover roughly 20,000 background counts. We expect statistical limitations at about $\sigma_{\text{stat}} \sim \sqrt{20,000} \sim 140$ counts. Thus, a 1000 count signal is small, but can appear with ~ $7\sigma_{\text{stat}}$ in

the limit of no systematic uncertainties.

Pad Label	Integrated Counts	Inferred ^{11}Be Normalization	Inferred $\beta^- p$ for $b_p = 10^{-5}$
B	$3.825 \cdot 10^6$	$1.16(4) \cdot 10^8$	$1.16(4) \cdot 10^3$
C	$3.080 \cdot 10^6$	$9.3(3) \cdot 10^7$	$9.3(3) \cdot 10^2$
D	$3.244 \cdot 10^6$	$9.8(3) \cdot 10^7$	$9.8(3) \cdot 10^2$
E	$3.419 \cdot 10^6$	$1.04(3) \cdot 10^8$	$1.04(3) \cdot 10^3$

Table 4.1: Integrated number of observed $\beta^-\alpha$ counts, inferred ^{11}Be normalization, and inferred ^{11}Be($\beta^- p$) counts assuming a branch of $b_p = 10^{-5}$, across pads.

4.1.1.2 Cathode-volume fraction, decay location determination

The relative intensity of the ^{10}Be+proton and p-alone peaks is determined by the location distribution of the ^{11}Be decays. This was determined by the relative intensity of ^{7}Li+α against ^{7}Li-alone and the α-alone peaks, which were determined by energy deposition and timing between detection of charge in the Proton Detector and a 478 keV γ ray in the SeGA array. Figure 4.4 shows a two dimensional histogram that was used to determine the location of ^{11}Be decays along the z-axis. At all times, there is an intense band above $\sim$ 400 keV, another below $\sim$ 800 keV, and another at $\sim$ 1200 keV. These are from accidental coincidences. This is shown by the sharp spike of events at times $\sim 7.2\mu$s. The detector drift field was set so that the drift time of the full length of the detector would be $7 - 8\mu$s, so the peak at $\sim 7.2\mu$s is interpreted as decays originating from the upstream detector cathode. Similarly, there are two spots in this spike, one at $E \sim 260$ keV and one $E \sim 440$ keV. The peak at $E \sim 260$ keV is the ^{7}Li-alone detection and the $E \sim 440$ keV peak is the α-alone detection. At lower time, there is a blob of intensity that comes from the in-gas detection of both the ^{7}Li and α together.

With this understanding of the feature at $\sim 7.2\mu$s as the cathode, the events at greater times are certainly accidental coincidences. One can perform a background subtraction to remove these at earlier times. There are several possible methods to perform this, but the simplest is to project the coincident-events from this histogram to a one dimension histogram of energy. The formula for this background subtraction is below, if E and t are discrete bin values. Note that Δt is then

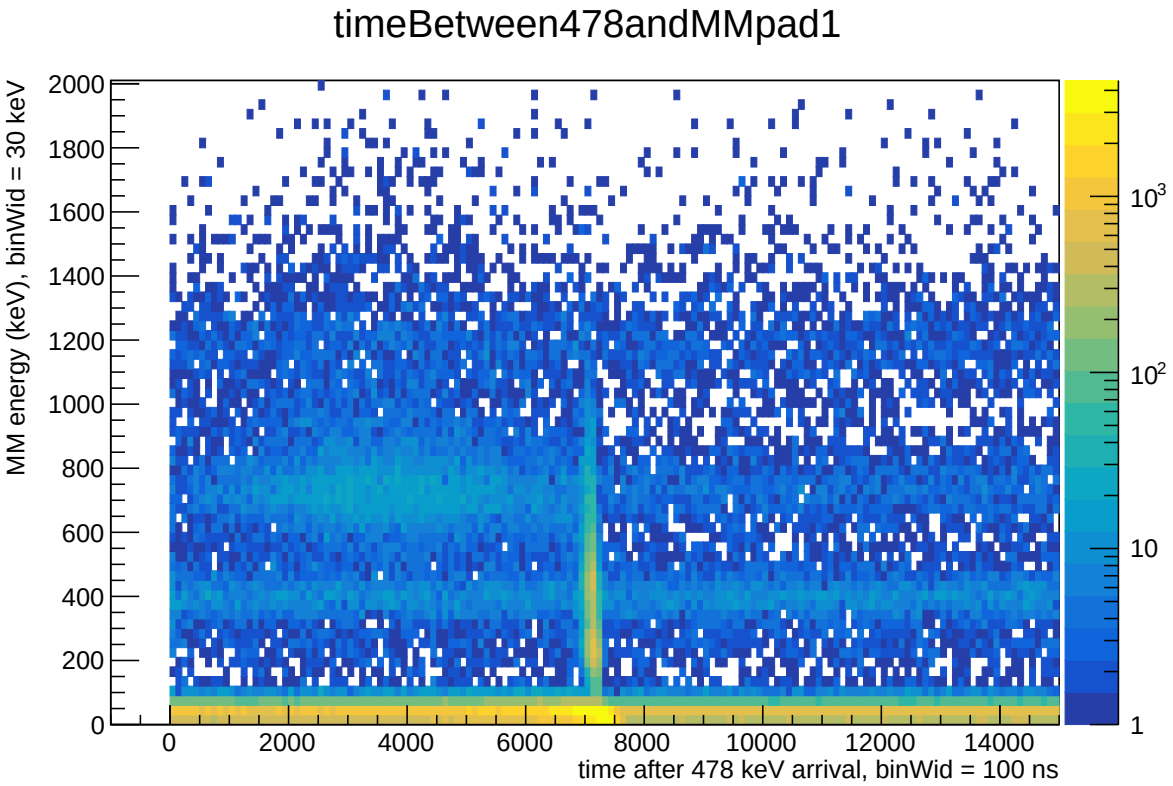

Figure 4.4: Coincidence histogram of the Pad B energy and pad signal arrival time when coincident with a 478 keV γ ray. Events after $\sim 7.2\mu$s are accidental coincidences. The spike at $\sim 7.2\mu$s comes from detection of only one of the light ions from cathode-originated $^{11}\mathrm{Be}(\beta^-\alpha)^7\mathrm{Li}^*$ decay. The diffuse cloud of events at time $< 7.2\mu$s and energy ~ 700 keV are from full-energy ^{7}Li+α events originating in the detector gas. The low-energy events at all times are β^- particles.

a number of bins. The background subtracted histogram calculated bin-by-bin from the original spectrum and the time-integrated projection of the late-time spectrum.

$$h_{\mathrm{sub}}(E,t) = h_{\gamma-\mathrm{coinc.}}(E,t) - \frac{h_{\mathrm{acc.\ coinc.}}(E)}{\Delta t} \tag{4.1}$$

This subtraction yields Fig. 4.5. The features that remain are the diffuse in-gas decays that measure the full charged-particle energy from the $^{11}\mathrm{Be}(\beta^-\alpha)^7\mathrm{Li}^*$ decay that arrive up to $\sim 7.2\mu$s after the γ ray, the measurement of ^{7}Li-alone and α-alone originating from the cathode arriving $\sim 7.2\mu$s after the γ ray, and the intense β-particle background at low energy. Due to the long tracks of the β particles, the ionization from these radiations appears more diffusely in time than the heavy

ions with short ranges and more localized tracks.

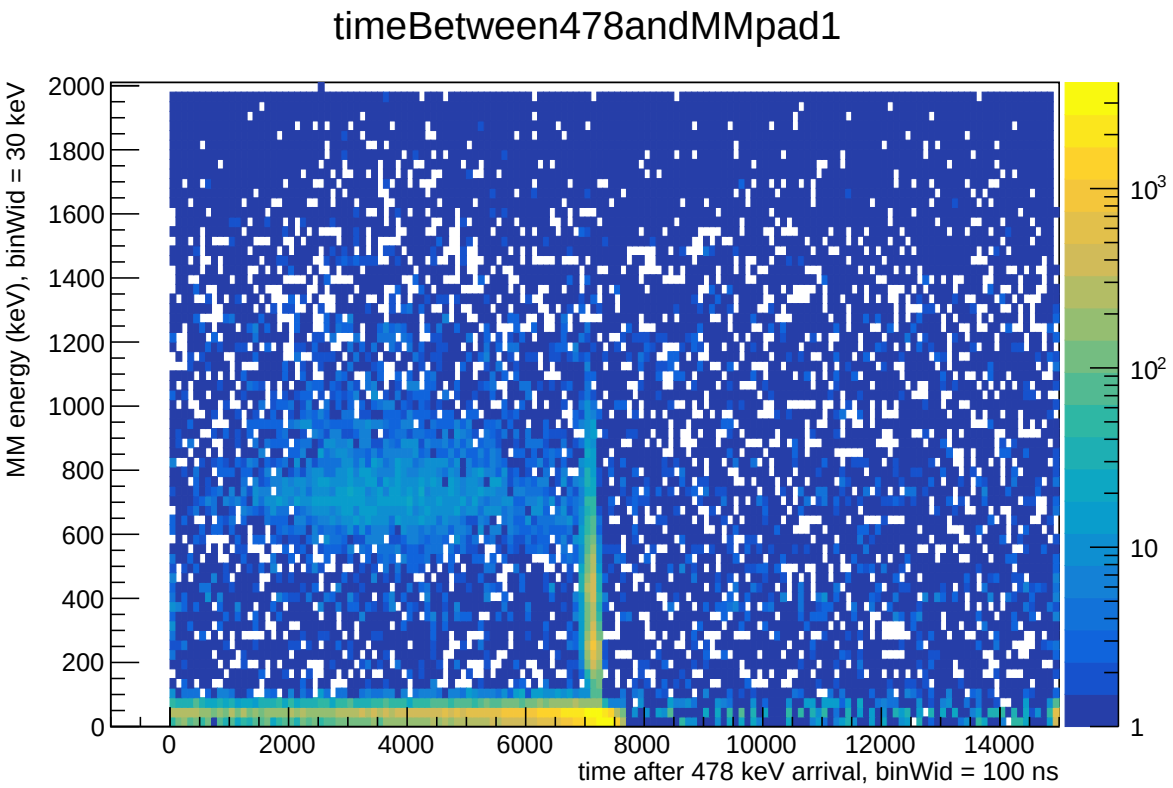

Figure 4.5: Coincidence histogram of the Pad B energy and pad signal arrival time when coincident with a 478 keV γ ray after subtraction of accidental coincidences. Events after $\sim 7.2\mu$s are statistically consistent with zero. The spike at $\sim 7.2\mu$s comes from detection of only one of the light ions from cathode-originated $^{11}\mathrm{Be}(\beta^-\alpha)^7\mathrm{Li}^*$ decay. The diffuse cloud of events at time $< 7.2\mu$s and energy ~ 700 keV are from full-energy $^7\mathrm{Li}+\alpha$ events originating in the detector gas.

The fraction of cathode and volume decays was taken by integrating the heavy ion $E > 200$ keV coincident events in the background-subtracted spectra. Events recorded for $0 < t < 6.8\mu$s were deemed in-gas volume events. Events recorded for $6.8 < t < 7.6\mu$s were deemed cathode-originated. Pads B, C, D, and E had cathode-originated fractions of 63.4%, 71.6%, 73.1%, and 67.4% respectively. The choice of the energy threshold creates a $\sim 1.5\%$ error in these numbers. The counting-statistics error is small compared to this threshold systematic error.

4.1.1.3 Detector Resolution Measurements

In the previous analysis, the anticipated detector resolution was determined by fitting historical resolution data in other GADGET experiments, with different gas pressures and operational voltages. Ideally, these were scaled proportionally to give historically similar behavior (see Fig.s A.1,A.2,A.3), but using data from within the E19030 experiment would still be best. Additionally, the Bayesian analysis does not strictly require Gaussian distributed errors and more general forms can be chosen.

Figure 4.6 shows a fit of the in-gas, full energy ^{7}Li+α peak. In Pad B, the measured resolution is 5.0(8)% FWHM and intrinsic width is 225(2) keV. For Pads C, D, and E, the detector resolution was measured to be 5.4(4)%, 6.4(4)%, and 5.2(4)% FWHM respectively. The intrinsic widths were 226(2), 230(2), and 222(2) keV respectively.

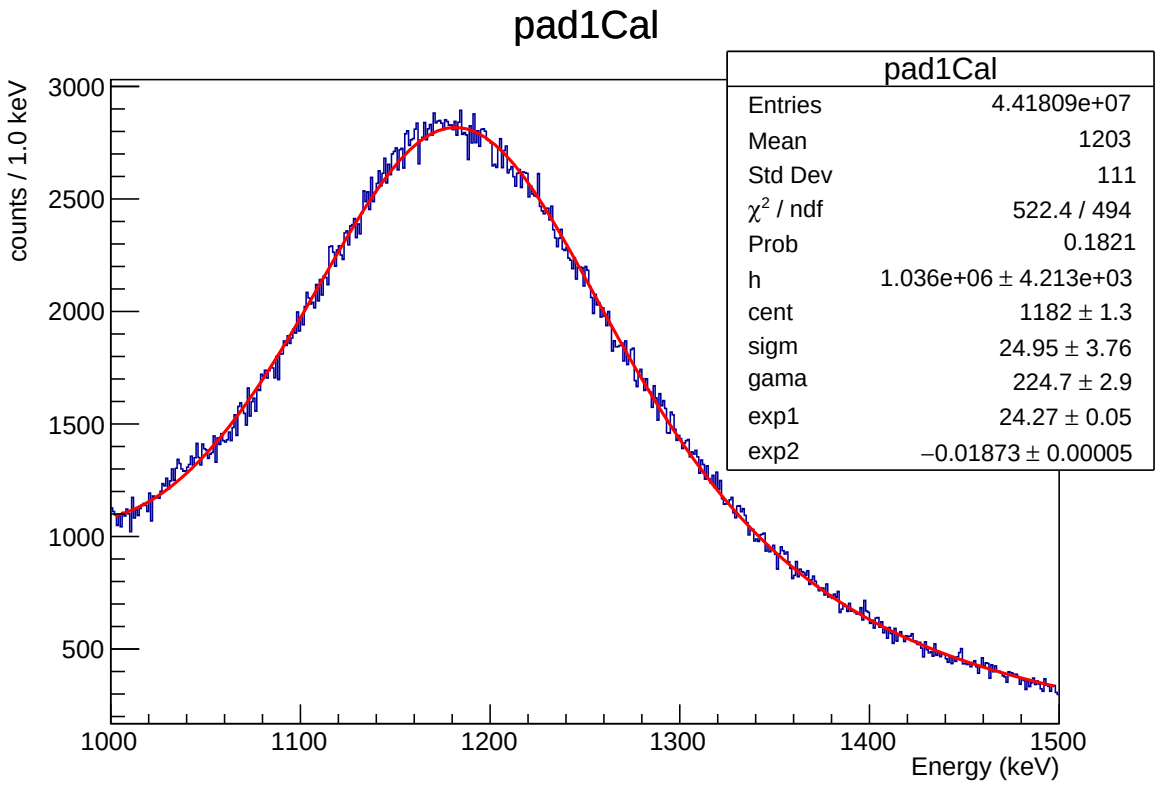

Figure 4.6: Pad B full-energy ^{11}Be($\beta^{-}\alpha$)^{7}Li decay peak with energy 1182 keV fit by a Voigt curve and an exponential curve, meant to model the high-energy tail of the $\beta^{-}\alpha$ spectrum to lower energy. The intrinsic width is 225(4) keV and the detector resolution is 5.0(8)% FWHM.

Figure 4.7 shows a fit to the low energy spectrum of Pad B, to extract detector resolution from the other isolated peak, the ^{7}Li* peak. The measured detector resolution here is zero, but is highly correlated with the assumed intrinsic width of the ^{7}Li* peak, which was fixed to 82 keV as a kinematic rescaling of the width measurement of the full decay (7sigm in Fig. 4.6). Freeing this parameter allowed fits returning up to ~ 30% FWHM resolution and hard-to-believe small intrinsic widths. The other pads had low-energy resolutions of 4.6(4)%, zero, and 8.6(14)% FWHM, respectively. With obvious caveats of the correlation between the detector width and intrinsic width, this is suggestive that the detector resolution at low energy is somewhere in the range of 4.5-10% FWHM, which is reasonable for such a detector [39].

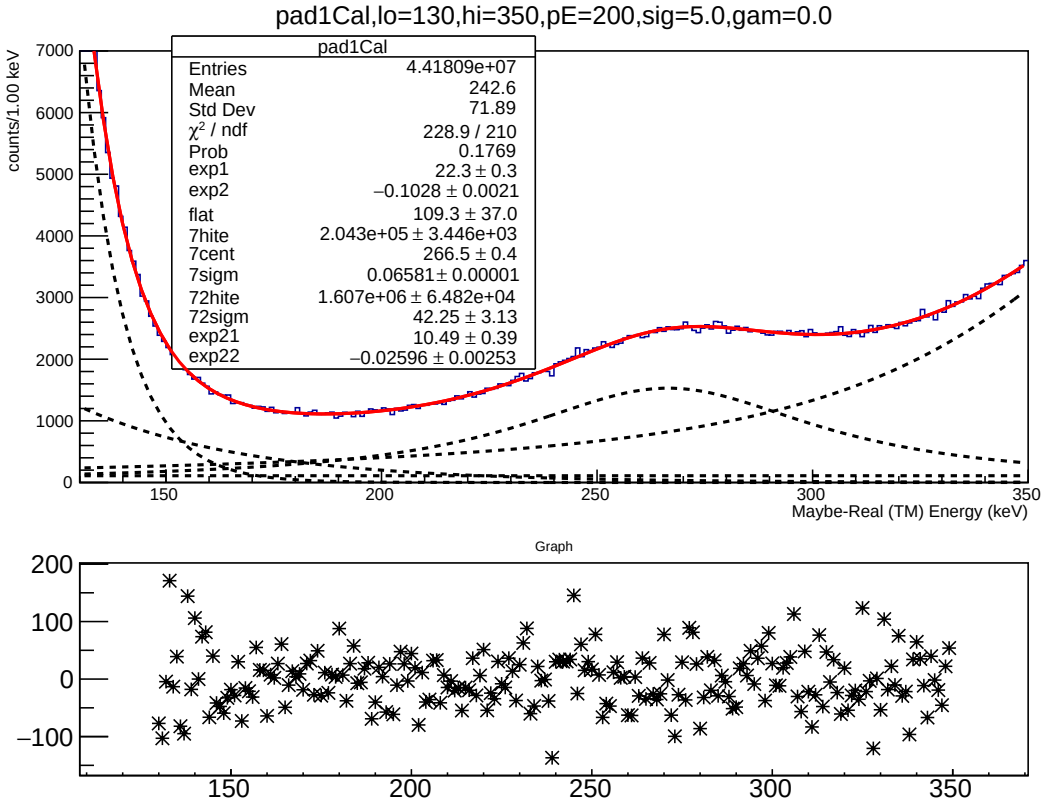

Figure 4.7: The low-energy spectrum of Pad B. The fit function is the sum of two exponential functions, a constant, a Voigt peak (^{7}Li*), and a semi-restricted Voigt peak (^{7}Li). The intrinsic width is fixed to 82 keV scaled from the width measured in 4.6. The fit resolution (7sigm) for Pad B is zero. Other pads show up to 5% FWHM.

4.2 R-matrix Insights to the $\beta^-\alpha$ Background

The R-matrix theory is a non-relativistic quantum mechanical scattering theory that was developed largely independently for atomic and nuclear physics [53]. The present utility of the R-matrix theory comes from the recent R-matrix characterization of the ^{11}Be($\beta^-\alpha$) decay spectrum by Refsgaard *et al.* [2]. R-matrix theory calculations using the Refsgaard suggested values were used to better understand the ^{11}Be($\beta^-\alpha$) background in GADGET.

4.2.1 Introduction to R-matrix theory

The R-matrix is a phenomenological multi-channel scattering theory, developed by numerous authors, although the fundamental inception is credited to Kapur and Peierls [54, 53]. The framework has been used widely to relate nuclear scattering observables to nuclear structure. Modern formulations, such as the Brune formalism [55] have theory inputs with clear physical analogs such as nuclear state energy, spin, parity, and mixing parameters with other states. Furthermore, the Brune convention is used in the R-matrix code Azure2 [35] which was used in R-matrix calculations of the ^{11}Be($\beta^-\alpha$) background.

In the R-matrix theory, the nuclear wavefunction is described with in two regions. The wavefunction of the internal region has well defined angular momentum J and M and can be expanded into a complete set of basis eigenstates. The wavefunction of the external region is assumed to be subject to just Coulomb interactions and well defined by allowed coupled-particle channels. The external wavefunction then is described by inbound and outbound Coulomb functions. These Coulomb functions are fully analytic and have well defined energy, charges, masses, and angular momenta. The utilization of the theory then falls out of matching the external Coulomb functions and their derivatives to solution to a complicated quantum many-body problem of the interior at the boundary surface.

The R-matrix is defined as:

$$R_{cc'} = \sum \frac{\gamma_{\lambda c}\gamma_{\lambda c'}}{E_\lambda - E} \tag{4.2}$$

where $\gamma_{\lambda c}$ is the integral of the internal eigenstate wavefunction of the λ^{th} level and the external wavefunction corresponding to the c-channel. Thus, $\gamma_{\lambda c}$ is a measure of the contribution of the λ^{th} level to the observation of the c-channel. With this R-matrix defined, calculations can be performed with the *collision matrix*, which is calculated from the following inputs: the R-matrix, channel energies, wavefunction-matching boundary radius, and the incoming and outbound Coulomb wavefunctions.

Alternatively, to simplify computation of the collision matrix in the case of few levels, one may use the A-matrix formalism. The A-matrix is defined by its inverse:

$$(A^{-1})_{\lambda\lambda'} = (E_\lambda - E)\delta_{\lambda\lambda'} + \Delta_{\lambda\lambda'} - \frac{\Gamma_{\lambda\lambda'}}{2} \tag{4.3}$$

with the following definitions:

$$\Delta_{\lambda\lambda'} = -\sum_c \gamma_{\lambda c}\gamma_{\lambda' c}(S_c - B_c) \tag{4.4}$$

$$\Gamma_{\lambda c} = 2P_c\gamma_{\lambda c}^2 \tag{4.5}$$

$$\Gamma_{\lambda\lambda'} = \sum_c 2P_c\gamma_{\lambda c}\gamma_{\lambda' c} \tag{4.6}$$

Where S_c is the shift factor, P_c is the penetration factor and B_c is the boundary condition parameter. These values are related to the wavefunction matching and the logarithmic derivatives of the outbound Coulomb wavefunction at the boundary [56].

Barker and Warburton [57] write the β-fed spectral function in terms of this mathematically equivalent A-matrix:

$$N_c(E) = f_\beta P_c |\sum_{\lambda\mu} B_\lambda \gamma_{\mu c} A_{\lambda\mu}|^2 \tag{4.7}$$

Here, f_β is the phase-space factor for the β decay, B_λ is the β decay feeding strength, and $A_{\lambda\mu}$ is an element of the A-matrix. The form of Eq. 4.7 is simpler than in Barker and Warburton, but this is due to the consideration of Gamow-Teller decays only in the Refsgaard analysis of ^{11}Be($\beta^-\alpha$). Gamow-Teller decays have $\Delta S = 1$ from spin alignment of the emitted electron and anti-neutrino. Fermi decays are the opposite, having $\Delta S = 0$ and anti-alignment of electron and anti-neutrino spin. The ground state of ^{11}Be is 1/2+ and the $\beta^-\alpha$ emitting state in ^{11}B has been identified as 3/2+.

Allowed β decays impart no angular momentum (that is, $\Delta L = 0$). Angular momentum algebra requires a $1/2+ \longrightarrow 3/2+$ decay to be Gamow-Teller, $\Delta S = 1$.

The Azure2 code performs these calculations, taking as input structure information and β decay feeding information. One output of the Azure2 calculations is the spectral shape from each channel, that is the shape as a function of energy of the ^{11}Be$(\beta^-\alpha)^7$Li and ^{11}Be$(\beta^-\alpha)^7$Li* decays.

4.2.2 R-matrix Calculations of ^{11}Be$(\beta^-\alpha)$

The suggested R-matrix parameters from [2] are summarized in Table 4.2. They report statistical and systematic errors both, and we consider parameters in these values as the root of the sum of squared errors. The radial boundary term r_0, which sets the R-matrix boundary radius at $R = r_0(A_1^{1/3} + A_2^{1/3})$, is adopted to be 1.6 fm.

	$\lambda = 1$	$\lambda = 2$
E_λ (keV)	9846(1)[10]	11490(80)[50]
$\Gamma_{\lambda 1}$ (keV)	233(3)[3]	430(150)[50]
$\Gamma_{\lambda 2}$ (keV)	20.4(3)[3]	50(60)[50]
M(GT)	0.717(12)[7]	1.05(17)[5]
B(GT)	0.318(11)[6]	0.7(2)[1]
ln(ft)	4.08(3)[2]	3.8(3)[1]

Table 4.2: R-matrix parameters adopted from [2]. Values in parentheses are their statistical errors and values in square brackets are their systematic errors.

Figure 4.8 shows the output of the R-matrix calculation with the central values of Tab. 4.2. The energy scale is relative to the 8.664 MeV α separation energy in ^{11}B. The two output channels and sum are color coded. It is the primary peak of each channel that is seen in the GADGET data. The upturn in the R-matrix output above 2 MeV of excitation energy is not seen in the individual pad data, but is somewhat in the composite pad scheme. Rather, there is an absence of events above $\sim$ 2750 keV. The "turn-off" energy in the R-matrix is $\sim$ 2800 keV. The Q-value for the $\beta^-\alpha$ is 2.834 MeV and drives this "turn-off" of the spectral strength. The small difference in the "turn-off" energies is a nice test of our energy calibration extrapolation from $\sim$ 1.2 MeV.

(The energy calibration will be revisited in light of the exploration of very-low energy ionization processes, Sec. 4.3.2.)

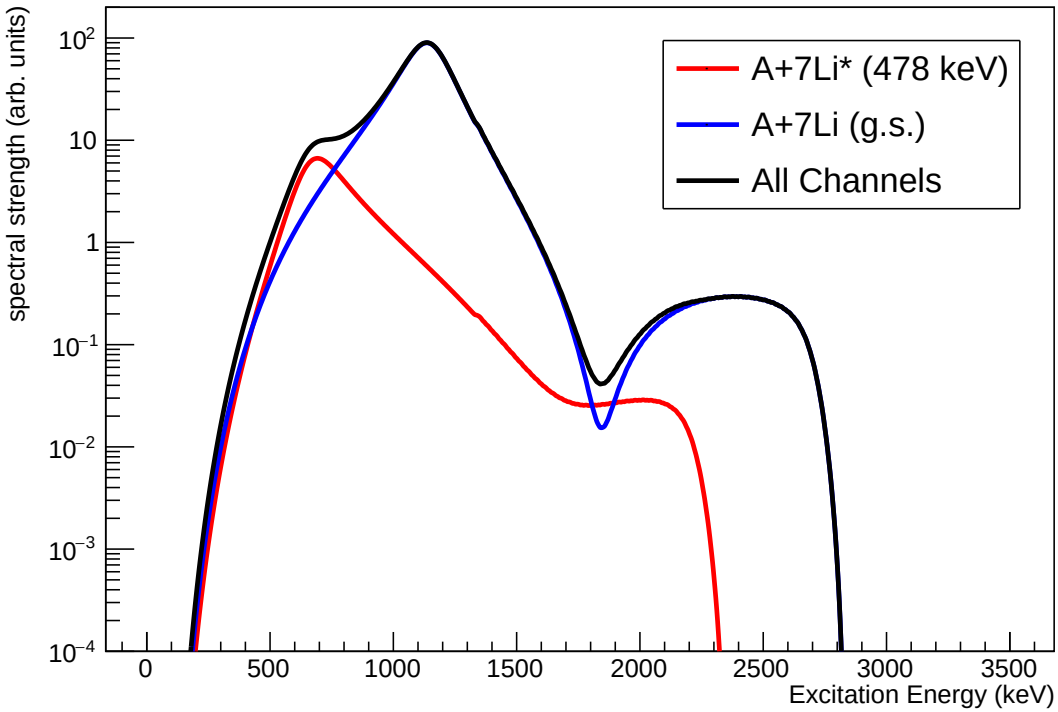

Figure 4.8: The R-matrix calcuated spectral strength of the ^{11}Be($\beta^-\alpha$) with the central values of Table 4.2 [2]. The curves are the ^{7}Li*-fed channel (red), ^{7}Li grounds state -fed channel (blue), and the sum of the two channels (black). The two-state structure is evident in the two-peak behavior of the spectral output, despite the strong β-feeding preference of the lower-energy state.

Figure 4.9 shows the R-matrix output representing the physical spectra and also the inferred individual α and ^{7}Li spectra. The α and ^{7}Li individual spectra are not output from Azure2, but are calculated by rescaling of the energy of the output. The rescaling comes from the two-body kinematics of the ^{11}B(α)^{7}Li breakup.

The initial thought was to use the R-matrix calculations directly in the fit to the GADGET spectra. However, it was quickly determined that such a scheme would be computationally challenging. In this scheme, we would want to smear the output by an assumed detector response, but early tests showed this taking prohibitively long if the smearing would be parameterized and included in the

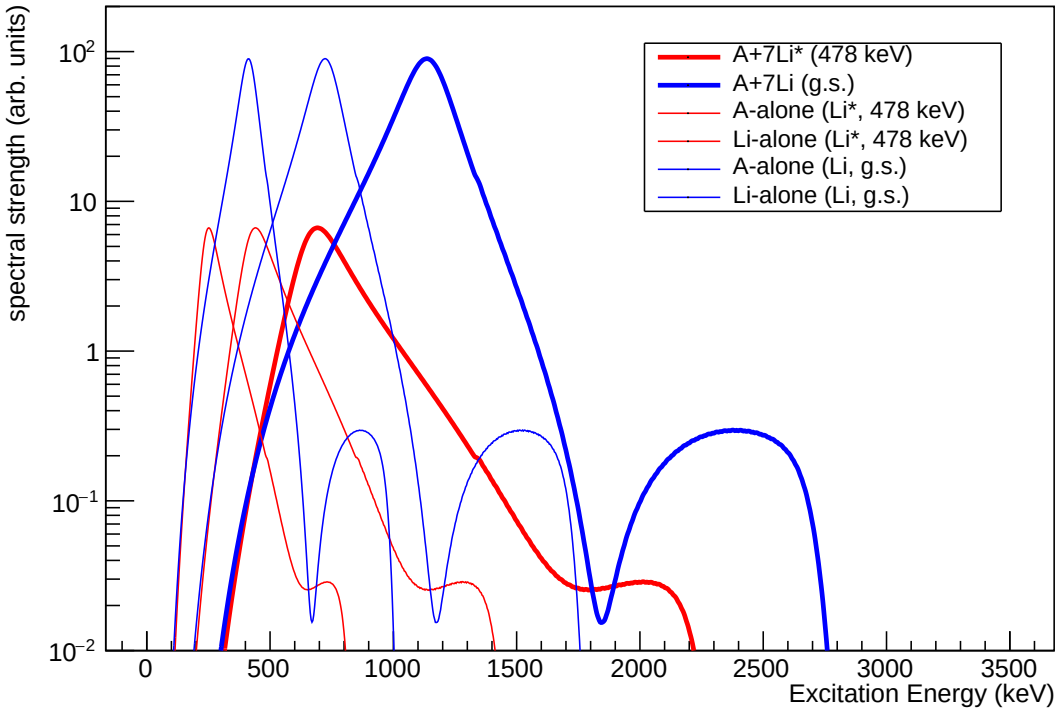

Figure 4.9: The R-matrix calculate strength of ^{11}Be($\beta^-\alpha$) with the central values of Table 4.2 [2]. The thick curves are the ^{7}Li*-fed channel (red), ^{7}Li grounds state -fed channel (blue). The thin curves show the kinematically scaled distributions for the ^{7}Li-alone (lower energy of a color) and the α-alone (higher energy of a color). Note the strong overlap of the ^{7}Li(g.s.)-alone and α-alone from the ^{7}Li* feeding, and the α-alone from the ^{7}Li(g.s.) feeding and the full-energy α+^{7}Li*.

fit and not merely calculated once at the beginning of a fitting code. Furthermore, which R-matrix curve should be used? Refsgaard *et al.* [2] gives individual R-matrix parameters and associated errors. It is not these parameters that are comparable to GADGET data, but instead the curves they generate, which add additional computational overhead. Due to these challenges in using actual R-matrix calculations in the fit to data, we investigated if the R-matrix output could be approximated locally, in the region of interest, with a quickly-evaluated curve that could take its place in the analysis.

The lowest energy peak, the ^{7}Li* peak with $E \sim 256$ keV of energy is the primary $\beta^-\alpha$ background. The ^{7}Li* peak calculated by Azure2 was fit by a Lorentzian. The fit is shown in Fig. 4.10. This is quite similar to and actually a test of the previous fit of GADGET data with a

Voigt curve, assuming a Lorentzian-described physical spectrum smeared by a Gaussian detector response. Qualitatively, the two curves are similar, but this discrepancy is unacceptable for the search of our precision. Local fits with a Lorentzian were better, such as just the region lower in energy than the peak, but even this isn't sufficient. To quantify these claims, we first need to quantify the quality of the fit. For a rough estimate of the precision needed here, we first need to estimate the branching ratio into the ^{7}Li*-alone peak measured in GADGET: 0.5 for the cathode efficiency of ^{7}Li-alone and not α-alone, ~ 0.6 for the fraction of decays originating on the cathode, ~ 0.1 for the fraction of $\beta^-\alpha$ decays that populate the ^{7}Li 478 keV excited state, and ~ 0.03 for the $\beta^-\alpha$ branching ratio. All together, the ^{7}Li*-alone decay from the detector cathode occurs with intensity of $\sim 9 \cdot 10^{-4}$, which is large compared to the $\sim 1 \cdot 10^{-5}$ nominal branch of the signal.

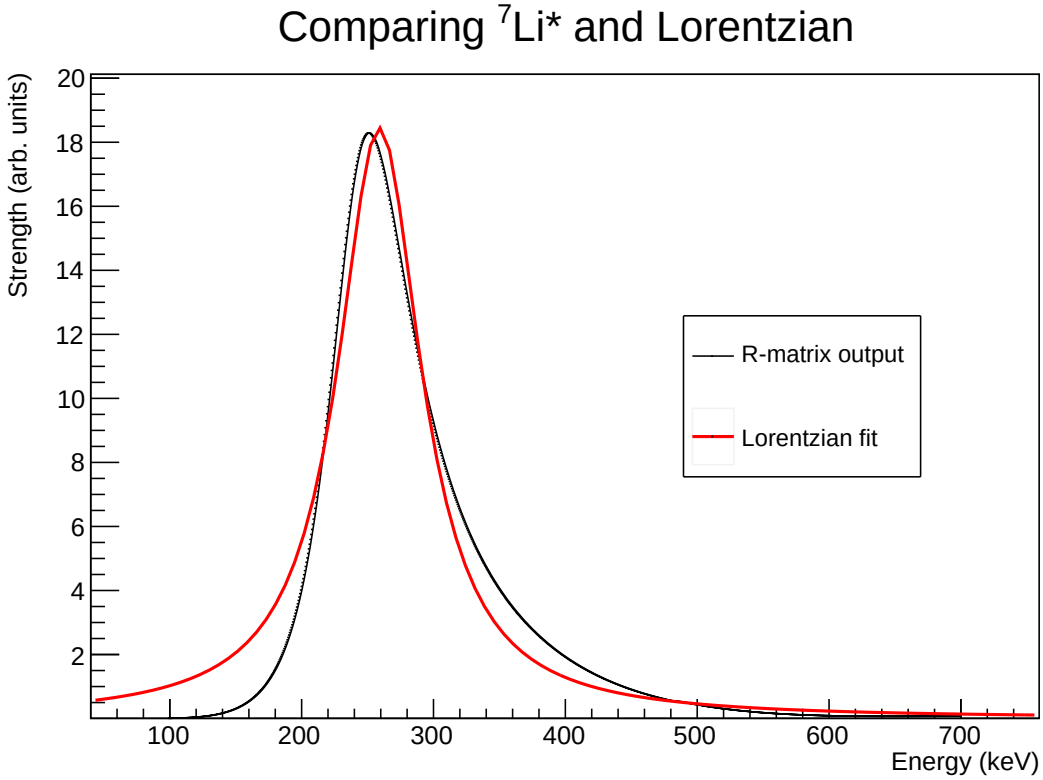

Figure 4.10: R-matrix prediction of the isolated spectrum of ^{7}Li*-alone (black) and comparison of a Lorentzian curve (red). Despite the reasonable fit to data using a Voigt curve, the R-matrix calculation output spectrum has notable differences than the Lorentzian that is implicit in the Voigt curve.

The integral of a peak is roughly proportional to the product of its height and its width. The R-matrix spectrum is peaked at ~ 20 and has width ~ 80 keV. The area then is ~ 1600 *units* (of some sort). If we take the branching ratio intensity of this peak as the $\sim 9 \cdot 10^{-4}$ from before, the spectral intensity per unit of β decay intensity is $\sim \frac{1600}{9 \cdot 10^{-4}} \simeq 1.8 \cdot 10^{6}$. If our approximation is to be useful, we want the mis-match to introduce not more than $\sim 1 \cdot 10^{-6}$ branching ratio error. This corresponds to a spectral intensity error of ~ 1.8 *units*. If we assume a $\beta^{-}p$ signal peak with width of 20 keV and a constant residual error between the approximation and the R-matrix output over the signal-peak width, the magnitude of the residue needs to be less than $\sim \frac{1.8}{20\ \text{keV}} \simeq 0.09$. The Lorentzian fit of Fig. 4.10 is different from the R-matrix curve by up to ~ 2 *units* in some places, which could show up at a $\sim 2 \cdot 10^{-5}$ systematic error, twice that of the $\beta^{-}p$ branching ratio reported in Ayyad *et al.* [3]!

To improve the estimation of the R-matrix output, the output was fit with the product of a Voigt profile and a polynomial function. The idea here is that the Voigt curve is peak-like, but symmetric. Multiplication by a polynomial can make the approximate function asymmetric and behave closer to the R-matrix output. If the general shape of the Voigt is close to the R-matrix output, then the polynomial would make small corrections to the Voigt to bring it in line with the R-matrix curve. However, the Lorentzian is tricky as starting with a polynomial with degree two, the polynomial can overwhelm the $\sim 1/x^2$ behavior of the curve. The Gaussian is safe and and will overcome any polynomial of any order. (As an aside, this peak-like requirement can be enforced in a Bayesian fitting analysis so even the polynomial order constraint from the $\sim \frac{1}{x^2}$ Lorentzian form is not a true a constraint.)

With this mapping between the residual in the R-matrix fit and the systematic-error induced branching ratio, the order of the polynomial in the approximation function was increased until the residual error was less than 0.09. This first occurred for a linear "correcting" polynomial. This fit and its residuals are shown in Fig. 4.11. The linear corrective fit has residual errors of less than 0.06, so systematic shifts in the $\beta^{-}p$ branching ratio from this approximation should be held under $\sim 1 \cdot 10^{-6}$.

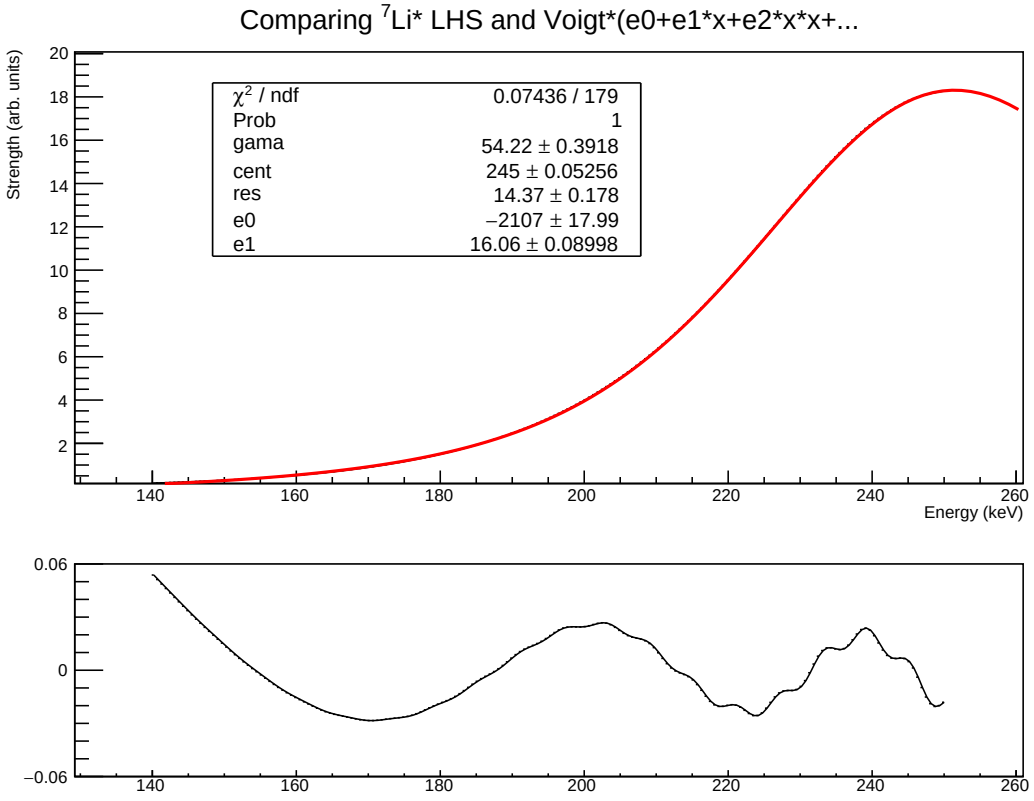

Figure 4.11: (Top) in black, the R-matrix output for the excited state spectra, energy-scaled to give the shape of just the ^{7}Li*-alone peak, but this is largely obscured by the fit in red. The fit is the product of a Voigt curve and a polynomial. (Bottom) fit residuals, in the same scale as the top.

4.3 Low-Energy Ionization Processes

Gaseous proportional counters, like the Proton Detector in GADGET, ideally have a fair degree of linearity in their detector response. That is, the energy of radiation lost as an ion traverses the detector gas, ideally, is proportional to the charge measured at the end of the detector. Non-linearity can be caused by a multitude of effects, but can generally be described as detector physics or signal processing effects. Physics-driven non-linearity in the detector's response is generically described as the *pulse height defect*. The first source is related to the detector *dead layer*, the surface layer of the detector that engages in ion energy-loss processes, but is not part of the sensitive portion of the detector. Another source of the pulse height defect is due to charge recombination of the radiation-created ion pairs. Decays in the Proton Detector are internal to the gas, so there are no windows or dead layers. As for charge recombination, the low density of the detector gas leads to

long particle tracks and low charge-pair density, making recombination less likely than in a solid state detector.

One contribution to the pulse height defect that is equally present in the gaseous detectors is related to a ion-species dependence on the stopping, with partitioning of energy-loss processes depending on the ion's mass and charge [39]. In addition to producing ionization, impinging ions can perform non-ionizing electronic excitation, impart kinetic energy to target atoms with elastic scattering, and (primarily reserved for electron radiations) produce "breaking" *Bremsstrahlung* photons, which may or may not be reabsorbed by the detector in a different location. This is notable for energies of $\lesssim$ 200 keV/u, where ion velocity has a dramatic effect on the stopping and ionization [58]. This threshold is several times the Bohr velocity $\sim$ 25 keV/u, where the ion-stopping physics is very different than at higher energies. In the high energy regime, the ion and target interaction is eikonal. In a classical picture, the target atom is functionally "frozen" in space for the duration of the interaction. As the ion velocity decreases, the electron cloud of the target atom is capable of responding to the presence of the bombarding ion, providing more effective charge screening of the target atom's nuclear charge. Generally, at lower velocities, ions more easily charge-exchange electrons with their environment changing their charge state ([59] proton on argon gas, [60] helium on argon gas, [61] lithium on argon gas), stronger charge screening changes the weights of interactions between the targets' nuclei and electrons, and interaction times are longer. These effects generate a pulse height defect as the detector only measures liberated electrons, which is only one of the many channels by which the ion can lose energy.

Understanding the pulse height defect is important for our case. It influences the energy calibration as our data has no internal reference of $\beta^- p$ to calibrate against, only $\beta^- \alpha$, of which the ^{7}Li radiations have $\sim$ 35 and $\sim$ 65 keV/u, which is quite near this Bohr velocity threshold. It influences the shape of our assumed $\beta^- p$ signal in that the spacing of the p-alone cathode peak and the p+^{10}Be in-gas peak depends on both the proton ionization and the ^{10}Be ionization. The ^{10}Be energy is $\sim$ 2 keV/u, far below the Bohr velocity. The proton and ^{10}Be recoil will have about an order of magnitude different energy, (because of) an order of magnitude different mass, and a

factor of four different nuclear charge. In this section, I will show evidence that each of these are important to understand.

4.3.1 Estimating P-10 Ionization

There exists a dearth of experimental data on low-energy, energy-loss partitioning of ions traversing of P-10 gas. A great number of measurements were conducted in the 1970s and before to measure the ionization yields of different ions in a variety of gasses, mostly air, air constituents, noble gases, and so-called *tissue-equivalent* gases meant to model the stoichiometric makeup of human tissue. Much of this is summarized in the ICRU Report 31 [62]. Despite being published more than 40 years ago, it remains an influential compilation of this work [39], but it lacks information on gas mixtures used in low-energy nuclear physics like P-10 and CO_2/He mixtures, as well as impinging ions heavier than α particles.

This is not to say that P-10 is not characterized. In fact, it is a well studied gas and the pulse height defect is well-characterized for a wide range of masses and charges at energies of hundreds of keV and up with the LSS theory by Linehard *et al.* [63], demonstrated nicely with a recent measurement of ^{252}Cf spontaneous fission in P-10 [64]. Fragments are peaked at $\sim$ 110u and $\sim$ 145u and have $\sim$ 185 MeV to share. Assuming a two-body decay, the lowest energy fragments would have $\sim$ 500 keV/u or about five times the Bohr velocity.

The data that are missing are these Bohr velocity ionization yields such as those measured for a variety of low-energy ion beams impinged on argon gas [65, 66, 67, 68, 69, 70, 71, 72] or on methane gas [73, 74, 75, 76, 77]. In light of a lack of experimental information, two approaches were taken to approximate the pulse height defect of the $\beta^-\alpha$ spectrum and set the shape of the assumed $\beta^- p$ signal. The first approach was the now familiar ion-stopping simulation software SRIM. The second was a compilation, parameterization, and uncertainty quantification of the literature of the ionization yields (measured as W values, see Sec. 4.3.1.2) of beams impinged on pure argon and methane gas that was used with a gas mixing calculation to estimate unmeasured gas properties of P-10.

	ion	recoils	sum
ionization	99.63	0.05	99.68
vacancies	0.02	0.03	0.05
phonons	0.01	0.25	0.26

Table 4.3: SRIM calculated energy loss partioning for a 170 keV proton. The vast majority (99.7%) of the energy loss goes into electronic stopping and ionization production.

4.3.1.1 Estimating Ionization Yields with SRIM

The SRIM code was first introduced in Sec. 3.2.1.2. There, we used it to calculate particle ranges in P-10 gas. We use this code again to study the partitioning of energy loss processes. SRIM categorizes the energy loss into six bins. There is energy lost to: ionization, vacancies, and phonons, for each the primary ion and for secondary ions. A secondary ion is an ion that receives kinetic energy (above a threshold, for computation speed) from the primary ion. Energy lost to ionization is energy that is spent creating ion pairs in the target material. Energy lost to vacancies is energy that is spent when a target atom receives a kick that removes it from the atomic lattice it occupies. (SRIM was developed to estimate exactly this, the *damage*, in solid targets and electronics.) Finally, the energy into phonons is a catch-all bucket for energy conservation in the code. Energy in this bucket comes from target atoms that receive energy, but not sufficient to leave their lattice location.

SRIM uses a interatomic potential developed by its authors [78] to calculate the energy sharing of ions to target atoms (nuclear stopping) and electrons (electronic stopping) [58]. At typical nuclear physics experimental energy and higher, the electronic stopping dominates the total stopping. At very low energies, the nuclear stopping and electronic stopping are similar. SRIM stopping powers are quoted to have an error of 4.3% from experimental stopping values [47].

The breakdown of energy loss for various ions follows: 170 keV proton in Tab. 4.3, 20 keV ^{10}Be in Tab. 4.4, 266 keV ^{7}Li in Tab. 4.5, 440 keV ^{7}Li in Tab. 4.6, and 770 keV α in Tab. 4.7. The exact meaning of vacancies and phonons values are hard to interpret in the P-10 gas, but taking the sum of the ion and recoil ionization values, we have that most particles will deposit the vast majority of their energy in the form of ionization: 170 keV protons 96%, 20 keV ^{10}Be 49%,

	ion	recoils	sum
ionization	38.87	10.53	49.40
vacancies	0.97	7.38	8.35
phonons	0.36	41.88	42.24

Table 4.4: SRIM calculated energy loss partioning for a 20 keV ^{10}Be. The energy loss is spread out between primary interactions and recoil interactions. Only about 50% of the energy goes into electronic stopping and ionization production.

	ion	recoils	sum
ionization	91.89	1.52	93.41
vacancies	0.14	0.96	1.10
phonons	0.04	5.45	5.49

Table 4.5: SRIM calculated energy loss partioning for a 266 keV ^{7}Li. The bulk of the energy loss is goes into primary ionization, but some ionization from recoiling ions is recovered. About 93% of the energy ends up going to ionization. Compare to Tab. 4.6 to see the effect of ion energy on energy loss partitioning.

	ion	recoils	sum
ionization	94.76	1.00	95.76
vacancies	0.09	0.62	0.71
phonons	0.03	3.51	3.54

Table 4.6: SRIM calculated energy loss partioning for a 440 keV ^{7}Li. The bulk of the energy loss is goes into primary ionization, but some ionization from recoiling ions is recovered. About 96% of the energy ends up going to ionization. Compare to Tab. 4.5 to see the effect of ion energy on energy loss partitioning.

	ion	recoils	sum
ionization	98.87	0.19	99.06
vacancies	0.03	0.12	0.15
phonons	0.01	0.77	0.78

Table 4.7: SRIM calculated energy loss partioning for a 770 keV α. The vast majority (99.1%) of the energy loss goes into electronic stopping and ionization production.

266 keV ^{7}Li 93%, 440 ^{7}Li 96%, and 770 keV α 99%. The efficiency of an in-gas ^{7}Li+α decay of energy E should then be $\sim 4/11 \cdot E \cdot 96\% + 7/11 \cdot E \cdot 99\% \sim 98\%$. The large pulse height defect calculated for ^{10}Be was somewhat surprising and SRIM provides no error quantification. In private communication Ziegler recommended referencing experimental results from similar experiments, if they existed, as the ^{10}Be energy is low, suggesting errors in stopping could be as large as 30%.

4.3.1.2 Estimating Ionization Yields of Gas Mixtures

The more detailed approach and that which was adopted in the final analysis was to consider data on the ionization yields of the P-10 components and average them to create an estimate for the P-10. This is not merely calculating an average ionization, molecule for molecule, according to the gas mixture, as the gas has properties from both its constituents and the interactions of its constituents. The role of the methane in P-10 is that of a quench gas. The quench gas has a lower ionization potential than the primary gas (12.61 eV [79] and 15.76 eV [80], respectively) and helps with localization of charge production in the vicinity of radiations by absorbing UV radiations and by the *Penning Ionization* mechanism, where excited states of argon gas can de-excite by collisions with the methane, producing an ion pair off the methane [39].

Ionization yields will now be discussed by their inverse, normalized to ion pair. That is, the following discussion will involved the *W value*, which has units of energy per pair and has some analog to the work function of the photoelectric effect. It is the average amount of energy required to liberate a single ion pair and is often written as $W(E)$, emphasising the role of the energy of the impinging ion. This is incomplete as the W value is sensitive to ion species as well.

The form of the W value averaging equation was first described in the 1950s by the Basel group [81, 82] and extended in 1987 by Tawara *et al.*[83]. Tawara *et al.* parameterized the W value function curve for α particles of $\sim 1 - 5$ MeV in various mixtures of argon and methane detector gas. The W value of a mixture of a primary component x with a quench gas y can be calculated by the following equation:

$$W_{xy}(E)^{-1} = (W_x(E)^{-1} - W_y(E)^{-1}) \cdot Z(E) + W_y(E)^{-1} + Z(E) \cdot B_{xy} \tag{4.8}$$

where $Z(E)$ is the fractional stopping between gas components with stopping powers S_i and partial pressures P_i

$$Z(E) = (1 + \frac{S_y P_y}{S_x P_x})^{-1} \tag{4.9}$$

and the mixture-dependent parameter $B_{xy} = 0.09$ for P-10 gas. The B_{xy} term is new with Tawara *et al.* [83]. Due to the absence of data on the W value of P-10 for low-energy ions, the W value was estimated by the Tawara formula. The pulse height defect is related to the W value in that as the W value increases, fewer ion pairs are created for the same impinging energy.

Parameterization of Argon Gas W value

First, argon was studied. The nominal W value for argon gas is 26.3 eV/pair in [39] and 27(1) eV/pair in [62]. The following W values for ions impinging on argon were compiled and are shown in Fig. 4.12:

- Phipps *et al.* [69]: H, He, C, N, O, Ar on Ar
- Chemtob *et al.* [71]: H, He, Ar on Ar
- Chappell and Sparrow [70]: He on Ar
- Leimgruber *et al.* [72]: N, O on Ar
- Nguyen *et al.* [68]: H, He, Ar on Ar
- Larson [67]: H on Ar
- Lowry and Miller [65]: H on Ar

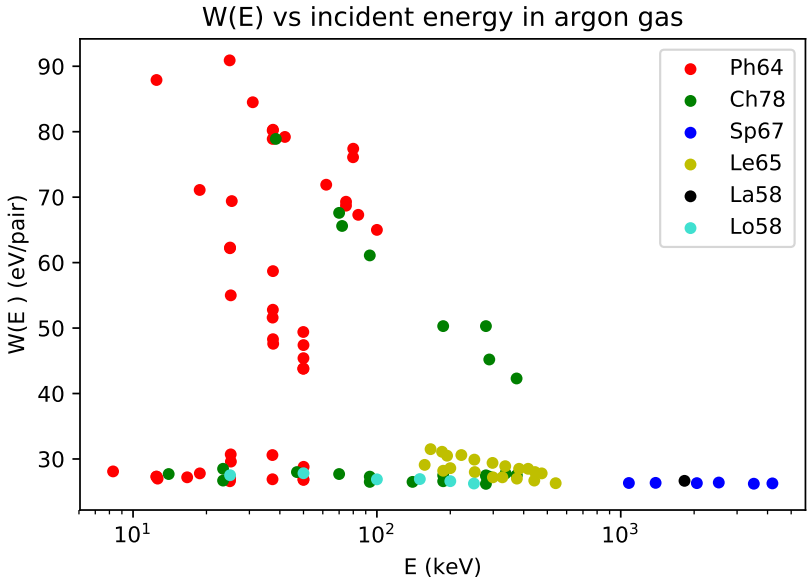

Figure 4.12: The W value against incident ion energy into argon gas. The data are color coded according to their publication. The W value is multi-valued for a particular value of energy and this due to the impinging ion species, shown later. There is overlap between most evaluations, so consistency of W values can be checked.

Error bars aren't shown. The spread in data is due to different impinging species, shown better in Fig. 4.13. In general, it looks as if all values may converge to the ~ 27 eV/pair from the compilations at sufficiently high energy, but the W value of heavy ions is a function of energy. The heavier the ion, the stronger the energy dependence. Figure 4.14 shows much of the complexity in the W value is actually due to the ion's mass. Velocity is calculated as $v = \sqrt{E/A(\text{keV/u})}$. Furthermore, this velocity is the incident velocity, so these W values are integrated over the whole energy loss. The fit shown is a power law, with the high-energy behavior reducing to the nominal W value of 26.3 eV/pair.

$$W(v) = 26.3 + \alpha \cdot v^{\beta} \tag{4.10}$$

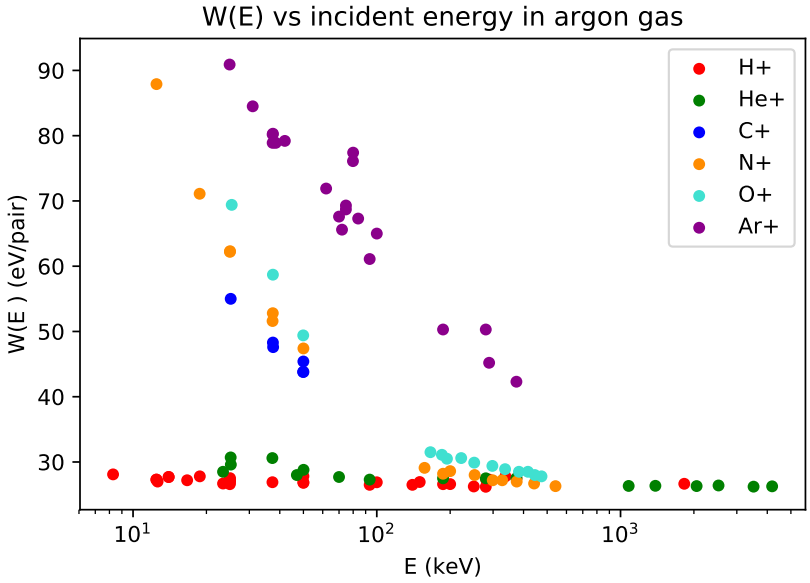

Figure 4.13: The W value against incident ion energy into argon gas. The data are color coded according to the impinging ion species. The W value is not a function of energy, or at least is a very weak function of energy, for impinging H^+ and He^+. There W value a strong dependence on energy for all other chemical species shown.

While the velocity isn't a perfect predictor of W value and clear patterns exist in the fit residuals, it is quite suggestive. This matches some of the qualitative arguments about ion velocity determining stopping physics in the target from [58] and leads some credence to the ~ 0.5 ionization of the ^{10}Be calculated by SRIM. In these units, a 20 keV ^{10}Be has velocity of ~ 1.4, a 250 keV ^{7}Li has velocity of ~ 6, a 430 keV α has velocity of ~ 10. Thus, of the particles in our data, the largest pulse height defect occurs for the ^{10}Be recoil. Additional terms for the Z of the impinging ion can improve the fit some, but a simple function seems sufficient for our purposes.

The fit yields parameters of $\alpha = 61.6$ and $\beta = -2.05$. Parameter errors are not shown as fit was performed without defined error bars to data. Error in the parameterization was estimated by taking the standard deviation of the fit residuals over the interval (-25%,+30%) ($\sim \pm 0.26$ in natural log scale). With these definitions, we have the following description of the W value of our spectra in pure argon gas.

ion	W value (eV/pair)	$\sim 1\sigma$ error (eV/pair)
^{10}Be, 20 keV	56.6	5.8
^{7}Li, 256 keV	27.9	0.7
^{7}Li, 430 keV	27.2	0.6
α, 752 keV	26.6	0.4

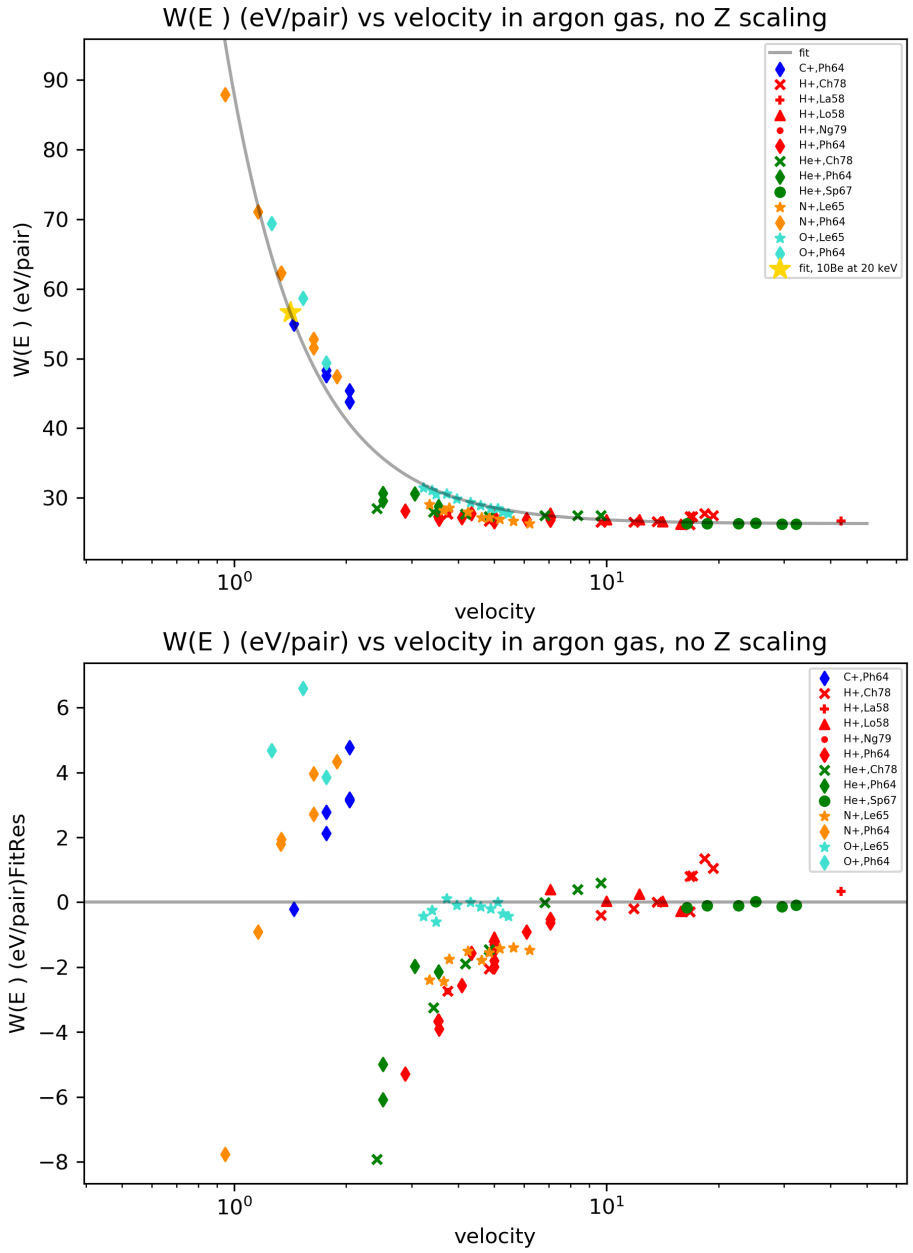

Figure 4.14: (Above) The W value against incident ion velocity into argon gas. Velocity is in units of $\sqrt{\text{keV/u}}$. The data are color coded according to the impinging ion species and markers represent data source. By plotting in velocity and not energy, much of the spread in W values has disappeared. The smooth line is a power-law equation Eq. 4.10. (Below) Residuals between data and the fit.

Parameterization of Methane Gas W value

Similarly, the available W value data for methane gas was collected. The nominal W value for methane is 29.1 eV/pair in [39] and 29(1) eV/pair in [62]. The following W values for ions impinging on methane were compiled and shown in Fig 4.15:

- Nguyen *et al.* [76]: H, He, C, O, N on methane
- MacDonald and Sidenius [77]: $Z \leqslant 22$ on methane (with select elements shown)
- Jesse [73]: He on methane
- Varma and Baum [74] He on methane
- Tawara *et al.* [75] He on methane

Here, we see similar behavior to the argon data, but perhaps an even more dramatic effect in the W value as a function of velocity. A similar power law function was fit to data, but with the high energy W value of methane in place of that for argon.

$$W(v) = 29.1 + \alpha \cdot v^{\beta} \tag{4.11}$$

In the methane data, $\alpha = 59.7$ and $\beta = -1.22$. With the same error assesment as in the argon data, we have the following W values for methane:

ion	W value (eV/pair)	$\sim 1\sigma$ error (eV/pair)
^{10}Be, 20 keV	68.3	9.8
^{7}Li, 256 keV	35.8	3.8
^{7}Li, 430 keV	34.0	3.8
α, 752 keV	31.6	2.9

Hidden in plain sight is a strong dependence on the chemical group of the inpinging ion. Group I, alkali metals have larger W values than other groups. This pattern was noted in the original paper, but no mechanism was prescribed to this behavior [77]. Given the richness of this data (*all* elements for $Z \leqslant 22$ and very low energy/mass ratios), some time was spent modeling this behavior in light of chemical electronegativity and only weak patterns were found beyond the Group I elements, low electronegativity, and large W values. (Fluorine, with near maximal electronegativity falls under the fit, but not by much and other elements with modest electronegativity have still lower W values.) This effect likely is the culmination of many related effects, each with ties to atomic shell structure.

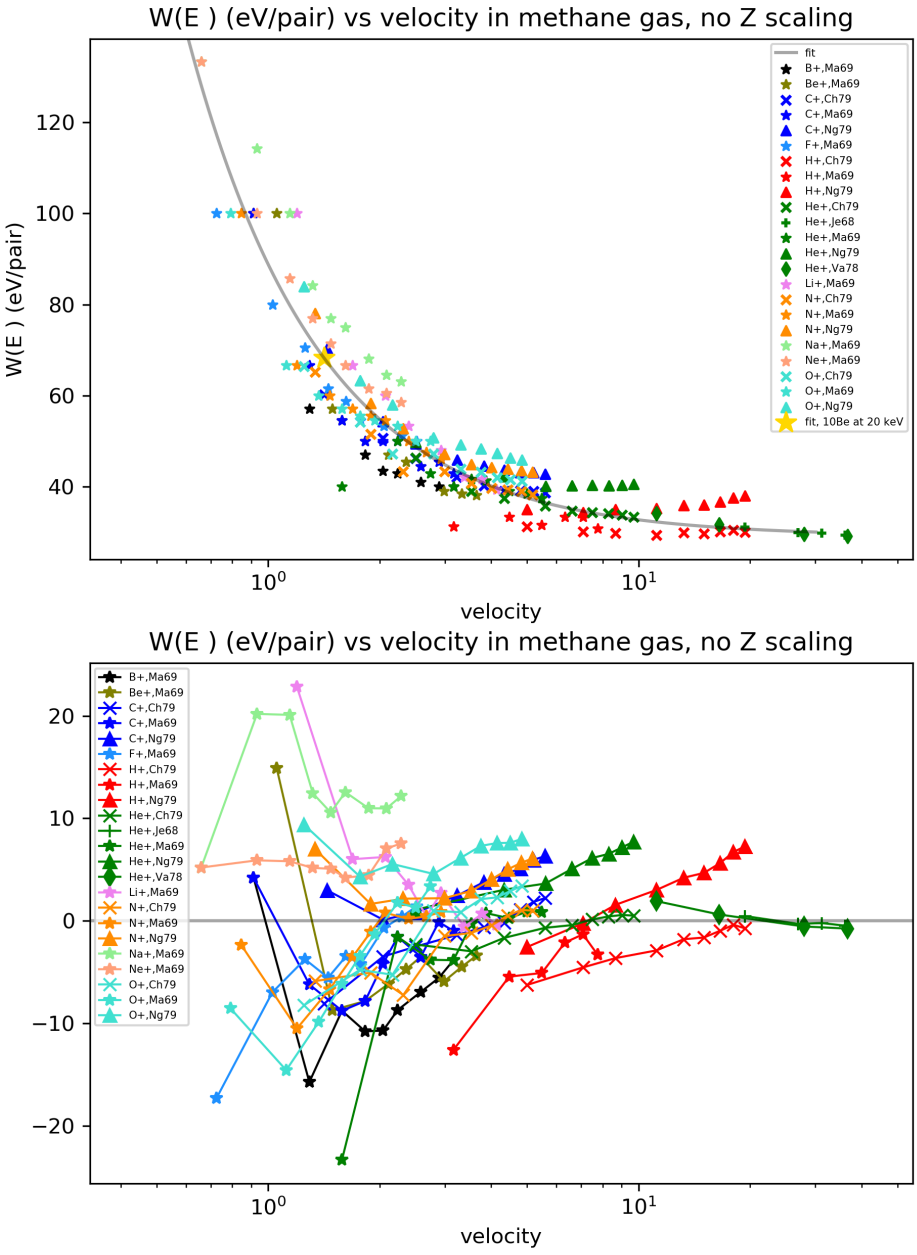

Figure 4.15: (Above) The W value against incident ion velocity into methane gas. Velocity is in units of $\sqrt{\text{keV/u}}$. The data are color coded according to the impinging ion species and marker shapes represent data source. The smooth line is a power-law equation Eq. 4.11. (Below) Residuals between data and the fit.

ESTIMATION OF P-10 GAS W VALUE

With each element of the Tawara formula [83] defined, P-10 W values were estimated. To perform error propagation, a Monte Carlo calculation was performed for each ion of interest in the previous tables. Values were sampled according to a Gaussian probability density function centered on the power-law fit function values and the errors defined by the standard deviation of the fit residuals, the same as the tables above. Samples were drawn 100,000 times and applied in the Tawara formula. Results were saved. The mean of the results is the central value of the final (Gaussian-enough) probability density function and the standard deviation is the 1σ error.

ion	W value (eV/pair)	1σ error (eV/pair)	W value fraction	1σ error
^{10}Be, 20 keV	39.4	3.0	0.56	0.08
^{7}Li, 256 keV	23.2	0.7	0.94	0.03
α+^{7}Li, 1182 keV	22.4	0.6	0.98	0.02
nominal	21.9	0.5	1.00	0.02

Most of the W values calculated in the Tawara formula are a bit lower than the nominal value of P-10 (26.5 eV/pair). As done in Tawara *et al.* [83], these calculated W values are normalized to the "nominal" high-energy value calculated in the Tawara formula using the high-energy values of the constituent gases. Thus, the full energy ^{7}Li+α peak will create 98(2)% of the charge per unit energy if it was higher in energy. The other isolated peak, the 256 keV ^{7}Li *-alone peak, creates 94(3)% of the ionization a higher-energy particle would. The ^{10}Be peak does, in fact, produce only about half the ionization than one would expect assuming linearity in the detector gas, as was calculated by SRIM.

4.3.2 Effects on Analysis

With a more thorough accounting of the behavior of the P-10 gas pulse height defect, several items will be reevaluated. First, the energy calibration of the E18507 analysis and E18507-style analysis

will change. In light of these gas effects and the publication of Refsgaard *et al.* [2], which provides a $\sim$ 30 keV lower-energy state for the $\beta^-\alpha$-emitting state in ^{11}B, the energy calibration will be redone. The energy scale will be set to the physical center of mass energy, so the 1182 keV ^{7}Li+α in-gas, full energy peak will appear with $1182 \cdot 0.98(2) = 1158(24)$ keV and the 256 keV ^{7}Li*-alone cathode-originated peak will appear with $256 \cdot 0.94(3) = 241(8)$ keV. Secondly, the large pulse height defect of the ^{10}Be will change the shape of the assumed $\beta^- p$ search peak. Assuming a 200 keV $\beta^- p$ resonance, the proton will carry $10/11 \cdot 200 = 182$ keV and the ^{10}Be will carry the remaining $1/11 \cdot 200 = 18$ keV. However, while the proton will efficiently create charge, the ^{10}Be will create some 18 keV $\cdot$ 0.56(8) = 10(2) "keV" of charge. This pushes the two constituent peaks closer together toward a single peak appearing at $\sim$ 96% the center of mass energy.

4.4 Bayesian Inference of $\beta^- p$ with Markov Chain Monte Carlo

With many of the fit parameters being constrained in intuitive, but highly relational ways like a prohibition on the very flexible R-matrix approximation function creating a local maximum that could fit and hide a $\beta^- p$ signal, a more flexible fitting scheme was needed. Additionally, some parameters, such as the ^{10}Be ionization efficiency have well-described errors. Others, like the detector resolution at $\sim$200 keV are less clear, but experience and some data from the spectra inform us that the resolution is not worse than 10% FWHM. In the case of the detector resolution, a Gaussian probability density function requires a choice of a central value, but it is unclear which value to pick and it really needs a fairly sharp cut-off past 10%. Gaussian probability density functions have non-zero value at all values.

All these points can be solved by the marriage of Bayes' Theorem and a Markov Chain Monte Carlo (MCMC) sampling algorithm.

4.4.1 Introduction to Bayes' Theorem

Bayes' Theorem is

$$p(\mathrm{H}|\mathrm{d}) = \frac{p(\mathrm{d}|\mathrm{H}) \cdot p(\mathrm{H})}{p(\mathrm{d})} \tag{4.12}$$

It says that the *posterior*, or updated, probability density function of a hypothesis H, in light of new data d, is the confluence of the quality of agreement of your data to the assumed hypothesis $p(\mathrm{d}|\mathrm{H})$, your *prior* belief in the hypothesis $p(\mathrm{H})$, and your belief in the ability to obtain data d across all possible hypotheses $p(\mathrm{d})$. While *belief* in a hypothesis strains some desire for absolute objectivity in analysis, this is merely semantics. Taking $p(d) = p(H) = 1$ yields the typical statistical inference relation

$$p(\mathrm{H}|\mathrm{d}) = p(\mathrm{d}|\mathrm{H}) \tag{4.13}$$

from which classical parameter estimation are inferred. It was this inference relation that was implicit in the E18507 style analysis that sometimes yielded large negative values for the $\beta^- p$, clearly driven by a systematic error, likely by poor choice of a background model, as negative event counts are not physical. Presented another way, the form of Eq. 4.13 is a statement of statistical uncertainty, within a particular model, alone. Varying the model assumptions and repeating the analysis to characterize the results' influence by model assumptions is a common way to estimate *systematics* of the analysis. This distinction is unnecessary and, in fact, can complicate such a systematic search if multiple parameters are correlated and not varied according to to this correlation, which itself is a complicating factor. Rather, the classical form of the inference equation is an artifact of a historical lack of computational power required to numerically "solve" Bayes' Theorem and extract the posterior probability distributions.

The model limits that are tested to infer the influence of systematic errors are a choice. Model selection, including model complexity (such as the degree of a polynomial or the choice between a Gaussian, Lorentzian, or Voigt), is a choice. The classical inference equation 4.13 does not exist separate from systematic-influencing choices based on model *beliefs*, but is *embedded* within them with the details hidden away from a reader and maybe even an incurious practitioner. While the discussion has grown into the unification of statistical and systematic errors in the Bayesian scheme, here is an example that shows the application of a prior distribution $p(H)$ is a standard tool in the analyst's tool-belt and not something entirely new.

An Example: When reducing multiple independent measurements with central values x_i and

Gaussian distributed errors σ_i, one performs the calculation

$$\bar{x} = \frac{\sum \frac{x_i}{\sigma_i^2}}{\sum \frac{1}{\sigma_i^2}} \tag{4.14}$$

to find the error-weighted average. If we considered the probability density functions of each of these measurements, they would be of the form

$$p_i(x) \sim \exp\left(\frac{-(x - x_i)^2}{2\sigma_i^2}\right). \tag{4.15}$$

The probability of independent events is simply the product of the probability of each, so the composite probability is

$$P(x) = \prod p_i(x) \sim \exp\left(-\frac{1}{2}\sum \frac{(x - x_i)^2}{\sigma_i^2}\right). \tag{4.16}$$

Expanding the sum and collecting terms in powers of x yields

$$P(x) \sim \exp\left(-\frac{1}{2}\cdot(x^2\sum \frac{1}{\sigma_i^2} - 2x\sum \frac{x_i}{\sigma_i^2} + \sum \frac{x_i^2}{\sigma_i^2})\right). \tag{4.17}$$

Completion of the square yields (and dropping constant terms that are wrapped up in the proportionality symbol)

$$P(x) \sim \exp\left(-\frac{1}{2}\cdot\sum \frac{1}{\sigma_i^2}\cdot(x - \sum \frac{x_i}{\sigma_i^2}\cdot(\sum \frac{1}{\sigma_i^2})^{-1})^2\right) \tag{4.18}$$

The joint probability is maximized for

$$\bar{x} = \frac{\sum \frac{x_i}{\sigma_i^2}}{\sum \frac{1}{\sigma_i^2}}, \tag{4.19}$$

which is the usual result for error-weighted averaging. To make the example clear, we invoke multiplicative associativity applied to Eq. 4.16. That is, the joint probability can be written as the product of new measurements and old (*prior*) measurements

$$P(x) = \prod p_i(x) = \prod_{i,\text{new}} p_i(x) \prod_{j,\text{old}} p_j(x) \tag{4.20}$$

or new measurements against theory

$$P(x) = \prod p_i(x) = \prod_{i,\text{experiment}} p_i(x) \prod_{j,\text{theory}} p_j(x) \tag{4.21}$$

or equivalently and more generally,

$$P(x) = p_{\text{data}} \cdot p_{\text{prior}} \tag{4.22}$$

which is identically Bayes' Theorem, Eq. 4.12, without the denominator.

4.4.2 Introduction to Markov Chain Monte Carlo

The Markov chain Monte Carlo is a class of algorithms that is useful in exploring a probabilistic parameter space. MCMC algorithms are numerical in nature and the results are numerical strings or *chains* of sampled parameters. That is, instead of solving an integral or solving a χ^2-minimization analytically and calculating *the* solution and errors in *the* solution by the shape of the probability surface around *the* solution, the algorithm is run to generate samples of interest in the chain, and upon completion, the values of the chain can be interpreted as part of a set of solutions to the problem of interest with more frequently sampled values being preferred. Less abstractly, the Metropolis-Hastings algorithm performs a "random walk" through a probability-like space, $f(\vec{x})$, which is proportional to the probability space, $p(\vec{x})$, and the generated chains will be sampled according to the probability space.

The basic steps of the algorithm follow:

- Assuming $\vec{x}_i$, compute a test value $\vec{t}$ according to some generator $g(\vec{t}|\vec{x}_i)$
- Calculate the probability fraction $\alpha = \frac{f(\vec{t})}{f(\vec{x}_i)} = \frac{p(\vec{t})}{p(\vec{x}_i)}$ and a random number r from a uniform distribution
- Compare α and r. Accept the trial value if $\alpha > r$ and set $\vec{x}_{i+1} = \vec{t}$. Reject the trial value $\vec{x}_i$ if $\alpha < r$ and set $\vec{x}_{i+1} = \vec{x}_i$
- Repeat with $\vec{x}_{i+1}$

The stored values of $\vec{x}$ make the Markov chain and these values will have the same properties as a sample set sampled directly from $p(x)$.

While simple at a high level, there are some assumptions and tricks related to the generator $g(\vec{t}|\vec{x}_i)$. As written, the generator must be symmetric $g(\vec{x}|\vec{y}) = g(\vec{y}|\vec{x})$. In principle, asymmetric generators can be used, but this biases your trial samples and must be accounted for to correctly sample the probability distribution $p(x)$. In a large number of sampled dimensions, the odds of performing a "bad" step in one or more dimension increases. To solve for this, a common generator to use is the multi-variate Gaussian, which is a multi-dimensional Gaussian defined by a covariance matrix. An alternative is Gibbs sampling, which is a subset of Metropolis-Hasting schemes and is implemented similarly, but only one component of the parameter space is varied in each step. The individual components are updated cyclically. The Gibbs-sampled component may be an individual parameter of the probability space or a linear combination of parameters. This sampling reduces the dimensionality of each step, but increases the number of steps required to achieve the same coverage in the entire probability space.

These MCMC solutions are robust to high-dimensional problems that may have local minima, as solutions will enter and exit minima in the probability distributions during the parameter walk. Furthermore, they allow for non-Gaussian-distributed probability surfaces which can more closely model the inference problem at hand.

4.4.3 Implementation of Bayesian Inference with MCMC

A Bayesian Markov Chain Monte Carlo code was written to perform the fit of the E19030 spectra for Pads B, C, D, and E.

Trial steps across the model parameter space were generated with ROOT's RooMultiVar object that provides the mathematics of a multi-variate Gaussian. It is easily trained by passing data to other ROOT objects. Historical steps were stored in a TPrincipal object that was used to generate the data covariance matrix (TMatrixD) which the multi-variate Gaussian object (RooMultiVar) was trained to. New trial parameter steps were pseudo-randomly generated and passed to the

step-evaluation portion of the code.

The probability-proportional function ($f(\vec{x})$ in Sec. 4.4.2) for a particular set of model parameters was done in two steps: fitting to data and evaluation against the Bayesian priors.

4.4.3.1 Fitting To Data

The data was fit from 120 keV to 245 keV in the 100% ionization efficiency center of mass energy scale and $\beta^- p$ peaks were tested for center mass energy from 145 keV to 215 keV. The low energy range limit comes from the shape of the β background becoming less exponential in shape. The high energy range limit is roughly the peak of the 256 keV ^{7}Li* after accounting for incomplete ionization processes of the slow ^{7}Li. The fit background function was the sum of an exponential curve, a flat offset, and the product of a Voigt and quadratic polynomial, written below

$$f_{\text{back}}(E) = \exp(a + b \cdot E) + c + \text{Voigt}(E, \bar{E}_7, \sigma_7, \gamma_7) \cdot (A_0 + A_1 \cdot E + A_2 \cdot E^2) \tag{4.23}$$

and the peak function was

$$\begin{aligned} f_{\text{peak}}(E) = N \cdot \Bigg[& \frac{1}{2} c_{\text{frac}} \text{Voigt}(E, \bar{E} = m_{10} q_p E_p, \sigma, \gamma = m_{10} q_p \Gamma) \\ & + (1 - c_{\text{frac}}) \text{Voigt}\big(E, \bar{E} = (m_{10} q_p + m_p q_{10}) E_p, \sigma, \gamma = (m_{10} q_p + m_p q_{10}) \Gamma\big) \Bigg] \end{aligned} \tag{4.24}$$

where c_{frac} is the fraction of decays originating on the Proton Detector cathode, m_{10} is the mass fraction of the ^{10}Be to the ^{10}Be+proton system, m_p is the mass fraction of the ^{10}Be to the ^{10}Be+proton system, q_p was the proton ionization efficiency, q_{10} was the ^{10}Be ionization efficiency, E_p was the center of mass energy of the $\beta^- p$ resonance, σ was the Gaussian width detector resolution, and Γ was the intrinsic width of the $\beta^- p$ resonance. The total (background and peak-search both) model has 14 parameters.

The fit was judged by the χ^2 sum of the squared difference between data and the model function, divided by the square of the expected data error, which was the root of the data in the

bin, from Poisson counting statistics. The probability of a particular data given the model is then $p(\mathrm{d}|\mathrm{H}) = \exp(-\chi^2/2)$.

4.4.3.2 Evaluation of model against priors

The next part was to evaluate a particular model against the priors. Strictly speaking, many of these priors are un-normalizable, so these priors are not true probabilities that integrate to 1. This is alright as the MCMC code requires only a function that is proportional to probability, so un-normalized priors are fine if not true probabilities. Here is a list of individual priors p_i that are multiplied to generate the entire model prior $p_M = \prod p_i$:

- $p_0 = 1$ if the exponential slope meant for the β background is negative, $b < 0$
- $p_1 = 1$ if the constant flat background is positive AND less than the minimum data bin, $0 \leq c \lesssim 1200$
- $p_2 = \exp\big(-\frac{(c_{\mathrm{frac}}-\bar{c}_{\mathrm{frac}})^2}{2\cdot 0.006^2}\big)$, so the cathode fraction is within ~1.5% of the value measured using the $\beta^-\alpha-\gamma(478\mathrm{keV})$ coincidence
- $p_3 = 1$ if proton counts, N, are positive
- $p_4 = 1$ if the detector resolution is between 4.5% and 10% of the center of mass energy E_p
- $p_5 = 1$ if the $\beta^- p$ intrinsic width is less than 30 keV
- $p_6 = \exp\big(-\frac{(q_{10}-\bar{q}_{10})^2}{2\cdot 0.08^2}\big)$, so the ^{10}Be ionization efficiency matches that calculated in Sec. 4.3.1.2
- $p_7 = 1$ if the nominal Voigt center is between 210 and 260 keV, $210 < \bar{E}_7 < 260$
- $p_8 = 1$ if the Voigt·Polynomial is positive, that is $A_0 + A_1 \cdot E + A_2 \cdot E^2$ over the fit window
- $p_9 = 1$ is the nominal Voigt widths are less than 300 keV, that is $\sigma_7 < 300$ and $\gamma_7 < 300$

- $p_{10} = 1$ if the Voigt· Polynomial curve is increasing on the interval 120-150 keV. This guarantees the peak-like behavior far from the peak

otherwise, $p_i = 0$. That is, most of our priors are "ignorant" to model parameters, granting the model great flexibility, and instead only excludes unphysical behavior of the background model.

This point is critical. We did not and do not have access to a $^{11}\mathrm{Be}(\beta^-\alpha)^7\mathrm{Li}$ "calibration" that guarantees no $^{11}\mathrm{Be}(\beta^- p)^{10}\mathrm{Be}$. We need a background model that can accommodate the convolution of real $^{11}\mathrm{Be}(\beta^-\alpha)^7\mathrm{Li}$ and the detector response to a precision exceeding that of any previous GADGET experiment, due to asymmetry of the nominal $\sim 1 \cdot 10^{-5}\beta^- p$ branch against the $\sim 3 \cdot 10^{-2}\beta^-\alpha$. In the scenario of an incorrectly simple model, the Bayesian posterior distribution will still incur a systematic shift from the signal compensating for a deficiency in the background model. However, in the scenario of a too-complicated model, where one has model redundancies between signal and nuisance parameters, all confusions between signal and background will be represented with their quality-of-fit probabilistic weights. Complicated correlations are explored across the entirety of the parameter space and not merely at *the* "most probable" point, and are easily visualized in 2D plots of signal vs nuisance-parameter.

4.4.3.3 The MCMC Algorithm

This next section outlines the explicit coding details of the MCMC code. Initial parameter values were determined by a χ^2 fit of the data with the background function alone, Eq. 4.23. Initial step sizes were selected by the χ^2 fit error bars. Each of the Pads B, C, D, and E were treated independently, so the algorithm was run for each pad and assumed resonance energy E_p on the interval 145 to 215 keV with 1 keV spacing for a total of 280 implementations.

There were five burn in periods of the MCMC. Each burn in consisted of 10,000 saved samples spaced every 20 steps along the chain. The burn-in chains were thus 200,000 samples long. As many of the model parameters are correlated and high-dimensionality steps are less likely to succeed than single-dimension steps, the first burn in was sampled according to the Gibbs scheme with individual parameters. That is, the first parameter was updated by $t_0 = x_0 + r(0, \sigma_0)$, where

r is a random number generated from a Gaussian distribution with mean zero and width σ_0. The step was evaluated and either accepted or rejected, then the second parameter was varied by $t_1 = x_1 + r(0, \sigma_1)$ and evaluated, and so on.

Once this primary chain completed, four additional burn in chains were sampled. These chains proposed steps that updated all model parameters using steps sampled from a multi-variate Gaussian defined by the covariance of the previous burn in chain, dx. That is, the trial steps were calculated by $\vec{t} = \vec{x}_i + \vec{dx}_i$. The burn in periods allowed the MCMC code to reach the statistical distribution if the initial parameter values or step sizes were not in equilibrium with the posterior distribution. This was nearly guaranteed.

The "data-taking" chain followed. Here, the step sizes are the values drawn from the multi-variate Gaussian distribution scaled by 0.25. From this chain 1 million samples were drawn, spaced every 20 steps, for a total of 20 million steps. The covariance matrix from which the trial steps are generated was reevaluated every 500 saved samples (10,000 steps) in the chain. If a batch of 500 samples had poor update success (> 10% of saved samples were identical to the previous saved sample), then that block of steps was repeated with 33% smaller step sizes. Resampling allowed more efficient motion throughout the parameter space. The check against high failure rates of the proposed trial steps safeguarded against the MCMC "getting stuck" leading to a singular covariance matrix and new trial step generation.

CHAPTER 5

RESULTS AND DISCUSSION: EVIDENCE FOR NOVEL $\beta^- p$

Following the Bayesian Markov Chain Monte Carlo procedure described in Sec. 4.4 was applied to GADGET Pads B, C, D, and E. A number of metrics to judge the quality of the performance of the MCMC will be presented and then the inferred $\beta^- p$ branching ratio. This branching ratio will be compared to existing theory work and the other experimental work.

5.1 Results of Bayesian Markov Chain Monte Carlo

The first results we will show are related to the behavior of the MCMC. The MCMC generates a great deal of data. To store 1,000,000 double precision floating point numbers requires 8M bytes. 1 million samples over 14 parameters requires 112 MB of storage per fit. We can study 1D parameter distributions, 2D parameter correlation distributions, conditional distributions (e.g. "What is the branching ratio and detector resolution correlation, assuming a $\beta^- p$ intrinsic width $\Gamma = 5$ keV?"), as well as the actual path of the MCMC through the parameter space, which can be used to ensure the chain is exploring the space efficiently. These distributions and tests exist for all fits, across all pads and energies.

5.1.1 Convergence of the Markov Chain

A first test of the MCMC is to look at the parameter *traces*. (These are sometimes called *caterpillar plots* for aesthetic reasons.) If the MCMC is sampling the parameter space efficiently, then samples are fairly uncorrelated, as random samples ought to be if they are truly random. Figures 5.1, 5.2, 5.3, 5.4 shows the trace from the MCMC fit of Pad B at $E = 160$ keV. The sampling here is showing every 100th saved point. Most traces are fairly random in appearance, but to demonstrate some behavior of correlation, consider the ^{7}Li* center parameter in the middle of Fig. 5.3. The sampling appears fairly random around $E_7 \sim 230$ keV most of the time. However, there is another solution for $E_7 \sim 250$ keV. By considering the χ^2 value at different times (Fig. 5.5), we can see these

transitions from $E_7 \sim 230$ keV to $E_7 \sim 250$ keV are not met with any sort of decrease in the quality of the fit. However, there is still correlation in the sample as once the value of the E_7 parameter jumps, it fluctuates about this new value for some thousands of samples. While this correlation is not ideal, the MCMC steps into and out of this region several times, and does not become "stuck" in a bad region nor does it become "un-stuck" and move into a new, better, region. That is, this motion is probably fairly statistical.

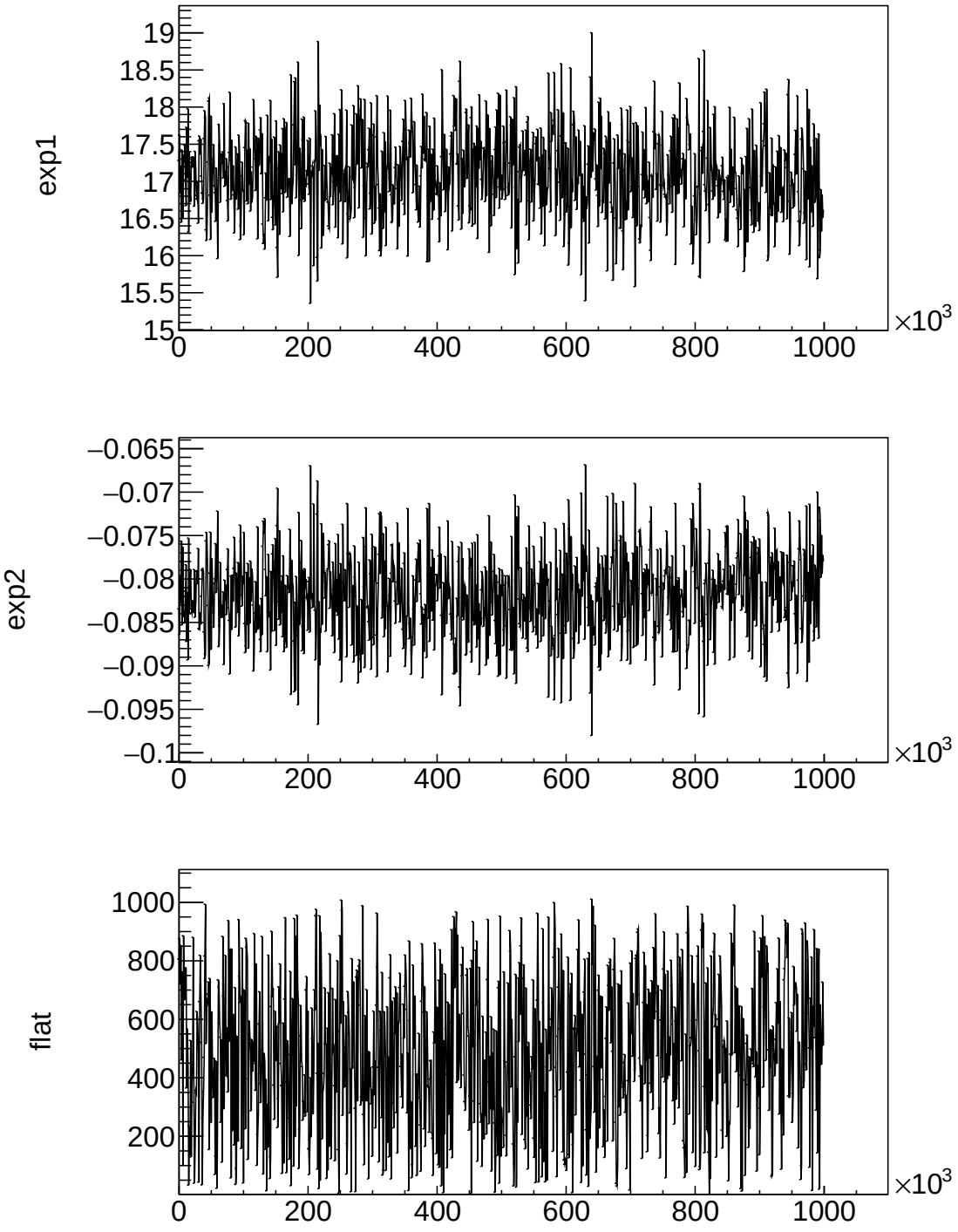

Figure 5.1: MCMC parameter traces for Pad B and E_p = 160 keV. The parameters are the exponential scaling, exponential slope, and constant background. Parameter values are plotted in the y-axis and the sample number along the MCMC are plotted along the x-axis. (1/5)

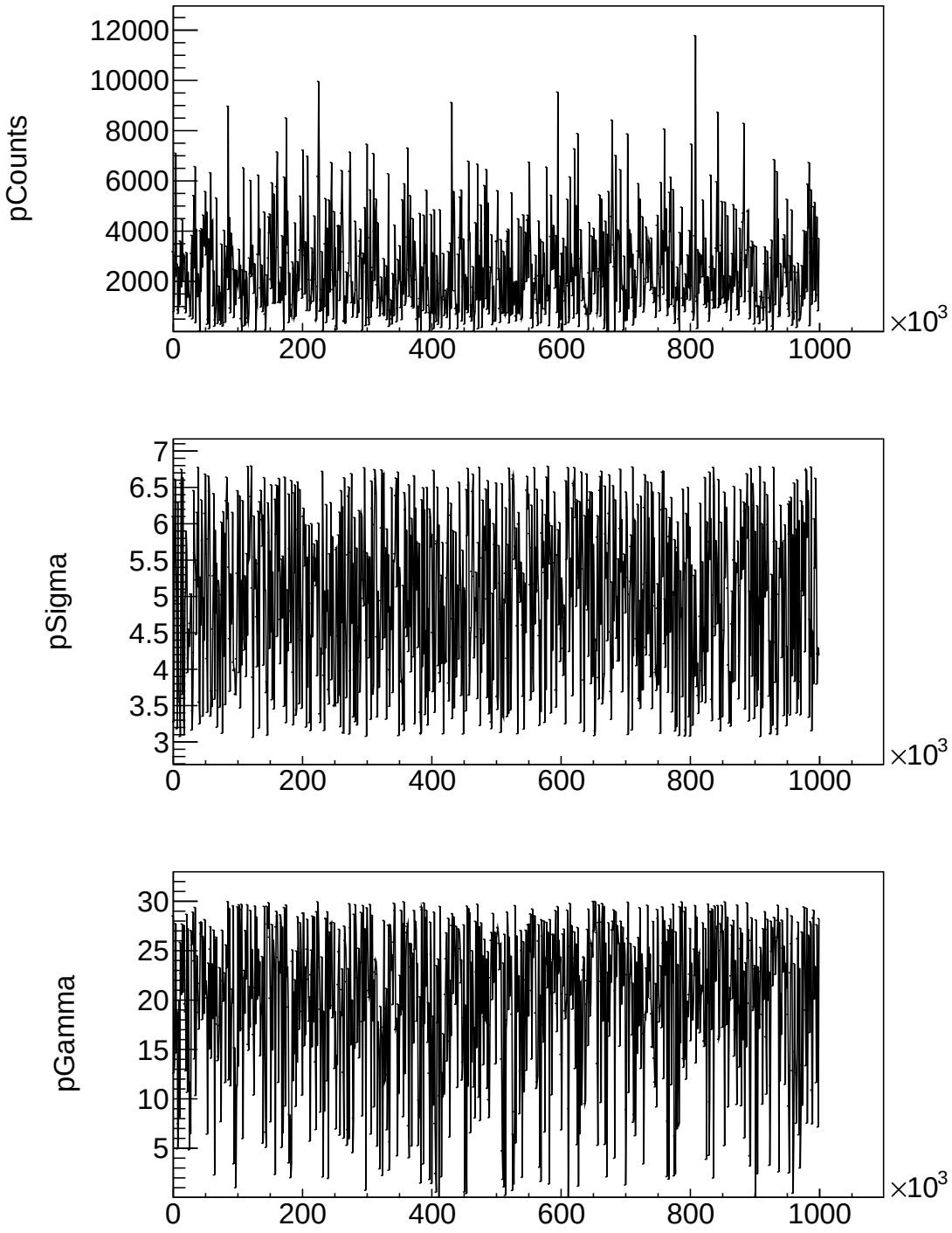

Figure 5.2: MCMC parameter traces for Pad B and E_p = 160 keV. The parameters are the $\beta^- p$ counts, detector resolution applied to the $\beta^- p$ signal, and assumed intrinsic width Γ_p. Parameter values are plotted in the y-axis and the sample number along the MCMC are plotted along the x-axis. (2/5)

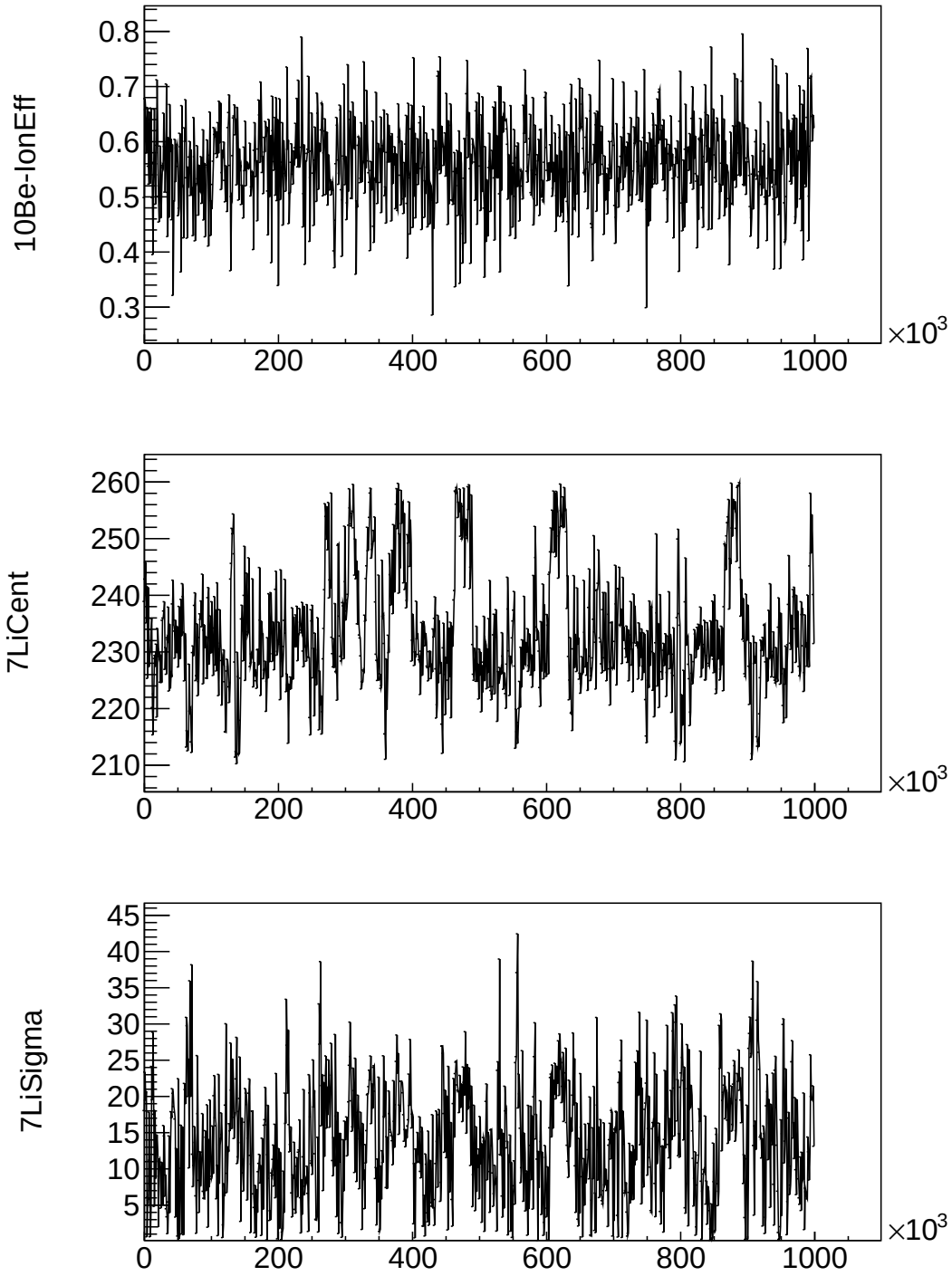

Figure 5.3: MCMC parameter traces for Pad B and E_p = 160 keV. The parameters are the ^{10}Be ionization efficiency, the Voigt center of the ^{7}Li* peak, and the Gaussian width of the ^{7}Li* peak σ_7. Parameter values are plotted in the y-axis and the sample number along the MCMC are plotted along the x-axis. (3/5)

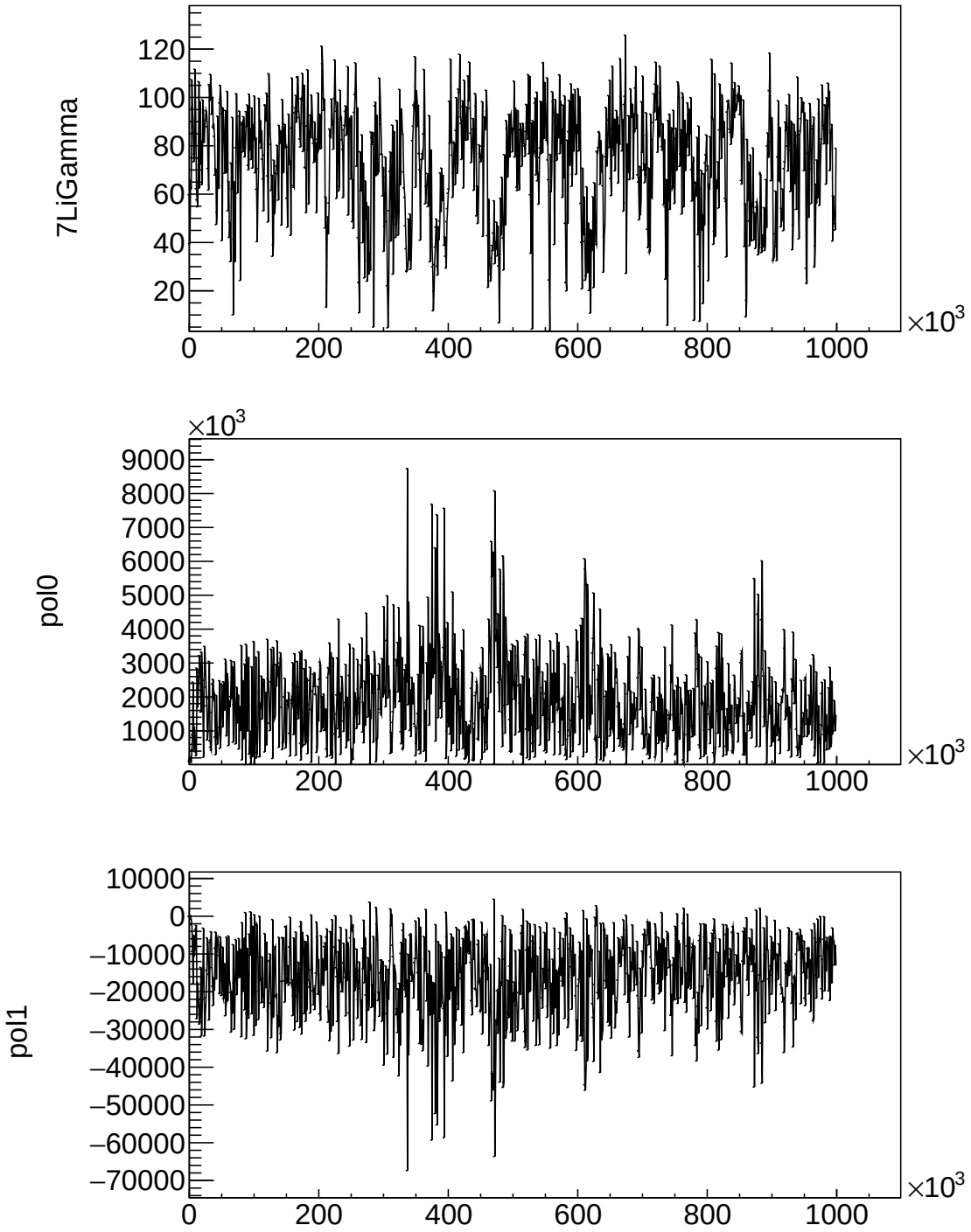

Figure 5.4: MCMC parameter traces for Pad B and E_p = 160 keV. The parameters are the Lorentzian width of the ^{7}Li* peak γ_7, the zeroth term in the polynomial applied to the ^{7}Li* peak Voigt, and the linear term in the polynomial applied to the ^{7}Li* peak Voigt. Parameter values are plotted in the y-axis and the sample number along the MCMC are plotted along the x-axis. (4/5)

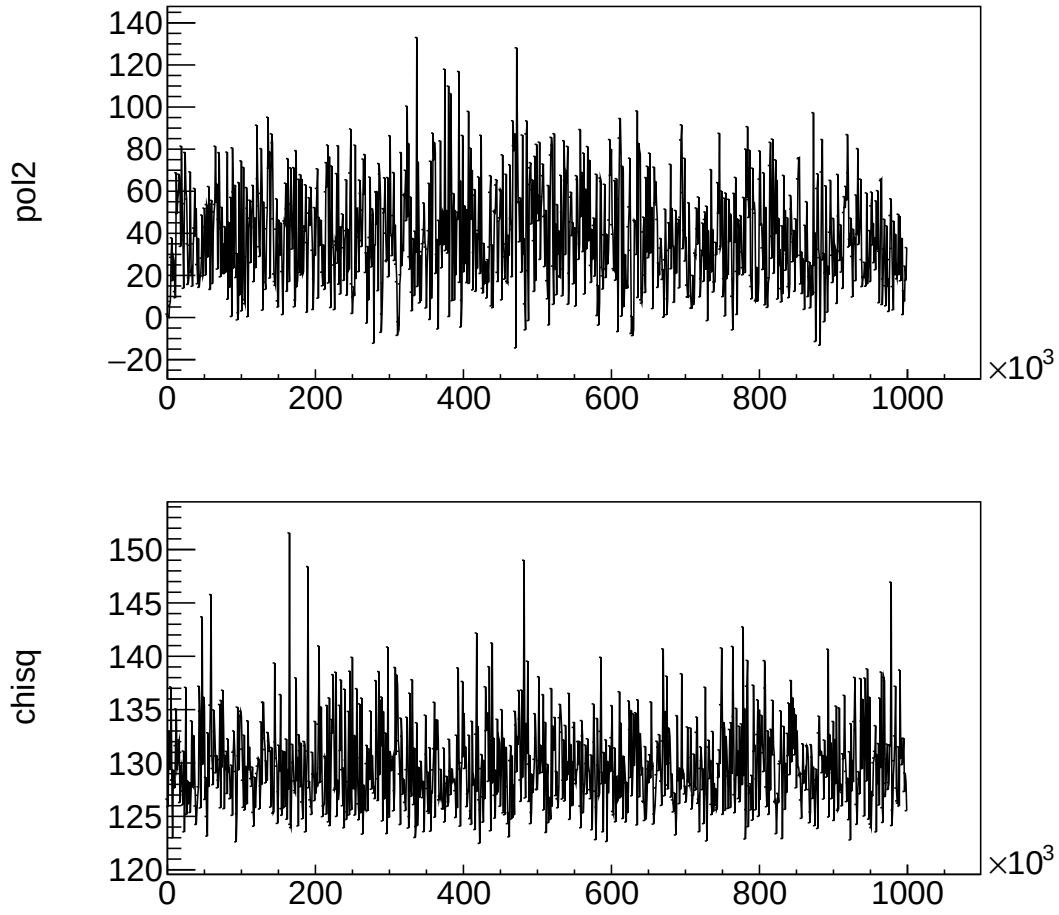

Figure 5.5: MCMC parameter traces for Pad B and E_p = 160 keV. The parameters are the quadratic term in the polynomial applied to the ^{7}Li* peak Voigt and (not a parameter) the Bayesian-modified χ^2 of the fit. Parameter values are plotted in the y-axis and the sample number along the MCMC are plotted along the x-axis. (5/5)

One example of unambiguously poor behavior is walking behavior, with high correlation and a clear direction. Such behavior can be seen in the burn-in chains, moving from non-ideal fit parameters toward the statistical distribution of fit parameters. As these walking samples are never revisited, they arguably aren't truly part of the true probability distribution, but are instead an artifact of the MCMC implementation. Similarly, parameters that rarely update are unfavorable. A stepping scheme that rarely makes a successful step should still have the desired statistical properties of stepping scheme that has more successful stepping, but will take a very long time to converge to a desirable distribution. In shorter times, the final sample distributions will have "spikes" in the distributions because of the rarity of steps and, when steps are rare, the same step is "sampled" and saved repeatedly.

This is to argue that while obvious correlations exist in this chain, every unusual space is sampled several distinct times and these traces still exhibit nice statistical properties in both regions. One quantitative metric of this is the success rate of the sampling. If the success rate is too high, then the chain likely is taking very small steps relative to the features in the N-dimensional probability space. These small steps mean the whole space is not explored as quickly as if the trial steps were larger. Similarly, if the trial-step success rate is too low, then the trial steps are likely too large, or with a correlation different than the shape of the probability space. Gelman *et al.* showed that for high dimensional systems, such as our 14 parameter model that the convergence of the sampling is optimized for a trial step success rate of 23.4% [84]. These traces are for just the fit of Pad B with the assumed energy $E_p = 160$ keV, but all traces that were visually inspected appear similar in their sampling and across Pads and across assumed energies. All MCMC iterations had success rates of $22 - 26\%$, which is close to the ideal success rate.

One benefit of the MCMC that was discussed in 4.4.3 was that complicated parameter correlations can be investigated over the entirety of the probability space and not merely in the vicinity of the χ^2-minimum location. Figures 5.6, 5.7, 5.8, 5.9, 5.10, 5.11, 5.12, 5.13, 5.14 show the full correlation output of the MCMC run on Pad C at $E_p = 160$ keV. The nine pages are sections of the same type of graphic. The parameters are plotted row-wise and column-wise to make a 14x14 ma-

trix of the two-parameter correlations and the two-dimensional, color-coded histograms are filled with the specified parameter values along the Markov Chain. More intense regions are regions where the MCMC spent more "time"/samples and are to be interpreted as proportionally more probable. (The histograms are not normalized to integrate to unity, so the intensity is proportional to probability.) Uncorrelated parameters will have ellipse-like shapes in their sample distributions and highly correlated parameters, like the exponential background scaling and decay parameters, will appear as tight lines or curves. Additional graphics will be available in Chapter B, but several patterns found here are general to the visually inspected correlation matrices for other Pads and assumed resonance energies.

Parameters within a component of the background tend to be highly correlated. This can be seen in the *exp1* and *exp2* exponential parameters modelling the β background. Similarly, the ^{7}Li* peak's σ and γ are well correlated in an ellipse shape, even if $\gamma \sim 70$ keV and $\sigma \sim 10$ keV are the favored values. Finally, the polynomial terms of the same peak *pol0, pol1, pol2* are all very correlated and in complicated ways between all three parameters.

What is *not* strongly correlated with background parameters is the inferred proton counts. Proton counts are shown in the fourth row of Fig. 5.6, 5.7, and 5.8. A lack of correlation with background parameters is suggestive that our model description of the background is modeling the background and our model description of the signal is modeling the signal, with minimal "mixing" of the two. (Again, a great example of "mixed" parameters is the interplay of the two Voigt widths.) The proton counts parameter, however, is not entirely uncorrelated with parameters associated with the shape of the $\beta^{-}p$ peak. The strongest example of this is the correlation between the counts parameter and the intrinsic width parameter, shown in Fig. 5.15. This correlation shows that at $E_p = 160$ keV, as measured by Pad C, for all values of Γ_p, there is an inference of non-zero proton counts. Secondly, if we assume a large value of Γ, we must infer a large number of $\beta^{-}p$ counts. Conversely, an assumed large number of $\beta^{-}p$ counts implies a large intrinsic width Γ_p.

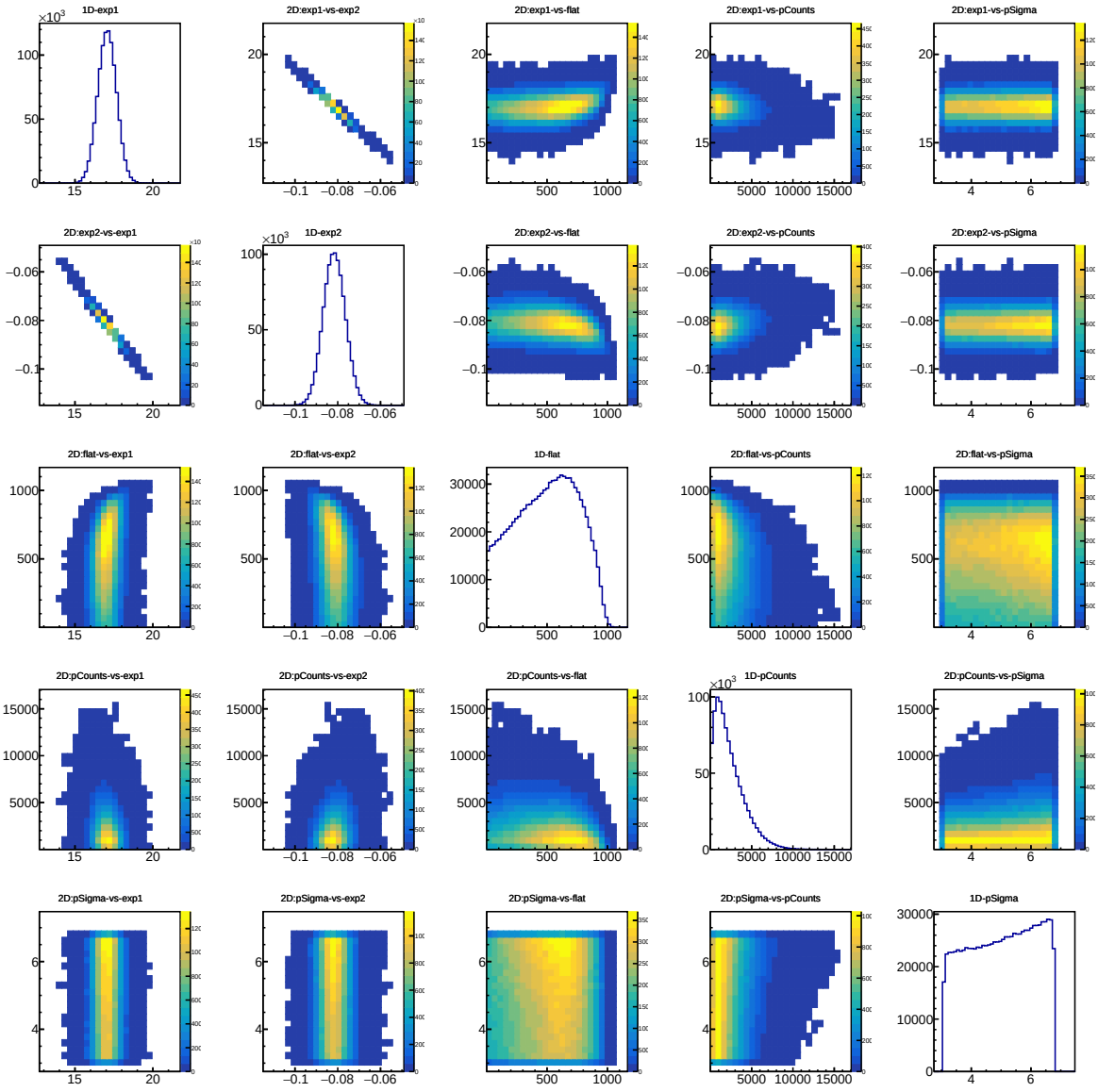

Figure 5.6: (1/9) 1-D distributions and 2-D correlations for Pad B and E_p = 160 keV

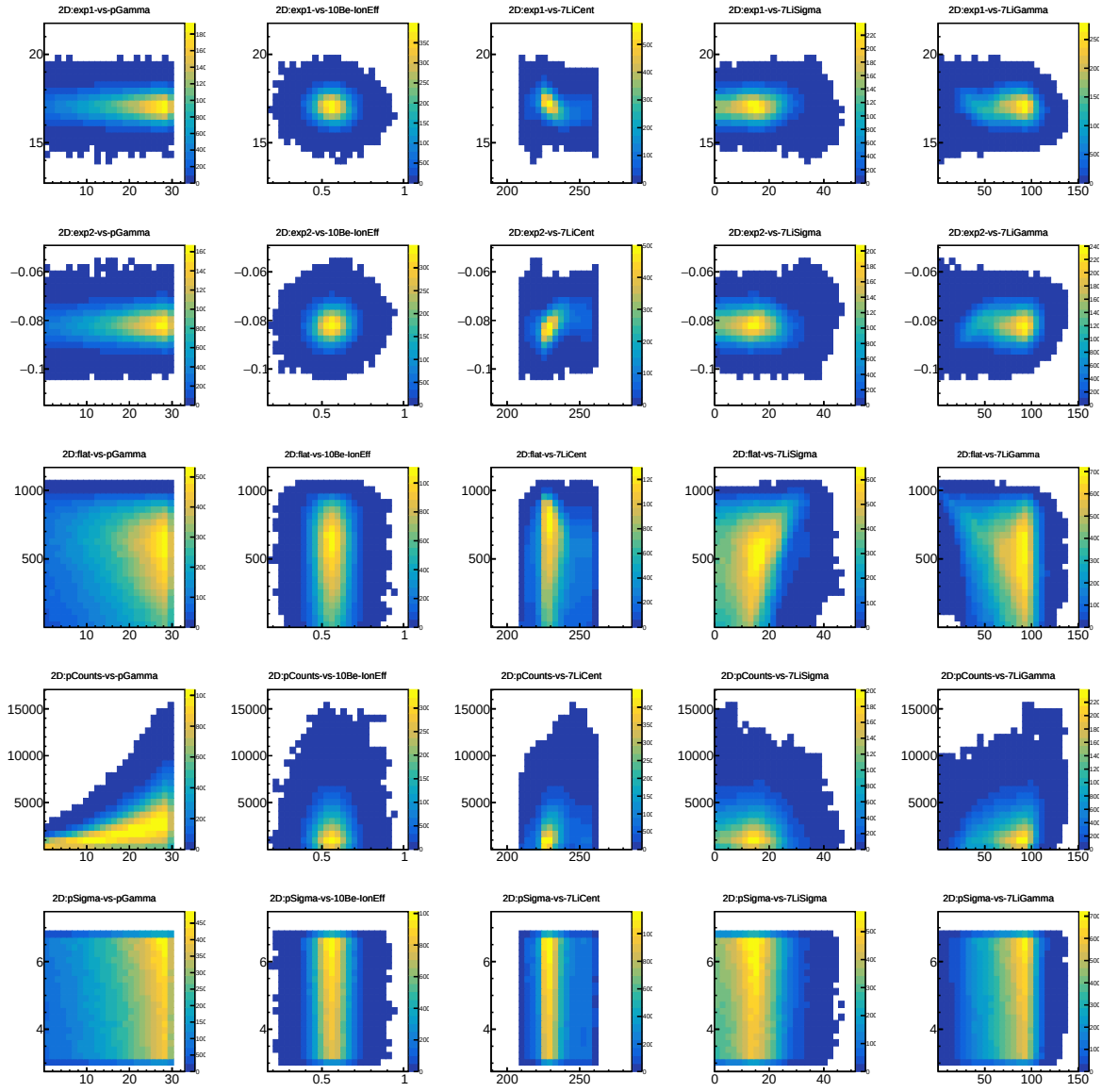

Figure 5.7: (2/9) 1-D distributions and 2-D correlations for Pad B and E_p = 160 keV

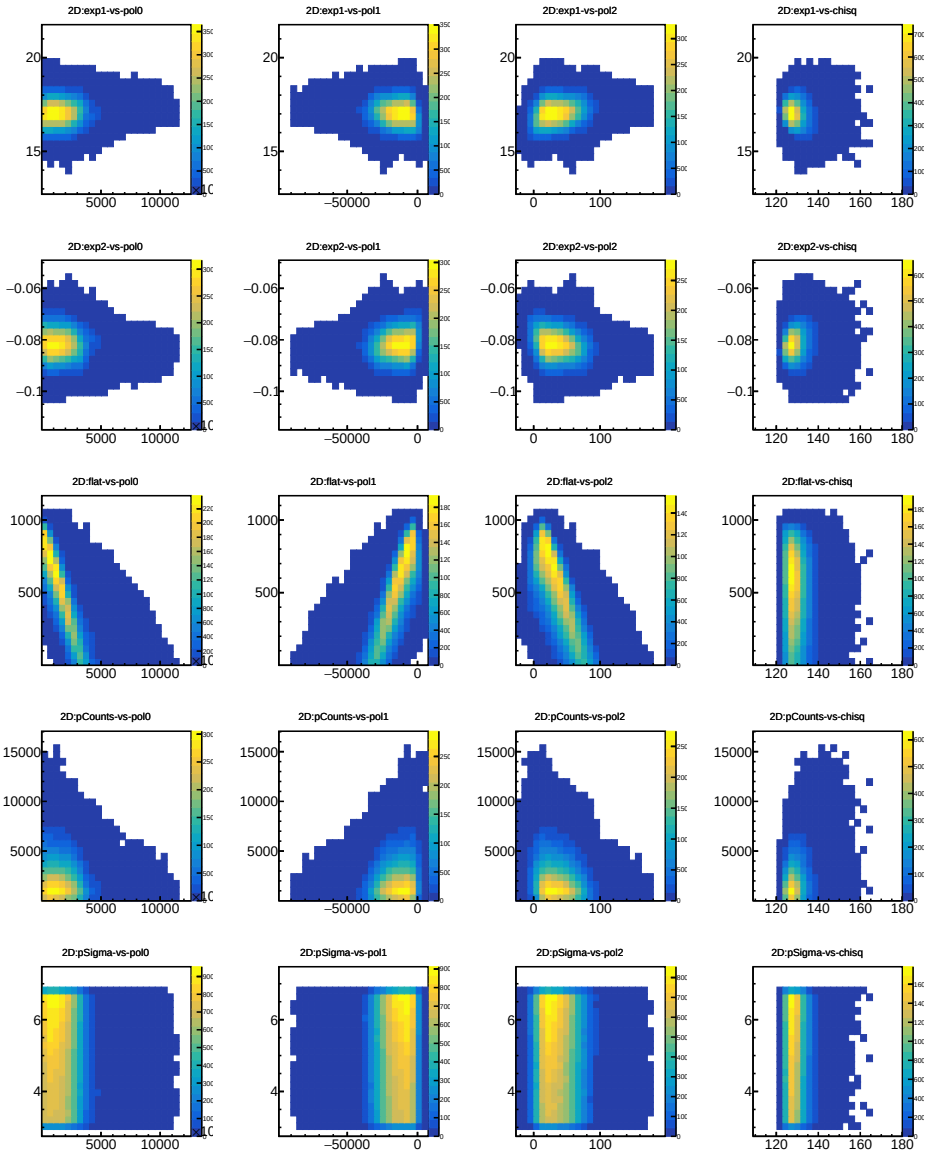

Figure 5.8: (3/9) 1-D distributions and 2-D correlations for Pad B and E_p = 160 keV

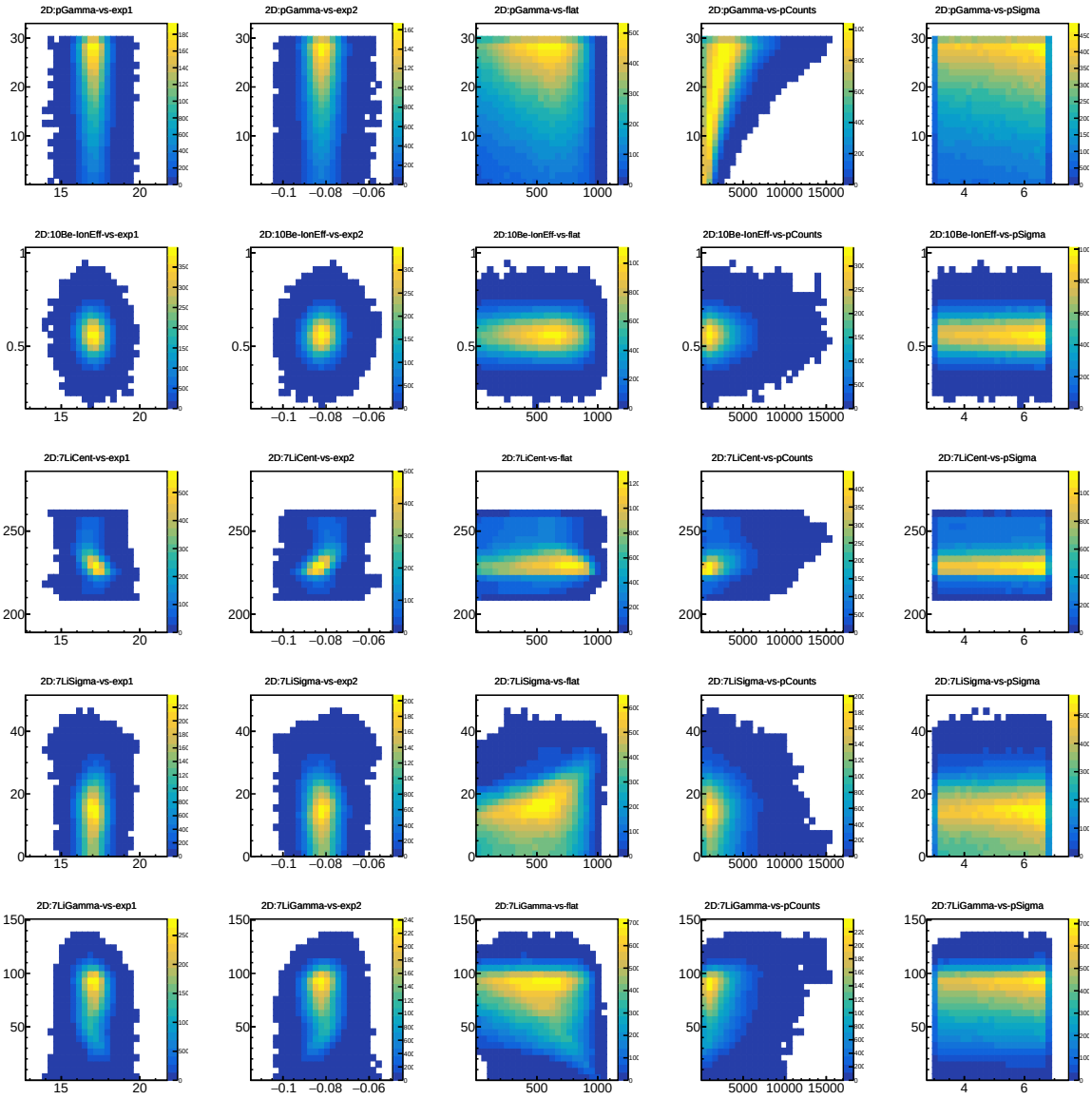

Figure 5.9: (4/9) 1-D distributions and 2-D correlations for Pad B and E_p = 160 keV

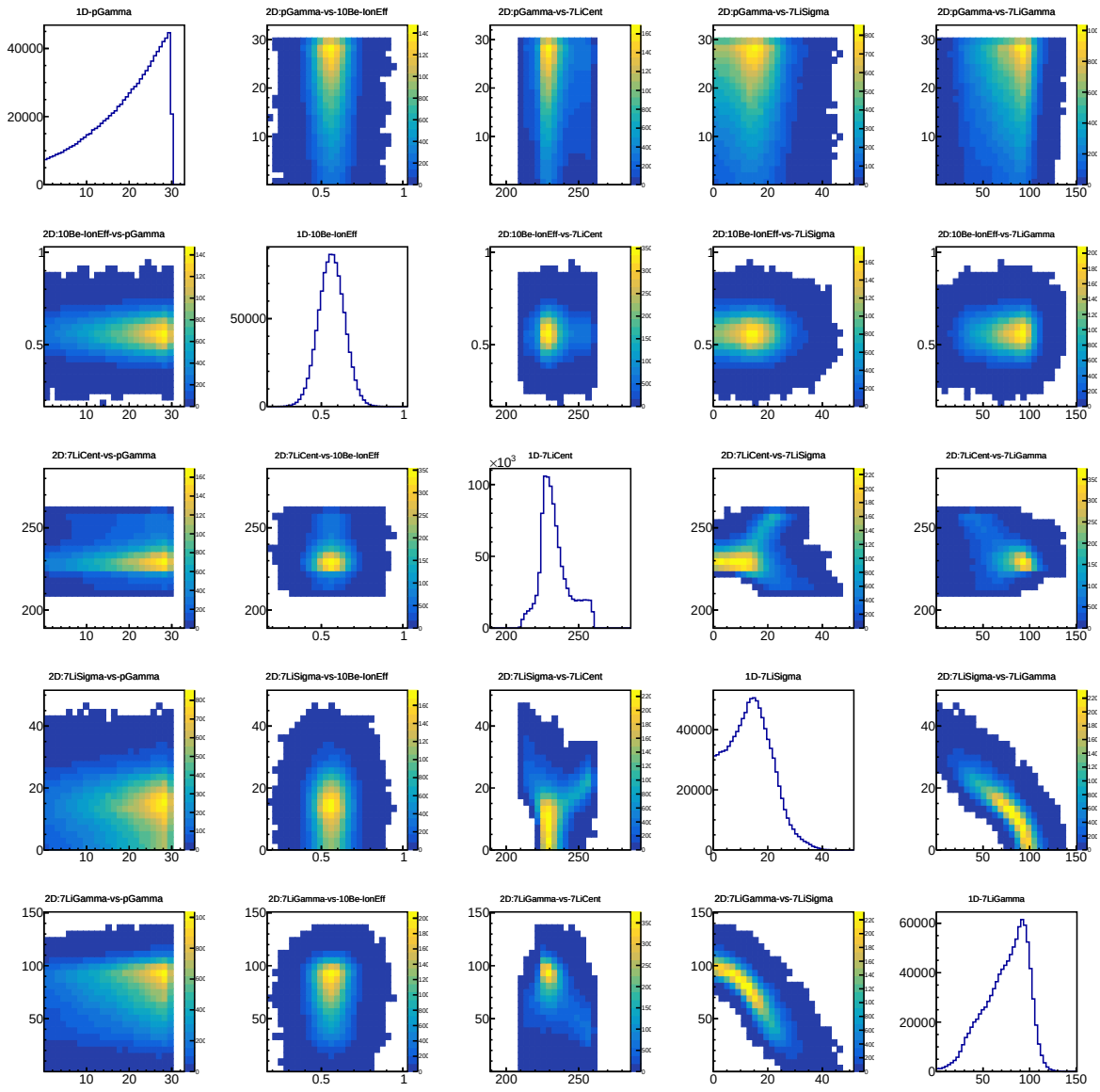

Figure 5.10: (5/9) 1-D distributions and 2-D correlations for Pad B and E_p = 160 keV

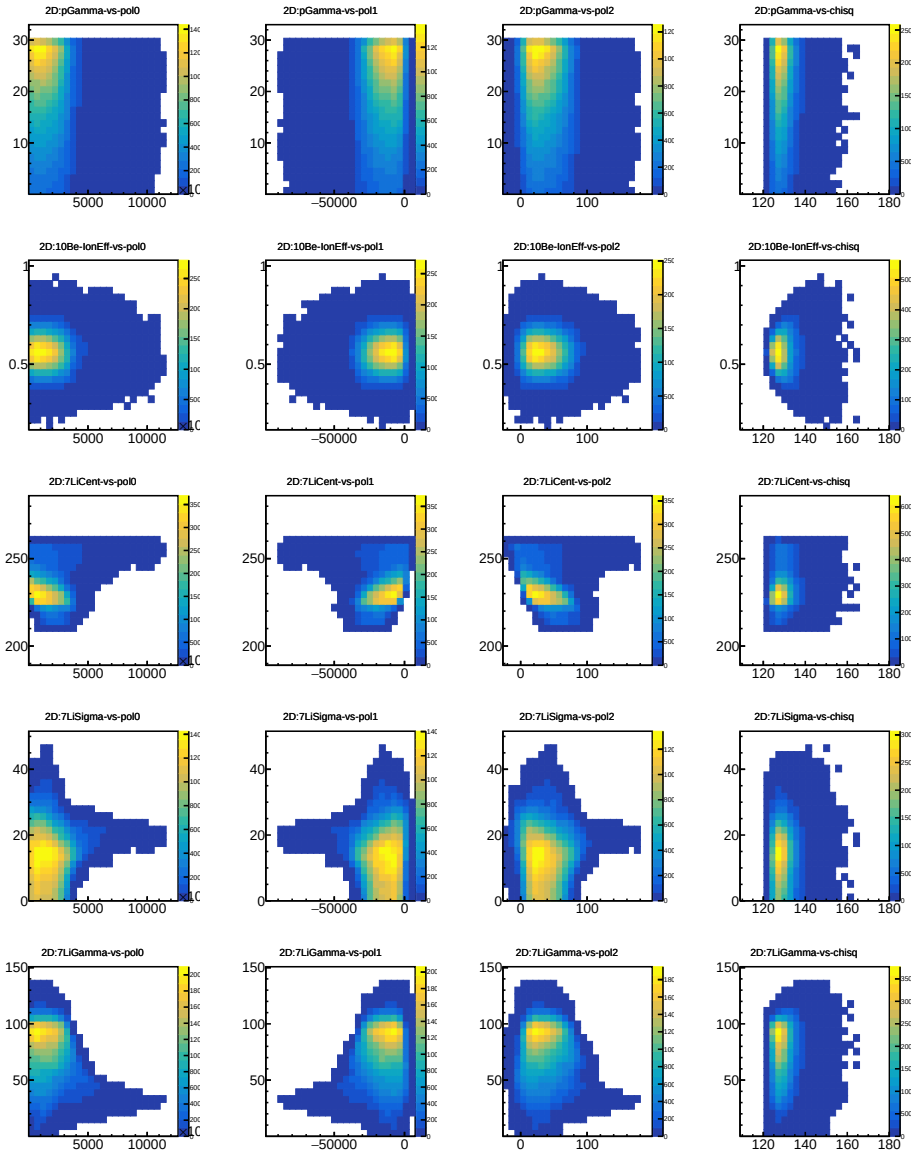

Figure 5.11: (6/9) 1-D distributions and 2-D correlations for Pad B and E_p = 160 keV

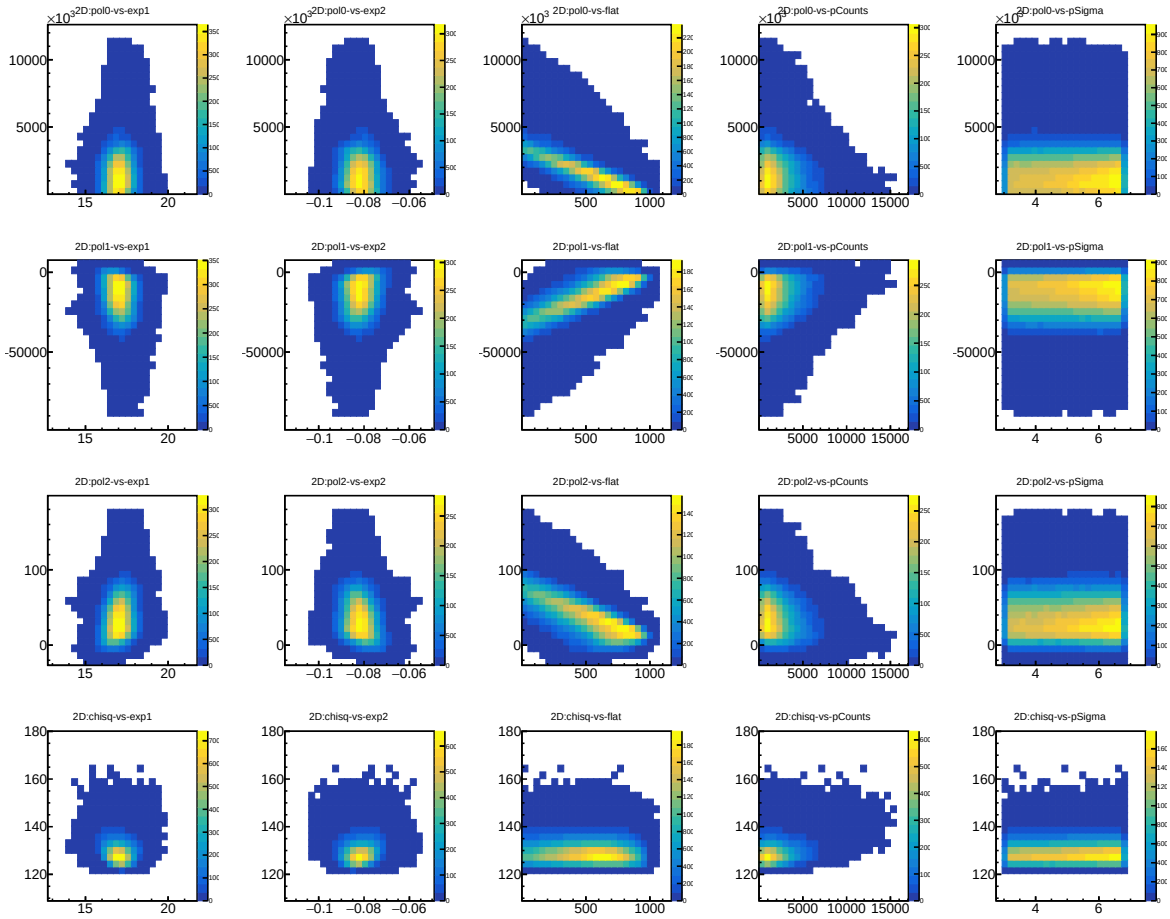

Figure 5.12: (7/9) 1-D distributions and 2-D correlations for Pad B and E_p = 160 keV

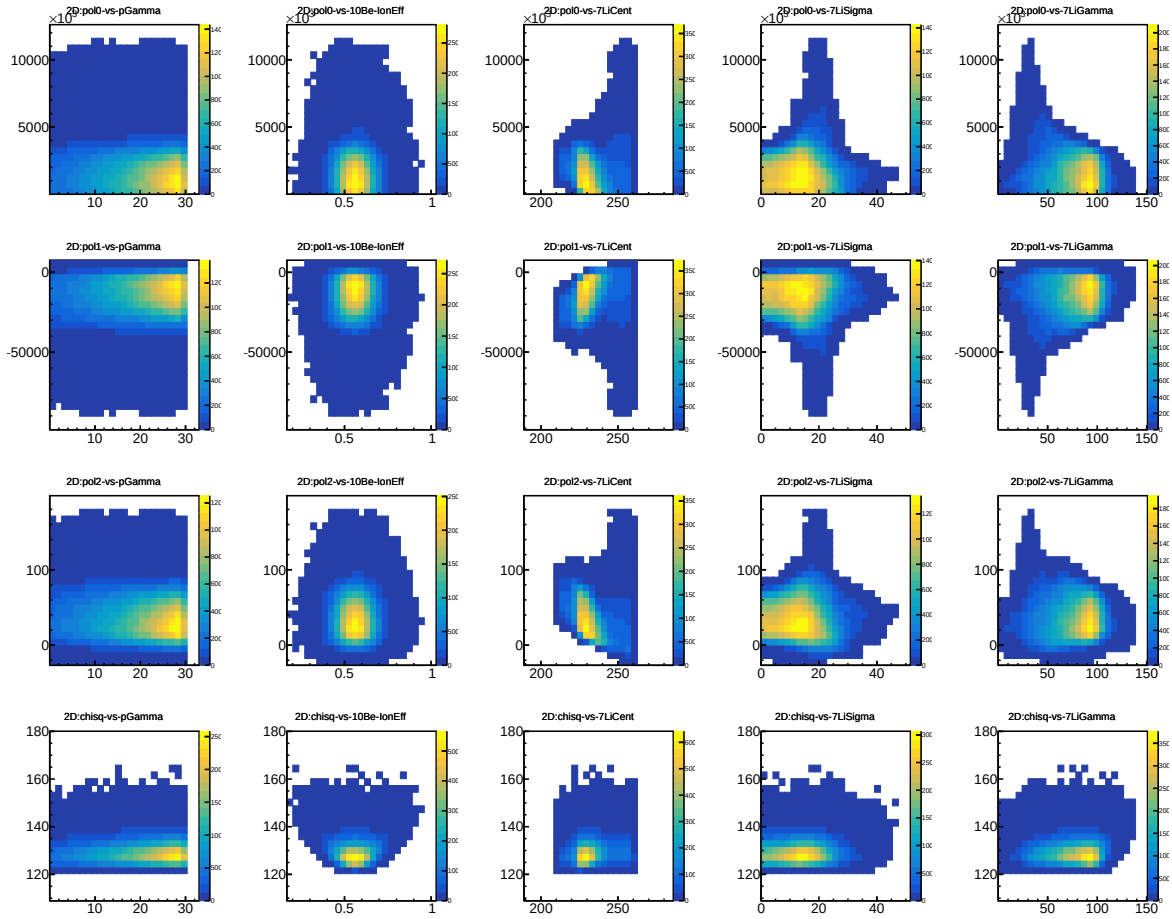

Figure 5.13: (8/9) 1-D distributions and 2-D correlations for Pad B and E_p = 160 keV

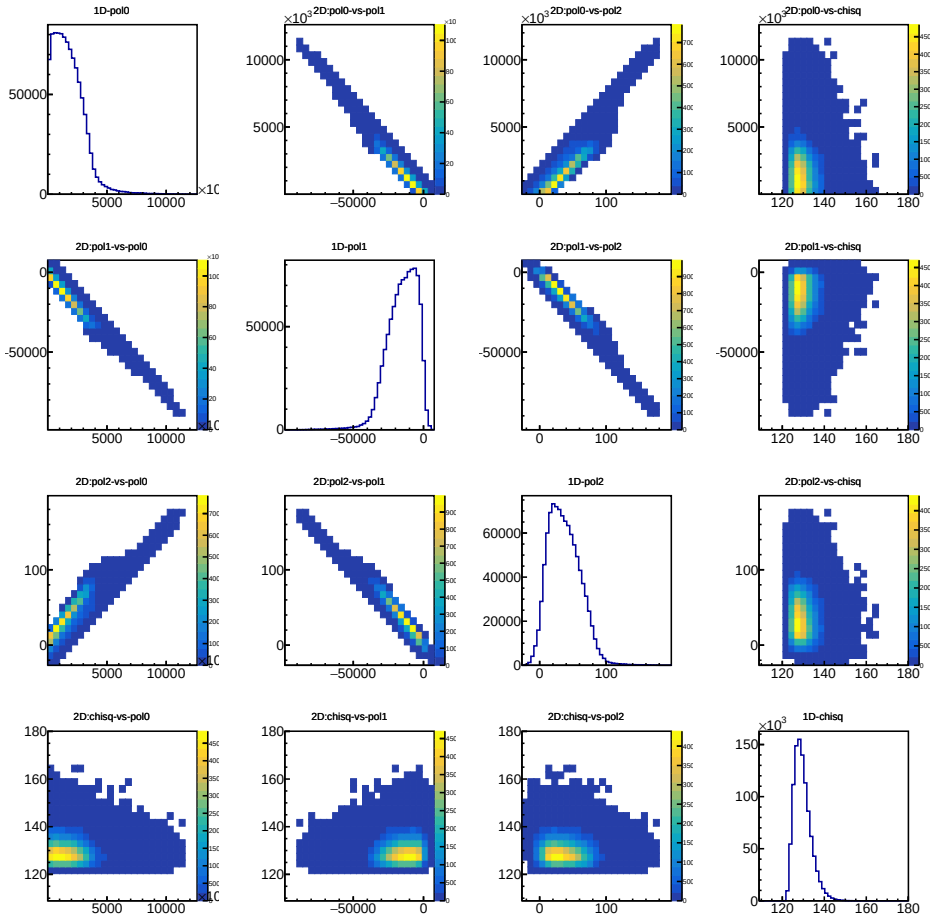

Figure 5.14: (9/9) 1-D distributions and 2-D correlations for Pad B and E_p = 160 keV

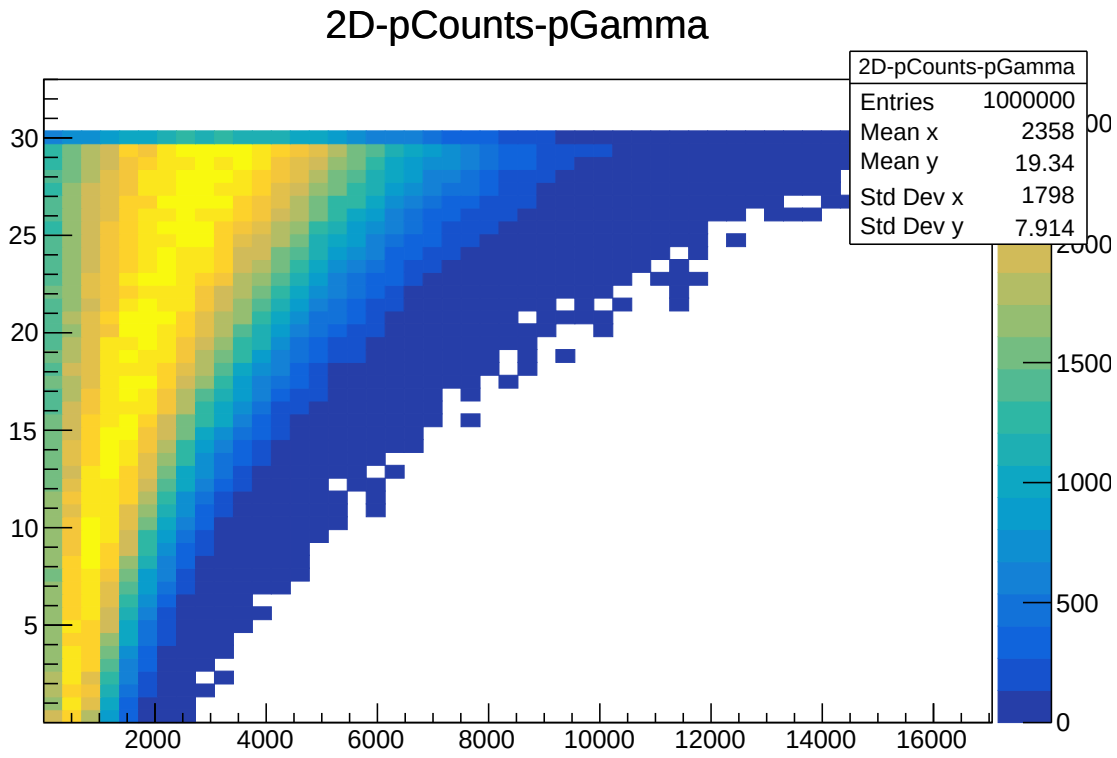

Figure 5.15: 2D parameter sample distribution between the proton intrinsic width Γ_p and proton counts for Pad B at $E_p = 160$ keV. For large values of Γ_p, a large number of $\beta^- p$ counts is inferred. Conversely, a large number of $\beta^- p$ counts implies a large intrinsic width Γ_p.

5.1.2 $\beta^- p$ intensity maps

The previous section was a deep dive into just one fit to the data to test the convergence of the MCMC code. Ultimately, the primary observable of interest here is the intensity of the ^{11}Be($\beta^- p$) decay and its energy. The MCMC algorithm gives us the Markov Chain of parameter samples assuming a proton resonance energy E_p. By plotting the proton counts parameter for each E_p in a 2D histogram, we arrive at an intensity map showing the inferred $\beta^- p$ branching ratio as a function of assumed resonance energy. Figure 5.16 shows this map for Pads B and C. Figure 5.17 shows this map for Pads D and E.

These intensity maps are probability density profiles. Since each pad is operated independently of the others, each map from each pad is an independent measurement of the inferred branching ratio b_p. To combine, a bin-by-bin multiplication of the intensity map for each of the four pads

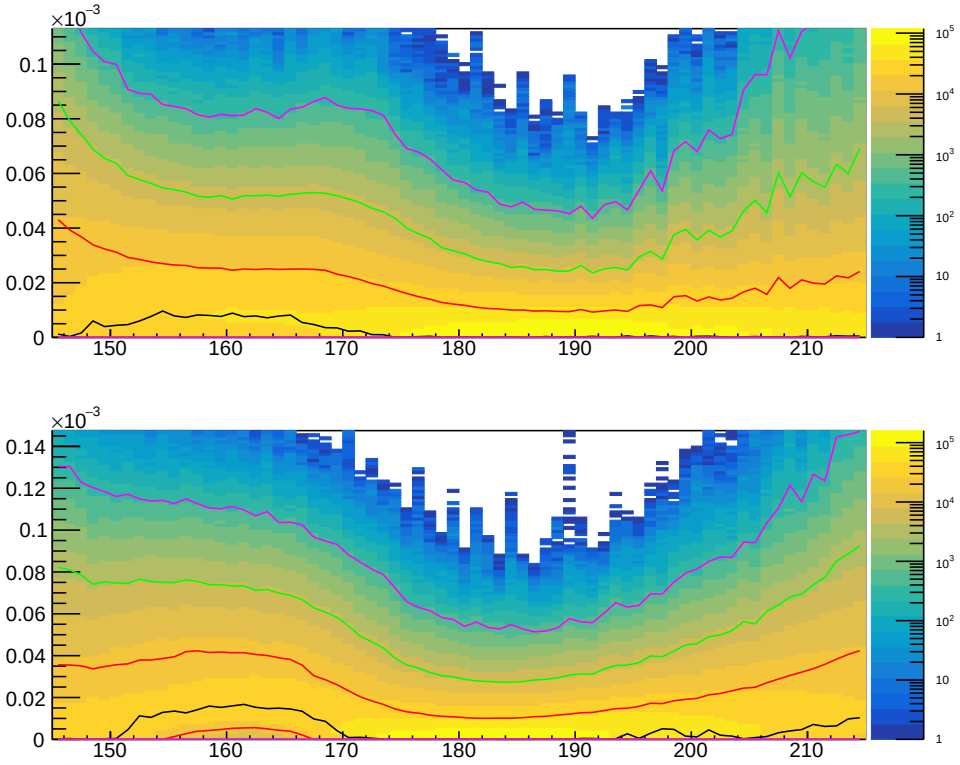

Figure 5.16: Intensity map from the MCMC sampling for Pad B (top) and Pad C (bottom). Inferred proton counts are normalized to a branching ratio and plotted against resonance energy. The black curve shows the most probable value; red shows the 68% confidence interval boundaries; green shows the 95% confidence interval boundaries; purple shows the 99.7% confidence interval boundaries. Pad B is suggestive of a finite value but consistent with a zero value for $E_p < 170$ keV. Above $E_p = 170$ keV, there is no indication of an excess caused by $\beta^- p$. Pad C is suggestive of a finite value but consistent with a zero value for $150 < E_p < 170$ keV and $E_p \gtrsim 200$ keV. Elsewhere, there is no indication of an excess caused by $\beta^- p$.

was performed. To keep the interpretation of probability for an assumption of E_p, the combined probability distribution was normalized to unity for each E_p. The results of this multiplication is shown in Fig. 5.18.

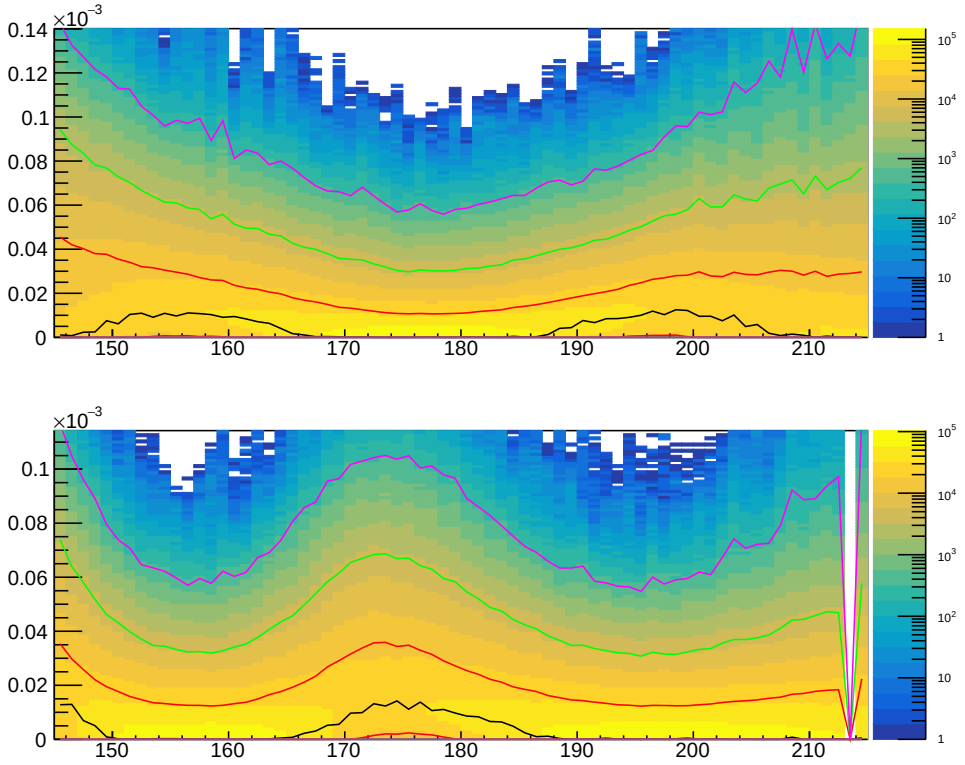

Figure 5.17: Intensity map from the MCMC sampling for Pad D (top) and Pad E (bottom). Inferred proton counts are normalized to a branching ratio and plotted against resonance energy. The black curve shows the most probable value; red shows the 68% confidence interval boundaries; green shows the 95% confidence interval boundaries; purple shows the 99.7% confidence interval boundaries. Pad D is suggestive of a finite value but consistent with a zero value for $150 < E_p < 165$ keV and $185 < E_p < 210$. Pad E is suggestive of a finite value but consistent with a zero value for $E_p < 150$ keV and $165 < E_p < 185$ keV. Above $E_p = 180$ keV, there is no indication of an excess caused by $\beta^- p$.

The energy uncertainty in the region of interest comes primarily from the uncertainty in the pulse height defect of the ^{7}Li* peak which was determined to be $\sim$ 3% in Sec. 4.3, or $\sim$ 8 keV. Additional uncertainty comes from the extrapolation of the energy calibration between the ^{7}Li* peak and full-energy ^{7}Li+α peak. The relative uncertainty from the extrapolation is roughly the uncertainty of the pulse height defect for the full-energy peak, or $\sim$ 2%, measured from the ^{7}Li* peak at $E_p = 241(8)$ keV. The energy uncertainty from the energy extrapolation to a peak at $E_p = 150$ keV would be be less than $\sim$ 2 keV, which is small relative to the $\sim$ 8 keV uncertainty of the location of the ^{7}Li* peak.

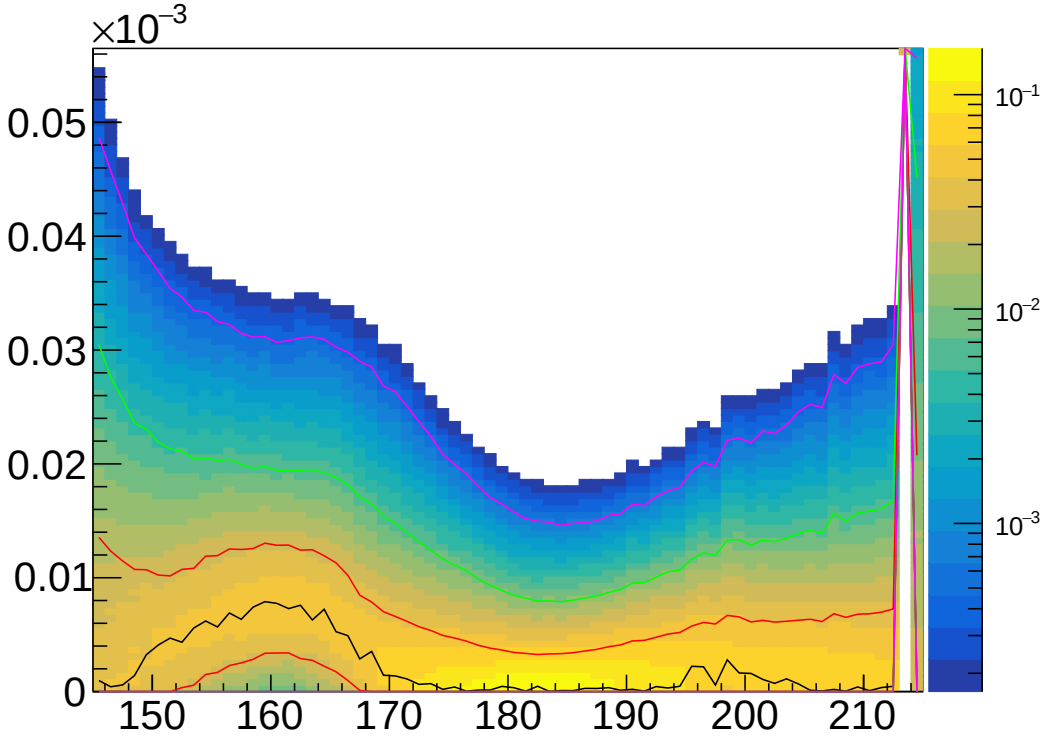

Figure 5.18: Combined intensity map of all four pads. Probability density below $\sim 10^{-4}$/bin is truncated. The black curve shows the most probable value; red shows the 68% confidence interval boundaries; green shows the 95% confidence interval boundaries; purple shows the 99.7% confidence interval boundaries. There is evidence of a $\beta^- p$ -like excess at $E_p \sim 160$ keV.

5.2 Discussion

With the composite heatmap of Fig. 5.18, there is a clear excess at $E_p = 160(8)$ kev with a maximum in the branching ratio intensity of $b_p = 8^{+5}_{-4} \cdot 10^{-6}$. The central value comes from the most intense value and the asymmetric errors come from integrating the most likely values out to 68% of the probability space for the assumed E_p. This is done to preserve the most probable regions in the confidence interval integral. For a further argument for this construction of a confidence interval, see Chapter C.

The choice of intrinsic width Γ is highly correlated with the inferred $\beta^- p$ branching ratio. For all fits, the smaller the Γ, the smaller the inferred branching ratio. The branching ratios shown in Fig. 5.18 are integrated over all values of Γ, some of which are sizable. That is, much of the

uncertainty in this result is driven by our choice of a flat prior in the width Γ for $\Gamma < 30$ keV.

It is also worth noting that Pad E yields slightly different results than the other pads. In Pads B, C, and D, there are small excesses peaking at $b_p \sim 10^{-5}$ from $150 \lesssim E_p \lesssim 170$ keV and Pads C and D have similar or smaller excesses for $E_p > 190$ keV. Pad E, however, has a $b_p \sim 10^{-5}$ excess at $165 \lesssim E_p \lesssim 185$ keV. All pads were treated with the same analysis procedure, from data sorting, to the energy calibration, to statistical inference, so it is hard to ascertain the source of this, if it is significant beyond statistical fluctuations. The effect of a non-statistical energy shift in Pad E would be to lower the composite branching ratio at $E_p = 160(8)$ keV.

5.2.1 Comparison To Other Experiments

Several other experiments have been conducted to understand the ^{11}Be($\beta^- p$) branching ratio. Most directly comparable to our results are those of Ayyad *et al.* (2019) [3], where they reported $E_p = 196(20)$ keV, $\Gamma = 12(5)$ keV and $b_p = 1.3(3) \cdot 10^{-5}$ in a gaseous time projection chamber. The our energy is $\sim 2\sigma$ lower than that reported in Ayyad *et al.* (2019) and our $\beta^- p$ branching ratios are consistent. The newest AMS measurement can only measure a total^{10}Be production rate and their suggested value of the branching ratio was $< 2.2 \cdot 10^{-6}$, which is lower than our measured value.

Additionally, two reaction measurements have been published that provide ^{11}B resonance structure information that we can compare. A measurement of the ^{10}Be$(p, p')^{10}$Be by Ayyad *et al.* (2022) [34] reported observation of a resonance with energy $E_p = 171(20)$ keV, proton width $\Gamma_p = 4.5(11)$ keV, total width $\Gamma_T = 16(3)$ keV. Our energy agrees with this measurement and is more than a factor of two more precise. A measurement of ^{10}Be$(d, n)^{10}$Be+p reported observation of a resonance with energy $E_p = 211(40)$ keV. We are consistent with this second measurement, but that is due to the large 40 keV uncertainty in the resonance energy.

The comparable experimental values are in Tab. 5.1. Our resonance energy $E_p = 160(8)$ keV is consistent with all literature resonance energies. Our measurement of the branching ratio $b_p = 8^{+5}_{-}4 \cdot 10^{-6}$ is consistent with the Ayyad *et al.* $\beta^- p$ measurement and somewhat at odds with

AMS inferred limit by Riisager *et al.*. We are not able to make strong claims about the intrinsic width of the state, however, if the width is determined precisely in the future, then the probability density plots from the analysis of our experimental data can be used to refine the experimental branching ratio.

Reference	E_p (keV)	Γ_p (keV)	BR($\beta^- p$)	production mechanism
Ayyad *et al.* (2019) [3]	196(20)	12(5)	$1.3(3) \cdot 10^{-5}$	$\beta^- p$
Riisager *et al.* [28]	-	-	$< 2.2 \cdot 10^{-6}$	^{10}Be AMS
Ayyad *et al.* (2022) [34]	171(20)	4.5(11)	-	$^{10}\mathrm{Be}(p, p')$
Lopez-Saavedra *et al.* [36]	211(40)	-	-	$^{10}\mathrm{Be}(d, n)^{10}\mathrm{Be}{+}p$

Table 5.1: Summary of experimental results for the branching ratio of the $^{11}\mathrm{Be}(\beta^- p)$ decay and candidate resonant state properties.

5.2.2 Comparison To Theory

A number of theory models have been applied to this question of a $\beta^- p$ branching ratio larger than expected a decade ago. Different models can calculate different physical observables and patterns between observables. The following papers report calculations of the $\beta^- p$ branching ratio: Baye and Tursunov ($b_p \sim 3 \cdot 10^{-8}$) [18], Volya ($b_p \sim 5 \cdot 10^{-10}$, unless there is an unpredicted resonant state then $b_p < 1 \cdot 10^{-7}$) [29], Okołowicz *et al.* ($b_p \sim 3 \cdot 10^{-7}$) [85], Elkamhawy *et al.* ($b_p = 4.9^{+5.6}_{-2.9}(\mathrm{ex.})^{+4.0}_{-0.8}(\mathrm{th.})$, assuming the resonant state parameters and errors of [3]) [32, 86], and Atkinson *et al* ($b_p = 1.3(5) \cdot 10^{-6}$) [33] predict branching ratios for the $^{11}\mathrm{Be}(\beta^- p)$ decay. These model predictions are summarized in Table 5.2.

Generally, theory predicts small widths $\Gamma < 10$ keV and small branching ratios $b_p < 10^{-5}$. Many of these branching ratios are smaller than the precision of our measurement and are effectively zero-valued, which our data excludes at more than 68% confidence at $E_p = 160$ keV. Elkamhawy *et al.* (2022) [86] is a follow-up paper to the 2021 paper [32] that goes into detail regarding these effective field theory calculations, which predict the relationship between the resonance energy E_p, width Γ_p, and the branching ratio b_p. Especially given this data's correlation between the width Γ_p and branching ratio b_p, more comparison is needed.

Reference	E_p (keV)	Γ_p (keV)	BR($\beta^- p$)
Baye and Tursunov [18]	~ 150 keV	-	$\sim 3 \cdot 10^{-8}$
Volya [29]	-	-	$\sim 5 \cdot 10^{-10}$
Okołowicz *et al.* (2020) [30]	~ 142 keV	-	-
Okołowicz *et al.* (2022) [85]	~ 160 keV	-	$\sim 3 \cdot 10^{-7}$
Elkamhawy *et al.* (2021) [32]	(196)*	$9.0^{+4.8}_{-3.3}$(ex.)$^{+5.3}_{-2.2}$(th.)	$4.9^{+5.6}_{-2.9}$(ex.)$^{+4.0}_{-0.8}$(th.)
Atkinson *et al.* [33]	-	-	$1.3(5) \cdot 10^{-6}$
Le Ahn *et al.* [87]	~ 182	~ 6	-

Table 5.2: Summary of theory predictions for the branching ratio of the ^{11}Be($\beta^- p$) decay and candidate intermediary resonant state properties.
* The energy of Elkamhawy *et al.* (2021) was set to the experimental value of [3]

In terms of energy predictions, the $\beta^- p$-like excess in our data is found at $E_p \sim 160(8)$ keV. The Baye and Tursunov value is not a resonance energy, so we'll disregard. Our resonance energy is similar to Okołowicz *et al.*, especially the 2022 value of $E_p \sim 160$ keV, which includes β decay feeding weights. Our value is somewhat low compared to the value of Le Ahn *et al.* ($E_p \sim 182$ keV), but there is no uncertainty reported from that calculation.

CHAPTER 6

CONCLUSIONS: INTERPRETING THIS WORK AND FUTURE EFFORTS

6.1 Conclusions

Concluding, the determination of the ^{11}Be($\beta^- p$) branching ratio is strongly motivated. The novel $\beta^- p$ decay is a probe of the three-fold near-threshold structure in ^{11}B. (The thresholds for n, p, and ^{3}H are all similar in ^{11}B.) This near-threshold structure likely has complex behavior, explaining the difficulty in theoretical calculations to report a consistent $\beta^- p$ branching ratio and the limited number of experimental results to report consistent partial widths of the participating state in ^{11}B. Prior to our measurement, only one direct observation of the $\beta^- p$ from ^{11}Be($\beta^- p$) had been reported and it suggested a finite value of the branching ratio. This is inconsistent with the most recent indirect measurement result inferred by counting the ^{10}Be residues which sets an upper limit on the production of ^{10}Be from ^{11}Be. The ^{11}Be($\beta^- p$) decay yields a ^{10}Be reside, so ^{11}Be($\beta^- p$) decay can explain the presence of ^{10}Be in the decay products of a sample of ^{11}Be. An excess of ^{10}Be production relative to ^{11}Be($\beta^- p$) decay is a signature of the hypothetical dark decay of bound neutrons. The converse, where ^{11}Be($\beta^- p$) is observed in excess of ^{10}Be production, defies physical explanation. As new measurements are performed, should the ^{10}Be production rate be deemed in excess of the ^{11}Be($\beta^- p$) decay rate one can again consider the hypothetical dark decay of the halo neutron in ^{11}Be.

The β^- -delayed charged particle spectrum of ^{11}Be was measured using the GADGET system at the National Superconducting Cyclotron Laboratory. We carefully characterized portions of the significant ^{11}Be($\beta^- \alpha$) background and our expected $\beta^- p$ signal, guided by R-matrix calculations and γ-ray coincidences with $\beta^- \alpha$ decays. We performed a search for a $\beta^- p$ -like excess in the β^- -delayed charged particle spectrum using a Bayesian statistical model, sampled by a Markov Chain Monte Carlo algorithm. Here, we report the second direct measurement of ^{11}Be($\beta^- p$). We found a $\sim 2\sigma$ $\beta^- p$ excess at resonant energy $E_p = 160(8)$ keV and branching ratio $b_p = 8^{+5}_{-4} \cdot 10^{-6}$,

which is consistent with the experimental literature. The energy of the $\beta^- p$ excess is compatible with resonances predicted by many structure models and, similar to the other $\beta^- p$ measurement, the measured branching ratio is larger than most models predict.

6.2 Outlook

Looking forward, several types of measurements could be performed to further investigate the interesting ^{11}Be($\beta^-\alpha$) decay:

Old ^{7}Li(α,α') scattering measurements could be repeated with very fine precision around 150-200 keV above the ^{11}B proton threshold. A recent Ph.D. project proposal at Michigan State University discussed performing such a measurement at Notre Dame in the near future. If the structure of ^{11}B around E_x = 11.4 MeV is multi-faceted, state selection may be probe- sensitive and the (α, α') scattering may yield not additional, but *unique* information.

The $\beta^- p$ from ^{11}Be could be remeasured. Our present measurement was systematically limited. The MICROMEGAS pad plane of GADGET was recently upgraded from the 13 pixel design discussed here to a new pad plane geometry with 1024 pixels. GADGET II, as it is called, can operate as a time projection chamber, which has demonstrated selective particle identification. Utilization may reduce the large β^- and $\beta^-\alpha$ backgrounds we contended with and limit the systematic uncertainties related to their modeling if a ^{11}Be measurement with GADGET II were performed.

The indirect measurements of the ^{11}Be($\beta^- p$) branching ratio with AMS could be improved. The indirect AMS ^{11}Be($\beta^- p$) branching ratio limit comes from the collection sample yielding the smallest branching ratio; other samples measured more than two orders of magnitude larger abundances of ^{10}Be, which the authors contend was due to molecular contamination of the ^{11}Be$^+$ sample beam with ^{10}BeH$^+$, which has a relative mass difference of $\sim 3 \cdot 10^{-5}$ from ^{11}Be$^+$. Standard magnetic cleaning of cocktail beams cannot separate these two ions and the techniques used in the past to produce intense beams of ^{11}Be will also produce ^{10}Be. An improvement to the AMS measurement could be to use some technique to purify sample beam against ^{10}BeH$^+$. Two such

techniques could be mass filtering using a Multi-Reflection Time-Of-Flight mass spectrometer or charge breeding the ^{11}Be beam to a high charge state, which would break any possible molecules. Such schemes suffer beam intensity losses, but new rare isotope production facilities may have the ^{11}Be production capability to suffer these losses and still deliver enough ^{11}Be to measure the minuscule branching ratios predicted by many theoretical models.

Changing focus, one could perform direct measurements of the W-value of modern detector gas mixtures at $\sim$ keV/u beam energies, similar to the work done in the 1960s, 1970s, and 1980s on chemically pure and tissue equivalent gas. It would seem that there is a gap in the scientific literature here and the model to parameterize detector gas behavior from its constituents is not well tested at very low energies or across elemental beam species. At these low beam energies, the beam velocity approaches that of the classical bound-electron velocity, so it is hard to imagine the absence of chemical effects in the beam stopping and ionization production.

Finally, another bound-neutron dark decay candidate was ^{15}C. One nice feature of ^{15}C is that the $^{15}\mathrm{C}(\beta^- p)$ decay is energetically forbidden, so the generation of ^{14}C from ^{15}C is a clear signal of a bound-neutron dark decay. However, ^{14}C is naturally abundant and presents an obvious hazard of a false detection. Additionally, the relative mass difference between $^{14}\mathrm{CH}^+$ and $^{15}\mathrm{C}^+$ is also $\sim 3 \cdot 10^{-5}$, so the difficulties of the ^{11}Be AMS measurements of removing a daughter-containing molecule from the beam holds true in ^{15}C. The AMS sample beam preparation techniques proposed for a re-measurement of $^{11}\mathrm{Be} \longrightarrow {}^{10}\mathrm{Be}$ could also be utilized with ^{15}C to reduce ^{14}C background in AMS sample collection.

APPENDICES

APPENDIX A

NSCL E18507

A.1 Historical GADGET Individual-Pad Resolution

This appendix section shows the historical GADGET peak resolution used to estimate the detector response in E18507.

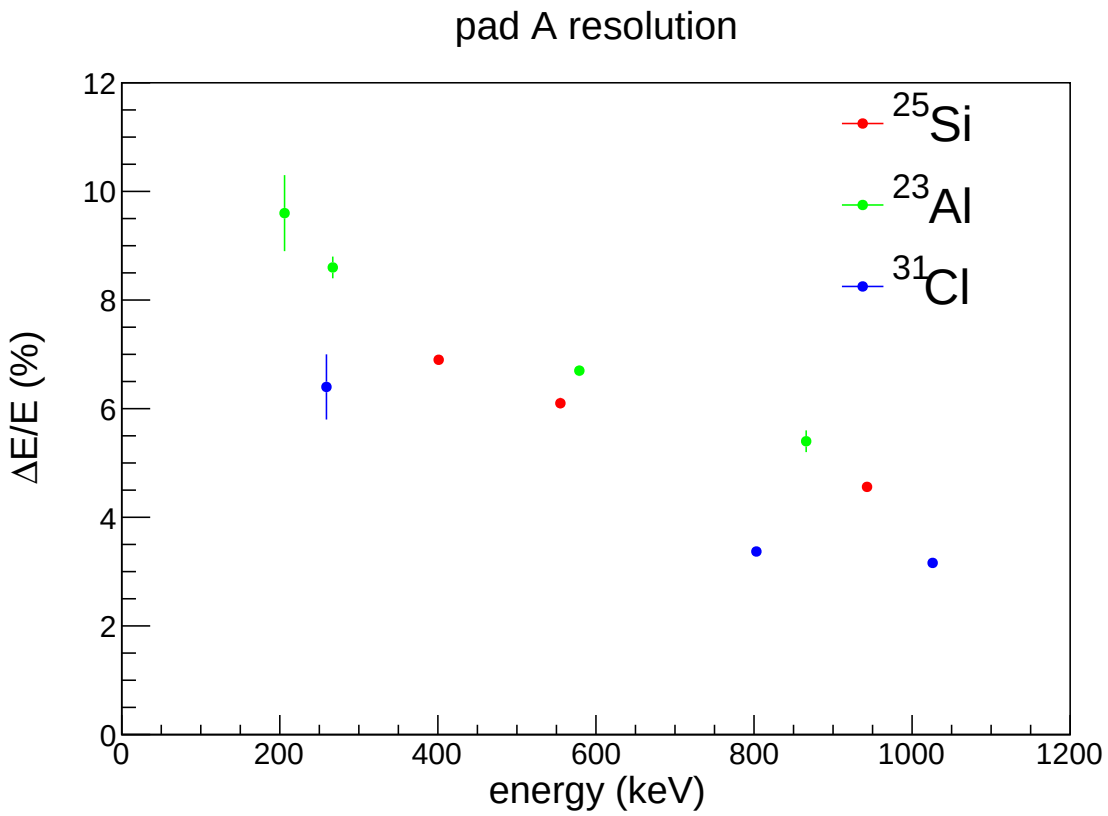

Figure A.1: Full width at half maximum energy resolution of GADGET Pad A in previous experiments [6, 7, 8]. Error bars not visible are smaller than the marker. Figure credit Moshe Friedman.

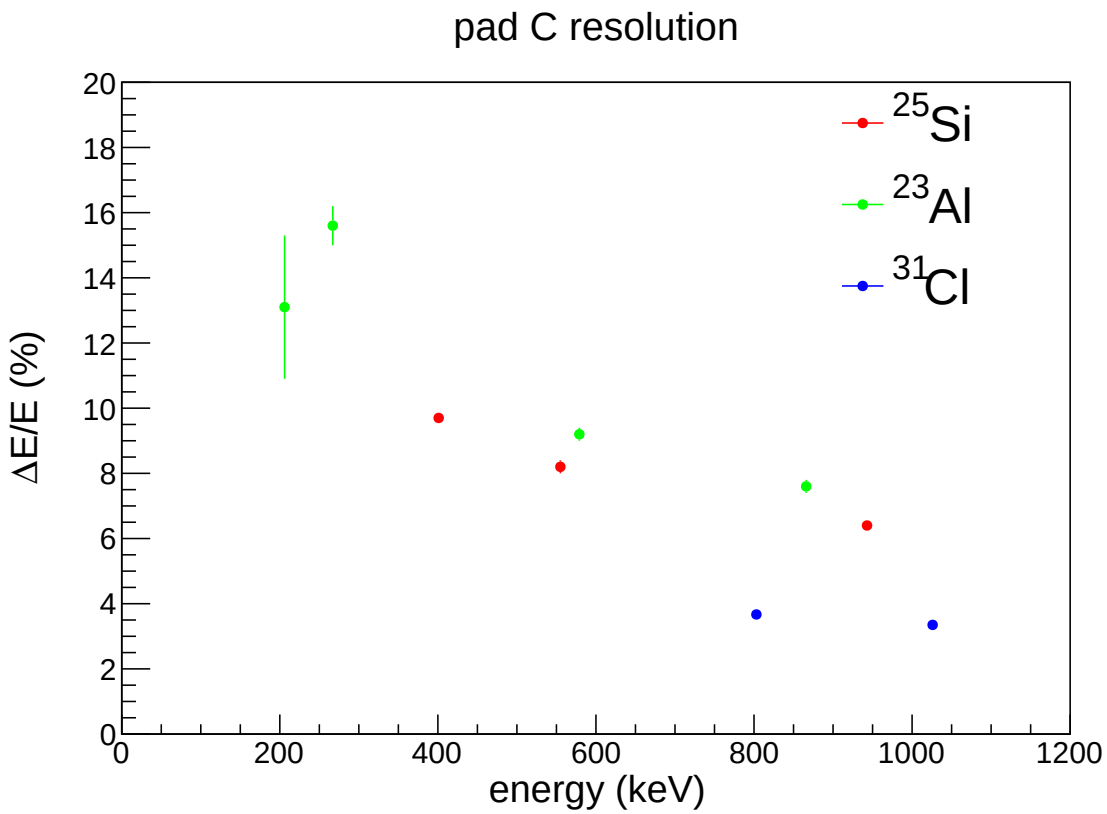

Figure A.2: Full width at half maximum energy resolution of GADGET Pad C in previous experiments [6, 7, 8]. Error bars not visible are smaller than the marker. Figure credit Moshe Friedman.

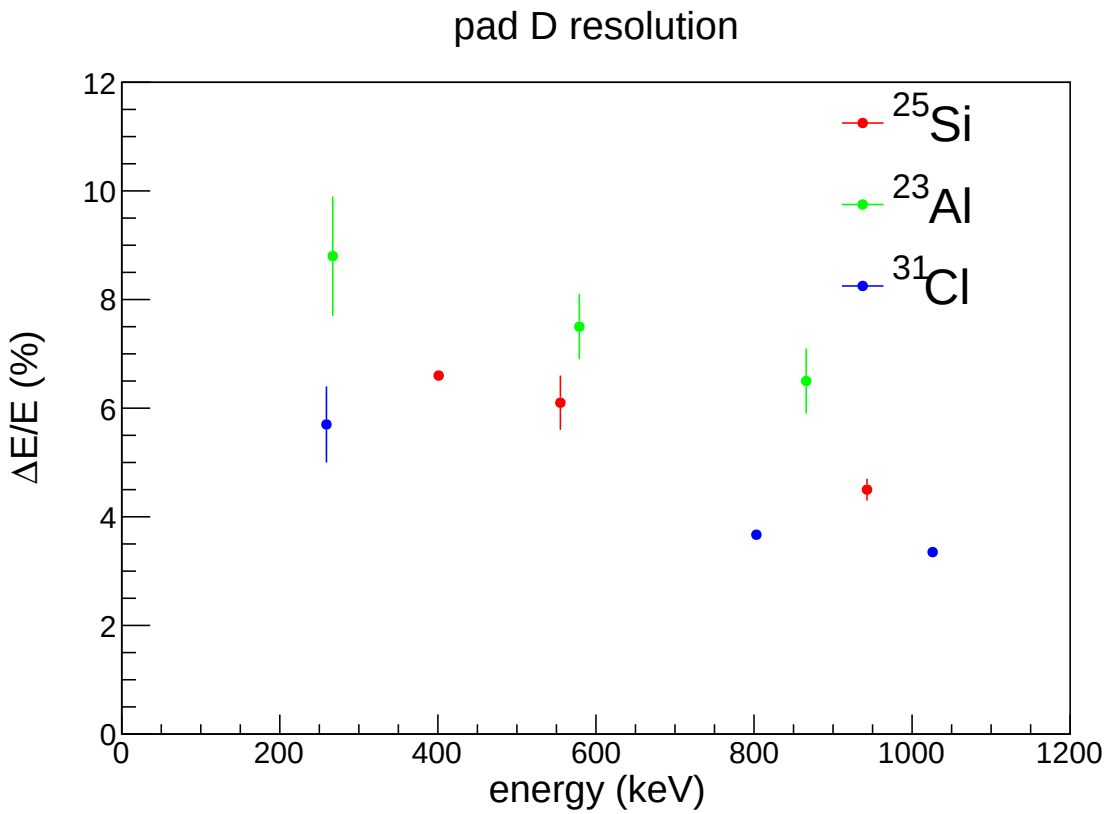

Figure A.3: Full width at half maximum energy resolution of GADGET Pad D in previous experiments [6, 7, 8]. Error bars not visible are smaller than the marker. Figure credit Moshe Friedman.

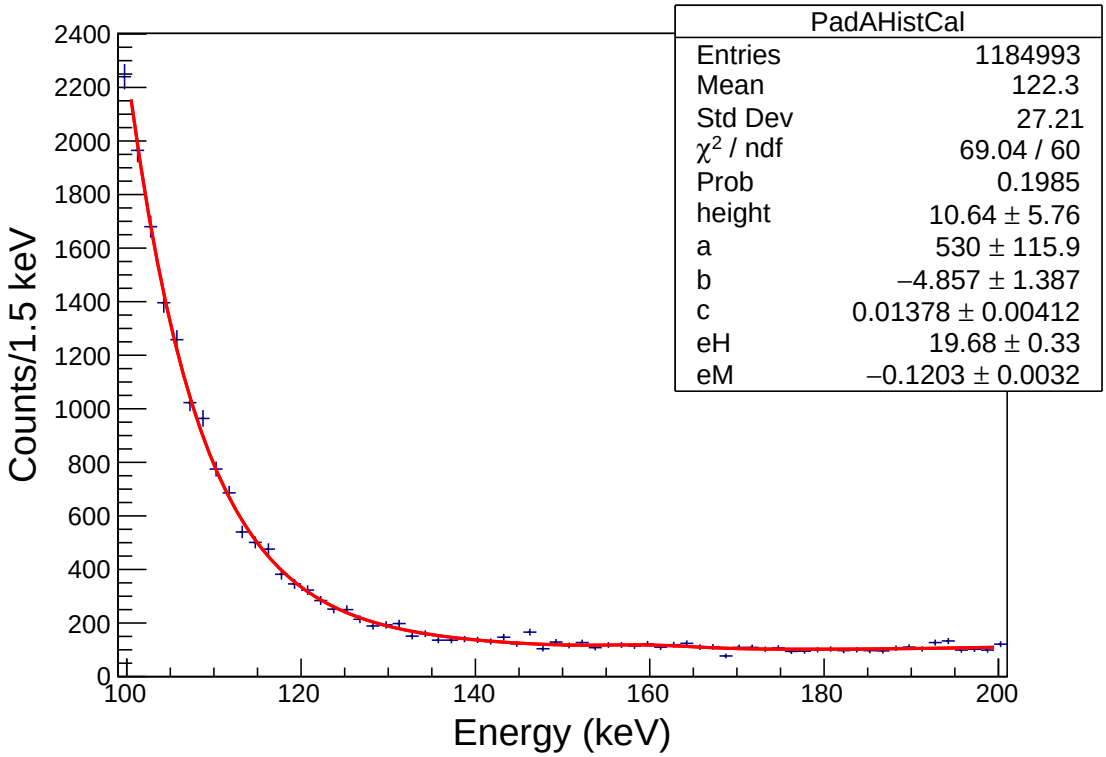

Figure A.4: Data of Pad A from E18507. The fit function is the sum of an exponential, quadratic polynomial, and Gaussian peak. The peak width is described in text and peak center is fixed to 160 keV.

A.2 Individual Pad Fits in E18507

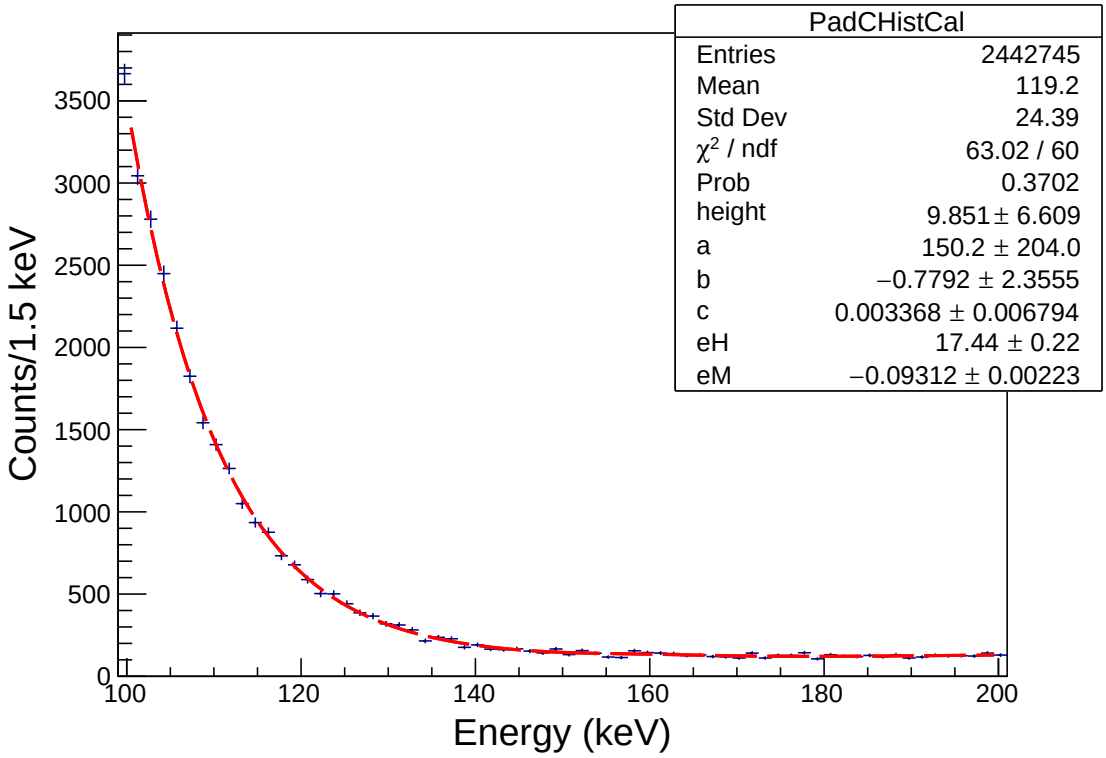

Figure A.5: Data of Pad C from E18507. The fit function is the sum of an exponential, quadratic polynomial, and Gaussian peak. The peak width is described in text and peak center is fixed to 160 keV.

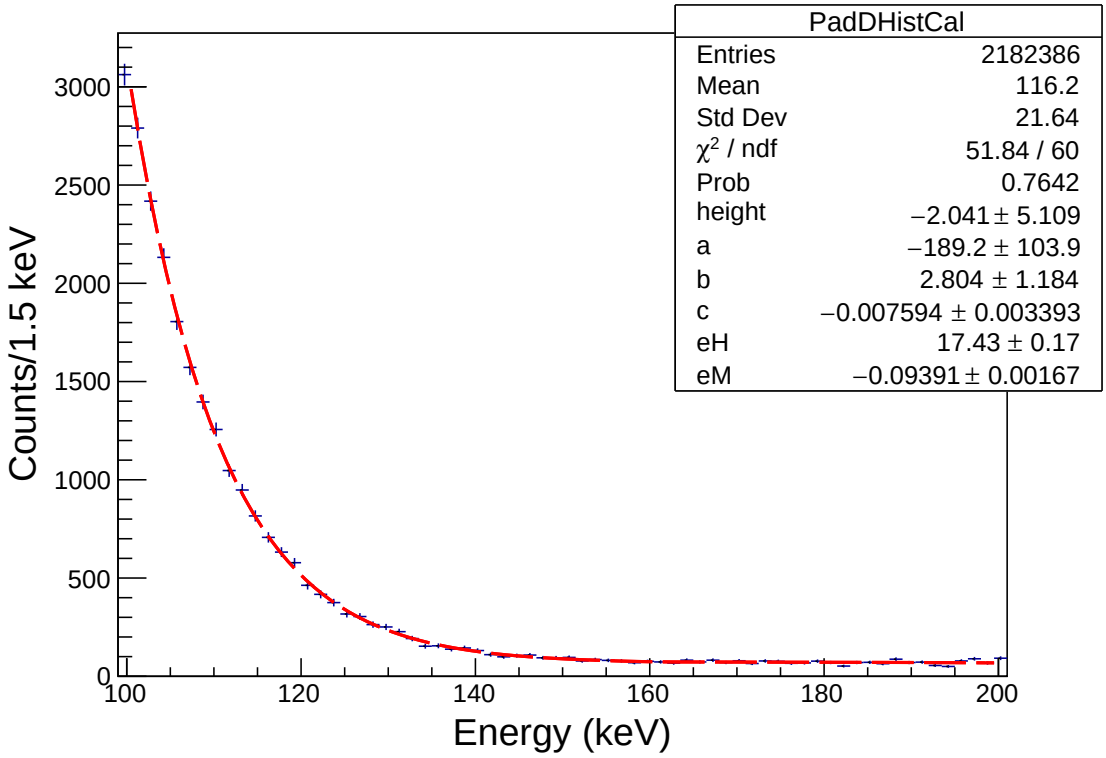

Figure A.6: Data of Pad D from E18507. The fit function is the sum of an exponential, quadratic polynomial, and Gaussian peak. The peak width is described in text and peak center is fixed to 160 keV.

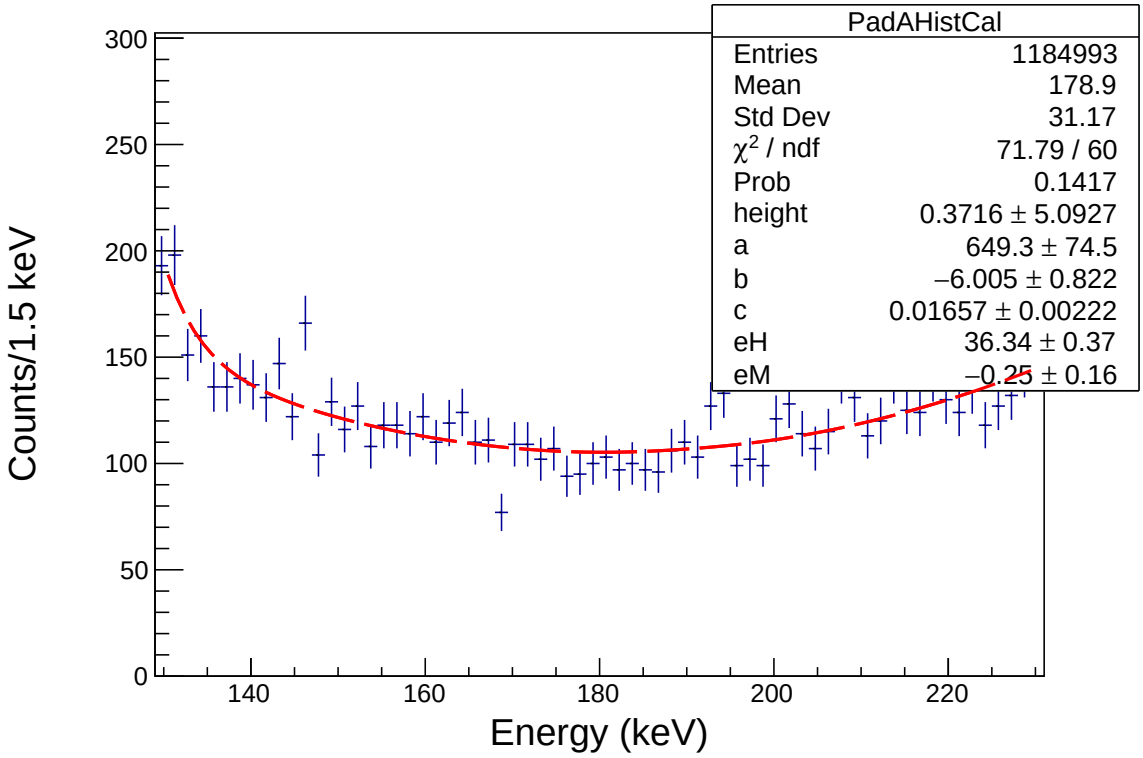

Figure A.7: Data of Pad A from E18507. The fit function is the sum of an exponential, quadratic polynomial, and Gaussian peak. The peak width is described in text and peak center is fixed to 190 keV.

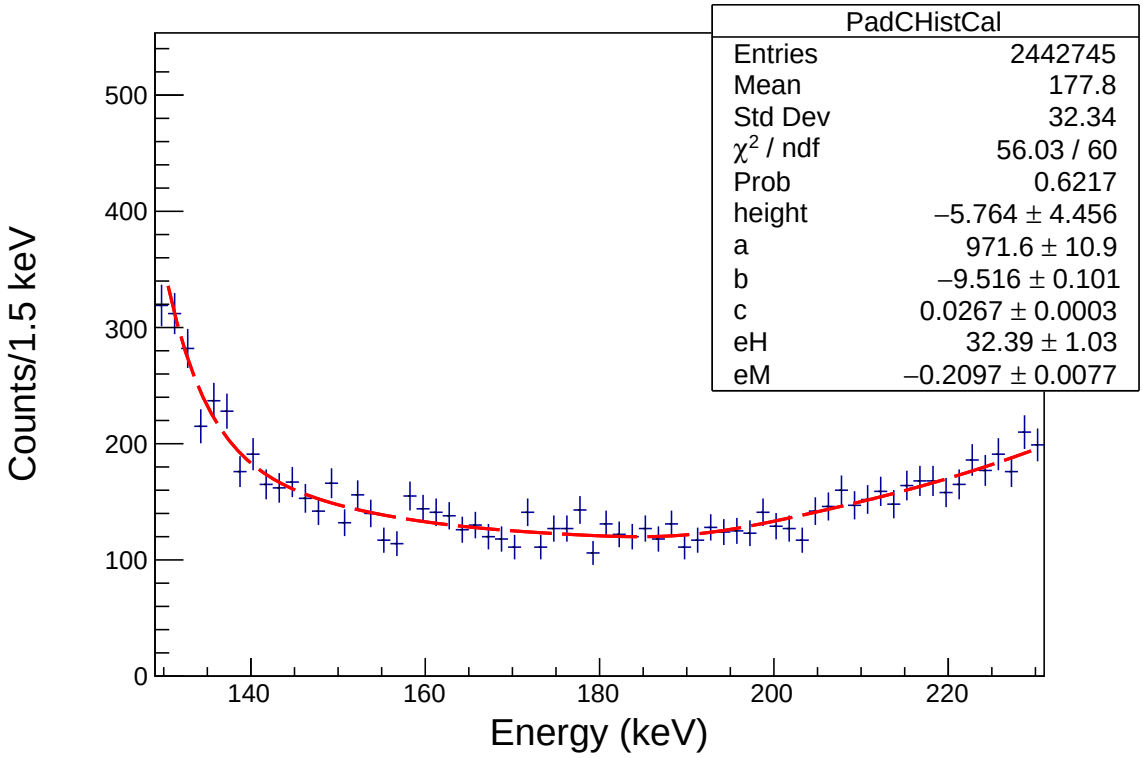

Figure A.8: Data of Pad C from E18507. The fit function is the sum of an exponential, quadratic polynomial, and Gaussian peak. The peak width is described in text and peak center is fixed to 190 keV.

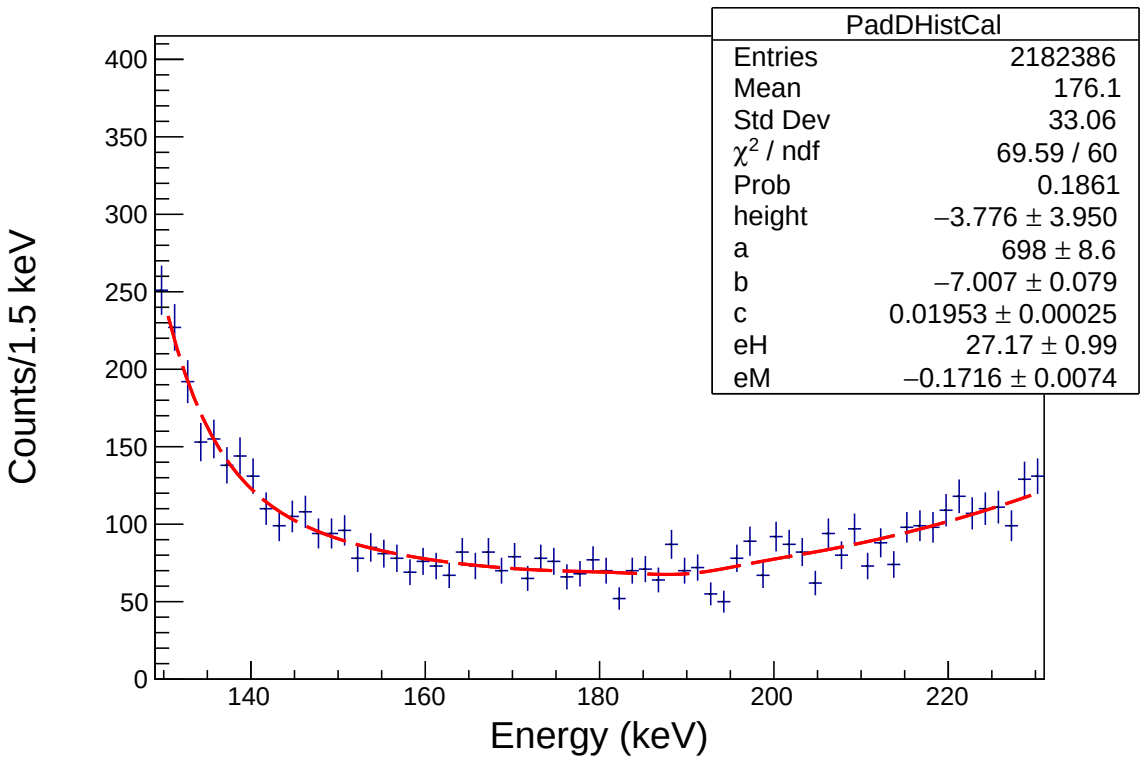

Figure A.9: Data of Pad D from E18507. The fit function is the sum of an exponential, quadratic polynomial, and Gaussian peak. The peak width is described in text and peak center is fixed to 190 keV.

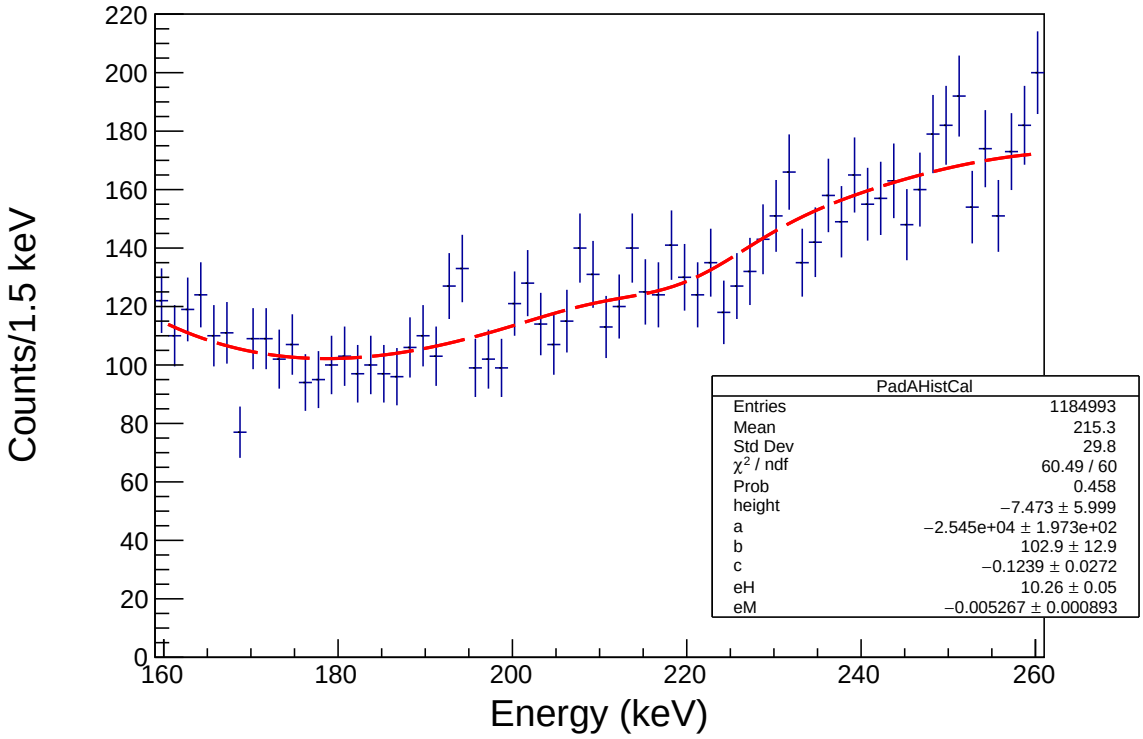

Figure A.10: Data of Pad A from E18507. The fit function is the sum of an exponential, quadratic polynomial, and Gaussian peak. The peak width is described in text and peak center is fixed to 220 keV.

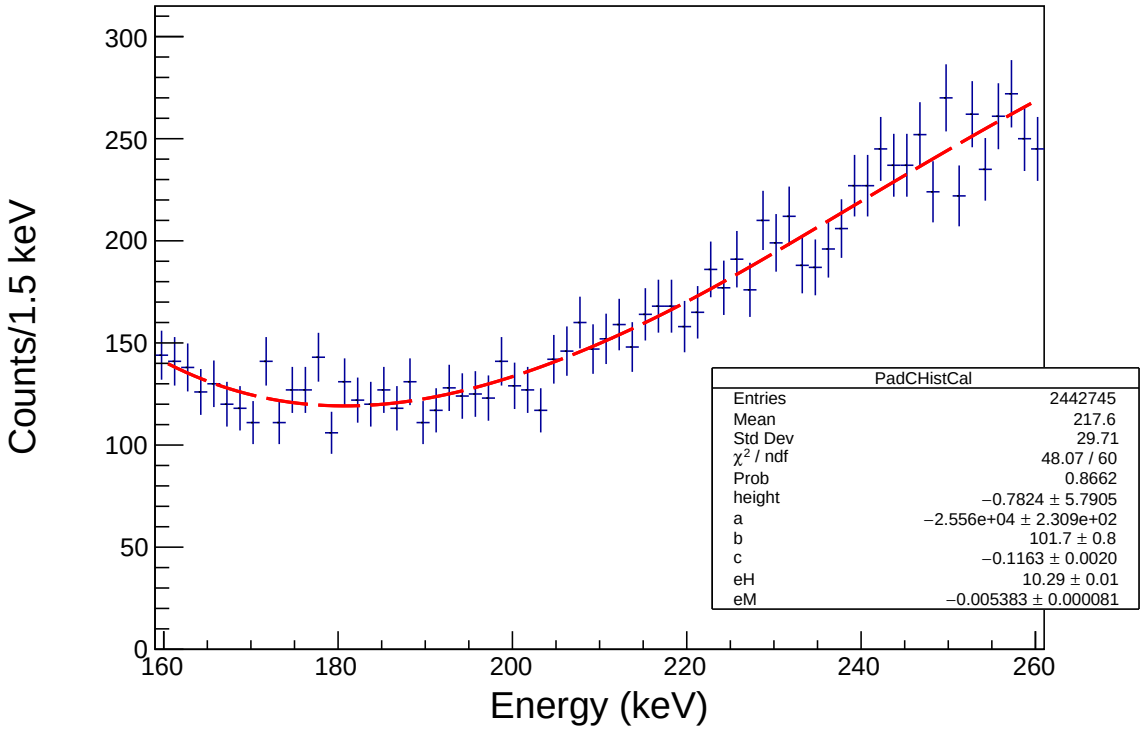

Figure A.11: Data of Pad C from E18507. The fit function is the sum of an exponential, quadratic polynomial, and Gaussian peak. The peak width is described in text and peak center is fixed to 220 keV.

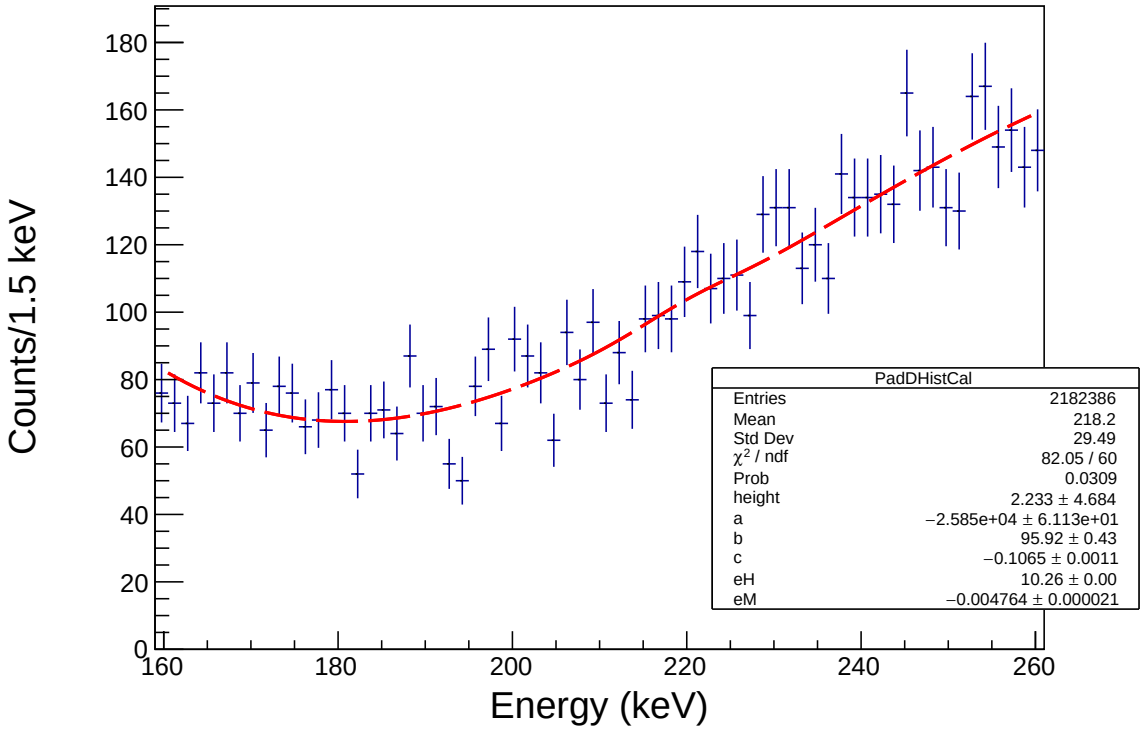

Figure A.12: Data of Pad D from E18507. The fit function is the sum of an exponential, quadratic polynomial, and Gaussian peak. The peak width is described in text and peak center is fixed to 220 keV.

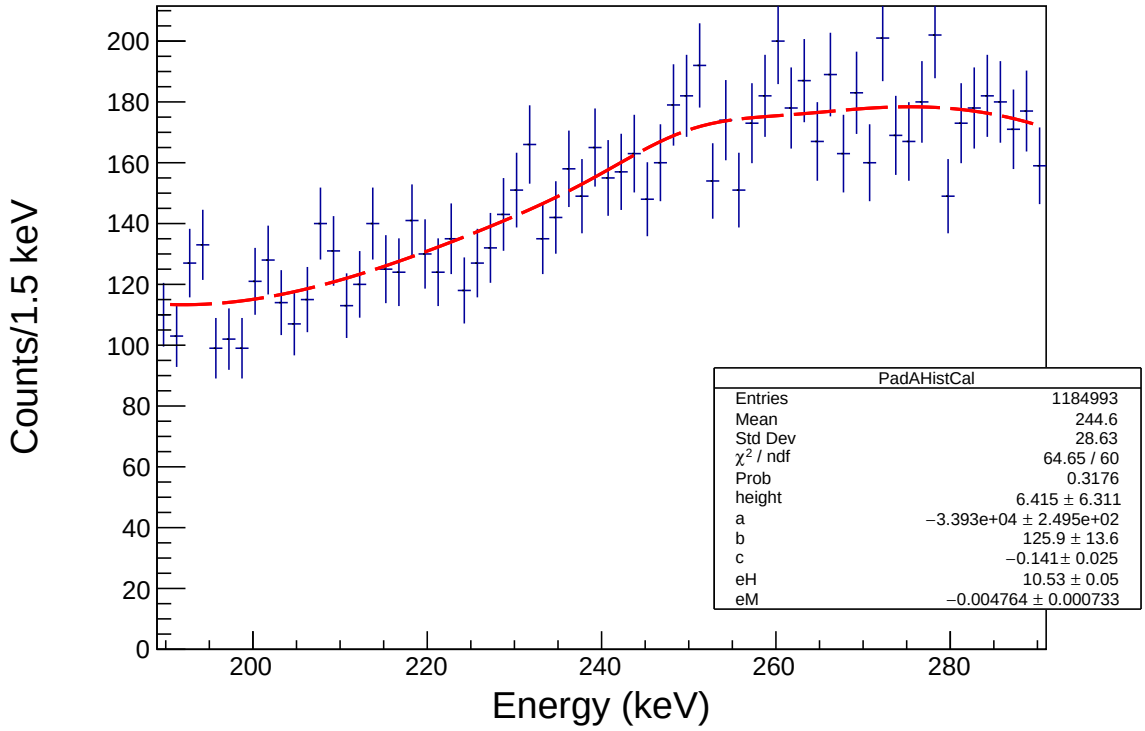

Figure A.13: Data of Pad A from E18507. The fit function is the sum of an exponential, quadratic polynomial, and Gaussian peak. The peak width is described in text and peak center is fixed to 250 keV.

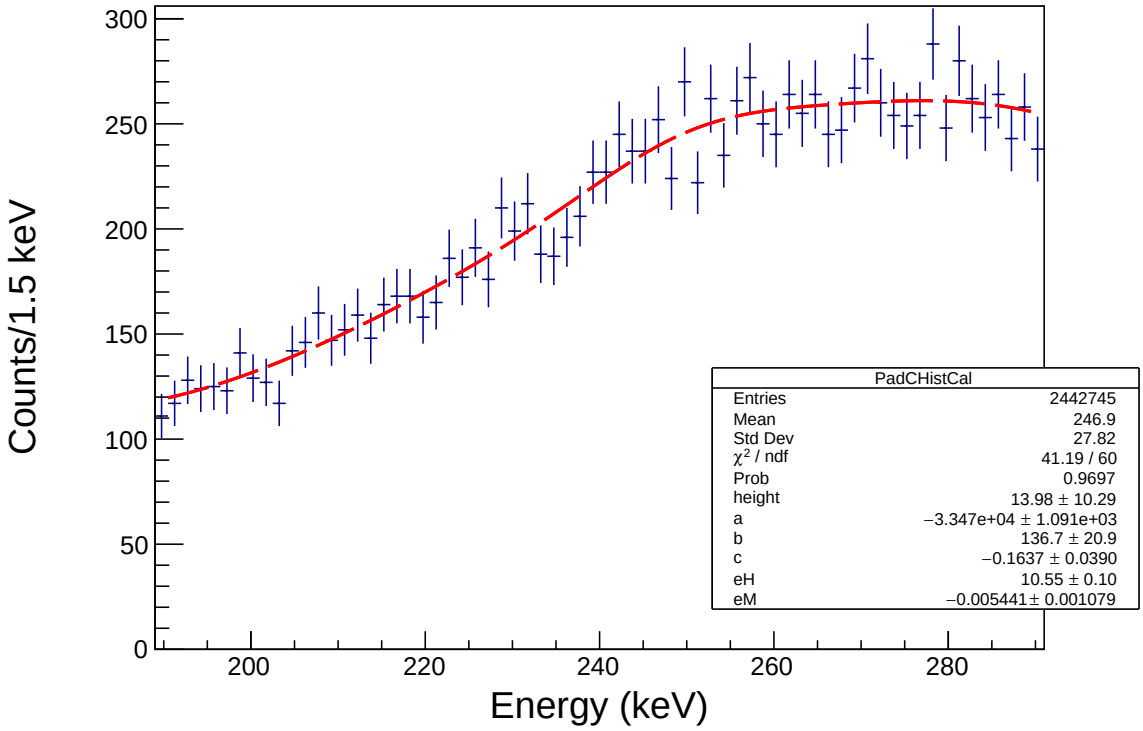

Figure A.14: Data of Pad C from E18507. The fit function is the sum of an exponential, quadratic polynomial, and Gaussian peak. The peak width is described in text and peak center is fixed to 250 keV.

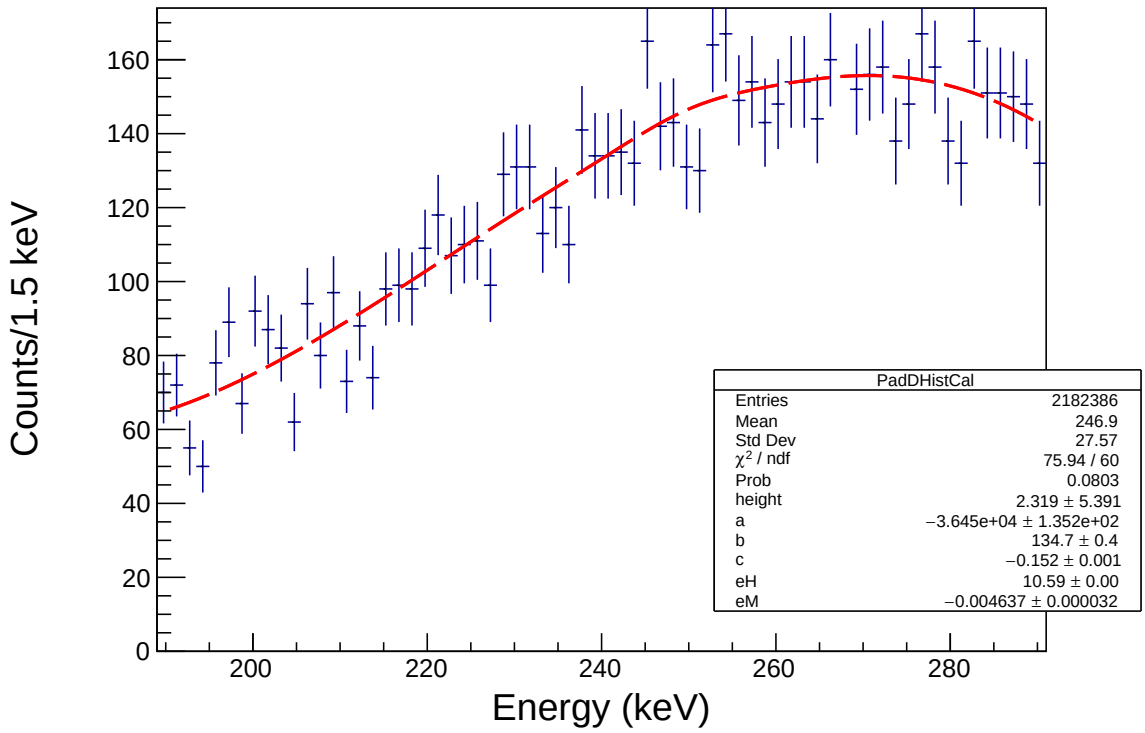

Figure A.15: Data of Pad C from E18507. The fit function is the sum of an exponential, quadratic polynomial, and Gaussian peak. The peak width is described in text and peak center is fixed to 250 keV.

APPENDIX B

NSCL E19030

B.1 Limitations of E18507 Analysis

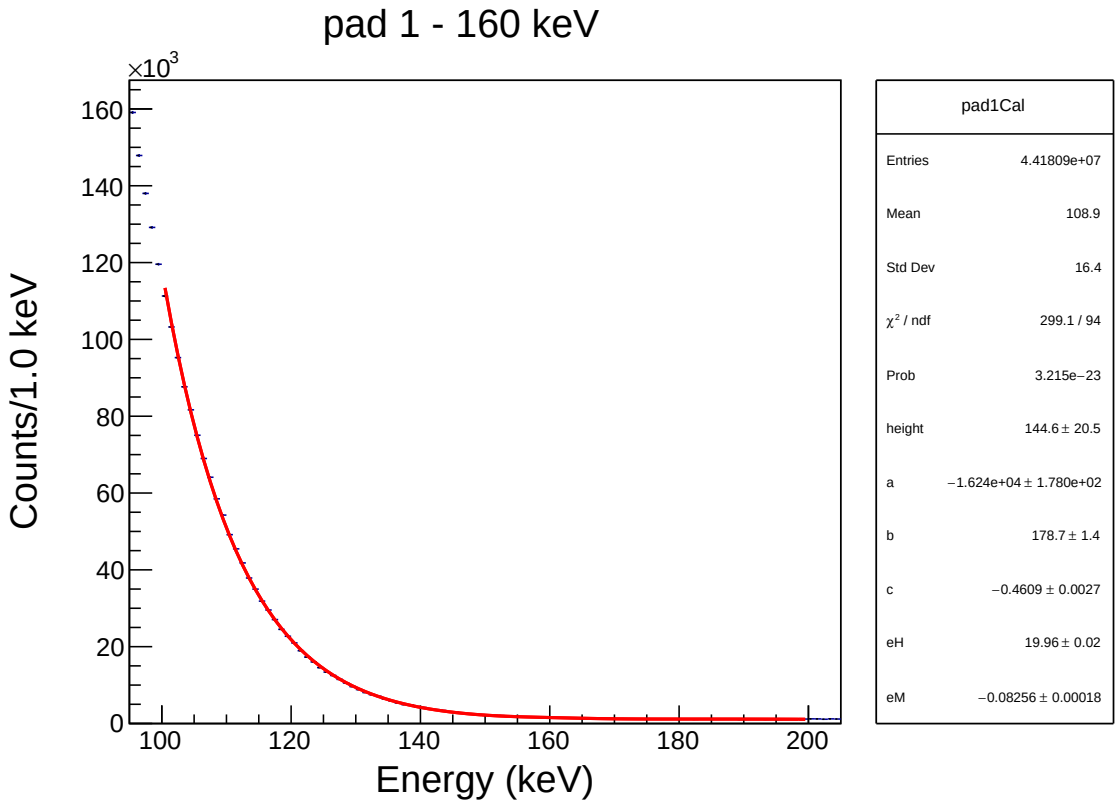

Figure B.1: Data of Pad B from E19030. The fit function is the sum of an exponential, quadratic polynomial, and Gaussian peak. The peak width is described in text and peak center is fixed to 160 keV.

B.2 Exponential + Flat + Voigt

B.3 2Expoential + Flat + 2 Voigt

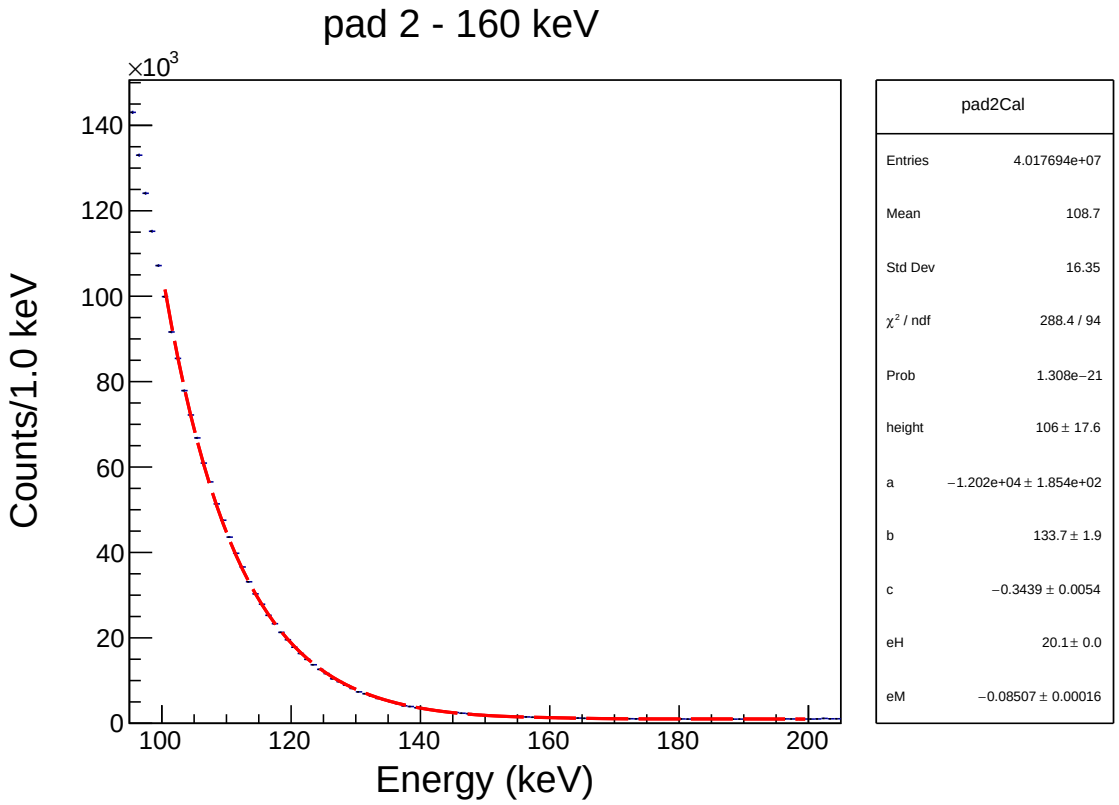

Figure B.2: Data of Pad C from E19030. The fit function is the sum of an exponential, quadratic polynomial, and Gaussian peak. The peak width is described in text and peak center is fixed to 160 keV.

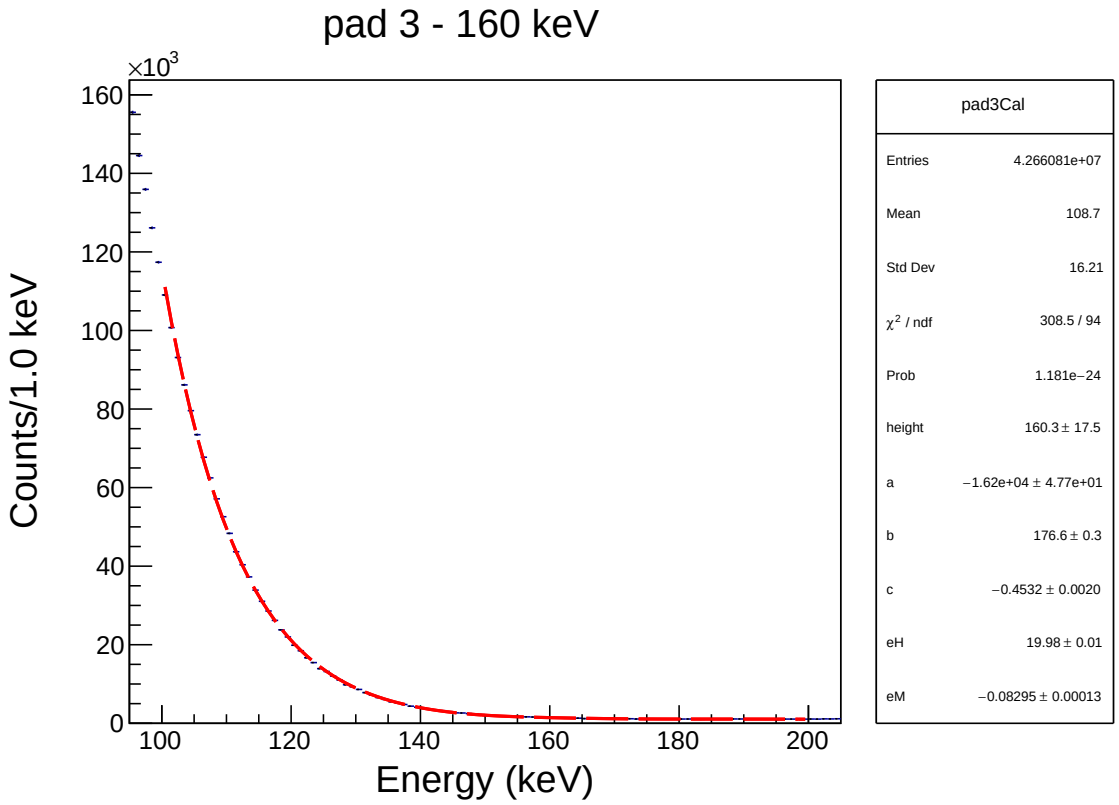

Figure B.3: Data of Pad D from E19030. The fit function is the sum of an exponential, quadratic polynomial, and Gaussian peak. The peak width is described in text and peak center is fixed to 160 keV.

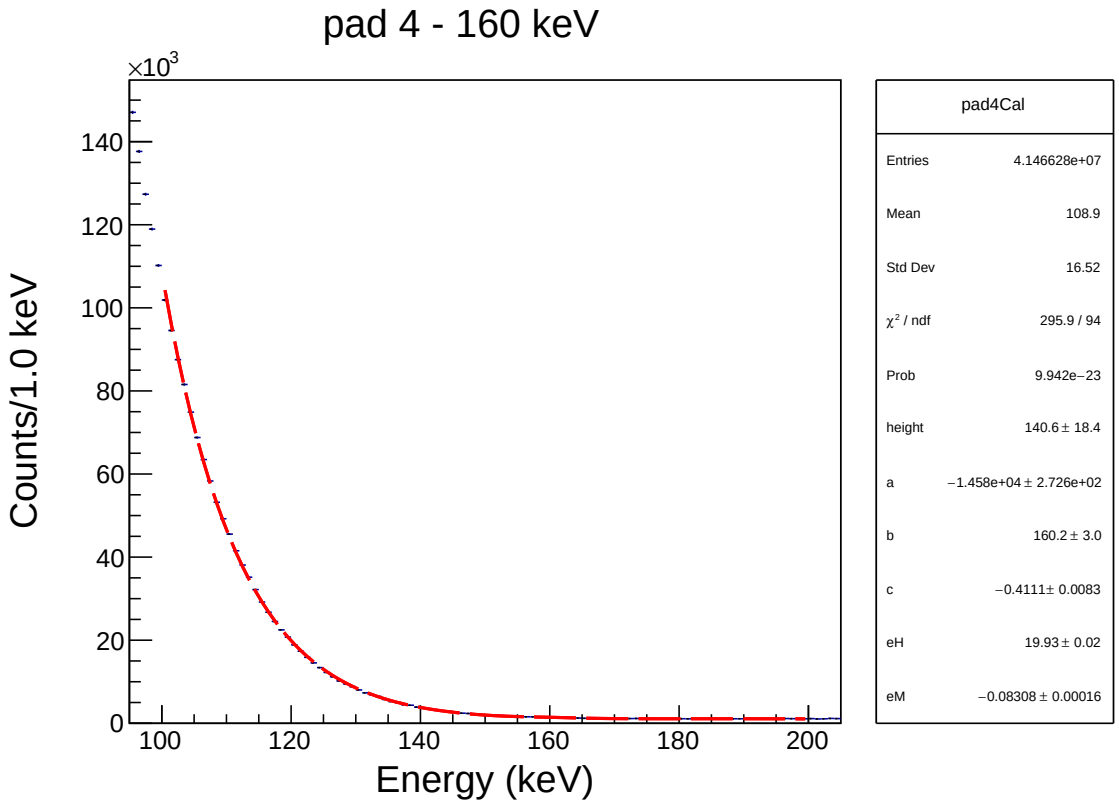

Figure B.4: Data of Pad E from E19030. The fit function is the sum of an exponential, quadratic polynomial, and Gaussian peak. The peak width is described in text and peak center is fixed to 160 keV.

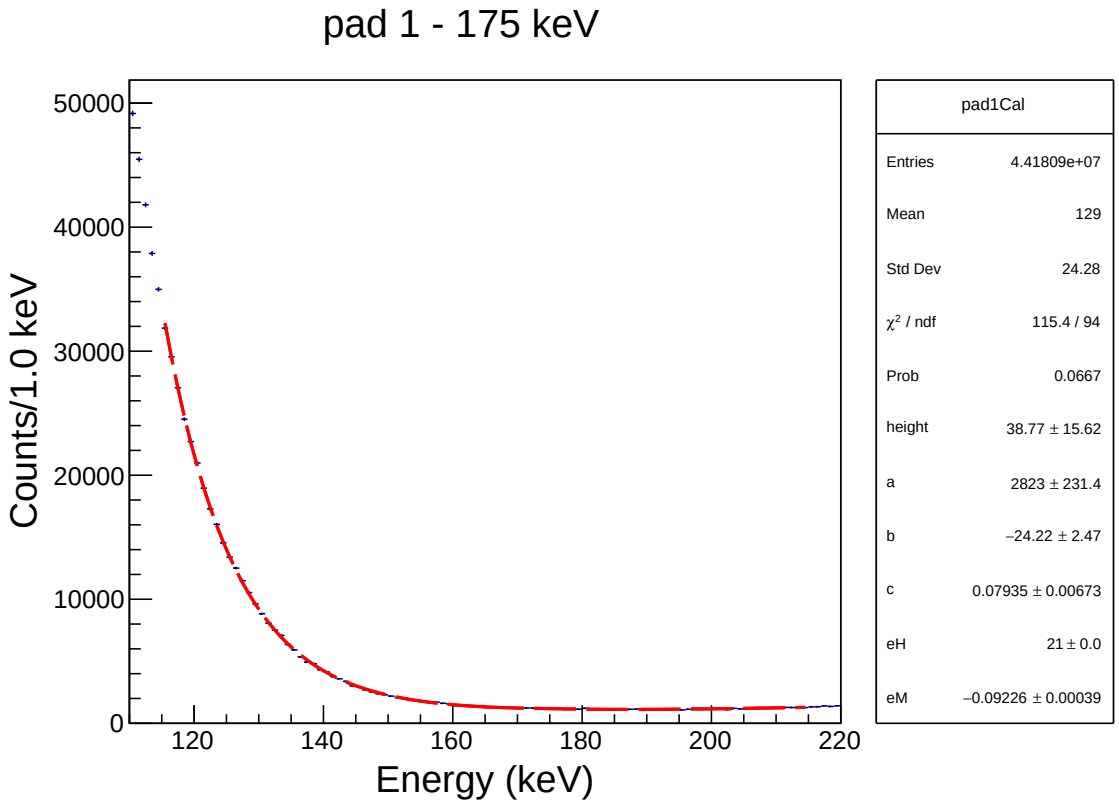

Figure B.5: Data of Pad B from E19030. The fit function is the sum of an exponential, quadratic polynomial, and Gaussian peak. The peak width is described in text and peak center is fixed to 175 keV.

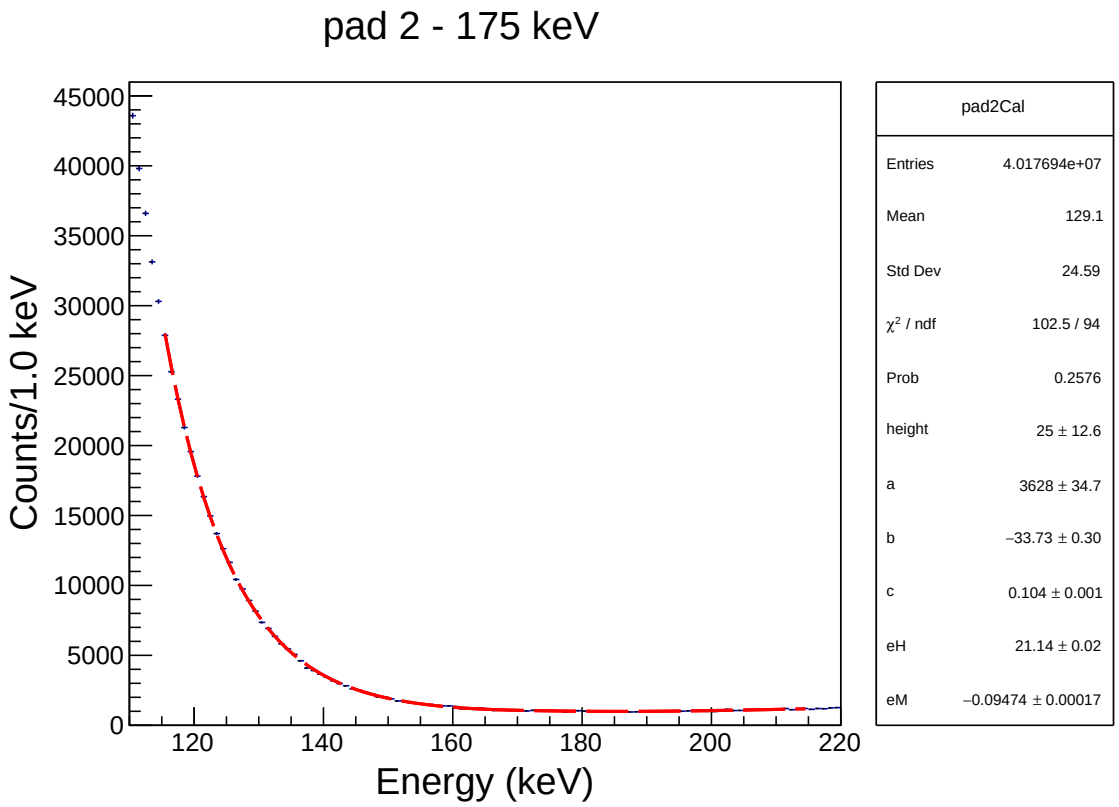

Figure B.6: Data of Pad C from E19030. The fit function is the sum of an exponential, quadratic polynomial, and Gaussian peak. The peak width is described in text and peak center is fixed to 175 keV.

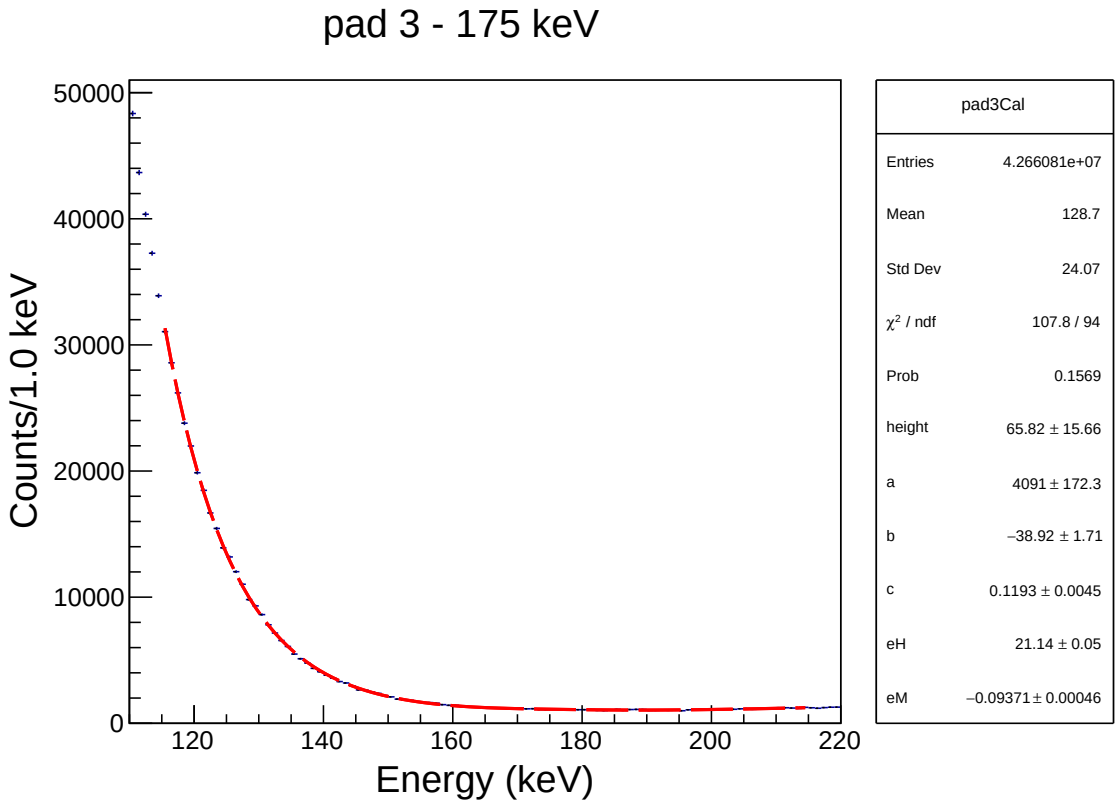

Figure B.7: Data of Pad D from E19030. The fit function is the sum of an exponential, quadratic polynomial, and Gaussian peak. The peak width is described in text and peak center is fixed to 175 keV.

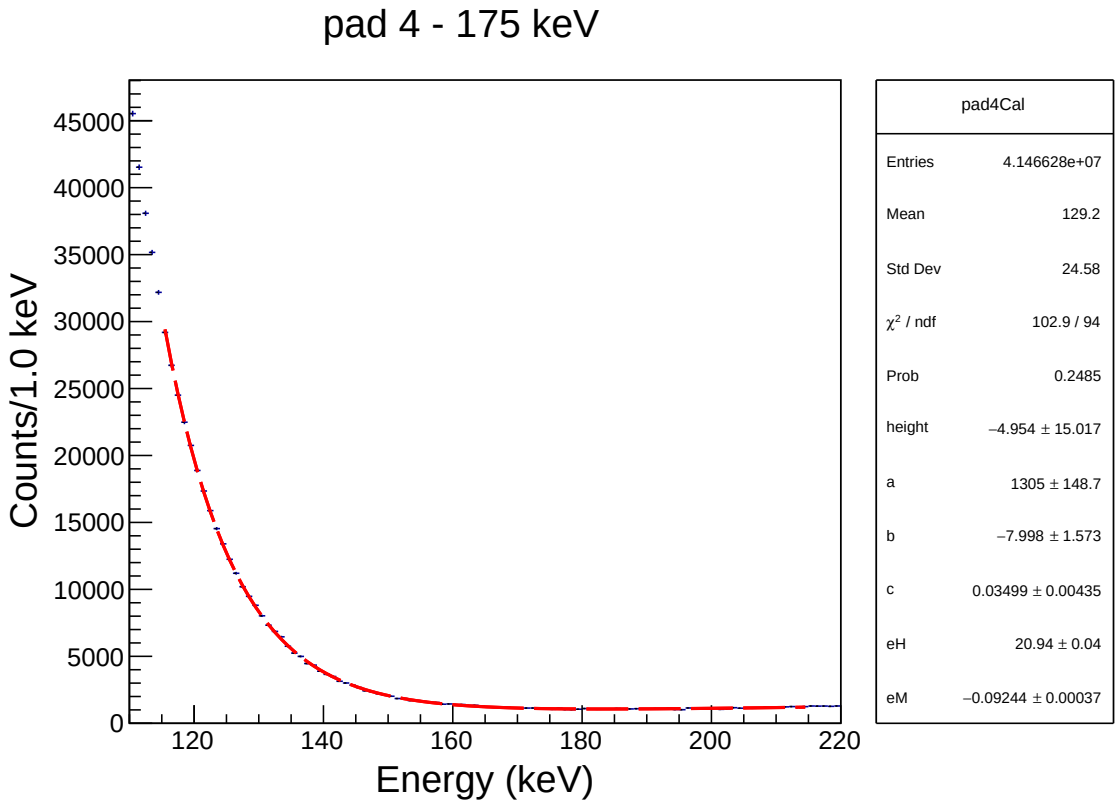

Figure B.8: Data of Pad E from E19030. The fit function is the sum of an exponential, quadratic polynomial, and Gaussian peak. The peak width is described in text and peak center is fixed to 175 keV.

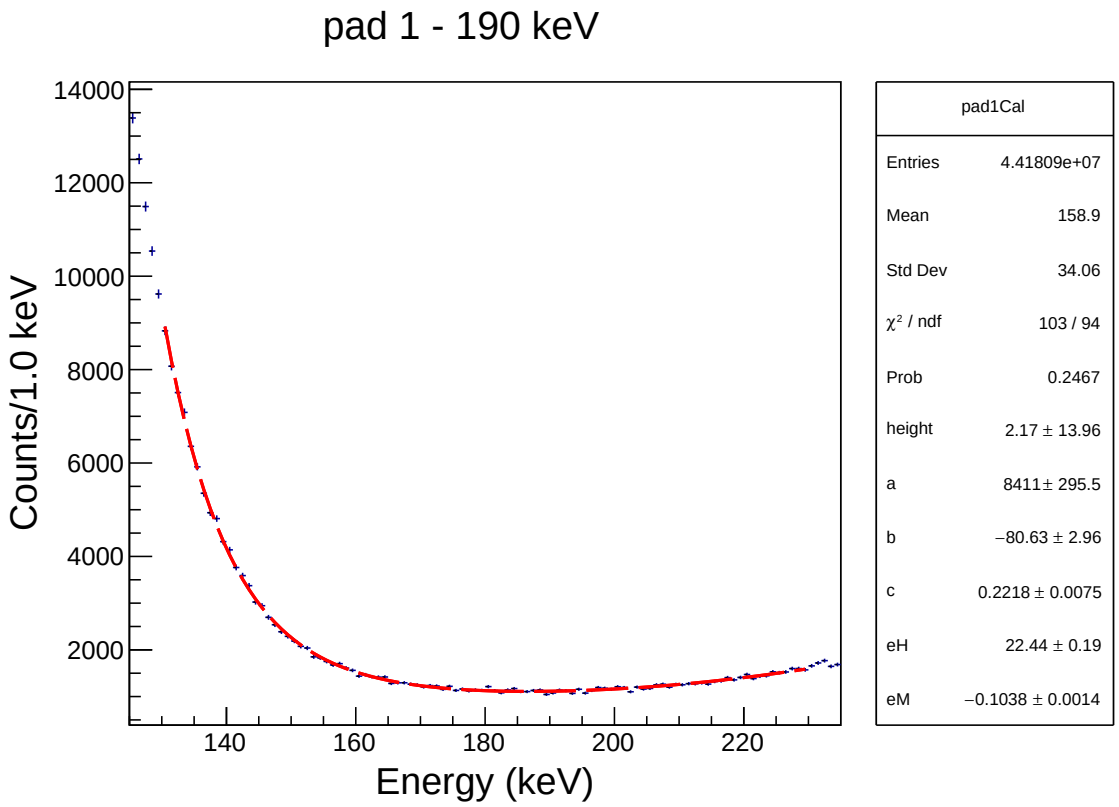

Figure B.9: Data of Pad B from E19030. The fit function is the sum of an exponential, quadratic polynomial, and Gaussian peak. The peak width is described in text and peak center is fixed to 190 keV.

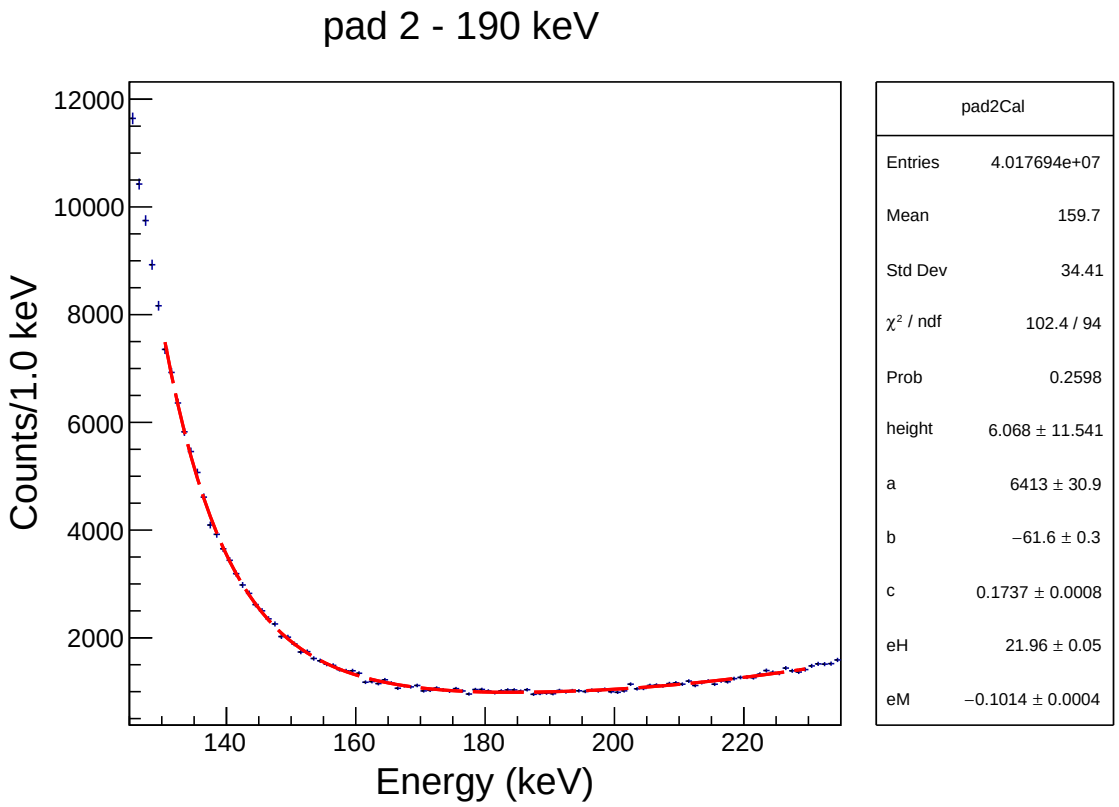

Figure B.10: Data of Pad C from E19030. The fit function is the sum of an exponential, quadratic polynomial, and Gaussian peak. The peak width is described in text and peak center is fixed to 190 keV.

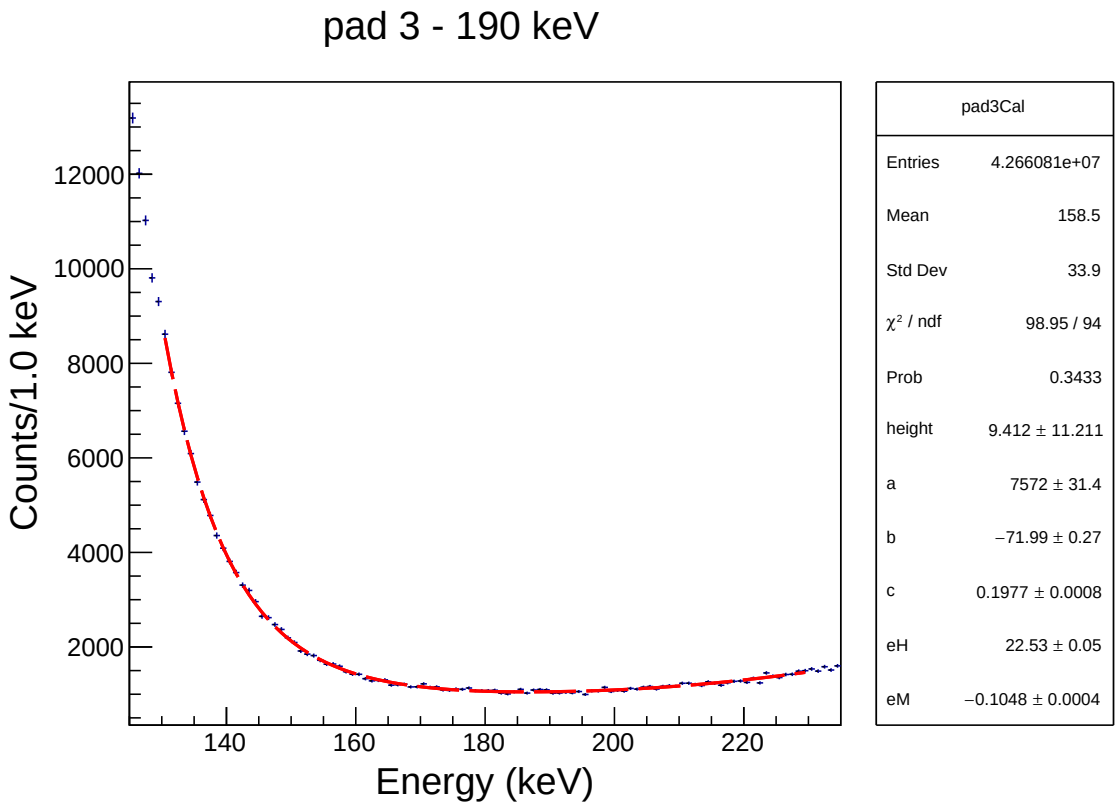

Figure B.11: Data of Pad D from E19030. The fit function is the sum of an exponential, quadratic polynomial, and Gaussian peak. The peak width is described in text and peak center is fixed to 190 keV.

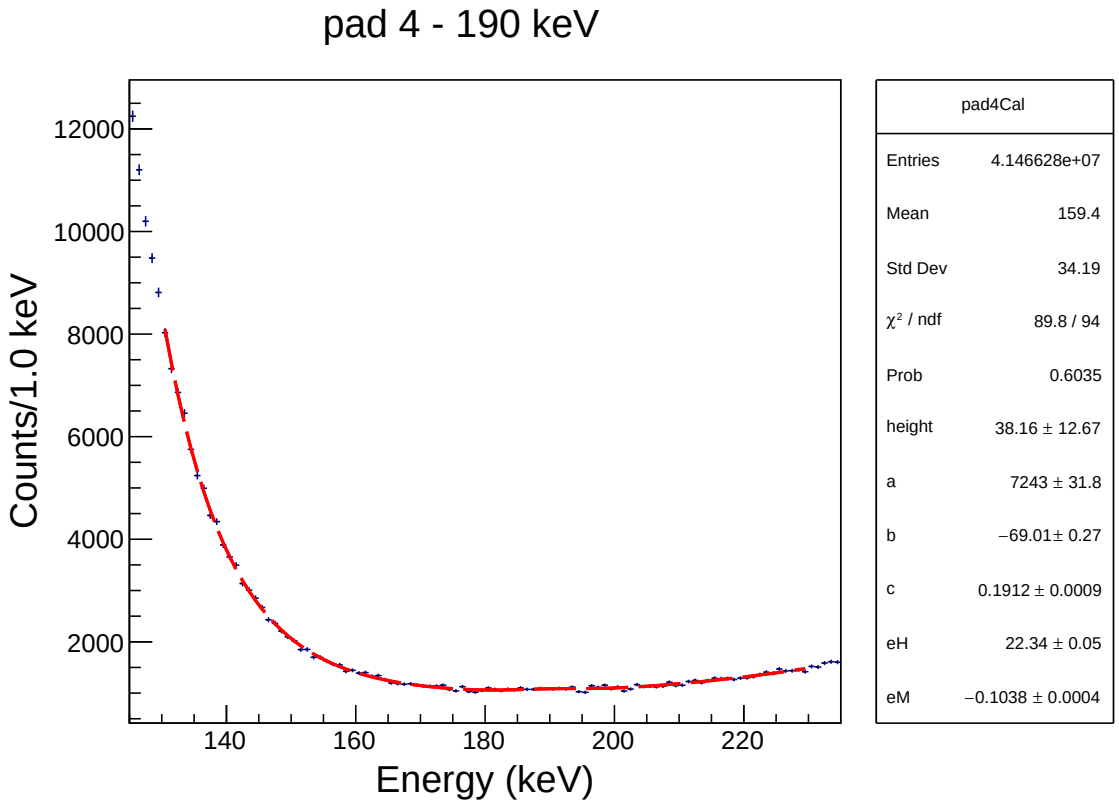

Figure B.12: Data of Pad E from E19030. The fit function is the sum of an exponential, quadratic polynomial, and Gaussian peak. The peak width is described in text and peak center is fixed to 190 keV.

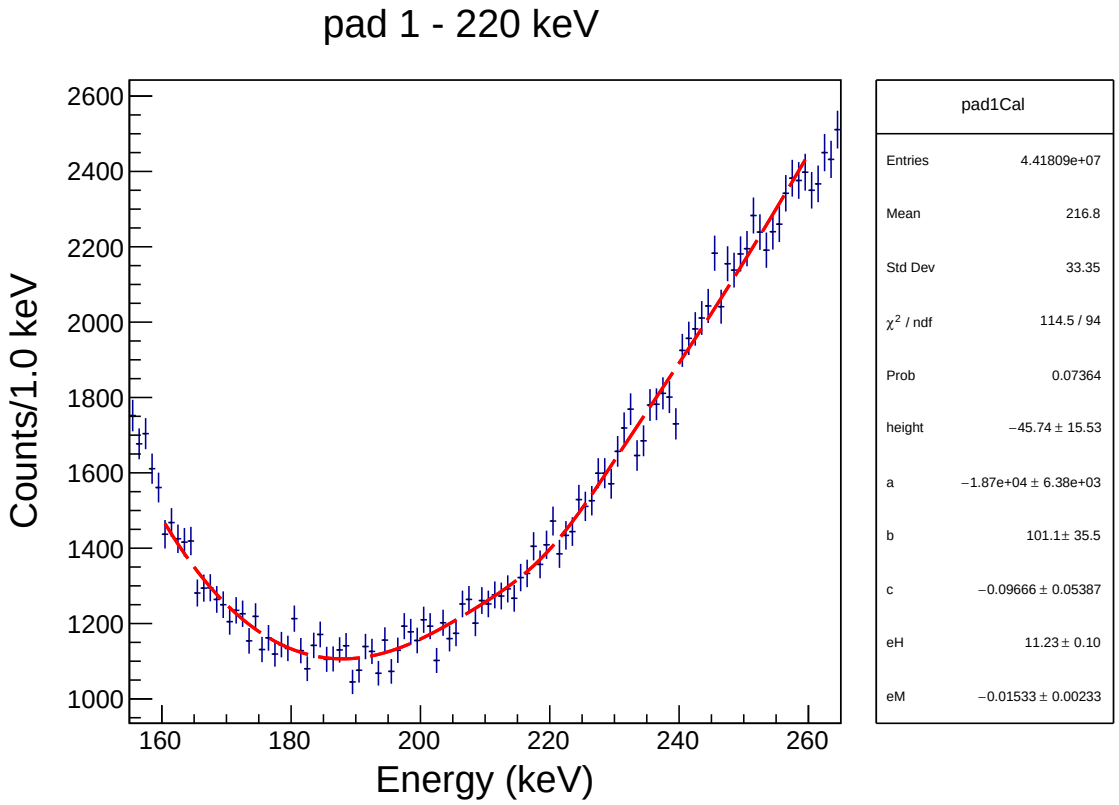

Figure B.13: Data of Pad B from E19030. The fit function is the sum of an exponential, quadratic polynomial, and Gaussian peak. The peak width is described in text and peak center is fixed to 220 keV.

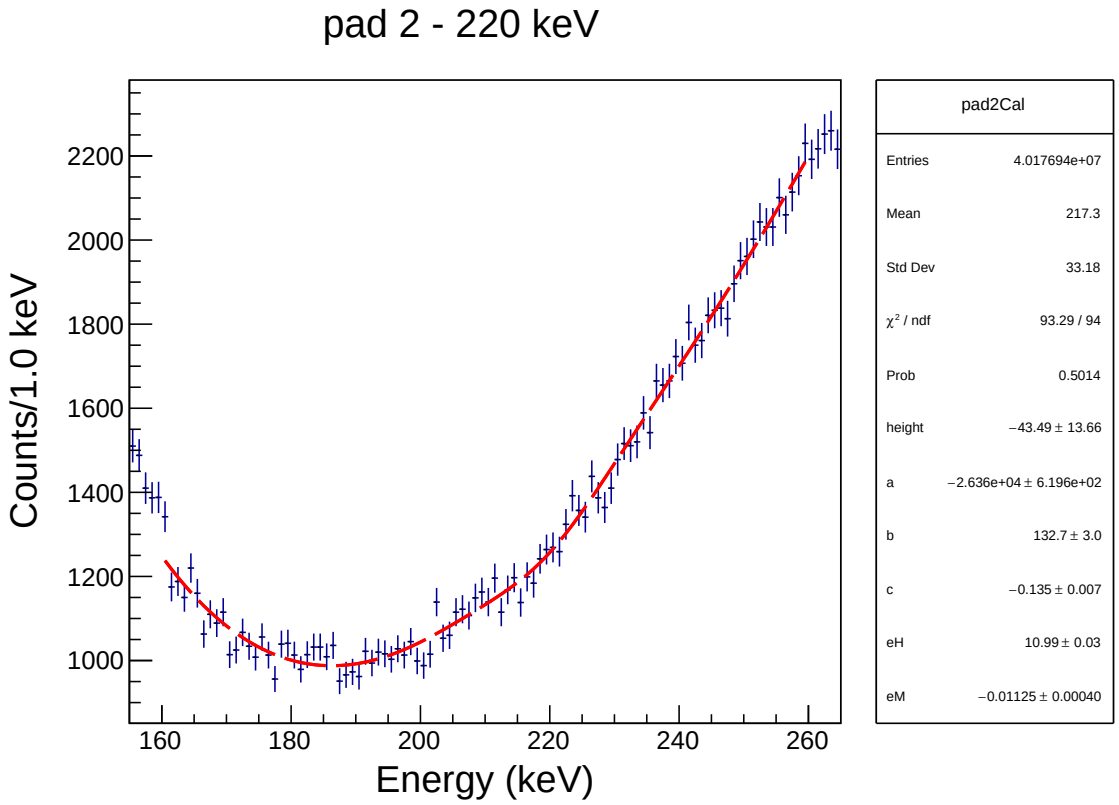

Figure B.14: Data of Pad C from E19030. The fit function is the sum of an exponential, quadratic polynomial, and Gaussian peak. The peak width is described in text and peak center is fixed to 220 keV.

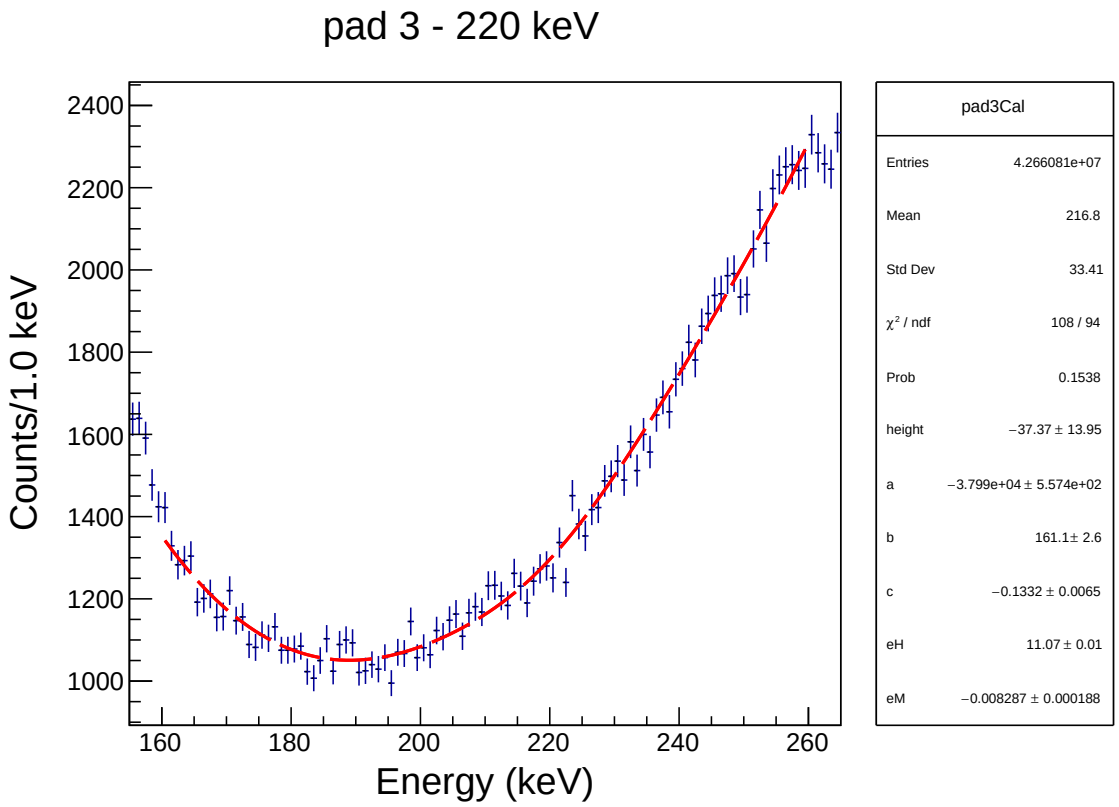

Figure B.15: Data of Pad D from E19030. The fit function is the sum of an exponential, quadratic polynomial, and Gaussian peak. The peak width is described in text and peak center is fixed to 220 keV.

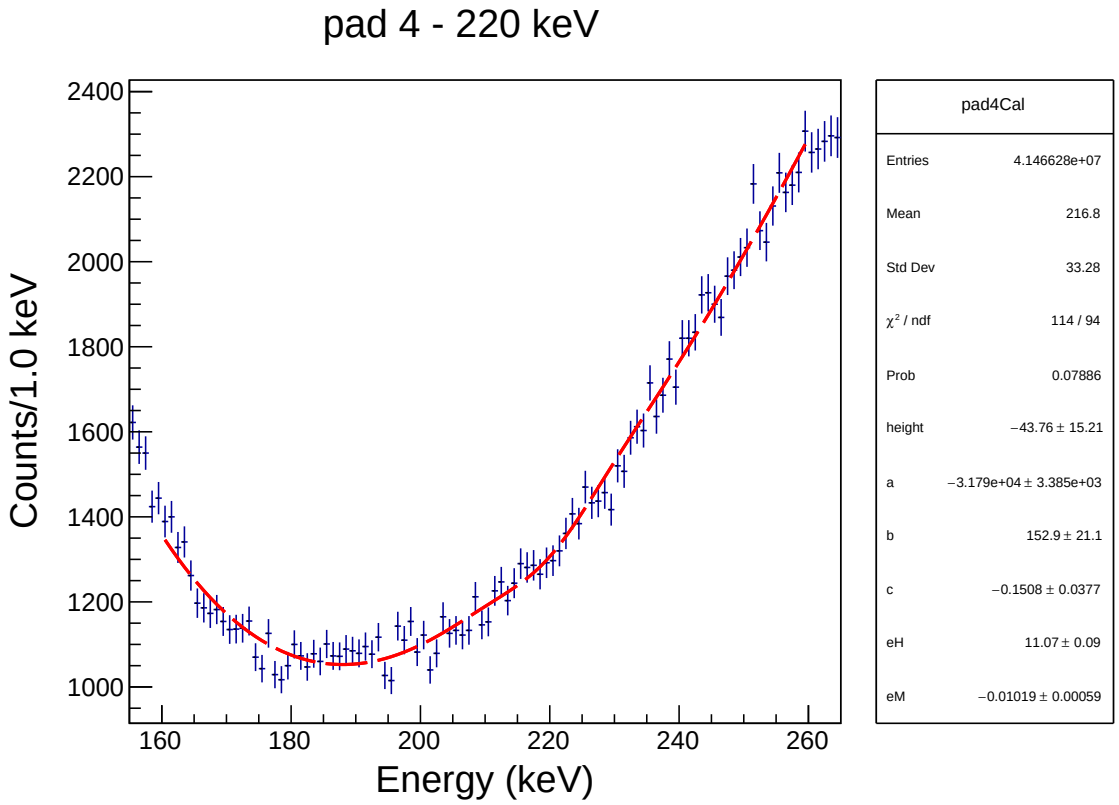

Figure B.16: Data of Pad E from E19030. The fit function is the sum of an exponential, quadratic polynomial, and Gaussian peak. The peak width is described in text and peak center is fixed to 220 keV.

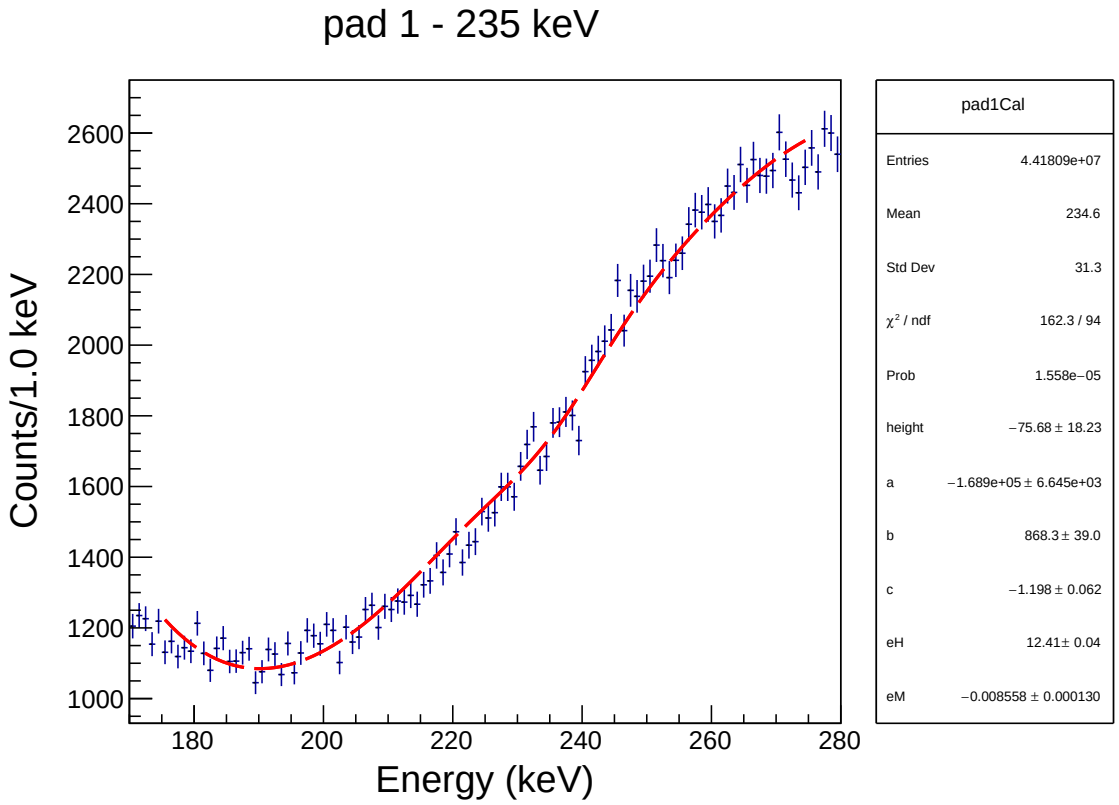

Figure B.17: Data of Pad B from E19030. The fit function is the sum of an exponential, quadratic polynomial, and Gaussian peak. The peak width is described in text and peak center is fixed to 235 keV.

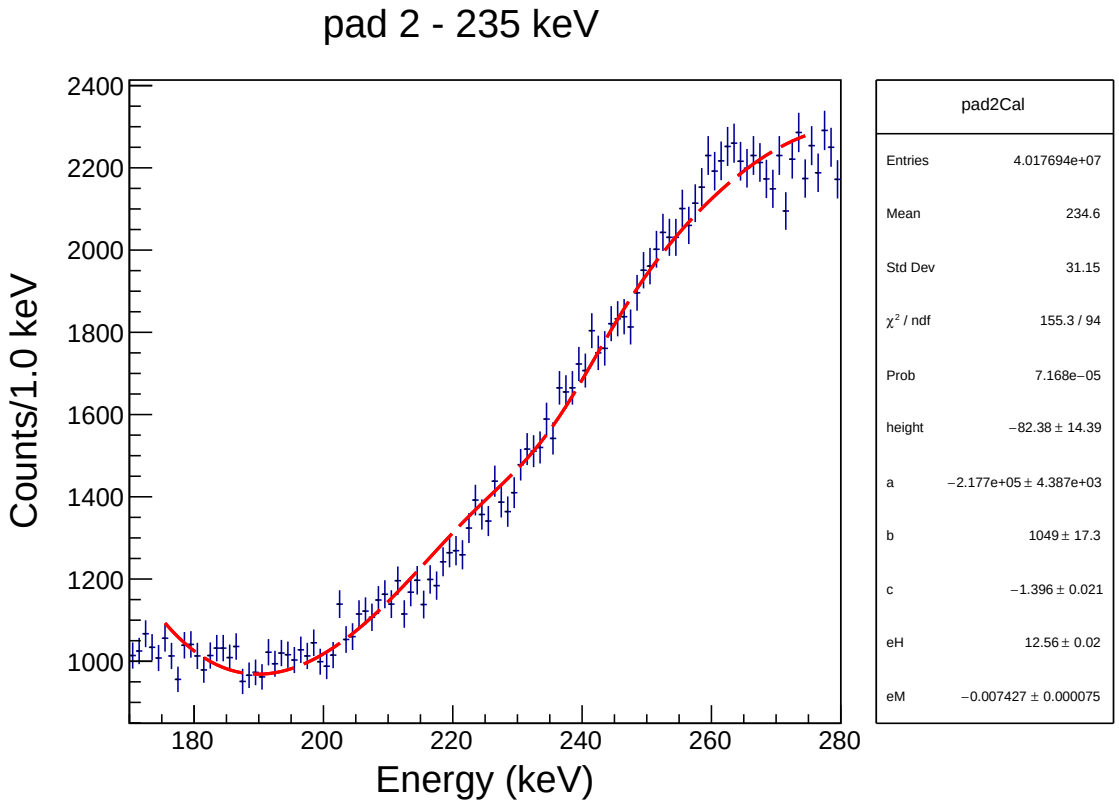

Figure B.18: Data of Pad C from E19030. The fit function is the sum of an exponential, quadratic polynomial, and Gaussian peak. The peak width is described in text and peak center is fixed to 235 keV.

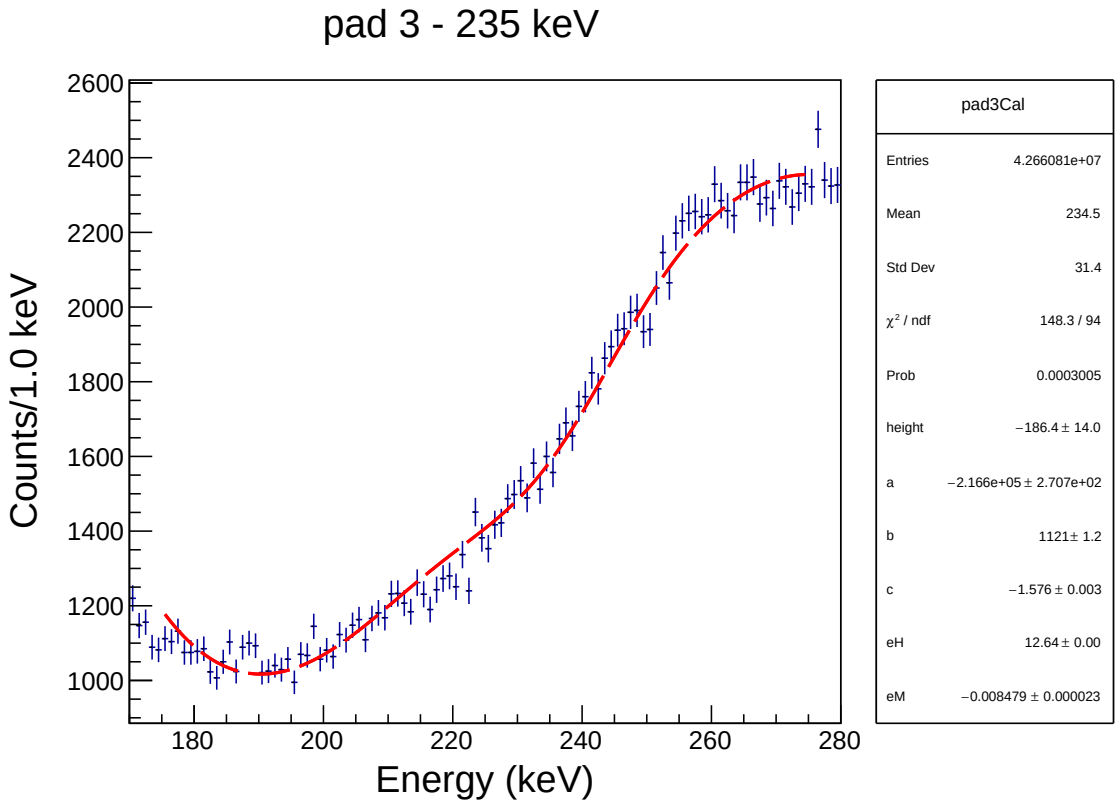

Figure B.19: Data of Pad D from E19030. The fit function is the sum of an exponential, quadratic polynomial, and Gaussian peak. The peak width is described in text and peak center is fixed to 235 keV.

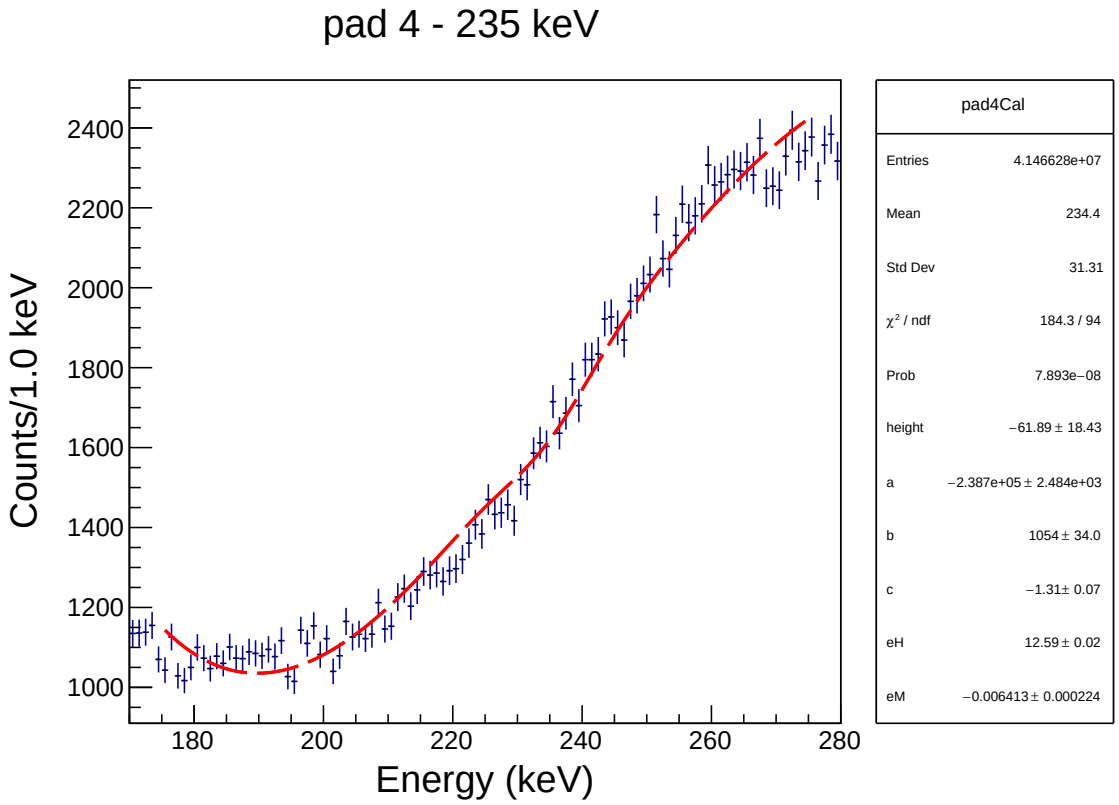

Figure B.20: Data of Pad E from E19030. The fit function is the sum of an exponential, quadratic polynomial, and Gaussian peak. The peak width is described in text and peak center is fixed to 235 keV.

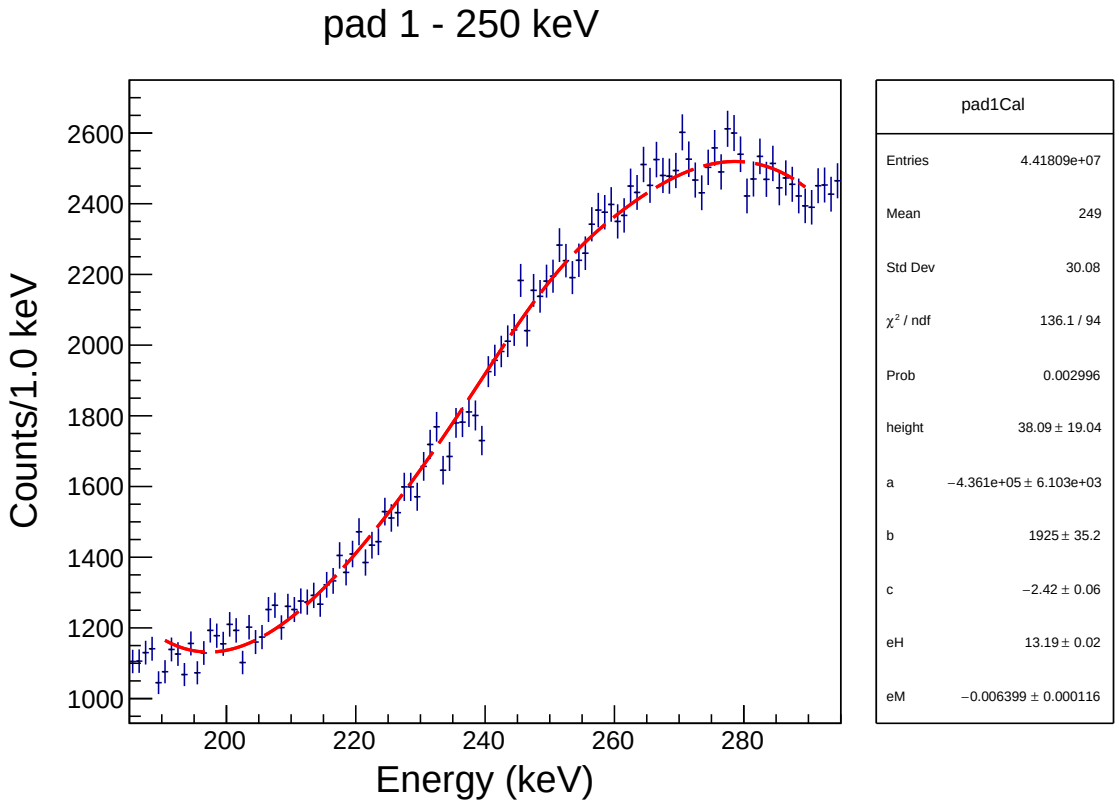

Figure B.21: Data of Pad B from E19030. The fit function is the sum of an exponential, quadratic polynomial, and Gaussian peak. The peak width is described in text and peak center is fixed to 250 keV.

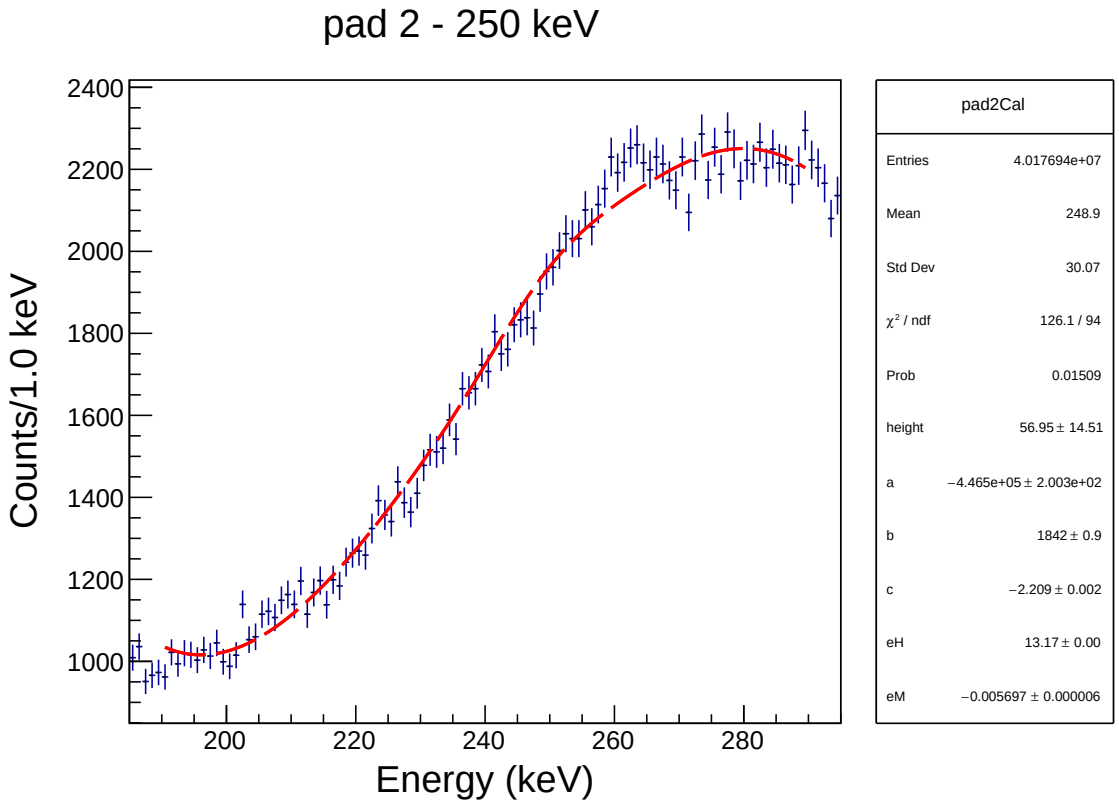

Figure B.22: Data of Pad C from E19030. The fit function is the sum of an exponential, quadratic polynomial, and Gaussian peak. The peak width is described in text and peak center is fixed to 250 keV.

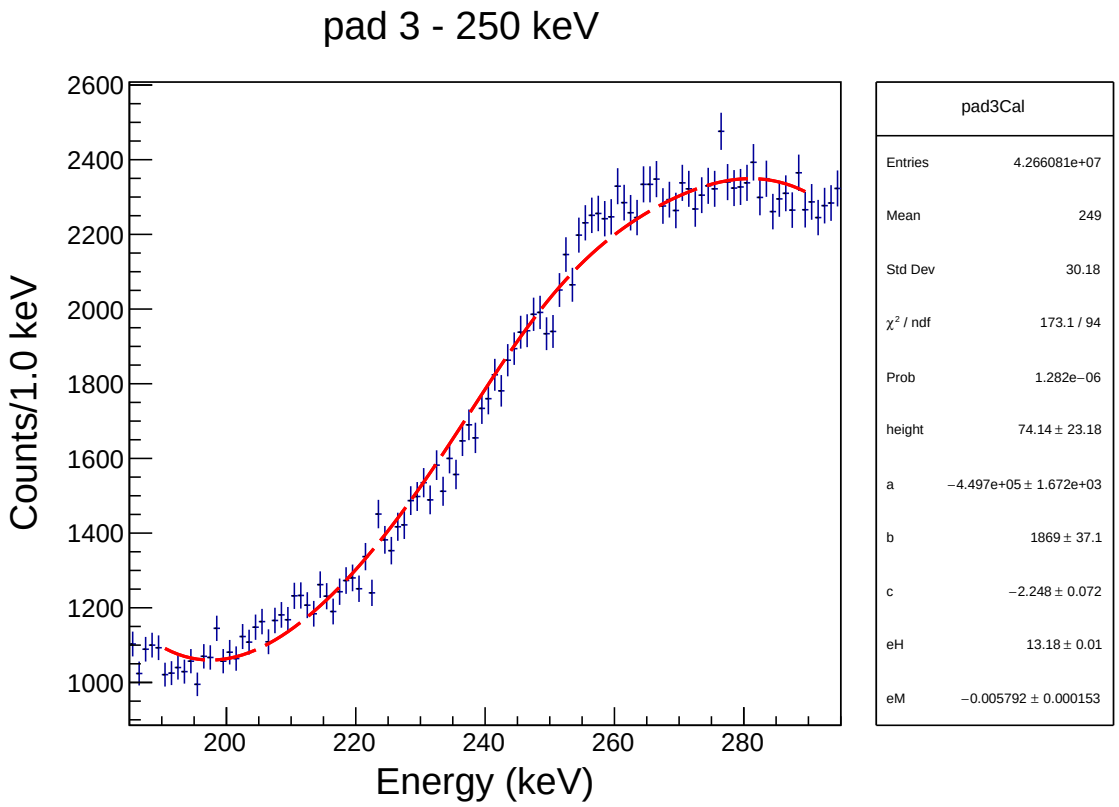

Figure B.23: Data of Pad D from E19030. The fit function is the sum of an exponential, quadratic polynomial, and Gaussian peak. The peak width is described in text and peak center is fixed to 250 keV.

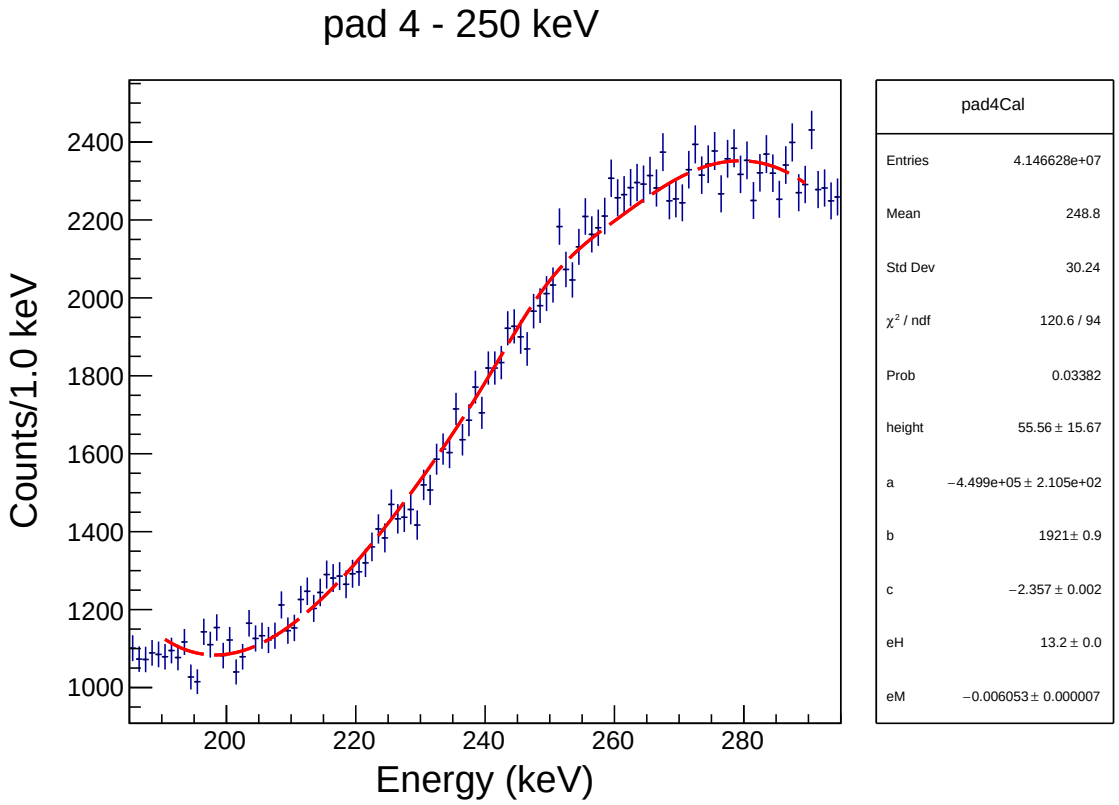

Figure B.24: Data of Pad E from E19030. The fit function is the sum of an exponential, quadratic polynomial, and Gaussian peak. The peak width is described in text and peak center is fixed to 250 keV.

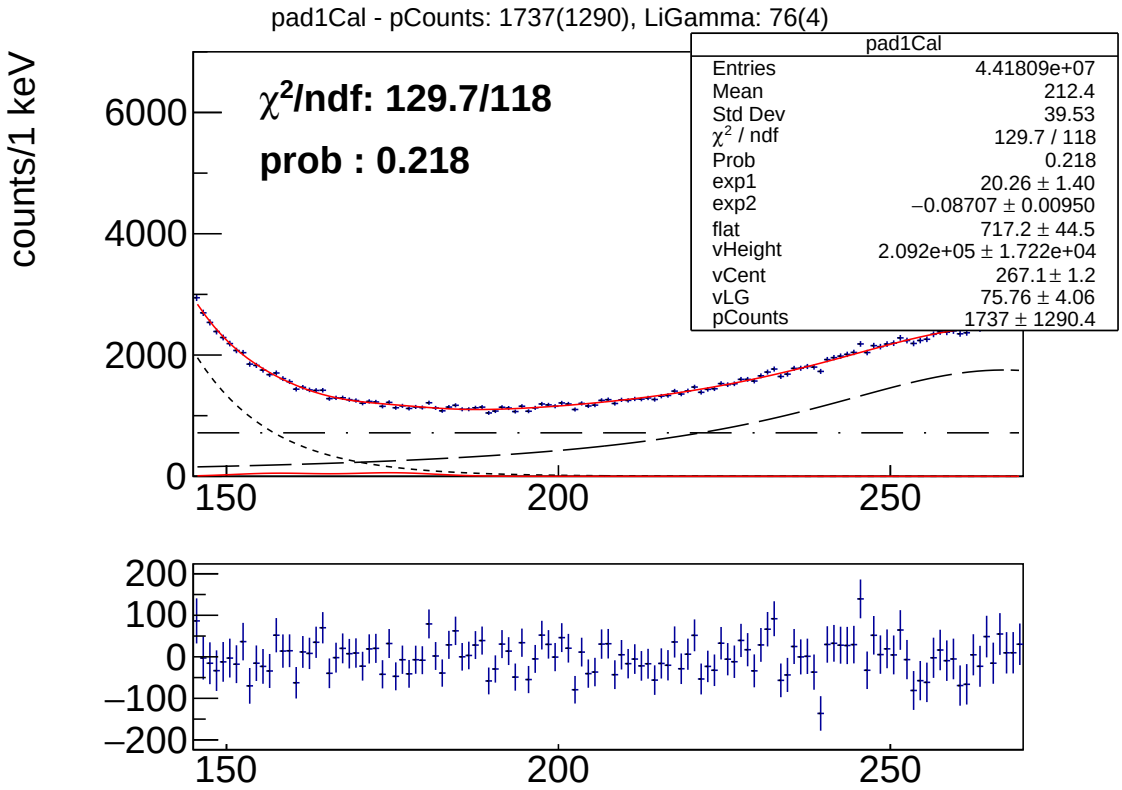

Figure B.25: Data of Pad B from E19030, fit to data (red), and fit components (dashed black). The fit function is the sum of an exponential, constant, and Voigt. The detector resolution is given in text and proton resonance width is fixed $\Gamma_p = 0.0$ keV. The search peak center is fixed to 175 keV.

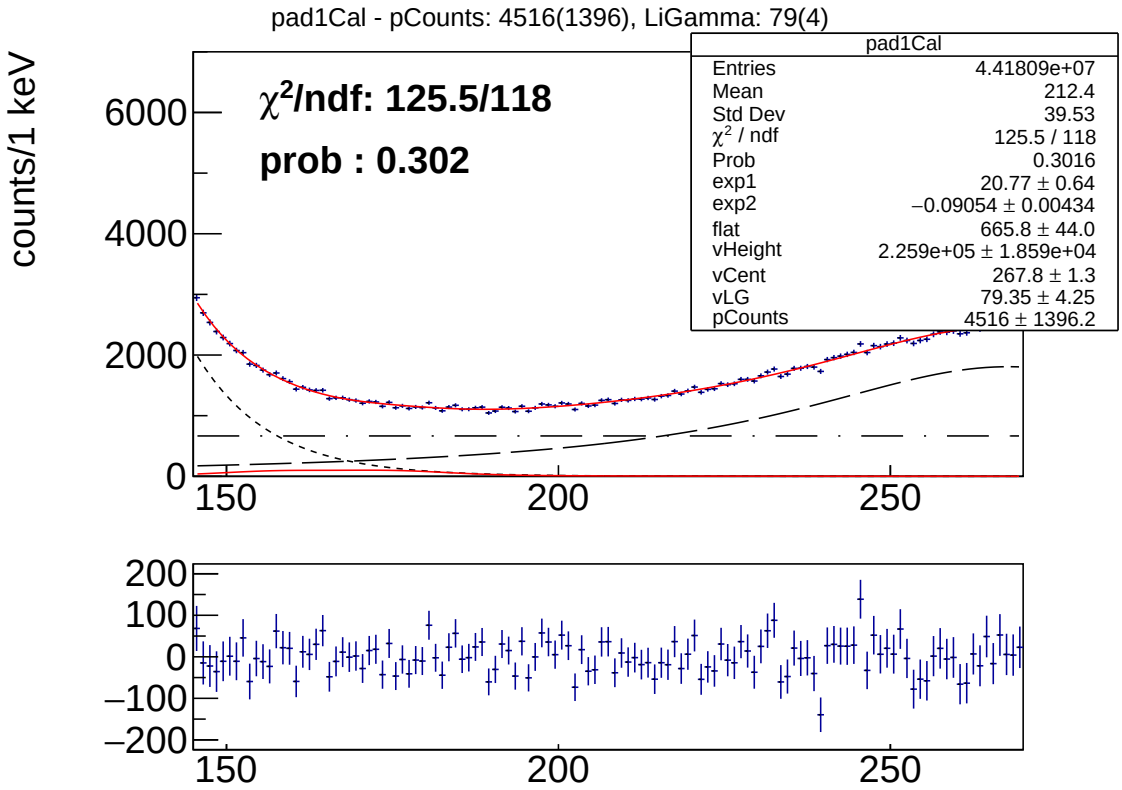

Figure B.26: Data of Pad B from E19030, fit to data (red), and fit components (dashed black). The fit function is the sum of an exponential, constant, and Voigt. The detector resolution is given in text and proton resonance width is fixed $\Gamma_p = 12.0$ keV. The search peak center is fixed to 175 keV.

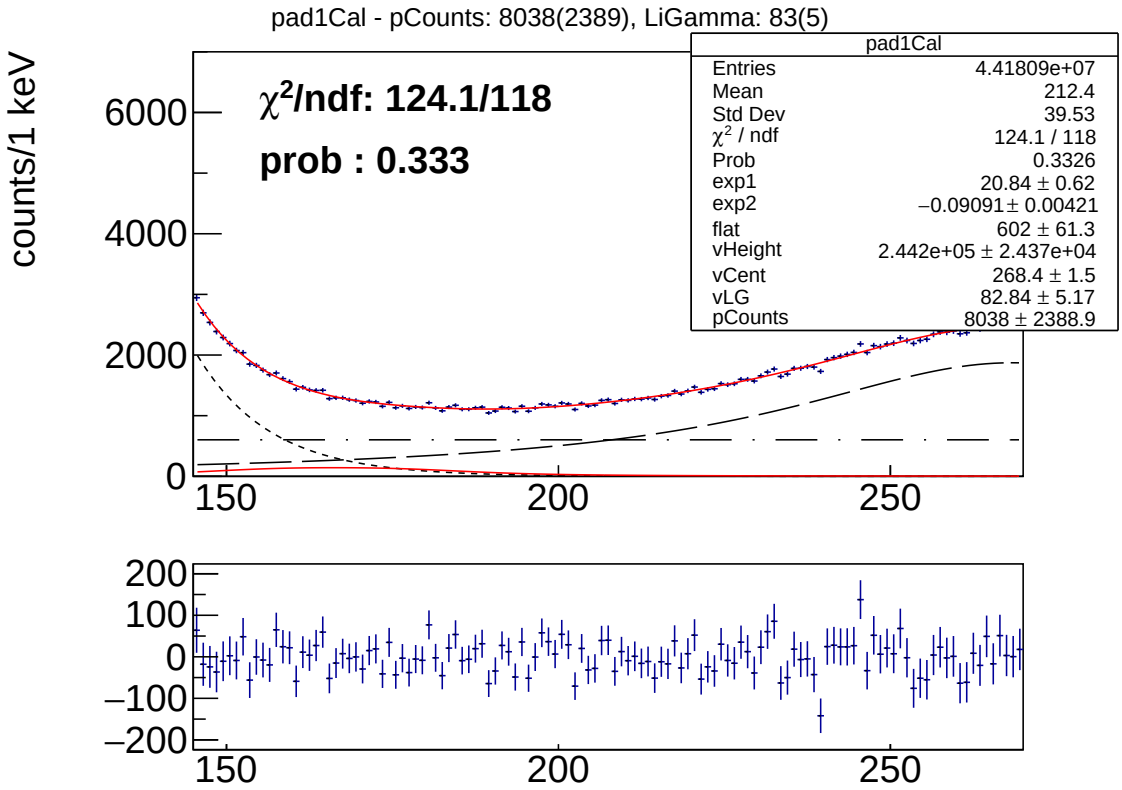

Figure B.27: Data of Pad B from E19030, fit to data (red), and fit components (dashed black). The fit function is the sum of an exponential, constant, and Voigt. The detector resolution is given in text and proton resonance width is fixed $\Gamma_p = 24.0$ keV. The search peak center is fixed to 175 keV.

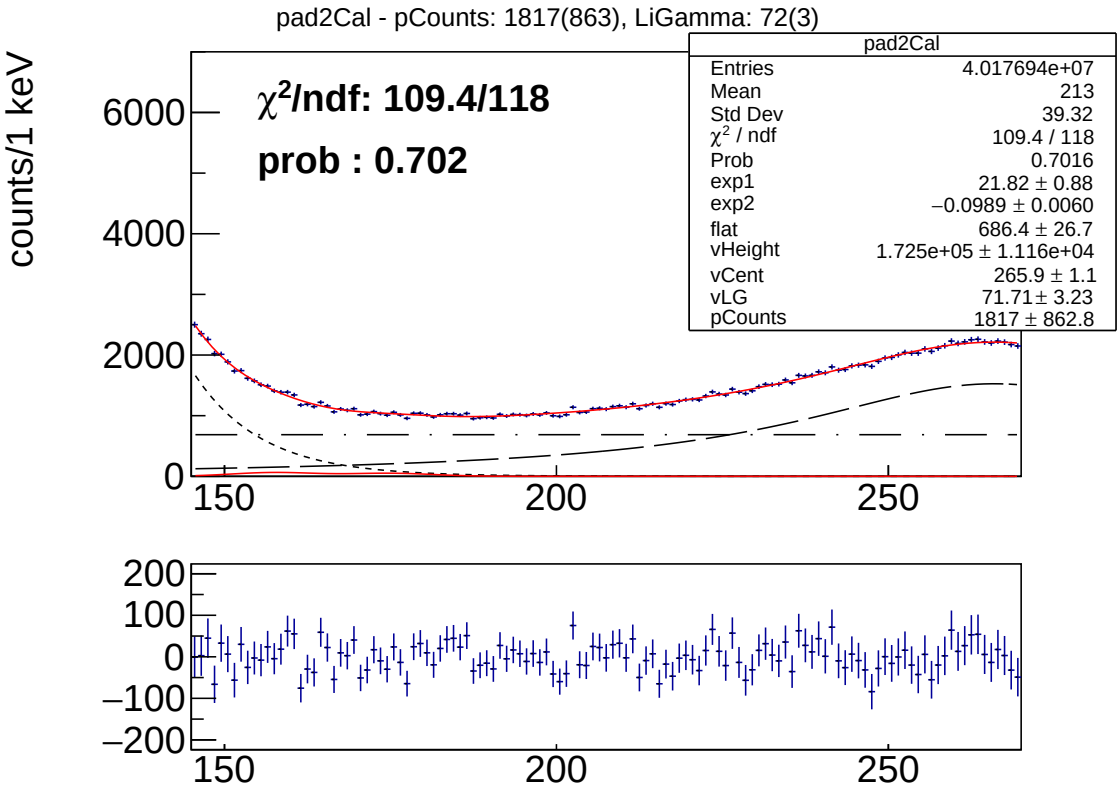

Figure B.28: Data of Pad C from E19030, fit to data (red), and fit components (dashed black). The fit function is the sum of an exponential, constant, and Voigt. The detector resolution is given in text and proton resonance width is fixed $\Gamma_p = 0.0$ keV. The search peak center is fixed to 175 keV.

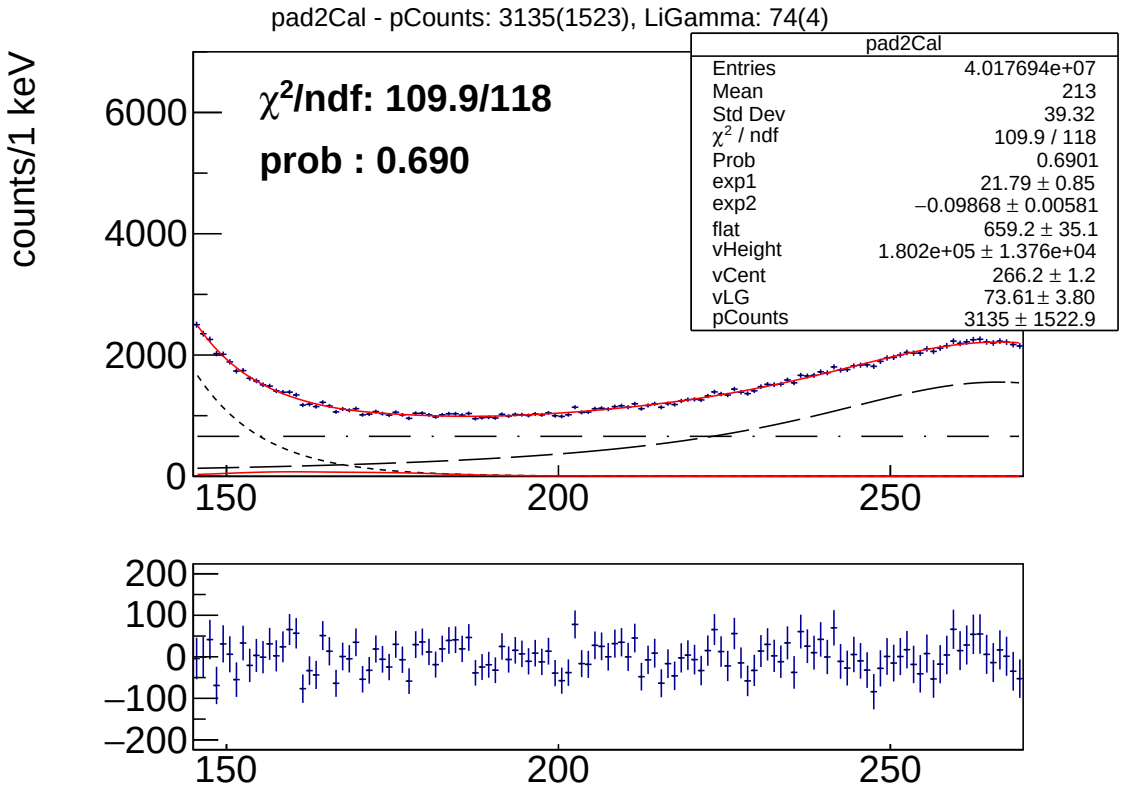

Figure B.29: Data of Pad C from E19030, fit to data (red), and fit components (dashed black). The fit function is the sum of an exponential, constant, and Voigt. The detector resolution is given in text and proton resonance width is fixed $\Gamma_p = 12.0$ keV. The search peak center is fixed to 175 keV.

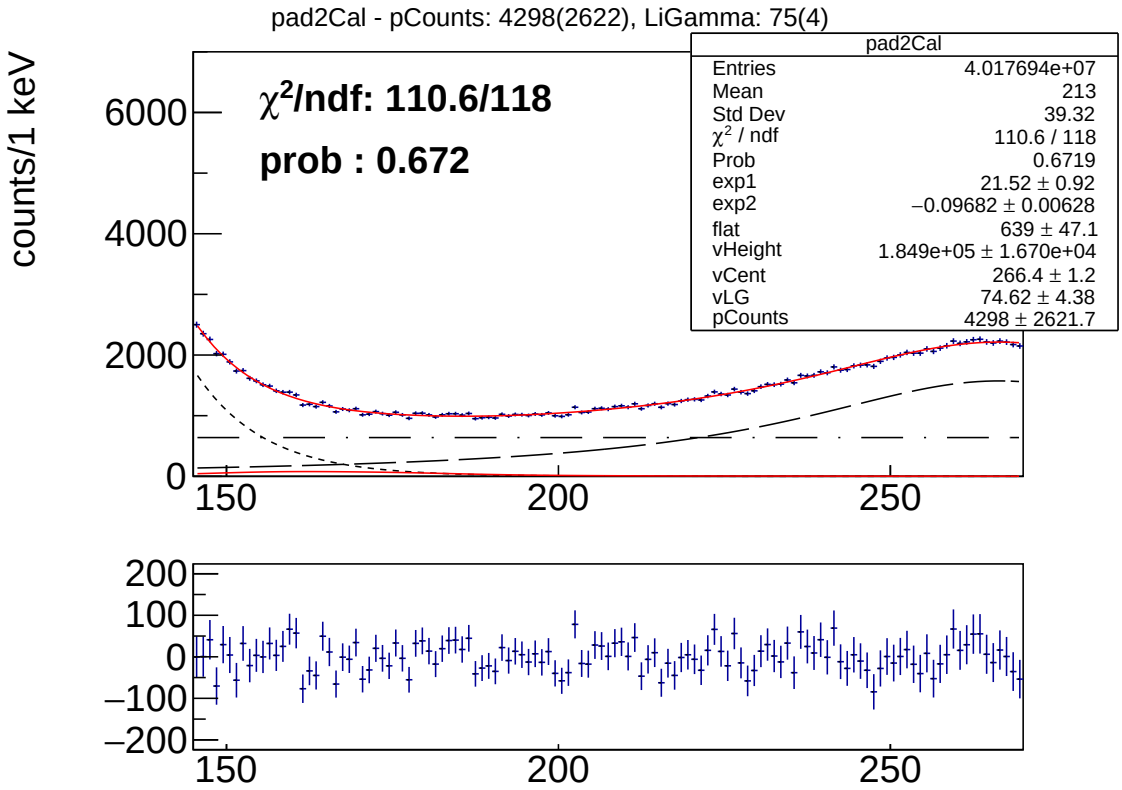

Figure B.30: Data of Pad C from E19030, fit to data (red), and fit components (dashed black). The fit function is the sum of an exponential, constant, and Voigt. The detector resolution is given in text and proton resonance width is fixed $\Gamma_p = 24.0$ keV. The search peak center is fixed to 175 keV.

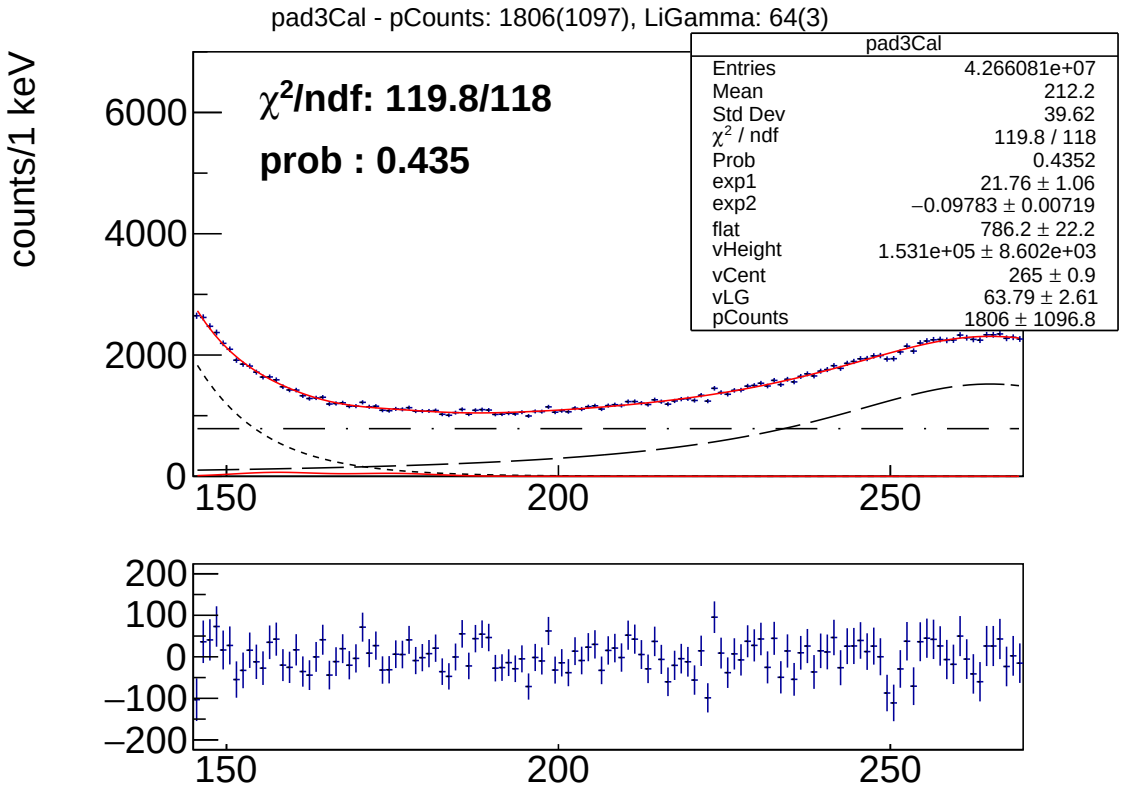

Figure B.31: Data of Pad D from E19030, fit to data (red), and fit components (dashed black). The fit function is the sum of an exponential, constant, and Voigt. The detector resolution is given in text and proton resonance width is fixed $\Gamma_p = 0.0$ keV. The search peak center is fixed to 175 keV.

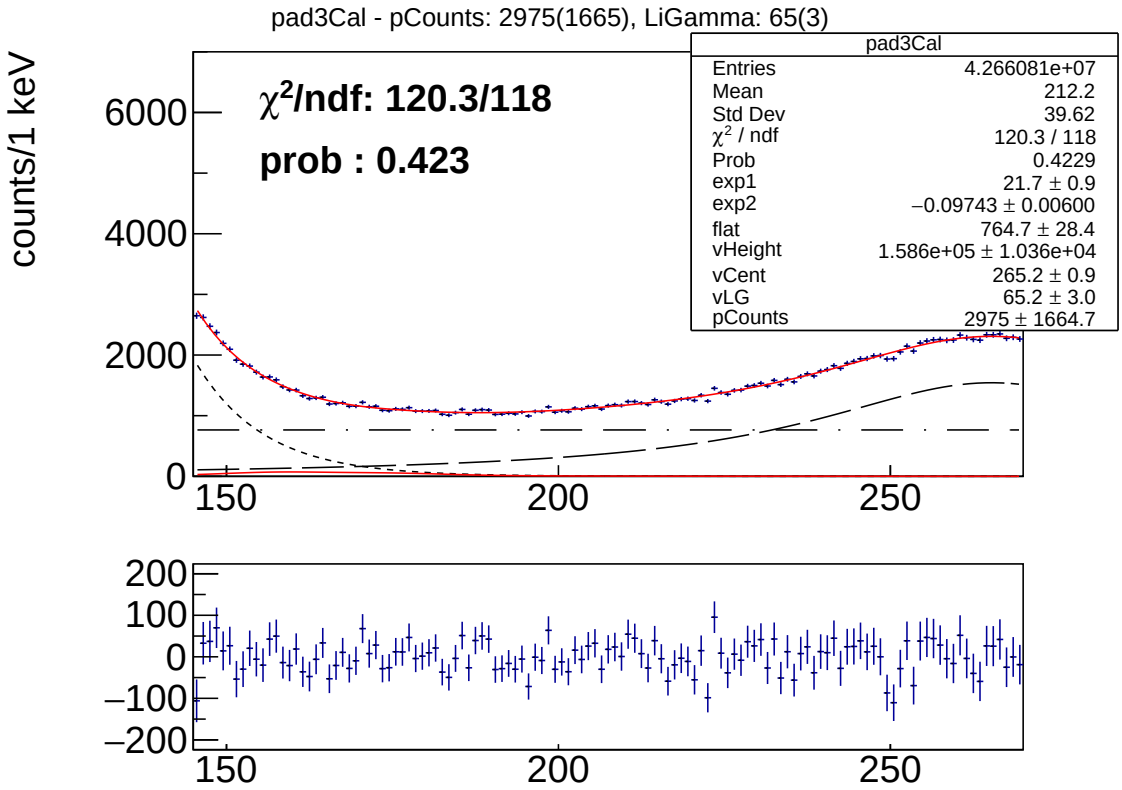

Figure B.32: Data of Pad D from E19030, fit to data (red), and fit components (dashed black). The fit function is the sum of an exponential, constant, and Voigt. The detector resolution is given in text and proton resonance width is fixed $\Gamma_p = 12.0$ keV. The search peak center is fixed to 175 keV.

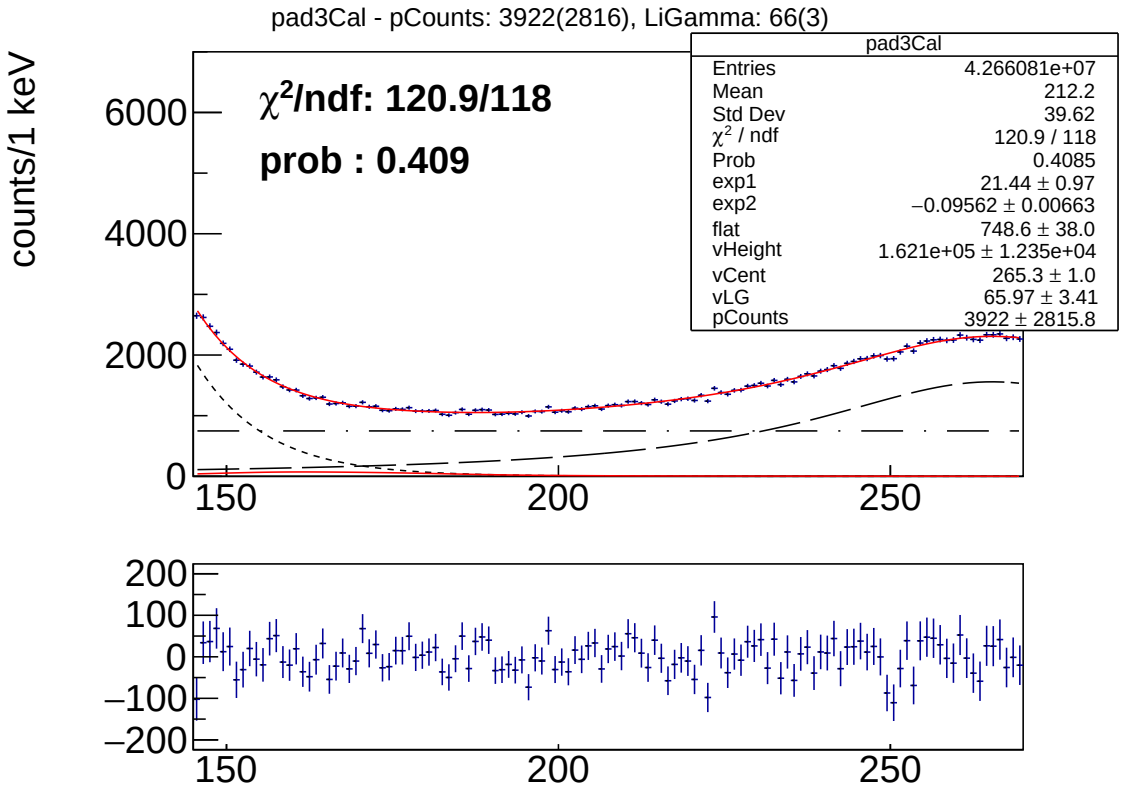

Figure B.33: Data of Pad D from E19030, fit to data (red), and fit components (dashed black). The fit function is the sum of an exponential, constant, and Voigt. The detector resolution is given in text and proton resonance width is fixed $\Gamma_p = 24.0$ keV. The search peak center is fixed to 175 keV.

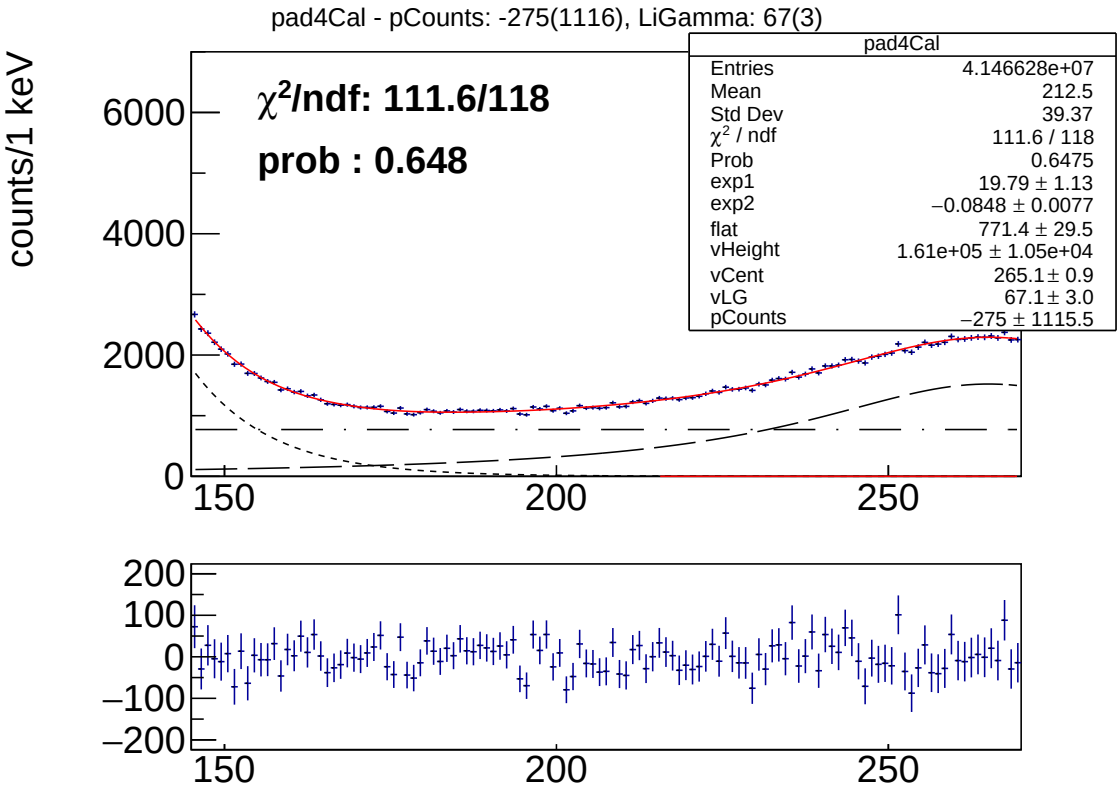

Figure B.34: Data of Pad E from E19030, fit to data (red), and fit components (dashed black). The fit function is the sum of an exponential, constant, and Voigt. The detector resolution is given in text and proton resonance width is fixed $\Gamma_p = 0.0$ keV. The search peak center is fixed to 175 keV.

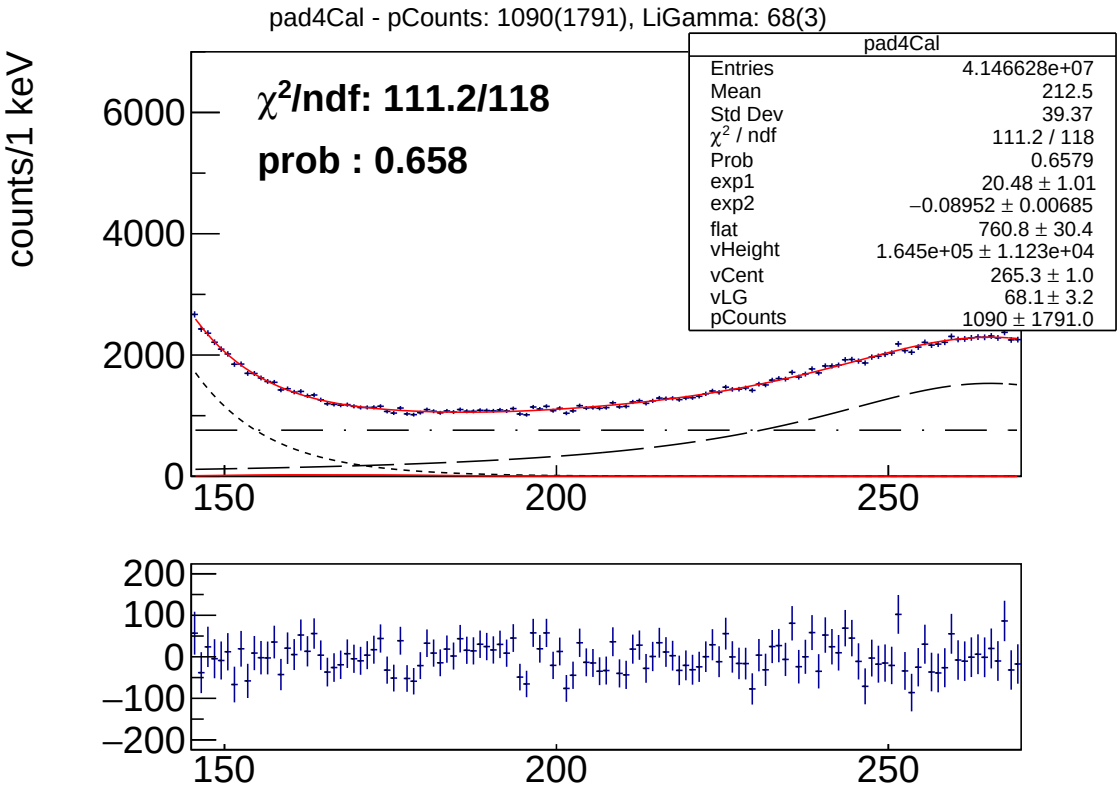

Figure B.35: Data of Pad E from E19030, fit to data (red), and fit components (dashed black). The fit function is the sum of an exponential, constant, and Voigt. The detector resolution is given in text and proton resonance width is fixed $\Gamma_p = 12.0$ keV. The search peak center is fixed to 175 keV.

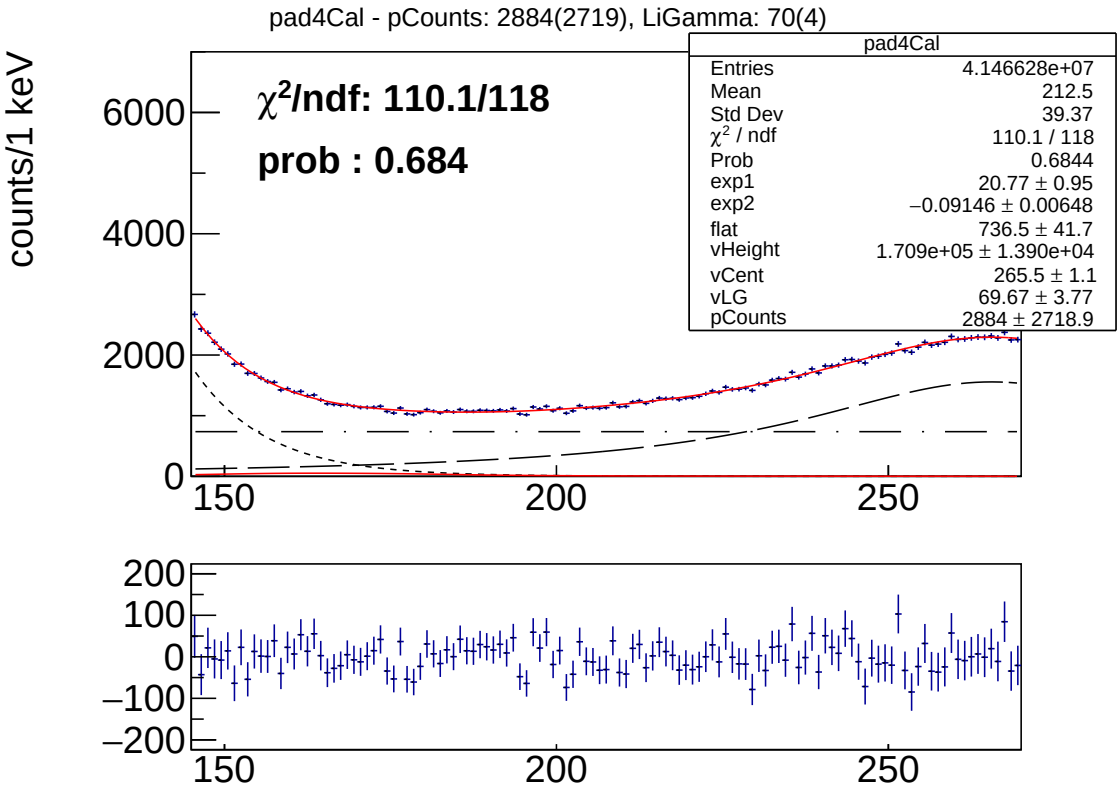

Figure B.36: Data of Pad E from E19030, fit to data (red), and fit components (dashed black). The fit function is the sum of an exponential, constant, and Voigt. The detector resolution is given in text and proton resonance width is fixed $\Gamma_p = 24.0$ keV. The search peak center is fixed to 175 keV.

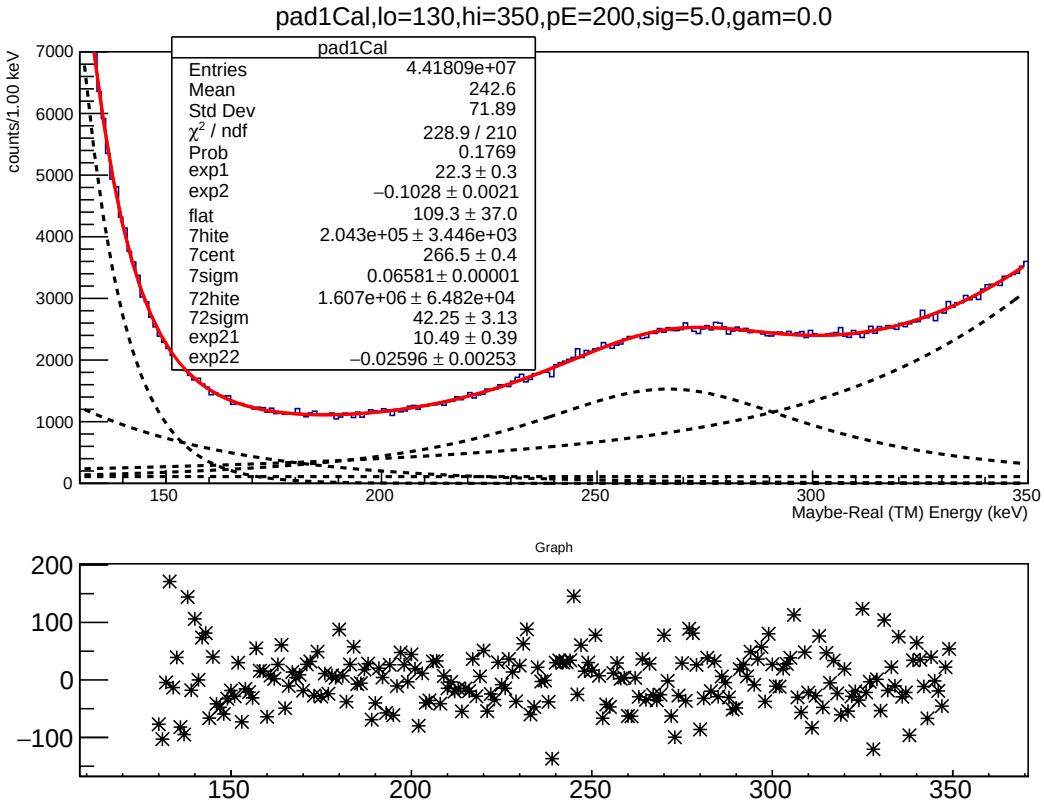

Figure B.37: (Top) Here shows the 2Exponential + Flat + 2Voigt fit to Pad B from E19030 with no $\beta^- p$ peak. The red line is the full fit and black dashed lines are individual components that are summed to create the red. (Bottom) Fit residuals. The fit quality is reasonable. For this choice of fit range, the χ^2 is 229 and the p-value is 0.177. Compare to Fig. B.38. The removal of the $\beta^- p$ peak hardly influences the quality of the fit.

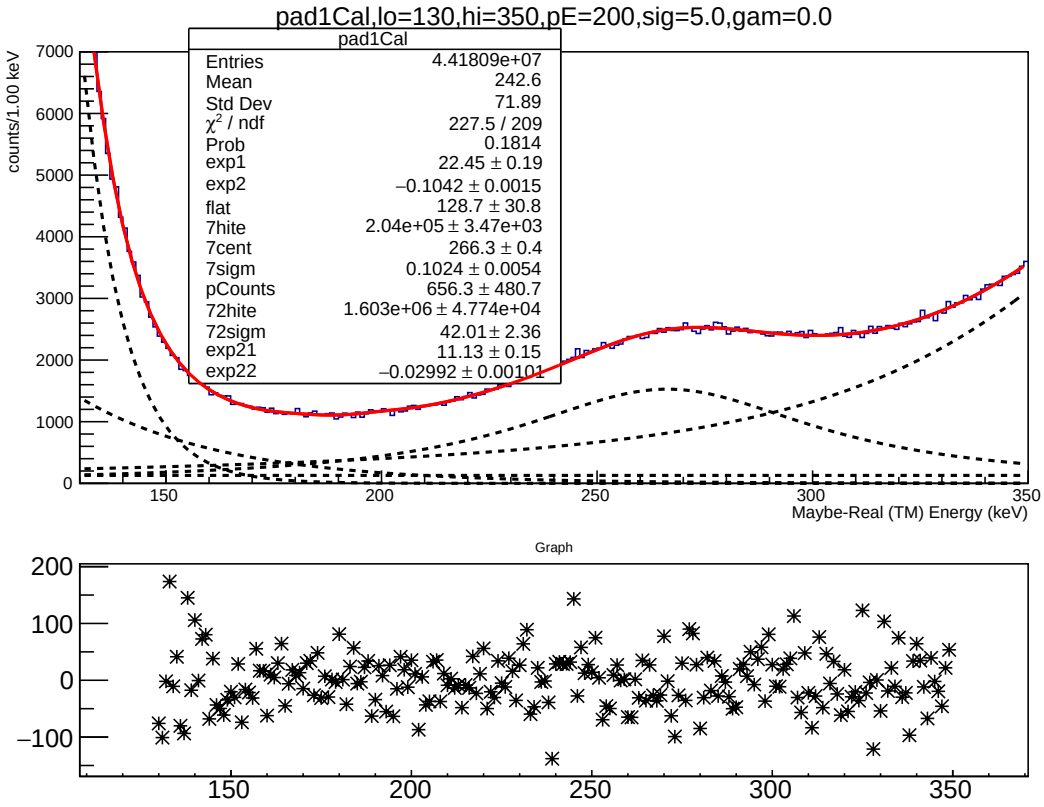

Figure B.38: (Top) Here shows the 2Exponential + Flat + 2Voigt fit to Pad B from E19030 with a $\beta^- p$ peak as a parameter. The red line is the full fit and black dashed lines are individual components that are summed to create the red. (Bottom) Fit residuals. The fit quality is reasonable. For this choice of fit range, the χ^2 is 229 and the p-value is 0.181. Compare to Fig. B.37. The addition of the $\beta^- p$ peak hardly influences the quality of the fit.

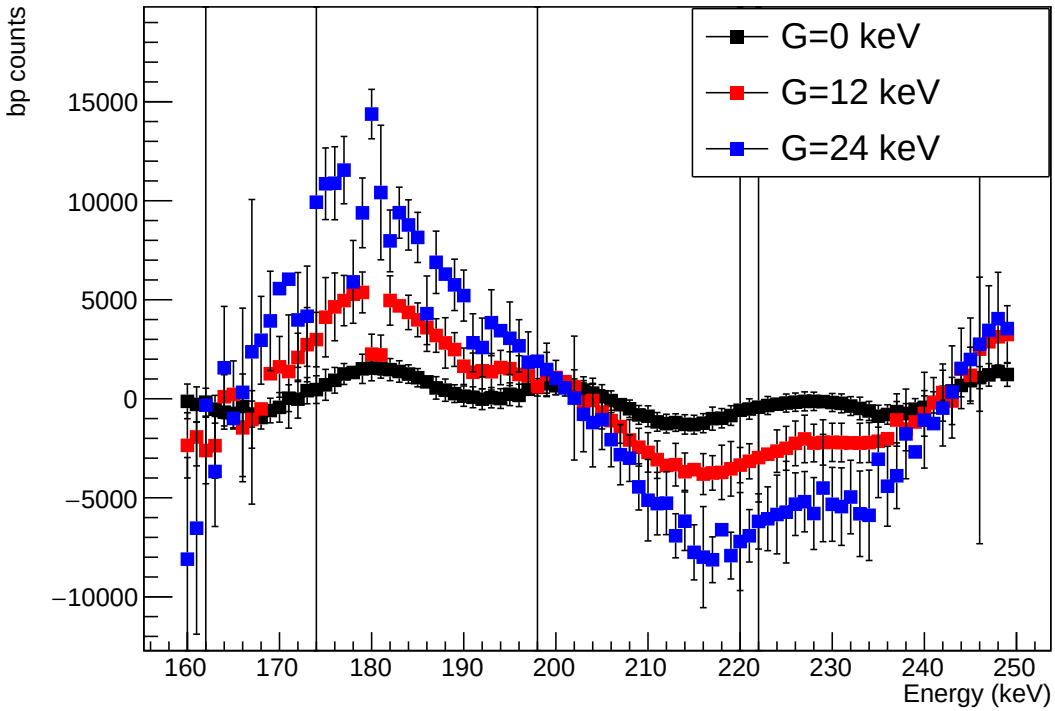

Figure B.39: Here shows inferred $\beta^- p$ counts from scanning the assumed energy and proton emitting state's width Γ_p for the 2Exponential + Flat + 2Voigt fit model for Pad B from E19030. Error bars are statistical. I speculate that the χ^2 surface has both bulk and small-scale features, especially for larger values of Γ_p. Note the non-statistical spread in data points that are 1 keV apart and sometimes wildly fluctuating error bars. (The detector resolution is 5-10% or 10-20 keV, so changes in results from changes in fit centers of 1 keV difference are artifacts of the fitting.) With the very similar quality of fits of Fig. B.37 and B.38 in mind, also note the behavior around $E \sim 180$ keV. Values of ~ 1000 counts are extracted assuming $\Gamma_p = 0$ keV. Values of ~ 1000 *or* ~ 5000 for $\Gamma_p = 12$ keV. Is one measurement correct and the other a systematic shift from fitting? Is the difference $\delta \sim 4000$ an estimate of the systematic error? Nevertheless, the minimization terminating point is a *reasonable* value. The χ^2 minimization chooses a *single* value and it seems that not a single value, but a variety of values are all *reasonable*.

APPENDIX C

BAYESIAN ANALYSIS

C.1 Confidence Interval Calculations

Converting a non-Gaussian probability density function to a confidence interval is not as straightforward as the Gaussian interval. In the Gaussian probability density function, distribution is such that 1) the most likely values are toward the median of the distribution and 2) the probability of increasingly/decreasingly extreme values diminishes symmetrically away from the median. However, in general, these properties are not guaranteed in probability density functions and are both untrue in the case of an exponential probability density function that might be used in describing an upper limit on a value.

Figure C.1, starts at the median of the distribution and moves symmetrically outward. Mathematically, this symmetry condition can be written as:

$$|\frac{dp(x_{\text{left}})}{dx} \cdot \Delta x_{\text{left}}| = |\frac{dp(x_{\text{right}})}{dx} \cdot \Delta x_{\text{right}}| \tag{C.1}$$

This symmetry only serves nicely in symmetric probability density functions. In asymmetric ones, you can find unfortunate circumstances such as physical boundaries never being included in a limit, no matter how probable, as the symmetric scheme requires probability be outside of the interval in equal amounts. This is undesirable in the case of an upper-limit against a physical boundary, where the exponential curve may nicely describe the probability density function, but the median-scheme never allows for an inference of a value of zero.

Now consider Fig. C.2. The scheme used here starts at the most probable value and integrates outwards in the probabilistically preferred direction. In the case of an exponential probability density function, this is necessarily one-sided. As the confidence interval increases, zero is always included, as is desired for an upper limit probability distribution.

The final example will be a suggestive, but not conclusive finite measurement, similar to some of the probability density functions that were extracted in the Bayesian analysis of Sec. 4.4 and Chapter 5. This distribution was generated by the sum of an arctangent function and a Gaussian curve. It is meant to have a clear peak representing a clearly favored value, but still substantial probability close to zero. The symmetric median scheme will return confidence intervals centered on the low-value shoulder of the peak. Again, at even high confidence, it excludes zero, which has substantial probability density. The mode scheme always includes the peak. Furthermore, for low confidence values, it reports a finite value with an upper and lower limit. At some degree of confidence, however, the interval reverts to being an upper limit. This ability to change from a finite measurement to a limit is valuable with these suggestive, in-between distributions that are not clearly limits nor finite valued; at low confidence, the interval is a finite value; at high confidence, the interval is a limit.

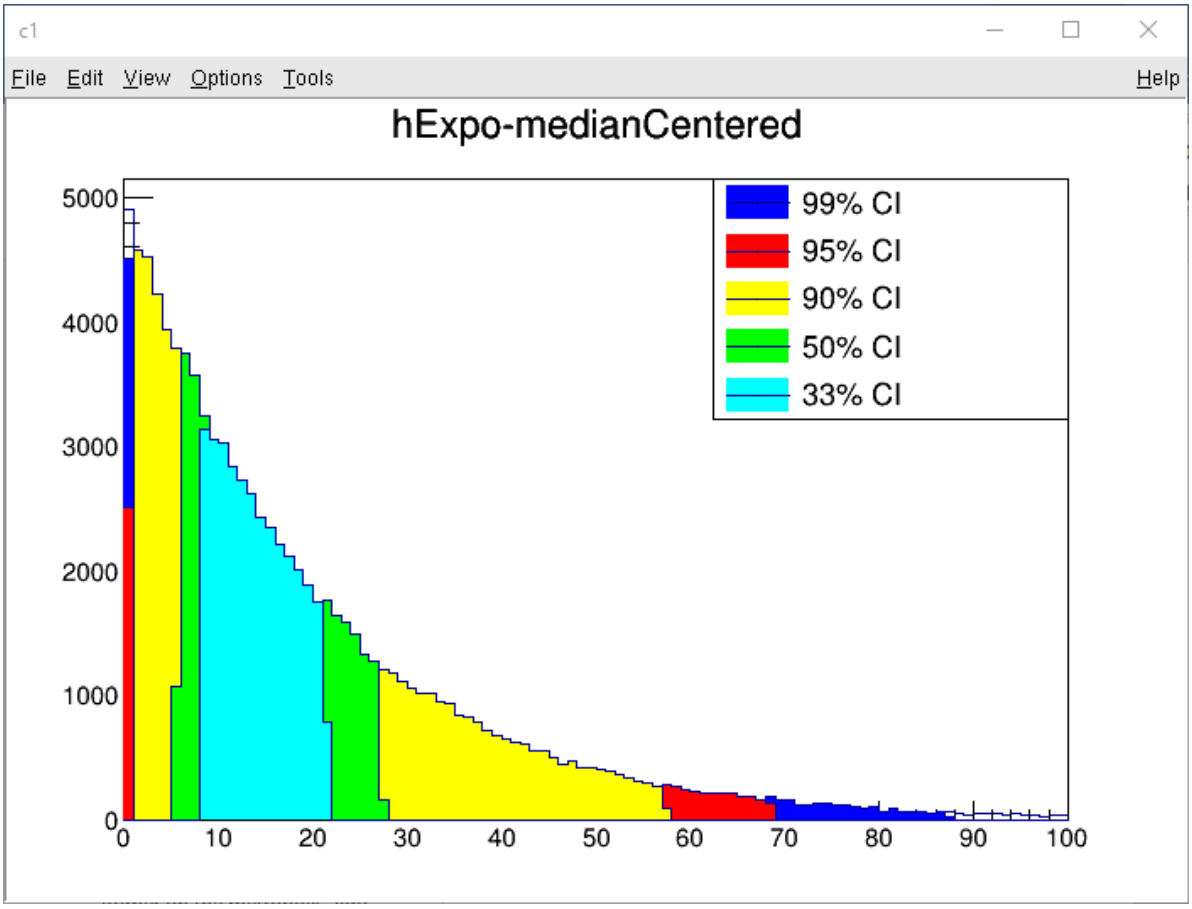

Figure C.1: Confidence intervals of an upper-limit-like exponential probability density function, taken symmetrically about the median. At no confidence level does the symmetric confidence interval include zero, which would likely be desirable.

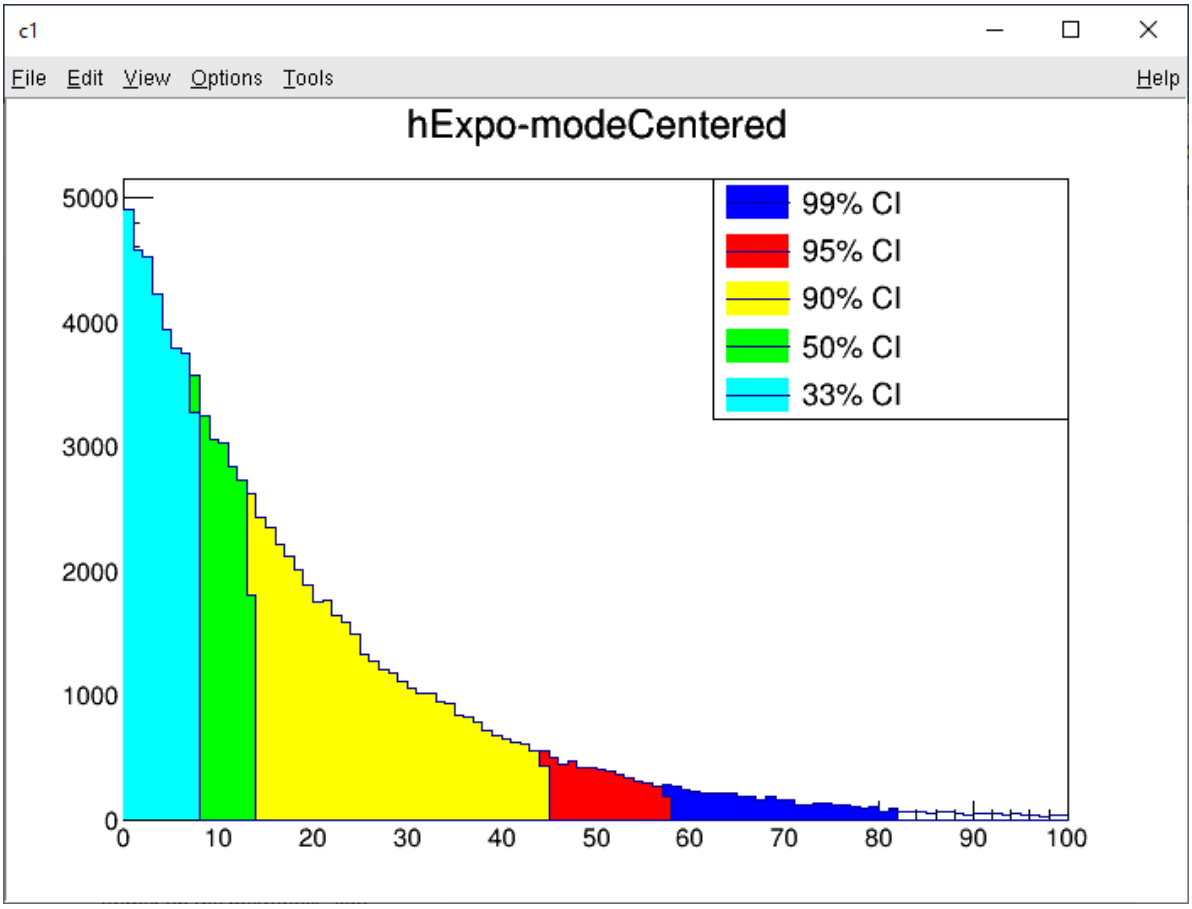

Figure C.2: Confidence intervals of an upper-limit-like exponential probability density function, taken asymmetrically about the mode and incremented according to the most probable direction. The asymmetric calculation nicely provides natural interpretations of limits.

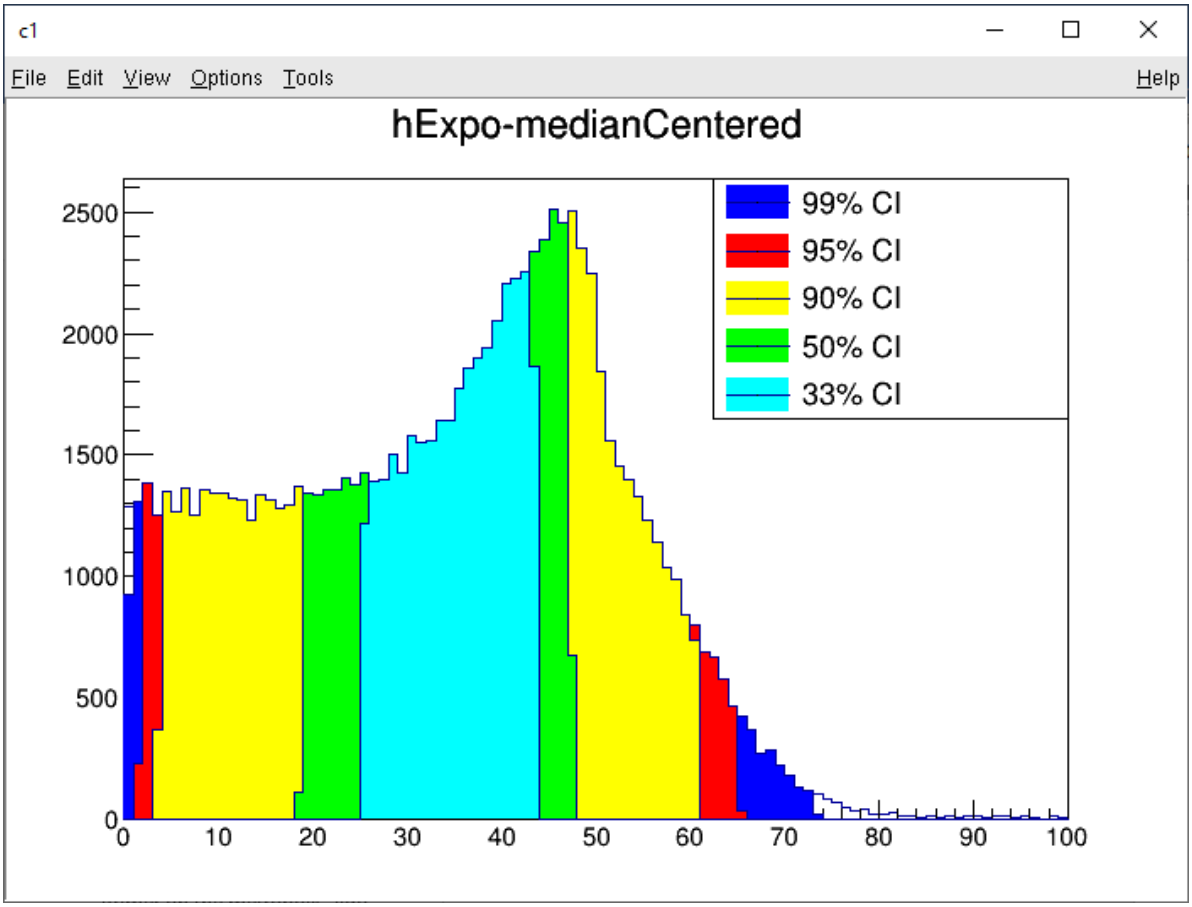

Figure C.3: Confidence intervals of a suggestive, but not conclusively non-zero probability density function, taken symmetrically about the median. At low values for the confidence interval, the peak in the probability density function is missed. Similarly to the median-scheme with the exponential distribution in Fig. C.1, zero is never included, even at high confidence.

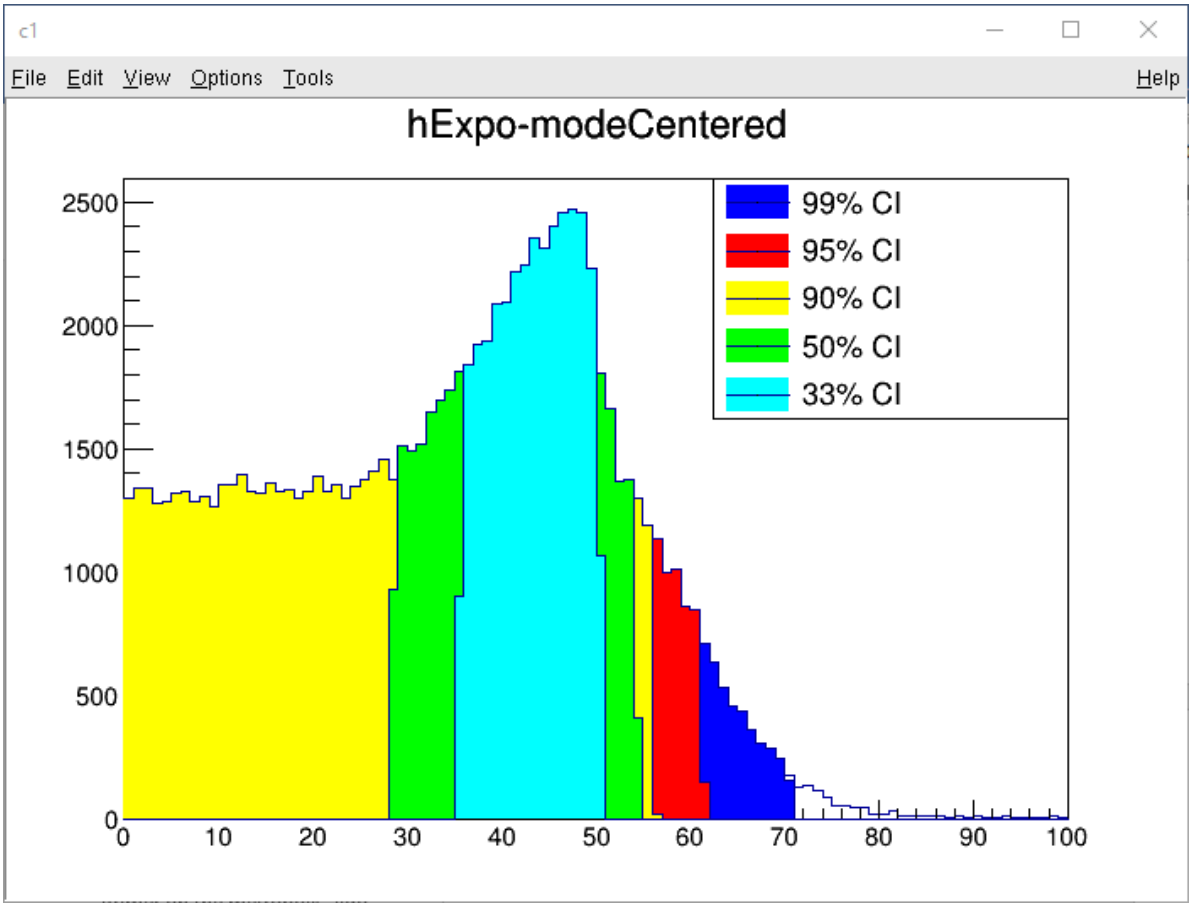

Figure C.4: Confidence intervals of a suggestive, but not conclusively non-zero probability density function, taken symmetrically about the median. At low values for the confidence interval, the peak in the probability density function is inferred. Similarly to the mode-scheme with the exponential distribution in Fig. C.2, at high confidence a limit-like confidence interval is retrieved.

BIBLIOGRAPHY

BIBLIOGRAPHY

[1] J.H. Kelley, E. Kwan, J.E. Purcell, C.G. Sheu, and H.R. Weller. Energy levels of light nuclei a=11. *Nuclear Physics A*, 880:88–195, 2012. ISSN 0375-9474. doi: https://doi.org/10.1016/j.nuclphysa.2012.01.010. URL https://www.sciencedirect.com/science/article/pii/S0375947412000413.

[2] J. Refsgaard, J. Büscher, A. Arokiaraj, H. O. U. Fynbo, R. Raabe, and K. Riisager. Clarification of large-strength transitions in the β decay of ^{11}Be. *Phys. Rev. C*, 99:044316, Apr 2019. doi: 10.1103/PhysRevC.99.044316. URL https://link.aps.org/doi/10.1103/PhysRevC.99.044316.

[3] Y Ayyad, B Olaizola, W Mittig, G Potel, V Zelevinsky, M Horoi, S Beceiro-Novo, M Alcorta, C Andreoiu, T Ahn, et al. Direct observation of proton emission in be 11. *Physical Review Letters*, 123(8):082501, 2019.

[4] A. Stolz, T. Baumann, T.N. Ginter, D.J. Morrissey, M. Portillo, B.M. Sherrill, M. Steiner, and J.W. Stetson. Production of rare isotope beams with the nscl fragment separator. *Nuclear Instruments and Methods in Physics Research Section B: Beam Interactions with Materials and Atoms*, 241(1):858–861, 2005. ISSN 0168-583X. doi: https://doi.org/10.1016/j.nimb.2005.07.168. URL https://www.sciencedirect.com/science/article/pii/S0168583X0501339X. The Application of Accelerators in Research and Industry.

[5] K Riisager, O Forstner, MJG Borge, JA Briz, M Carmona-Gallardo, LM Fraile, HOU Fynbo, T Giles, A Gottberg, A Heinz, et al. Be11 (βp), a quasi-free neutron decay? *Physics Letters B*, 732:305–308, 2014.

[6] L. J. Sun, M. Friedman, T. Budner, D. Pérez-Loureiro, E. Pollacco, C. Wrede, B. A. Brown, M. Cortesi, C. Fry, B. E. Glassman, J. Heideman, M. Janasik, A. Kruskie, A. Magilligan, M. Roosa, J. Stomps, J. Surbrook, and P. Tiwari. ^{25}Si β^+-decay spectroscopy. *Phys. Rev. C*, 103:014322, Jan 2021. doi: 10.1103/PhysRevC.103.014322. URL https://link.aps.org/doi/10.1103/PhysRevC.103.014322.

[7] M. Friedman, T. Budner, D. Pérez-Loureiro, E. Pollacco, C. Wrede, J. José, B. A. Brown, M. Cortesi, C. Fry, B. Glassman, J. Heideman, M. Janasik, M. Roosa, J. Stomps, J. Surbrook, and P. Tiwari. Low-energy ^{23}Al β-delayed proton decay and ^{22}Na destruction in novae. *Phys. Rev. C*, 101:052802, May 2020. doi: 10.1103/PhysRevC.101.052802. URL https://link.aps.org/doi/10.1103/PhysRevC.101.052802.

[8] T. Budner, M. Friedman, C. Wrede, B. A. Brown, J. José, D. Pérez-Loureiro, L. J. Sun, J. Surbrook, Y. Ayyad, D. W. Bardayan, K. Chae, A. A. Chen, K. A. Chipps, M. Cortesi, B. Glassman, M. R. Hall, M. Janasik, J. Liang, P. O'Malley, E. Pollacco, A. Psaltis, J. Stomps, and T. Wheeler. Constraining the ^{30}P$(p, \gamma)^{31}$S reaction rate in one novae via the weak, low-energy, β-delayed proton decay of ^{31}Cl.

Phys. Rev. Lett., 128:182701, May 2022. doi: 10.1103/PhysRevLett.128.182701. URL https://link.aps.org/doi/10.1103/PhysRevLett.128.182701.

[9] Jochen Erler, Noah Birge, Markus Kortelainen, Witold Nazarewicz, Erik Olsen, Alexander M Perhac, and Mario Stoitsov. The limits of the nuclear landscape. *Nature*, 486(7404):509–512, 2012.

[10] Bartosz Fornal and Benjamín Grinstein. Dark matter interpretation of the neutron decay anomaly. *Physical review letters*, 120(19):191801, 2018.

[11] Pieter Mumm. Resolving the neutron lifetime puzzle. *Science*, 360(6389):605–606, 2018.

[12] Fred E. Wietfeldt and Geoffrey L. Greene. Colloquium: The neutron lifetime. *Rev. Mod. Phys.*, 83:1173–1192, Nov 2011. doi: 10.1103/RevModPhys.83.1173. URL https://link.aps.org/doi/10.1103/RevModPhys.83.1173.

[13] K Abe, Y Haga, Y Hayato, M Ikeda, K Iyogi, J Kameda, Y Kishimoto, M Miura, S Moriyama, M Nakahata, et al. Search for proton decay via p→ e+ π 0 and p→ μ+ π 0 in 0.31 megaton· years exposure of the super-kamiokande water cherenkov detector. *Physical Review D*, 95(1): 012004, 2017.

[14] Robert E. Lopez and Michael S. Turner. Precision prediction for the big-bang abundance of primordial ^{4}He. *Phys. Rev. D*, 59:103502, Mar 1999. doi: 10.1103/PhysRevD.59.103502. URL https://link.aps.org/doi/10.1103/PhysRevD.59.103502.

[15] Particle Data Group, RL Workman, VD Burkert, V Crede, E Klempt, U Thoma, L Tiator, K Agashe, G Aielli, BC Allanach, et al. Review of particle physics. *Progress of theoretical and experimental physics*, 2022(8):083C01, 2022.

[16] FM Gonzalez, EM Fries, C Cude-Woods, T Bailey, M Blatnik, LJ Broussard, NB Callahan, JH Choi, SM Clayton, SA Currie, et al. Improved neutron lifetime measurement with ucn τ. *Physical review letters*, 127(16):162501, 2021.

[17] A. T. Yue, M. S. Dewey, D. M. Gilliam, G. L. Greene, A. B. Laptev, J. S. Nico, W. M. Snow, and F. E. Wietfeldt. Improved determination of the neutron lifetime. *Phys. Rev. Lett.*, 111:222501, Nov 2013. doi: 10.1103/PhysRevLett.111.222501. URL https://link.aps.org/doi/10.1103/PhysRevLett.111.222501.

[18] D. Baye and E.M. Tursunov. β delayed emission of a proton by a one-neutron halo nucleus. *Physics Letters B*, 696(5):464–467, 2011. ISSN 0370-2693. doi: https://doi.org/10.1016/j.physletb.2010.12.069. URL https://www.sciencedirect.com/science/article/pii/S0370269311000281.

[19] M Pfützner and K Riisager. Examining the possibility to observe neutron dark decay in nuclei. *Physical Review C*, 97(4):042501, 2018.

[20] Gordon Baym, D. H. Beck, Peter Geltenbort, and Jessie Shelton. Testing dark decays of baryons in neutron stars. *Phys. Rev. Lett.*, 121: 061801, Aug 2018. doi: 10.1103/PhysRevLett.121.061801. URL https://link.aps.org/doi/10.1103/PhysRevLett.121.061801.

[21] David McKeen, Ann E. Nelson, Sanjay Reddy, and Dake Zhou. Neutron stars exclude light dark baryons. *Phys. Rev. Lett.*, 121: 061802, Aug 2018. doi: 10.1103/PhysRevLett.121.061802. URL https://link.aps.org/doi/10.1103/PhysRevLett.121.061802.

[22] Benjamín Grinstein, Chris Kouvaris, and Niklas Grønlund Nielsen. Neutron star stability in light of the neutron decay anomaly. *Phys. Rev. Lett.*, 123:091601, Aug 2019. doi: 10.1103/PhysRevLett.123.091601. URL https://link.aps.org/doi/10.1103/PhysRevLett.123.091601.

[23] Jeffrey M Berryman, Susan Gardner, and Mohammadreza Zakeri. Neutron stars with baryon number violation, probing dark sectors. *Symmetry*, 14(3):518, 2022.

[24] JC Hardy and IS Towner. Superallowed 0+→ 0+ nuclear β decays: 2020 critical survey, with implications for v ud and ckm unitarity. *Physical Review C*, 102(4):045501, 2020.

[25] D Dubbers, H Saul, B Märkisch, T Soldner, and H Abele. Exotic decay channels are not the cause of the neutron lifetime anomaly. *Physics Letters B*, 791:6–10, 2019.

[26] Dirk Dubbers and Bastian Märkisch. Precise measurements of the decay of free neutrons. *Annual Review of Nuclear and Particle Science*, 71:139–163, 2021.

[27] M. Beck, F. Ayala Guardia, M. Borg, J. Kahlenberg, R. Muñoz Horta, C. Schmidt, A. Wunderle, W. Heil, R. Maisonobe, M. Simson, T. Soldner, R. Virot, O. Zimmer, M. Klopf, G. Konrad, S. Baeßler, F. Glück, and U. Schmidt. Improved determination of the β–$\overline{\nu}_e$ angular correlation coefficient a in free neutron decay with the aSPECT spectrometer. *Phys. Rev. C*, 101:055506, May 2020. doi: 10.1103/PhysRevC.101.055506. URL https://link.aps.org/doi/10.1103/PhysRevC.101.055506.

[28] K Riisager, MJG Borge, José Antonio Briz, M Carmona-Gallardo, O Forstner, LM Fraile, HOU Fynbo, A Garzon Camacho, JG Johansen, B Jonson, et al. Search for beta-delayed proton emission from ^{11}be. *The European Physical Journal A*, 56(3):1–8, 2020.

[29] A. Volya. Assessment of the beta-delayed proton decay rate of 11be. *Europhysics Letters*, 130(1):12001, may 2020. doi: 10.1209/0295-5075/130/12001. URL https://dx.doi.org/10.1209/0295-5075/130/12001.

[30] J. Okołowicz, M. Płoszajczak, and W. Nazarewicz. Convenient location of a near-threshold proton-emitting resonance in ^{11}B. *Phys. Rev. Lett.*, 124:042502, Jan 2020. doi: 10.1103/PhysRevLett.124.042502. URL https://link.aps.org/doi/10.1103/PhysRevLett.124.042502.

[31] J. Okołowicz, M. Płoszajczak, and I. Rotter. Dynamics of quantum systems embedded in a continuum. *Physics Reports*, 374(4):271–383, 2003. ISSN 0370-1573. doi: https://doi.org/10.1016/S0370-1573(02)00366-6. URL https://www.sciencedirect.com/science/article/pii/S0370157302003666.

[32] Wael Elkamhawy, Zichao Yang, Hans-Werner Hammer, and Lucas Platter. β-delayed proton emission from 11be in effective field theory. *Physics Letters B*, 821:136610, 2021. ISSN 0370-2693. doi: https://doi.org/10.1016/j.physletb.2021.136610. URL https://www.sciencedirect.com/science/article/pii/S0370269321005505.

[33] M. C. Atkinson, P. Navrátil, G. Hupin, K. Kravvaris, and S. Quaglioni. Ab initio calculation of the β decay from ^{11}Be to a ^{10}Be + p resonance. *Phys. Rev. C*, 105:054316, May 2022. doi: 10.1103/PhysRevC.105.054316. URL https://link.aps.org/doi/10.1103/PhysRevC.105.054316.

[34] Y. Ayyad, W. Mittig, T. Tang, B. Olaizola, G. Potel, N. Rijal, N. Watwood, H. Alvarez-Pol, D. Bazin, M. Caamaño, J. Chen, M. Cortesi, B. Fernández-Domínguez, S. Giraud, P. Gueye, S. Heinitz, R. Jain, B. P. Kay, E. A. Maugeri, B. Monteagudo, F. Ndayisabye, S. N. Paneru, J. Pereira, E. Rubino, C. Santamaria, D. Schumann, J. Surbrook, L. Wagner, J. C. Zamora, and V. Zelevinsky. Evidence of a near-threshold resonance in ^{11}B relevant to the β-delayed proton emission of ^{11}Be. *Phys. Rev. Lett.*, 129:012501, Jun 2022. doi: 10.1103/PhysRevLett.129.012501. URL https://link.aps.org/doi/10.1103/PhysRevLett.129.012501.

[35] RE Azuma, E Uberseder, EC Simpson, CR Brune, H Costantini, RJ De Boer, J Görres, M Heil, PJ LeBlanc, C Ugalde, et al. Azure: An r-matrix code for nuclear astrophysics. *Physical Review C*, 81(4):045805, 2010.

[36] E. Lopez-Saavedra, S. Almaraz-Calderon, B. W. Asher, L. T. Baby, N. Gerken, K. Hanselman, K. W. Kemper, A. N. Kuchera, A. B. Morelock, J. F. Perello, E. S. Temanson, A. Volya, and I. Wiedenhöver. Observation of a near-threshold proton resonance in ^{11}B. *Phys. Rev. Lett.*, 129:012502, Jun 2022. doi: 10.1103/PhysRevLett.129.012502. URL https://link.aps.org/doi/10.1103/PhysRevLett.129.012502.

[37] M. Friedman, D. Pérez-Loureiro, T. Budner, E. Pollacco, C. Wrede, M. Cortesi, C. Fry, B. Glassman, M. Harris, J. Heideman, M. Janasik, B.T. Roeder, M. Roosa, A. Saastamoinen, J. Stomps, J. Surbrook, P. Tiwari, and J. Yurkon. Gadget: a gaseous detector with germanium tagging. *Nuclear Instruments and Methods in Physics Research Section A: Accelerators, Spectrometers, Detectors and Associated Equipment*, 940:93–102, 2019. ISSN 0168-9002. doi: https://doi.org/10.1016/j.nima.2019.05.100. URL https://www.sciencedirect.com/science/article/pii/S0168900219308162.

[38] W.F. Mueller, J.A. Church, T. Glasmacher, D. Gutknecht, G. Hackman, P.G. Hansen, Z. Hu, K.L. Miller, and P. Quirin. Thirty-two-fold segmented germanium detectors to identify γ-rays from intermediate-energy exotic beams. *Nuclear Instruments and Methods in Physics Research Section A: Accelerators, Spectrometers, Detectors and Associated Equipment*, 466(3):492–498, 2001. ISSN 0168-9002. doi: https://doi.org/10.1016/S0168-9002(01)00257-1. URL https://www.sciencedirect.com/science/article/pii/S0168900201002571.

[39] Glenn F Knoll. *Radiation detection and measurement*. John Wiley & Sons, 2010.

[40] Kenneth S Krane. *Introductory nuclear physics*. John Wiley & Sons, 1991.

[41] LeCroy Corporation. 222 nim dual gate and delay generator, 0000. URL https://teledynelecroy.com/lrs/dsheets/222.htm.

[42] K. Starosta, C. Vaman, D. Miller, P. Voss, D. Bazin, T. Glasmacher, H. Crawford, P. Mantica, H. Tan, W. Hennig, M. Walby, A. Fallu-Labruyere, J. Harris, D. Breus, P. Grudberg, and W.K. Warburton. Digital data acquisition system for experiments with segmented detectors at national superconducting cyclotron laboratory. *Nuclear Instruments and Methods in Physics Research Section A: Accelerators, Spectrometers, Detectors and Associated Equipment*, 610 (3):700–709, 2009. ISSN 0168-9002. doi: https://doi.org/10.1016/j.nima.2009.09.016. URL https://www.sciencedirect.com/science/article/pii/S0168900209017392.

[43] C.J. Prokop, S.N. Liddick, B.L. Abromeit, A.T. Chemey, N.R. Larson, S. Suchyta, and J.R. Tompkins. Digital data acquisition system implementation at the national superconducting cyclotron laboratory. *Nuclear Instruments and Methods in Physics Research Section A: Accelerators, Spectrometers, Detectors and Associated Equipment*, 741:163–168, 2014. ISSN 0168-9002. doi: https://doi.org/10.1016/j.nima.2013.12.044. URL https://www.sciencedirect.com/science/article/pii/S0168900213017488.

[44] Inc Advanced Measurement Technology. Model 566 time-to-amplitude converter (tac) operating and service manual, 0000. URL https://www.ortec-online.com/-/media/ametekortec/manuals/5/566-mnl.pdf.

[45] D. J. Millener, D. E. Alburger, E. K. Warburton, and D. H. Wilkinson. Decay scheme of ^{11}Be. *Phys. Rev. C*, 26:1167–1185, Sep 1982. doi: 10.1103/PhysRevC.26.1167. URL https://link.aps.org/doi/10.1103/PhysRevC.26.1167.

[46] D. E. Alburger, D. J. Millener, and D. H. Wilkinson. Delayed particles from the beta decay of ^{11}Be. *Phys. Rev. C*, 23:473–479, Jan 1981. doi: 10.1103/PhysRevC.23.473. URL https://link.aps.org/doi/10.1103/PhysRevC.23.473.

[47] James F Ziegler, Matthias D Ziegler, and Jochen P Biersack. Srim–the stopping and range of ions in matter (2010). *Nuclear Instruments and Methods in Physics Research Section B: Beam Interactions with Materials and Atoms*, 268(11-12):1818–1823, 2010.

[48] OB Tarasov and D Bazin. Lise++: Radioactive beam production with in-flight separators. *Nuclear Instruments and Methods in Physics Research Section B: Beam Interactions with Materials and Atoms*, 266(19-20):4657–4664, 2008.

[49] Christian Iliadis. *Nuclear physics of stars*. John Wiley & Sons, 2015.

[50] Tamas Aleksei Budner. *31cl Beta-Delayed Proton Decay and Classical Nova Nucleosynthesis*. PhD thesis, Michigan State University, 2022.

[51] S.F. Biagi. A multiterm boltzmann analysis of drift velocity, diffusion, gain and magnetic-field effects in argon-methane-water-vapour mixtures. *Nuclear Instruments and Methods in Physics Research Section A: Accelerators, Spectrometers, Detectors and Associated Equipment*, 283(3):716–722, 1989. ISSN 0168-9002. doi: https://doi.org/10.1016/0168-9002(89)91446-0. URL https://www.sciencedirect.com/science/article/pii/0168900289914460.

[52] S.F. Biagi. Monte carlo simulation of electron drift and diffusion in counting gases under the influence of electric and magnetic fields. *Nuclear Instruments and Methods in Physics Research Section A: Accelerators, Spectrometers, Detectors and Associated Equipment*, 421(1):234–240, 1999. ISSN 0168-9002. doi: https://doi.org/10.1016/S0168-9002(98)01233-9. URL https://www.sciencedirect.com/science/article/pii/S0168900298012339.

[53] Pierre Descouvemont and D Baye. The r-matrix theory. *Reports on progress in physics*, 73 (3):036301, 2010.

[54] PL Kapur and Ro Peierls. The dispersion formula for nuclear reactions. *Proceedings of the Royal Society of London. Series A. Mathematical and Physical Sciences*, 166(925):277–295, 1938.

[55] Carl R Brune. Alternative parametrization of r-matrix theory. *Physical Review C*, 66(4): 044611, 2002.

[56] AM Lane and RG Thomas. R-matrix theory of nuclear reactions. *Reviews of Modern Physics*, 30(2):257, 1958.

[57] FC Barker and EK Warburton. The beta-decay of 8he. *Nuclear Physics A*, 487(2):269–278, 1988.

[58] James F Ziegler, Jochen P Biersack, and Matthias D Ziegler. Srim, 2003.

[59] M Eugene Rudd, RD DuBois, LH Toburen, CA Ratcliffe, and TV Goffe. Cross sections for ionization of gases by 5-4000-kev protons and for electron capture by 5-150-kev protons. *Physical Review A*, 28(6):3244, 1983.

[60] Claudia Carmen Montanari and Jorge Esteban Miraglia. Multiple ionization of argon by helium ions. *Journal of Physics B: Atomic, Molecular and Optical Physics*, 49(17):175203, 2016.

[61] ALC Losqui, F Zappa, GM Sigaud, W Wolff, MM Sant'Anna, ACF Santos, H Luna, and WS Melo. Absolute cross sections for electron loss, electron capture, and multiple ionization in collisions of li2+ with argon. *Journal of Physics B: Atomic, Molecular and Optical Physics*, 47(4):045202, 2014.

[62] A ICRU. Average energy required to produce an ion pair. *ICRU Report 31*, 1979.

[63] Jens Lindhard, Morten Scharff, and Hans E Schiøtt. *Range concepts and heavy ion ranges*, volume 33. Munksgaard Copenhagen, 1963.

[64] M. Peck, A. Göök, J. Enders, F.-J. Hambsch, and S. Oberstedt. Pulse-height defect of ar+cf4 mixtures as a counting gas for fission-fragment detectors. *Nuclear Instruments and Methods in Physics Research Section A: Accelerators, Spectrometers, Detectors and Associated Equipment*, 919:105–112, 2019. ISSN 0168-9002. doi: https://doi.org/10.1016/j.nima.2018.12.060. URL https://www.sciencedirect.com/science/article/pii/S0168900218318576.

[65] Ralph A Lowry and Glenn H Miller. Ionization yield of protons in nitrogen and argon. *Physical Review*, 109(3):826, 1958.

[66] JA Dennis. Ionization by low energy heavy ions in nitrogen, carbon dioxide, argon and hydrocarbon gases. *radiation effects*, 8(1-2):87–98, 1971.

[67] HV Larson. Energy loss per ion pair for protons in various gases. *Physical Review*, 112(6): 1927, 1958.

[68] Van Dat Nguyen and Maurice Chemtob. Calculated and measured w values in n 2, ar, ch 4 and co 2 gases for ions h+, he+, c+, n+, o+ and ar+ in the energy range 25 kev to 375 kev. Technical report, CEA Centre d'Etudes Nucleaires de Fontenay-aux-Roses, 1979.

[69] JA Phipps, JW Boring, and RA Lowry. Total ionization in argon by heavy ions of energies 8 to 100 kev. *Physical Review*, 135(1A):A36, 1964.

[70] SE Chappell and JH Sparrow. The average energy required to produce an ion pair in argon, nitrogen, and air for 1-to 5-mev alpha particles. *Radiation research*, 32(3):383–403, 1967.

[71] M Chemtob, N Parmentier, and VD Nguyen. Some experimental results on w-values for heavy particles. *Physics in Medicine & Biology*, 23(6):1197, 1978.

[72] R LEIMGRUBER, P HUBER, and E BAUMGARTNER. Messung der arbeit pro ionenpaar in verschiedenen gasen für stickstoff- und sauerstoffionen im energiegebiet von 0,14 bis 0,7 mev. *HELVETICA PHYSICA ACTA*, 38(5):499–513, 1965.

[73] William P Jesse. Alpha-particle ionization in argon-methane mixtures and the energy dependence of the ion pair-formation energy. *Physical Review*, 174(1):173, 1968.

[74] MN Varma and JW Baum. Energy dependence of w for alpha particles in n2, co2, ch4, ar, h2 and rossi-type tissue-equivalent gases. *Physics in Medicine & Biology*, 23(6):1162, 1978.

[75] H Tawara, N Ishida, J Kikuchi, and T Doke. Measurements of the w values in argon, nitrogen, and methane for 0.93 to 5.3 mev alpha particles. *Nuclear Instruments and Methods in Physics Research Section B: Beam Interactions with Materials and Atoms*, 29(3):447–455, 1987.

[76] VD Nguyen, M Chemtob, J Chary, F Posny, and N Parmentier. Recent experimental results on w-values for heavy particles. *Physics in Medicine & Biology*, 25(3):509, 1980.

[77] JR Macdonald and G Sidenius. The total ionization in methane of ions with 1<= z<= 22 at energies from 10 to 120 kev. *Physics Letters A*, 28(8):543–544, 1969.

[78] JP Biersack and JF Ziegler. Refined universal potentials in atomic collisions. *Nuclear Instruments and Methods in Physics Research*, 194(1-3):93–100, 1982.

[79] SG Lias. Ionization energy evaluation in nist chemistry webbook, nist standard reference database, number 69. *Linstrom PJ, Mallard WG, Eds*, page 20899, 2016.

[80] A. Kramida, Yu. Ralchenko, J. Reader, and and NIST ASD Team. NIST Atomic Spectra Database (ver. 5.10), [Online]. Available: https://physics.nist.gov/asd [2022, December 12]. National Institute of Standards and Technology, Gaithersburg, MD., 2022.

[81] W Haeberli, P Huber, and E Baldinger. Arbeit pro ionenpaar in gasgemischen fur alpha-teilchen (work per ion pair in gas mixtures for alpha-particle). *HELVETICA PHYSICA ACTA*, 23(5):481–484, 1950.

[82] Willy Haeberli, P Huber, and E Baldinger. Arbeit pro ionenpaar von gasen und gasmischungen fur alpha-teilchen (work per ion pair of gases and gas mixtures for alpha particles). *HELVETICA PHYSICA ACTA*, 26(2):145–180, 1953.

[83] H Tawara, J Kikuchi, and T Doke. Energy dependences of w values for mev alpha particles in ar-xe, ar-n2, and ar-ch4 mixtures. *Nuclear Instruments and Methods in Physics Research Section B: Beam Interactions with Materials and Atoms*, 29(3):456–460, 1987.

[84] A. Gelman, W. R. Gilks, and G. O. Roberts. Weak convergence and optimal scaling of random walk Metropolis algorithms. *The Annals of Applied Probability*, 7(1):110 – 120, 1997. doi: 10.1214/aoap/1034625254. URL https://doi.org/10.1214/aoap/1034625254.

[85] J Okołowicz, M Płoszajczak, and W Nazarewicz. β-p and $\beta - \alpha$ decay of the 11be neutron halo ground state. *Journal of Physics G: Nuclear and Particle Physics*, 49(10):10LT01, aug 2022. doi: 10.1088/1361-6471/ac8948. URL https://dx.doi.org/10.1088/1361-6471/ac8948.

[86] Wael Elkamhawy, Zichao Yang, Hans-Werner Hammer, and Lucas Platter. Weak decay of halo nuclei. *arXiv*, December 2022. doi: 10.48550/arXiv.2212.05087. URL https://arxiv.org/abs/2212.05087.

[87] Nguyen Le Anh, Bui Minh Loc, Naftali Auerbach, and Vladimir Zelevinsky. Single-particle properties of the near-threshold proton-emitting resonance in ^{11}B. *Phys. Rev. C*, 106:L051302, Nov 2022. doi: 10.1103/PhysRevC.106.L051302. URL https://link.aps.org/doi/10.1103/PhysRevC.106.L051302.